Visible Light-Induced and λ-Orthogonal Photochemical Tools for Bioorganic Chemistry

Zur Erlangung des akademischen Grades eines
DOKTORS DER NATURWISSENSCHAFTEN
(Dr. rer. nat.)

von der KIT-Fakultät für Chemie und Biowissenschaften
des Karlsruher Instituts für Technologie (KIT)

genehmigte
Dissertation
von
M.Sc. Rita Tabea Michenfelder
aus Baden-Baden

Dekan: Prof. Dr. Martin Bastmeyer
Referent: Prof. Dr. Hans-Achim Wagenknecht
Korreferent: Prof. Dr. Stefan Bräse
Cotutelle-Referent: Prof. Dr. Christopher Barner-Kowollik

Tag der mündlichen Prüfung: 18. April 2024

für Aaron Joshua

We cannot control anyone’s reactions but our own. Therefore, we shouldn’t work to please others or to gain their approval; we must, instead, set our own goals and work to satisfy those.

Katalin Karikó (2023 Nobel Prize Laureate*)*

Die vorliegende Arbeit wurde im Zeitraum von Februar 2021 bis April 2024 im Rahmen einer Cotutelle-Vereinbarung unter der Betreuung von Prof. Dr. Hans-Achim Wagenknecht und Prof. Dr. Christopher Barner-Kowollik am *Karlsruher Institut für Technologie* (KIT) in Deutschland und der *Queensland University of Technology* (QUT) in Australien angefertigt.

Statement of Original Authorship

The work contained in this joint doctoral thesis undertaken between *Queensland University of Technology* (QUT) and *Karlsruhe Institute of Technology* (KIT) has not been previously submitted to meet requirements for an award at these or any other higher educational institutions. To the best of my knowledge and belief, this thesis contains no material previously published by another person except where due reference is made.

6 February 2025

Rita T. Michenfelder Date

Eidesstattliche Erklärung

Ich versichere hiermit, dass ich die vorliegende Arbeit selbstständig verfasst und keine anderen als die angegebenen Quellen und Hilfsmittel verwendet habe. Wörtlich oder inhaltlich übernommene Stellen sind als solche gekennzeichnet und die Satzung des Karlsruher Instituts für Technologie (KIT) zur Sicherung guter wissenschaftlicher Praxis wurde in der jeweilis gültigen Fassung beachtet.

Des Weiteren erkläre ich, dass ich mich derzeit in keinem weiteren laufenden Promotionsverfahren befinde und auch keine vorausgegangenen Promotionsversuche unternommen habe.

6. Februar 2025

Rita T. Michenfelder Datum

Kurzfassung

Bioorthogonale Reaktionen haben sich in den vergangenen 20 Jahren zu einem der wichtigsten biochemischen Werkzeuge zur Visualisierung von Proteinen, Glykanen und Nukleinsäuren in Zellorganismen entwickelt. Neben der Möglichkeit, zelluläre Prozesse sichtbar zu machen, helfen bioorthogonale Reaktionen auch bei der Verbesserung des zielgerichteten Einsatzes von Chemotherapeutika. Viele Krebsmedikamente zielen darauf ab, die DNA-Replikation und damit einhergehend das Wachstum des Tumorgewebes in der Zelle zu hemmen. Dies führt zu einem verstärkten Interesse, neue Markierungsstrategien für die Visualisierung von Nukleinsäuren zu entwickeln, um ihre vielfältigen biologischen Funktionen besser zu verstehen.

Die vorliegende Doktorarbeit ist in zwei Hauptteile gegliedert. Im ersten Projekt wird eine neuartige licht-induzierte bioorthogonale Markierungsstrategie für Nukleinsäuren entwickelt und in lebenden Zellen angewandt. Hierbei wird eine [2+2] photoreaktive Styrylquinoxalin (SQ)-Einheit sowohl postsynthetisch in einen DNA-Strang eingebaut als auch in einen Farbstoff (Atto655) eingeführt. Die Markierung der DNA erfolgt durch Belichtung mit einer 450 nm LED und wird mit UV/Vis-Spektroskopie, HPLC-Analyse und Gelelektrophorese bestätigt. Dabei kann gezeigt werden, dass eine 30-minütige Belichtung bereits zu einer Markierungsaubeute von 58% führt. Anschließend wird die Anwendbarkeit des neu entwickelten licht-induzierten Markierungskonzepts in lebenden *HeLa*-Zellen untersucht. Erste Experimente bestätigen eine hohe Eigenfluoreszenz des Farbstoffs, weshalb ein Förster-Resonanzenergietransfer genutzt wird, um die DNA der lebenden *HeLa*-Zellen erfolgreich zu visualisieren. Insgesamt handelt es sich hierbei um das erste Beispiel einer licht-induzierten Markierung von Oligonukleotiden im sichtbaren Wellenlängenbereich. Durch die erfolgreiche [2+2] Cycloaddition in lebenden Zellen wird gezeigt, dass Styrylquinoxaline hohes Potenzial als bioorthogonale Werkzeuge aufweisen, da sie sehr selektiv unter physiologischen Bedingungen (neutraler pH-Wert, T = 37 °C, wässriges Medium) in hohen Ausbeuten reagieren und keine Nebenreaktionen mit anderen natürlich vorkommenden biologischen Molekülen eingehen.

Der zuvor erwähnte zielgerichtete Einsatz von Chemotherapeutika schließt mit ein, dass diese effizient von Trägersystemen an ihren Wirkungsort gebracht werden. Die Trägersysteme transportieren ihre Frachtmoleküle in einer inaktiven Form und überführen diese dann durch einen bestimmten Auslöser (bspw. Licht-, Temperatur- oder pH-Änderung) in eine aktive Form, wobei nur die Verwendung von Licht eine bedarfsgerechte sowie ort- und zeitgesteuerte Kontrolle über die Freisetzung zulässt.

Im zweiten Projekt der vorliegenden Doktorarbeit wird ein duales Trägersystem entwickelt und charakterisiert, das die sequenzielle und vollständig wellenlängengesteuerte Freisetzung von Frachtmolekülen ermöglicht. Hierbei werden 7-(Diethylamin)-Cumarin und 3-Perylen als photoaktivierbare Gruppen eingesetzt, die in einer *Passerini*-Reaktion mit Isocyaniden und Carbonsäuren kombiniert werden. Die Carbonsäuren dienen dabei als Modell-Freisetzungsreagenzien, deren vollständige Abspaltung in ersten LED-Belichtungsexperimenten (405 nm LED für Cumarin und 445 nm LED für Perylen) durch UV/Vis-Spektroskopie, LC-MS Analyse und NMR-Spektroskopie bestätigt wird. Um die am besten geeigneten Wellenlängen für die unabhängige Aktivierung beider Chromophore zu ermitteln, werden photochemische „Action Plots“ aufgezeichnet, die eine hohe Reaktivität beider Chromophore außerhalb ihrer jeweiligen Absorptionsmaxima aufdecken. Zudem wird gezeigt, dass beide Chromophore eine hohe Reaktivität in hochenergetischen Wellenlängen aufweisen (λ = 370 nm), was die λ-Orthogonalität zunächst vor Probleme stellt. Da die Quantenausbeute der Cumarin-modifizierten Verbindung höher ist als die des Perylen-modifizierten Substrats, kann dies jedoch durch eine unterschiedliche Anzahl an Photonen gelöst werden. Die Sequenzunabhängigkeit und vollständige Orthogonalität des Systems wird anschließend anhand eines einfachen LED-Aufbaus bei 405 nm (20 mW) und 505 nm (40 mW) demonstriert, wobei beide möglichen Übergänge (hochenergetisch zu niederenergetisch und niederenergetisch zu hochenergetisch) untersucht werden. Des Weiteren wird gezeigt, dass die Reaktivität unabhängig des Freisetzungsreagenzes ist. Die hier untersuchten Chromophore bieten daher ein breites Anwendungsspektrum für die wellenlängengesteuerte Freisetzung von Frachtmolekülen, wie z.B. die lichtinduzierte Verabreichung von Medikamenten.

Table of Contents

Kurzfassung..i

List of Figures...v

List of Tables xxi

List of Abbreviations xxiii

1 General Introduction 1

2 Theoretical Background 5

2.1 Bioorthogonal Reactions 5

2.2 Light-Induced Bioorthogonal Reactions 11

2.2.1 Photoclick Reactions...11

2.2.2 Light-Triggered Bond Forming Reactions.................................14

2.3 Laser Systems 18

2.4 Photochemical Action Plots 20

2.5 Photocleavage Reactions 23

2.5.1 Photoorthogonal Cleavage Reactions 26

2.6 Multicomponent Reactions...28

3 DNA Labelling in Live Cells via [2+2] Photocycloaddition...........................31

3.1 Synthesis of SQ-Modified DNA and SQ-Modified Atto655 Dye...............33

3.2 Irradiation Experiments 37

3.3 Labelling Experiments...40

3.4 Labelling Experiments in Live Cells 44

3.5 Conclusion and Outlook 53

4 Action Plots for Photochemical Release Systems 57

4.1 Synthesis of the Chromophore Systems 59

4.2 LED Cleavage Experiments 63

4.3 Action Plots of the Chromophore Systems 68

4.3.1 Action Plot of the Coumarin-Modified Compound 24 68

4.3.2 Action Plot of the Perylene-Modified Compound 26 70
4.4 Pathway-Independent λ-Orthogonal Cleavage 73
4.5 Drug Release by Visible Light Irradiation 77
4.6 Conclusion and Outlook 81

5 Experimental Section 85
5.1 Materials and Methods 85
5.2 Irradiation Setups 90
5.2.1 LED Irradiation 90
5.2.2 20 Hz Tuneable Laser System 90
5.3 Cell Experiments 93
5.4 Synthetic Procedures 94
5.4.1 DNA Building Blocks and SQ-modified Atto655 dye 94
5.4.2 SQ-modified DNA2 105
5.4.3 SQ-modified DNA6 and DNA7 106
5.4.4 Photocaged Compounds 107
5.5 Kinetic and Action Plot Measurements 130
5.5.1 Coumarin-Modified Compound 24 130
5.5.2 Perylene-Modified Compound 26 135
5.5.3 Coumarin-Modified Compound 28 138
5.6 Sequential LED Irradiation 141

6 References 143

7 Appendix 149
7.1 DNA Labelling in Live Cells via [2+2] Cycloaddition 149
7.2 Action Plots for Photochemical Release Systems 154

8 Acknowledgments 157

9 Curriculum Vitae 163
9.1 Publications 164
9.2 Conferences and Oral Presentations 165
9.3 Student Supervision 166

List of Figures

Figure 1: Schematic representation of bioorthogonal labelling of DNA. A building block (*e.g.*, a DNA base) of the biooligomer of interest (DNA) is modified with a chemical reporter (grey hemicircle) and subsequently incorporated metabolically to react with its reaction partner which is modified with a label (red sphere, *e.g.*, a fluorescent dye). 5

Figure 2: Overview of commonly used bioorthogonal reactions: copper-catalysed azide alkyne cycloaddition (CuAAC, red), strain-promoted azide alkyne cycloaddition (SPAAC, beige), inverse electron-demand Diels-Alder cycloaddition (iEDDA, bright green), and photoclick reaction (dark green). 7

Figure 3: A: Examples of strained cyclooctyne derivatives for SPAAC. Difluorocyclooctyne (DIFO), bicyclononyne (BCN) and biarylazacyclooctyne (BARAC), arranged according to their reactivity and lipophilicity. B: Simplified application of a BCN-modified building block and an azide-modified fluorescent dye for SPAAC bioorthogonal labelling in mice 8

Figure 4: A: Most commonly used dienophiles for iEDDA: Cyclopropene (CP), norbonene (NB), bicyclononyne (BCN) and trans-cyclooctene (TCO), organised according to their reactivity and steric hindrance. B: Simplified application of a TCO-modified building block and a tetrazine-modified fluorescent dye for iEDDA bioorthogonal labelling in *HeLa* cells. C: Orthogonal SPAAC or iEDDA click chemistry using BCN as mutual starting material. 9

Figure 5: Mechanism of the nitrile imine / alkene photoclick reaction: After irradiation of a 2,5-diaryltetrazole, nitrogen is released to generate a highly reactive nitrile imine that results in building a fluorescent pyrazoline product through reaction with an electron-deficient alkene. 11

Figure 6: Synthetic routes for photoinduced NITEC reactions of (*N*,*N*-dimethyl)aminopyrene aryl tetrazole (APAT). Left arrow: Polymer end-group modification using a 515 nm LED and a maleimide-functionalised polymer. Right arrow: Metabolic labelling of fixed *HeLa* cells, incubated with vinyl-deoxyuridine prior to irradiation with a 450 nm LED. 13

Figure 7: The highly reactive nitrile imine species shows cross-reactivity with moieties present in physiological environments, including water, amines, thiols and carboxylic acids as well as a dimerization as side reaction. 13

Figure 8: [2+2] photocycloaddition of unsymmetrically substituted double bonds that form a non-aromatic cyclobutan structure. Subsequent irradiation with short wavelength light may lead to cleavage into different monomers...14

Figure 9: A: Visible light-driven bioorthogonal [4+2] photocycloaddition reaction between dione vinylethers and phenanthrenequinones (PQs). B: Ligation strategy via double nucleophilic substitution of chloroquinoxalines (CQs) and *ortho*-dithiophenols (DTs)..........15

Figure 10: A: [2+2] Photocycloaddition of PEG-Styrylquinoxaline (PEG-SQ). B: Photocontrol of duplex formation between artificial serinol nucleic acid (SNA) and target RNA using 8-pyrenylvinyl adenine as photoresponsive nucleobase. 16

Figure 11: Simplified schematic illustration of the interaction of the three main components of a laser: pump source, active laser medium and resonator. The laser action begins as soon as the number of amplified photons is higher than the cavity loss and the photons are exiting through a partially reflective mirror as a spatiotemporally coherent, polarised laser beam...19

Figure 12: A: Simplified scheme of wavelength-orthogonal crosslinking of hydrogel networks using styrylpyrido[2,3-b]pyrazines (SPPs) and acrylpyrenes (APs). B: Example of an action plot with random red-shifted reactivity of the chromophore in comparison to its UV/Vis absorption band. 22

Figure 13: Overview over commonly used photoprotective groups (PPGs) and their respective cleavage wavelengths: nitrobenzenes (λ = 300-360 nm), coumarin (λ = 405-470 nm), perylenes (λ = 480-530 nm) and BODIPY ($\lambda \geq$ 540 nm). LG = Leaving group. 23

Figure 14: Assumed mechanism of coumarin-photocaged carboxylic acids. After light absorption and excitation (i), the photocaged substrate relaxes into the lowest (π,π)* excited single state, which is stabilised by the push-pull-system between the amine and the carbonyl group (ii). A heterocyclic bond cleavage follows, leading to the tight ion pair (TIP). The reaction with a nucleophile results in the formation of the free coumarin derivate and the uncaged carboxylic acid.[118] 25

Figure 15: Simplified concept for multiplexed photocleavage to trigger translation of different mRNAs by irradiation with two different wavelengths. The translation is inhibited for both mRNAs until the photocleavable groups are removed separately by irradiation with either blue or violet light. 27

Figure 16: Possible mechanisms for the *Passerini* three component reaction employing aldehydes (black), carboxylic acids (orange) and isocyanides (green). Top: “open-chain mechanism”. After protonation of the carbonyl component of the aldehyde, nucleophilic additions of the isocyanide and carboxylate residue take place. The resulting nitrilium ion is the key intermediate and is subjected to an acyl group transfer, leading to the *Passerini* product after a Mumm-like rearrangement. Bottom: “concerted mechanism". The three components undergo a sequence of nucleophilic additions to a five-membered ring, following Mumm-like rearrangements eventually lead to the *Passerini* product.....29

Figure 17: Visible light-induced orthogonal labelling in live cells, employing styrylquinoxaline (SQ)-modified DNA and an SQ-modified Atto655 dye (red sphere). Figure reproduced from ref.[169] with permission from the Royal Society of Chemistry. 31

Figure 18: Synthesis of SQ-NHS ester **7**: a) Ethyl-4-bromobutyrate, K_2CO_3, DMF, 50 °C, 2 h, 82%; b) Methylglyoxal, ZnI_2, EtOH / H_2O, 80 °C, 1 h, 61%; c) Piperidine, acetic acid, toluene, 115 °C, 48 h, 71%; d) LiOH, THF, r.t., 1 h, 81%; e) NHS·HCl, DMF, r.t., 6 h, 82 %. 33

Figure 19: Synthesis of phosphoramidite **13**: a) Copper(I) iodide, tetrakis(triphenylphosphine)-palladium(0), triethylamine, DMF, 50 °C, 5 h, 55%; b) Hydrogen, Pd/C, MeOH, r.t., 6 h, 80%; c) 4,4'-dimethoxytrityl chloride, silver(I) nitrate, pyridine, r.t., 16 h, 60%; d) 2-cyanoethyl *N,N*-diisopropyl-chlorophosphoramidite, DIPEA, DCM, r.t., 2 h, 63%. 34

Figure 20: a) Synthesis of **DNA1**: Incorporation of **13** into **DNA1** via DNA synthesiser, followed by cleavage of the TFAc group with 25% NH_4OH, 55 °C, 16 h; b) Synthesis of **DNA2**: **7**, DIPEA, DMF, r.t., 48 h; c) Synthesis of SQ-modified Atto655 dye **14**: DIPEA, DMF, r.t., 16 h, 69%. 35

Figure 21: UV/Vis absorbance of **DNA2**: 2.50 µM solution in 10 mM Na-P_i buffer with 250 mM NaCl at pH 7 at 20 °C. 36

Figure 22: Fusion of two non-complementarty **DNA2** strands via [2+2] cycloaddition to homo-dimerized **(DNA2)₂** through irradiation of 50 µM **DNA2** in H_2O, 10 mM Na-P_i buffer, 250 mM NaCl, pH 7 at 20 °C with a 450 nm LED for 24 h in total. 37

Figure 23: Left: UV/Vis spectroscopic changes and right: RP-HPLC analyses ($\lambda_{detection}$ = 260 nm) of 50 µM **DNA2** in H_2O, 10 mM Na-P_i buffer, 250 mM NaCl, pH 7 at 20 °C over 24 h of irradiation at 20 °C with a 450 nm LED. 38

Figure 24: Agarose gel electrophoretic analysis of **(DNA2)₂** after irradiation of 50 µM **DNA2** at 20 °C with a 450 nm LED for 5 h in aqueous solution containing 10 mM Na-P_i buffer and 250 mM NaCl in a total volume of 600 µL in a crimp vial. Staining was performed using SybrGreen™, followed by visualisation under UV light (λ_{exc} = 312 nm). 39

Figure 25: Synthesis of **DNA3** through [2+2] cycloaddition of **DNA2** and SQ-modified Atto655 dye **14** in H_2O, 10 mM Na-P_i buffer, 250 mM NaCl, pH 7 at 20 °C through irradiation with a 450 nm LED for 5 h. 40

Figure 26: Denaturing PAGE analysis of **DNA3** after irradiation of **DNA2** and SQ-modified Atto655 dye **14** (1:1 equivalents) at 20 °C with a 450 nm LED for 5 h in aqueous solution containing 5% DMF, 10 mM Na-P_i buffer and 250 mM NaCl in a total volume of 600 µL in a crimp vial. Staining was performed using SybrGreen™, followed by visualisation under UV light (λ_{exc} = 312 nm). 41

Figure 27: A: Agarose gel electrophoretic analysis and B: PAGE analysis of **DNA3** after irradiation of 50 µM **DNA2** and 250 µM SQ-modified Atto655 dye **14** at 20 °C with a 450 nm LED for 5 h in aqueous solution containing 5% DMF, 10 mM Na-P_i buffer and 250 mM NaCl in a total volume of 600 µL in a crimp vial. Staining was performed with SybrGreen™ followed by visualisation under UV light (λ_{exc} = 312 nm). 42

Figure 28: Confocal laser microscopy images of living *HeLa* cells. Left: *HeLa* cells were transfected for 24 h with 75 ng **DNA2**, followed by incubation for 16 h with 20 µM Atto655 dye **14**. Right: As a negative control, *HeLa* cells were incubated with 20 µM Atto655 dye **14** without prior transfection of **DNA2**. All cells were irradiated for 30 min at 37 °C with a 450 nm LED, followed by imaging at λ_{exc} = 638 nm and λ_{em} = 665-750 nm. Scale bar: 10 µm. 44

Figure 29: Synthesis of **DNA6:** a) Synthesis of **DNA4**: incorporation of **13** and **15** into **DNA4** via DNA synthesiser, followed by cleavage of the TFAc group with 25% NH_4OH, 55 °C, 16 h; b) Synthesis of **DNA5**: **7**, DIPEA, DMF, r.t., 48 h; c) Synthesis of **DNA6** through Cu(I)-Click reaction with commercially available Atto520-N_3. .45

Figure 30: UV/Vis absorbance (black) and emission spectra (orange) of **DNA6**: 5 µM solution in ddH_2O at 20 °C. 46

Figure 31: Schematic overview of visible light-induced DNA labelling in living *HeLa* cells via [2+2] cycloaddition of SQ. a) Transfection of *HeLa* cells for 24 h with 75 ng SQ- and Atto520-modified **DNA6**; b) Incubation for 16 h with SQ-modified Atto655 dye **14**; c) Irradiation with a 450 nm LED for 30 min at 37 °C to form **DNA7**; d) Confirmation of the labelling reaction by confocal microscopy using the FRET, exciting donor Atto520 dye (λ_{exc} = 488 nm) and reading acceptor Atto655 dye (λ_{em} = 665-750 nm). 47

Figure 32: Denaturing PAGE analysis of **DNA7** after irradiation of 5 µM **DNA6** and 50 µM SQ-modified Atto655 dye **14** at λ_{max} = 450 nm in aqueous media containing 5% DMSO, 10 mM Na-P_i buffer and 250 mM NaCl in a total volume of 500 µL in a crimp vial for 30 min at 37 °C. Staining was performed using SybrGreen™, followed by visualisation under UV light (λ_{exc} = 312 nm). 48

Figure 33: Confocal laser microscopy images of living *HeLa* cells. A: *HeLa* cells were transfected for 24 h with 75 ng **DNA6**, followed by incubation for 16 h with 20 µM Atto655 dye **14**. B: *HeLa* cells were transfected for 24 h with 75 ng **DNA6** without following incubation with Atto655 dye **14**. C and D: *HeLa* cells were incubated with 20 µM Atto655 **14** dye without prior transfection of **DNA6**. All cells were irradiated for 30 min with a 450 nm LED at 37 °C, followed by imaging at depicted excitation and emission wavelengths. The merge shows the combination of the pictures taken of direct excitation and the brightfield. Scale bar: 10 µm. 50

Figure 34: Confocal laser microscopy images of living *HeLa* cells. Left: *HeLa* cells were transfected for 24 h with 65 ng **DNA3** which was successfully labelled with the SQ-modified Atto655 dye **14** through [2+2] photocycloaddition prior to transfection. Imaging was performed at λ_{exc} = 638 nm and λ_{em} = 665-750 nm. Right: *HeLa* cells were transfected for 24 h with 75 ng SQ- and Atto520-modified **DNA6**, followed by incubation for 16 h with 20 µM Atto655 dye **14**. After irradiation for 30 min with a 450 nm LED, the success of the labelling reaction was confirmed using the FRET, exciting donor Atto520 at λ_{exc} = 488 nm and reading the acceptor Atto655 dye at λ_{em} = 665-750 nm. Scale bar: 10 µm.... 51

Figure 35: A: Coelenterazine and Renilla Luciferase as example of bioluminescence in the wild. The luciferase oxidises its complementary luciferin to yield photons of light in the blue wavelength region. B: Employment of renilla luciferase expressing *HeLa* cells in combination with the herein introduced transfection protocol and FRET readout. 54

Figure 36: Simplified overview of the chromophores examined in this study alongside their proposed release mechanism. Based on the findings of a photochemical action plot analysis, pathway-independent and λ-orthgonal photochemical release was performed in a one-pot reaction. 57

Figure 37: Synthesis of isocyanide **20**: a) MeOH, 50 °C, 2 h, quant.; b) EDC·HCl, DMAP, r.t., 16 h, 19%; c) Pyridine, *p*-TsCl, DCM, r.t., 2 h, 72%. 59

Figure 38: a) Synthesis of coumarin carboxaldehyde **22**: SeO_2, *o*-xylene, reflux, 5 h, 57%; b) Synthesis of photocaged coumarin-modified compound **24** via *Passerini* reaction: DCM, r.t., 16 h, 92%; c) Synthesis of photocaged perylene-modified compound **26**: $CHCl_3$ / toluene (3:1), r.t., 48 h, 3%. 60

Figure 39: Normalised UV/Vis absorbance of coumarin photocaged compound **24** (147 µM in MeCN) and perylene photocaged compound **26** (72 µM in MeCN). 61

Figure 40: A: UV/Vis absorbance changes and B: HPLC results of 20 µM **24** over 2 h of irradiation at 20 °C with a 405 nm LED in MeCN. ..63

Figure 41: Top: NMR spectroscopic changes of 8 mg **24** over 2 h of irradiation at 20 °C with a 405 nm LED in 400 µL DMSO-d_6. Bottom: Mass spectrometric analysis of coumarin-modified compound **24** after irradiation for 2 h with a 405 nm LED: m/z_{theo} = 417.2026 for $[M+H]^+$ and 833.3979 for $[2M+H]^+$. 65

Figure 42: A: UV/Vis absorbance changes and B: HPLC results of 40 µM perylene-modified compound **26** over 3.5 h of irradiation at 20 °C with a 445 nm LED in MeCN. C: Mass spectrometric analysis of **26** after irradiation for 3.5 h with a 445 nm LED: m/z_{theo} = 434.1751 for $[M-OH]^+$, 452.1856 for $[M+H]^+$, 903.3640 for $[2M+H]^+$ and 925.3459 for $[2M+Na]^+$. 66

Figure 43: Left: UV/Vis absorbance of 8 identical samples of the coumarin derivative **24** after irradiation with monochromatic light at λ_{Laser} = 388 nm to determine the reaction kinetics. Right: Reaction kinetics of **24**. To obtain approximately 25% consumption of the starting material, 0.69 µmol photons should be deposited into the reaction system. 69

Figure 44: Molar extinction of **24** overlayed with the action plot consumption of the starting material (*c* = 147 µM in MeCN). For each indicated wavelength, 0.69 µmol photons were deposited into the reaction system. 70

Figure 45: Left: UV/Vis absorbance of 7 identical samples of the perylene derivative **26** after irradiation with monochromatic light at λ_{Laser} = 440 nm to determine the reaction kinetics. Right: Reaction kinetics of **26**. To obtain approximately 25% consumption of the starting material, 7.09 µmol photons need to be deposited into the reaction system. 71

Figure 46: Molar extinction of **26** overlayed with the action plot consumption of the starting material (*c* = 72 µM in MeCN). For each indicated wavelength, 7.09 µmol photons were deposited into the reaction system. 72

Figure 47: A: Dual chromophore action plot for **24** and **26** as well as their respective molar extinction (blue line for coumarin-modified substrate **24** and green line for perylene-modified compound **26**). The blue squares display the percentage consumption of the starting material of **24**, while the green dots present the percentage consumption of the starting material of **26**. B: Dual chromophore action plot for **24** and **26** as conversion per photon overlayed with their respective molar extinction. 73

Figure 48: Normalised emission of the employed LEDs (405 nm, 0.20 mW and 505 nm, 40 mW) overlayed with the action plots of both photoreactive chromophores **24** and **26**. 74

Figure 49: Consumption of the starting material of coumarin-modified substrate **24** and perylene-modified compound **26** after sequential irradiation with LEDs at two disparate wavelengths (λ_1 = 405 nm, 0.20 mW and λ_2 = 505 nm, 40 mW). Between the two possible reaction pathways (high energy to low energy, low energy to high energy), a dark period of 45 min was added. Upon 405 nm irradiation, almost exclusively **24** releases the benzoic acid, while **26** only releases the acid when exposed to 505 nm light.........................75

Figure 50: Synthesis of photocaged valproic acid-modified compound **28**: DCM, r.t., 16 h, 22%. 77

Figure 51: UV/Vis absorbance changes of 50 µM valproic acid-modified compound **28** over 10 min of irradiation at 20 °C with a 385 nm LED in MeCN. 78

Figure 52: A: Molar extinction of **28** overlayed with the action plot consumption of the starting material (*c* = 150 µM in MeCN). For each indicated wavelength, 1.93 µmol photons were deposited into the reaction system. B: Molar extinction of **24** overlayed with the action plot consumption of the starting material (*c* = 147 µM in MeCN). For each indicated wavelength, 0.69 µmol photons were deposited into the reaction system. 79

Figure 53: Left: Structures of chlorambucil (**29**) and ciprofloxacin (**30**), bearing carboxylic acids and right: Structures of possible carboxaldehyde-modified chromophores to be potentially further investigated in *λ*-orthogonal drug release. 82

Figure S1: A: Normalised emission spectra of the used LEDs (385 nm, 20 mW; 405 nm, 0.20 mW; 445 nm, 40 mW, 450 nm, 20 mW, 505 nm, 40 mW). B: In-house build LED irradiation setup with thermostat, magnetic stirrer, and customised sample holder for crimp vials. 90

Figure S2: Experimental setup of the herein used 20 Hz tuneable laser system. Light from a monochromatic light source is expanded, passed through an external, mechanical shutter and directed upwards using a prism. The sample is inserted in a custom-made aluminium block, and the energy delivered to the sample is monitored using an energy meter. 91

Figure S3: Left: Calibration of the glass vial transmittance of the Supelco Vials, commercially available at *Merck* including a fit to obtain values that were not determined experimentally. Right: Calibration of the glass vial transmittance of the Clear Glass Vials, purchased at *ThermoFisher* including a fit to obtain values that were not determined experimentally. 92

Figure S4: ESI-HRMS analysis of compound **14**: m/z_{theo} = 916.4062 for $[C_{50}H_{58}N_7O_8S]^-$, m/z_{exp} = 916.4043 $[C_{50}H_{58}N_7O_8S]^-$. 104

Figure S5: ^{1}H-NMR spectrum of compound **17** (DMSO-d_6, 600 MHz). 108

Figure S6: ^{13}C-NMR spectrum of compound **17** (DMSO-d_6, 151 MHz). 109

Figure S7: ^{1}H-NMR spectrum of compound **19** (DMSO-d_6, 600 MHz). 111

Figure S8: ^{13}C-NMR spectrum of compound **19** (DMSO-d_6, 151 MHz). 112

Figure S9: LC-MS analysis of compound **19**: m/z_{theo} for $[C_8H_{14}NO_3]$, $[M+H]^+$ = 172.0984, m/z_{exp} = 172.0966. 113

Figure S10: ^{1}H-NMR spectrum of compound **20** (DMSO-d_6, 600 MHz). 115

Figure S11: ^{13}C-NMR spectrum of compound **20** (DMSO-d_6, 151 MHz). 116

Figure S12: ^{1}H-NMR spectrum of compound **24** (DMSO-d_6, 600 MHz, *: DMF, #: water). 119

Figure S13: ^{13}C-NMR spectrum of compound **24** (DMSO-d_6, 151 MHz). 120

Figure S14: LC-MS analysis of compound **24:** m/z_{theo} for $[C_{29}H_{33}N_2O_7]$, $[M+H]^+$ = 521.2210, m/z_{exp} = 521.2276. 121

Figure S15: ^{1}H-NMR spectrum of compound **26** (DMSO-d_6, 600 MHz, *: DCM, +: acetone, #: silicon grease). 123

Figure S16: ^{13}C-NMR spectrum of compound **26** ($CDCl_3$, 151 MHz) 124

Figure S17: LC-MS analysis of compound **26**: m/z_{theo} for $[C_{72}H_{62}N_3O_{10}]$, $[2M+NH_4]^+$ = 1128.4483, m/z_{exp} = 1128.4430. 125

Figure S18: ^{1}H-NMR spectrum of compound **28** (DMSO-d_6, 400 MHz, *: DCM). 127

Figure S19: ^{13}C-NMR spectrum of compound **28** ($CDCl_3$, 101 MHz) 128

Figure S20: ESI-HRMS analysis of compound **28**: m/z_{theo} for $[C_{30}H_{43}N_2O_{10}]$, $[M+H]^+$ = 543.3065, m/z_{exp} = 543.3050. 129

Figure S21: Extinction coefficient spectra of the starting material **24** (left) and of the photodegradation product (right). 131

Figure S22: Molar extinction coefficient spectra for both the starting material and the photoproduct. Solid lines show the average calculated from a serial dilution, with the shaded area showing the error. 131

Figure S23: Screenshot from the excel sheet used to deconvolte the absorption spectra after irradiation. 132

Figure A1: UV/Vis spectroscopic analysis of **DNA2** (left) and **DNA3** (right) after irradiation of 50 µM **DNA2** and 50 µM SQ-modified Atto655 dye **14** (1:1 equivalents) with a 450 nm LED in aqueous media containing 5% DMF, 10 mM Na-P$_i$ buffer and 250 mM NaCl in H_2O in a total volume of 600 µL in a crimp vial for 5 h at 20 °C. Pre-irradiation (dark green line), **DNA2** and **DNA3** both show two distinctive absorbance maxima at λ_{max1} = 260 nm, associated with the DNA absorbance and λ_{max2} = 397 nm, associated with the SQ moiety. Furthermore, **DNA3** shows a third maximum at λ_{max3} = 655 nm, that can be assigned to the Atto655 dye. During irradiation, one new maximum is emerging at λ = 325 nm whereas the assigned SQ maximum is decreasing (red line). Nevertheless, **DNA2** and **DNA3** predominantly show similar changes in absorbance after 5 h of irradiation, making clear differentiation and conclusion about the formation of **DNA3** challenging. 149

Figure A2: HPLC analysis ($\lambda_{\text{detection}}$ = 260 nm) of **DNA2** (left) and **DNA3** (right) after irradiation of 50 µM **DNA2** and 50 µM SQ-modified Atto655 dye **14** (1:1 equivalents) with a 450 nm LED in aqueous media containing 5% DMF, 10 mM Na-P$_i$ buffer and 250 mM NaCl in H_2O in a total volume of 600 µL in a crimp vial for 5 h at 20 °C.

Pre-irradiation (dark green line), the chromatograms of both **DNA2** and **DNA3** show one significant peak at t_R = 13.1 min. During irradiation, the peak decreases, and a new peak at t_R = 12.6 min (red line) is formed. The formation of the new peak in **DNA3** is not as significant as it is in **DNA2**, suggesting possible reaction of to **DNA3**. Nevertheless, clear confirmation of the formation of **DNA3** is not possible. 150

Figure A3: Agarose gel electrophoretic analysis of **DNA3** after irradiation of 50 µM **DNA2** and 50 µM SQ-modified Atto655 dye **14** (1:1 equivalents) with a 450 nm LED in aqueous media containing 5% DMF, 10 mM Na-P$_i$ buffer and 250 mM NaCl in H_2O in a total volume of 600 µL in a crimp vial for 5 h at 20 °C. Staining was performed using SybrGreen™, followed by visualisation under UV light (λ_{exc} = 312 nm). Lane 1 shows the commercial DNA marker. Lane 2 displays **DNA2** (pre-irradiation) with one gel band with the smallest size of all three lanes. **(DNA2)$_2$** in lane 3 shows two gel bands, one in the same position as lane 2 and one located between 15 bp and 20 bp in comparison to the marker in lane 1. Therefore, the smaller sized fragment can be assigned to the starting material **DNA2** whereas the larger sized fragment describes the dimerization product of **DNA2** to **(DNA2)$_2$**. **DNA3** is expected to feature a band between **DNA2** and **(DNA2)$_2$**. However, lane 4 displays the same wo fragments as lane 3, indicating no reaction between **DNA2** and the SQ-modified Atto655 dye **14**, but favoured reaction to homo-dimerized **(DNA2)$_2$**. 150

Figure A4: UV/Vis spectroscopic analysis of 50 µM SQ-modified Atto655 dye **14** after irradiation with a 450 nm LED in aqueous media containing 5% DMF, 10 mM Na-P$_i$ buffer and 250 mM NaCl in H_2O in a total volume of 600 µL in a crimp vial for 5 h at 20 °C. Pre-irradiation (dark green line), the dye shows three distinctive absorbance maxima at λ_{max1} = 260 nm, λ_{max2} = 298 nm and λ_{max3} = 397 nm associated with the SQ moiety and λ_{max4} = 655 nm, which displays the excitation maximum of the Atto655 dye. During irradiation, one new maximum is emerging at λ = 325 nm, whereas the assigned SQ maximum at λ = 397 nm is decreasing (red line), suggesting homo-dimerization between two Atto655 dyes. The assigned Atto655 maximum at λ_{max4} = 655 nm remains unchanged, confirming the stability of the dye after 5 h of irradiation. 151

Figure A5: ESI-HRMS analysis of homo-dimerized Atto655 dye **(14)$_2$**: m/z_{theo} = 1829.7906 for [$C_{100}H_{113}N_{14}O_{16}S_2^-$], m/z_{exp} = 1829.7976. After successful reaction of SQ-modified Atto655 dye **14** with itself to homo-dimerized Atto655 dye **(14)$_2$** through [2+2] cycloaddition of the two SQ moieties the resulting product features double the molecular weight. Although occurring as a competing reaction, the homo-dimerization between two fluorophore dyes was neither detectable though gel electrophoresis due to too low molecular weight nor distinguishable from hetero-dimerization of **DNA2** to **DNA3** in UV/Vis spectra. As this reaction is not interfering with the DNA strand itself, it is of minor concern. 151

Figure A6: UV/Vis spectroscopic analysis of **DNA2** (left) and **DNA3** (right) after irradiation of 50 µM **DNA2** and 250 µM SQ-modified Atto655 dye **14** (1:5 equivalents) with a 450 nm LED in aqueous media containing 5% DMF, 10 mM Na-P$_i$ buffer and 250 mM NaCl in H_2O in a total volume of 600 µL in a crimp vial for 5 h at 20 °C. Pre-irradiation (dark green line), **DNA2** and **DNA3** both show two distinctive absorbance maxima at λ_{max1} = 260 nm, associated with the DNA absorbance and λ_{max2} = 397 nm, associated with the SQ moiety. Furthermore, **DNA3** shows a third maximum at λ_{max3} = 655 nm, that can be assigned to the Atto655 dye. During irradiation, one new maximum is emerging at λ = 325 nm whereas the assigned SQ maximum is decreasing (red line). Nevertheless,

DNA2 and **DNA3** predominantly show similar changes in absorbance after 5 h of irradiation, making clear differentiation and conclusion about the formation of **DNA3** challenging. 152

Figure A7: HPLC analysis with $\lambda_{detection}$ = 260 nm (left) and $\lambda_{detection}$ = 655 nm (right) of **DNA3** after irradiation of 50 µM **DNA2** and 250 µM SQ-modified Atto655 dye **14** (1:5 equivalents) with a 450 nm LED in aqueous media containing 5% DMF, 10 mM Na-P_i buffer and 250 mM NaCl in H_2O in a total volume of 600 µL in a crimp vial for 5 h at 20 °C. The signals at t_R ~ 13 min represent **DNA2/(DNA2)$_2$**. Four new peaks are forming and increasing over the course of irradiation at t_R = 15.9, 17.4, 18.5 and 19.2 min. The last two peaks (t_R = 25 and 27 min) at $\lambda_{detection}$ = 655 nm (right) are assigned to the SQ-modified Atto655 dye. As two new peaks develop and increase at t_R = 18.5 and 19.2 min (gray shaded area), both showing absorbance at λ_1 = 260 nm and λ_2 = 655 nm, they suggest formation of **DNA3**. However, the HPLC results of **DNA3** are not as convincing as HPLC analyses of homo-dimerization to **(DNA2)$_2$**. 152

Figure A8: PAGE analysis (left) and yield determination (right) of **DNA3**. The software for the yield determination recognised five bands in total. 153

Figure A9: Reaction kinetics of compound **28**. To obtain approximately 25% consumption of the starting material, 1.93 µmol photons need to be deposited into the reaction system....................................... 155

List of Tables

Table 1: Theoretical and experimental *m/z* values of oligonucleotides **DNA1** and **DNA2** after purification via HPLC. 35

Table 2: Theoretical and experimental *m/z* values of oligonucleotides **DNA4** to **DNA6** after purification via HPLC. 45

Table S1: Detailed specifications of the laser parameters and the calculations for the action plot of coumarin-modified compound **24**. 133

Table S2: Detailed specifications of the laser parameters and the calculations for the action plot of perylene-modified compound **26**. 136

Table S3: Detailed specifications of the laser parameters and the calculations for the action plot of coumarin-modified compound **28**. 139

Table S4: Results of the sequential LED experiment. The consumption of the starting materials was determined via LC-MS. 141

Table A1: Determined yields after irradiation of **DNA2** with fivefold excess of SQ-modified Atto655 dye **14** for 1 h and 5 h with a 450 nm LED. 153

Table A2: Detailed specifications of the laser and results of the kinetic experiments of coumarin-modified compound **24**. 154

Table A3: Detailed specifications of the laser and results of the kinetic experiments of perylene-modified compound **26**. 154

Table A4: Detailed specifications of the laser and results of the kinetic experiments of valproic acid-modified compound **28**. 155

List of Abbreviations

°C	Degree Celsius
µg	Micro Gram, 10^{-6} g
µL	Micro Liter, 10^{-6} L
µM	Micro Molar, 10^{-6} Mol/L
λ	Wavelength
A	Absorption
ATP	Adenosine Triphosphate
AP	Acrylpyrene
APAT	(*N*,*N*-Dimethyl)aminopyrene Aryl Tetrazole
BARAC	Biarylazacyclooctyne
BCN	Bicyclononyne
$CHCl_3$	Chloroform
Cu	Copper
CuAAC	Copper-Catalysed Azide Alkyne Cycloaddition
CP	Cyclopropene
CQ	Chloroquinoxaline
DCM	Dichloromethane
DIFO	Difluorocyclooctyne
DIPEA	Diisopropylethylamin
DMAP	Dimethylaminopyridin
DMEM	Dulbecco’s Modified Eagle Medium
DMF	*N*,*N*-Dimethylformamide
DMSO	Dimethylsulfoxide

DMT	Dimethoxytrityl
DNA	Deoxyribonucleic Acid
DT	Dithiophenol
EDC·HCl	*N*-(3-Dimethylaminopropyl)-*N’*-Ethylcarbodiimide Hydrochloride
e.g.,	*exempli gratia* (for example)
equiv.	Equivalents
ESI	Electronspray Ionisation
et al.	*et alia* (and others)
EtOH	Ethanol
FRET	Förster Resonance Energy Transfer
h	hour(s)
HCl	Hydrochloride
HPLC	High Performance Liquid Chromatography
HOMO	Highest Occupied Molecular Orbital
i.e.,	*id est* (that is)
I	Intensity
iEDDA	Inverse Electron-Demand Diels-Alder Cycloaddition
K_2CO_3	Potassium Carbonate
LC-MS	Liquid Chromatography Coupled Mass Spectrometry
LED	Light Emitting Diode
LG	Leaving Group
LiOH	Lithium Hydroxide
LUMO	Lowest Unoccupied Molecular Orbital
m	Meter
mg	Milligram, 10^{-3} g
mL	Milli Liter, 10^{-3} L
mM	Milli Molar, 10^{-3} Mol/L
mRNA	Messenger Ribonucleic Acid

mW	Milli Watt, 10^{-3} W
MALDI	Matrix Assisted Laser Desorption Ionisation
MCR	Multicomponent Reaction
MeCN	Acetonitrile
MeOH	Methanol
MS	Mass Spectrometry
ng	Nanogram, 10^{-9} g
nm	Nanometer, 10^{-9} m
ns	Nanoseconds, 10^{-9} s
NaCl	Sodium Chloride
Na_2CO_3	Sodium Carbonate
Na-P_i	Sodium Phosphate
NB	Norbonene
NHS	N-Hydroxysuccinimid
NMR	Nuclear Magnetic Resonance Spectroscopy
NITEC	Nitrile Imine-Mediated Tetrazole-Ene Cycloaddition
OPO	Optical Parametric Oscillators
p-TsCl	*para*-Toluenesulfonyl Chloride
PAGE	Polyacrylamide Gel Electrophoresis
PBS	Phosphate Buffered Saline
PEG	Poly(ethylene glycol)
PET	Photoinduced Electron Transfer
PP	Photoproduct
PPG	Photoprotective Group
PQ	Phenanthrenequinone
r.t.	Ambient Temperature
RNA	Ribonucleic Acid
ROS	Reactive Oxygen Species

s	second(s)
SeO_2	Selenium Dioxide
SM	Starting Material
SPAAC	Strain-Promoted Azide Alkyne Cycloaddition
SPP	Styrylpyrido[2,3-b]pyrazines
SQ	Styrylquinoxaline
t	Time
T	Temperature
TCO	*trans*-Cyclooctene
TFAc	Trifluoroacetyl
THF	Tetrahydrofuran
TIP	Tight Ion Pair
ToF	Time of Flight
UV	Ultraviolet
Vis	Visible
ZnI_2	Zinc Iodide

1 General Introduction

The driving forces behind modern chemistry are not only important discoveries and improvements but also the formulation of concepts that catalyse and accelerate new development. When the SARS-CoV-2[1] epidemic emerged in late 2019[2] and eventually evolved into a worldwide pandemic in early 2020,[3] few thought that the development of vaccines will be fast enough to help curb the increasing global disease burden. However, unparalleled investments by industry and government in combination with researcher's insatiable motivation to discover a vaccine platform when it is most needed led to the approval of several vaccines[4] in record time with two of the fastest approved and most successful vaccines based on the new mRNA technology.[5] The fundamental discoveries[6] of *Katalin Karikó* and *Drew Weissman* regarding the importance of base modifications on mRNA to block the activation of signalling molecules (Scheme 1) provide an avenue to not only protect the world against a wide variety of infectious diseases but also for finding applications in *e.g.*, cancer treatment in the future, leading to the award of the Nobel Prize in Medicine in 2023.[7]

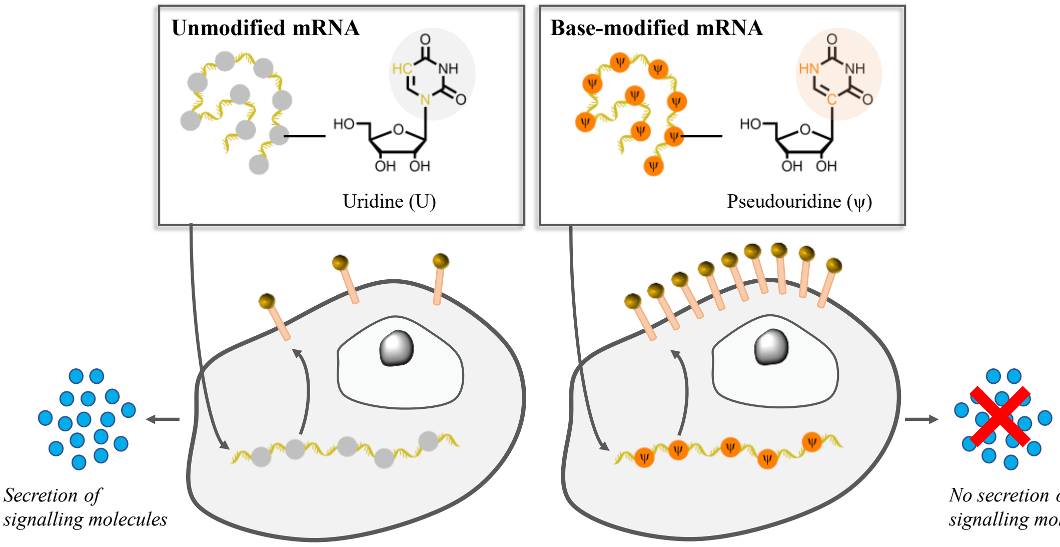
Unmodified mRNA
HC
NH
N
O
O
HO
O
OH OH
Uridine (U)
Base-modified mRNA
HN
NH
C
O
O
HO
O
OH OH
Pseudouridine (ψ)
ψ
Secretion of signalling molecules
No secretion of signalling molecules

Scheme 1: 2023 Medicine Nobel Laureates discovered that base-modified mRNA can be used to block the activation of inflammatory reactions (secretion of signalling molecules) and increase protein production when mRNA is delivered to cells.

To develop such new methods based on *e.g.*, mRNA delivery to cells, it is of particular interest for medical research to visualise the processes of (abnormal) cells to understand biological interactions in living systems and draw conclusions about possible treatments. Therefore, special imaging techniques have been developed and employed in the last six decades with proteins being the first fluorescently labelled biopolymer[8] (*i.e.*, green fluorescent protein).[9] Only with the introduction of "bioorthogonal reactions" by *Carolyn Bertozzi* in 2003,[10] imaging of glycans, lipids and nucleic acids in living cells[11] was made accessible.[12] *Bertozzi's* innovative two step concept took "click chemistry", which was initially developed by *Barry Sharpless*[13] and *Morten Meldal*,[14] to a new level as she designed molecular building blocks that snap together quickly and efficiently inside living organisms without disrupting the normal chemistry of the cell.[15]

Bioorthogonal reactions do not only offer the opportunity to visualise cellular processes but are also used for the improvement of the targeting of anti-cancer pharmaceuticals, which are now being tested in clinic trials.[16] Many chemotherapeutics aim to inhibit the nucleic acid synthesis of cells to suppress the growth of the tumour tissue.[17] As a result, the DNA replication as a prerequisite for an organism to grow and regenerate is brought into the focus of scientific attention, leading to an increased interest of establishing new labelling strategies for the visualisation of nucleic acids to better understand their diverse biological functions.[18]

The current PhD thesis is divided into two major parts. The first project focuses on the development and application of a novel light-induced bioorthogonal labelling strategy of DNA in live cells, introducing a [2+2] photoreactive styrylquinoxaline moiety into both oligonucleotide and Atto655 dye. After investigation of the DNA labelling concept by UV/Vis spectroscopy, HPLC analysis and gel electrophoresis, the applicability of the newly developed photoinduced ligation approach should be studied in live *HeLa* cells.

The aforementioned need for a quick establishment of novel vaccines enabled the development of effective delivery methods to efficiently transport cargo molecules to their place of action (*e.g.*, mRNA into viral cells). Stimulus-responsive delivery systems offer the advantage of transporting the cargo in an inactive form, followed by its activation upon a specific trigger (*i.e.*, light, temperature, or pH change), whereby only the use of light allows the on-demand, remote and spatially addressable release.

The second part of the current PhD thesis contributes to the development and characterisation of a dual carrier system that allows for the sequential and fully wavelength-controlled release of cargo molecules, introducing 7-(diethylamino)-coumarin and 3-perylene as photoprotective groups into the model release entities. After synthesis of the compounds bearing the photosensitive groups and initial investigation of their light-induced cleavage process by UV/Vis spectroscopy, LC-MS and NMR spectroscopy, the most suitable wavelengths for λ-orthogonal reactivity should be determined by the recording of action plots, followed by transfer to LED irradiation to study the pathway-independent λ-orthogonal cleavage in a one-pot reaction.

2 Theoretical Background

2.1 Bioorthogonal Reactions

The term “bioorthogonal chemistry” was coined by the *Bertozzi* group in the early 2000s,[10a] classifying chemical reactions that occur under physiological conditions without adverse effects to cells or living systems with good biocompatibility and high chemoselectivity.[12a, 19] Ever since, bioorthogonal reactions have been widely utilised as an important tool in chemical biology for the investigation, manipulation and labelling of proteins,[20] glycans,[21] and nucleic acids[22] without perturbing the living system.

For the implementation of a bioorthogonal reaction, typically two successive steps are required: Firstly, a monomeric building block (*e.g.*, a DNA base) of the biooligomer of interest (*e.g.*, nucleic acids) is modified with a chemical reporter – a functional group that is ideally not present in the biological system and does not alter the structure of the substrate dramatically to avoid losing its bioactivity. Such a modified building block is incorporated metabolically into the biooligomer by either a native or an engineered biosynthetic pathway.

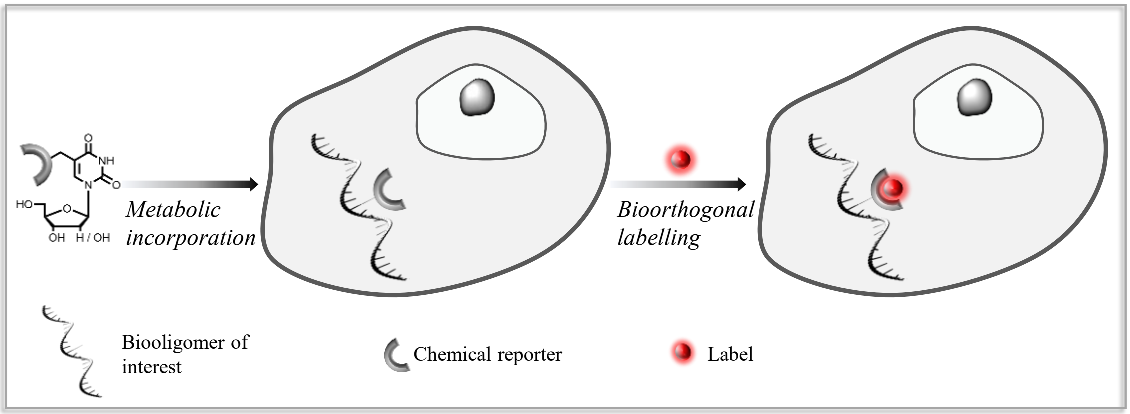

Figure 1: Schematic representation of bioorthogonal labelling of DNA. A building block (*e.g.*, a DNA base) of the biooligomer of interest (DNA) is modified with a chemical reporter (grey hemicircle) and subsequently incorporated metabolically to react with its reaction partner which is modified with a label (red sphere, *e.g.*, a fluorescent dye).

Secondly, a reaction partner offering the complementary chemical functionality and a label (*e.g.,* a fluorescent dye) is introduced into the system to react selectively with the chemical reporter. Thereby, the biooligomer of interest can be visualised by fluorescence microscopy (Figure 1).

To be classified as bioorthogonal, a reaction needs to fulfill the following criteria: (i) the reaction between the introduced chemical reporter and the reaction partner should be chemoselective, offer high yields and function under physiological conditions (neutral pH, physiological temperature, aqueous medium) to avoid side reactions with naturally occurring biological compounds, (ii) the starting materials, products and potential side products should be non-toxic and offer a high stability in the cellular environment, (iii) bioorthogonal reactions should be rapid and provide high rate coefficients (and thus reactions rates) to ensure efficient labelling, preventing problems concerning the solubility and toxicity of the used reagents.[20a, 23]

During the past two decades, several reactions meeting these criteria have been developed and provided unprecedented opportunities for the study and manipulation of biological processes in biological systems. The most well-established bioorthogonal reactions are copper-catalysed azide alkyne cycloadditions (CuAAC),[24] inverse electron-demand Diels-Alder cycloadditions (iEDDA),[25] strain-promoted azide alkyne cycloadditions (SPAAC),[26] and photoclick reactions[27] (Figure 2). Due to the involvement of two reactive species, bioorthogonal reactions typically follow second-order kinetics.

The CuAAC (Figure 2, red) is one of the fastest bioorthogonal labelling methods (up to $k_2 = 200\ \text{M}^{-1}\text{s}^{-1}$). The uncatalysed, thermally induced reaction had already been introduced by *Huisgen* in the 1960s.[28] However, it was first employed as a biocojugation method by the groups of *Sharpless*[29] and *Meldal*[14] in 2002. Their groundbreaking work underpinned the necessity of copper(I) salts as catalysts to achieve high regioselective conversion of various azides and alkynes to the resulting triazoles at ambient temperature, relinquishing the – prior to this discovery – need of elevated temperatures for the reaction to proceed.[14, 28-29] Azides and terminal alkynes are practically non-existent in living systems, relatively stable under physiological conditions and react regioselectively to 1,4-disubstituted 1,2,3-triazoles, making them a suitable reagent for bioorthogonal labelling strategies.[14, 29] Ever since, the CuAAC has been widely employed in the labelling of various biomacromolecules, such as nucleic acids,[30] glycans,[31] proteins,[32] and lipids.[33] During the past few years, a few examples of CuAAC labelling in live cells have been reported,[34] nevertheless, the use of this reaction type in living systems is generally limited due to the cytotoxicity of Cu(I) and Cu(II) ions.[35] Moreover, Cu ions can lead to the formation of reactive oxygen species (ROS)[36] that are not only cell-toxic, but also perturb cellular function, lead to DNA damages, and might cause diseases, such as Alzheimer's or *Parkinson's* disease.[37]

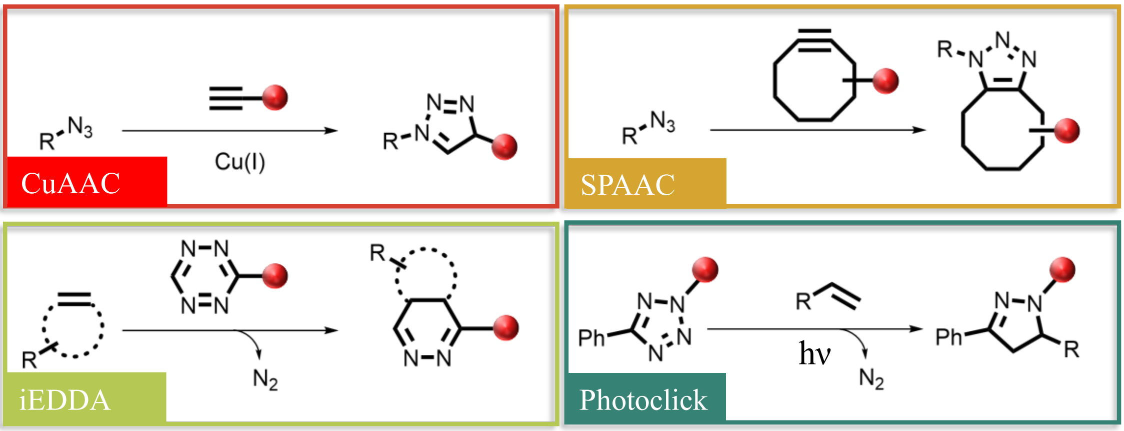

Figure 2: Overview of commonly used bioorthogonal reactions: copper-catalysed azide alkyne cycloaddition (CuAAC, red), strain-promoted azide alkyne cycloaddition (SPAAC, beige), inverse electron-demand Diels-Alder cycloaddition (iEDDA, bright green), and photoclick reaction (dark green).

A direct alternative for metal-free labelling *in vivo* is given by the SPAAC (Figure 2, beige) that uses cyclic alkene or alkyne substrates that are under ring tension in their system. In 2004, *Bertozzi* and coworkers first applied the reaction between azides and strained alkynes in a bioorthogonal environment, synthesising a biotinylated cyclooctyne derivative to react with an azide-modified sugar for glycan labelling.[26] Although being a copper-free labelling technique, the first generation of SPAAC reactions was about 10 000 to 20 000 times slower than the CuAAC with rate coefficients of k_2 comprised between 0.01 to 0.02 $M^{-1}s^{-1}$.[26] About six years later, second-generation SPAAC reactions with reaction coefficients of $k_2 = 0.96\ M^{-1}s^{-1}$ (200 times slower than the CuAAC) were introduced, exploiting new strained alkynes (*e.g.*, difluorocyclooctynes (DIFO)[11b] or biarylazacyclooctynes (BARAC, Figure 3A).[38] These compounds bear a strained cyclooctyne core in combination with either electron-withdrawing substituents, condensed aromats and/or heteroatoms. However, the enhanced reactivity due to the higher ring strain is limited by both the increase in lipophilicity and steric hindrance, making the application of SPAAC in aqueous, living systems challenging. This was remedied by the development of bicyclononynes (BCN) by the group of *van Delft* in 2010,[39] finding initial application in the live cell staining of glycans. In the meantime, the concept of BCN-modified SPAAC labelling was transferred to numerous molecule classes, most notably nucleic acids. The BCN moiety can be attached to either the base (5-position in pyrimidines, 7-position in 7-deazapurines),[40] or as reaction partner, coupled to a fluorescent dye.[41] With a BCN-modified building block and an azido-modified fluorescent dye, even labelling in *HeLa* cells as well as zebrafish and mice[42] was accomplished (Figure 3B). Nevertheless, the cyclooctyne is generally unstable[43] and their syntheses are challenging due to long reaction times and low reaction yields.[11b]

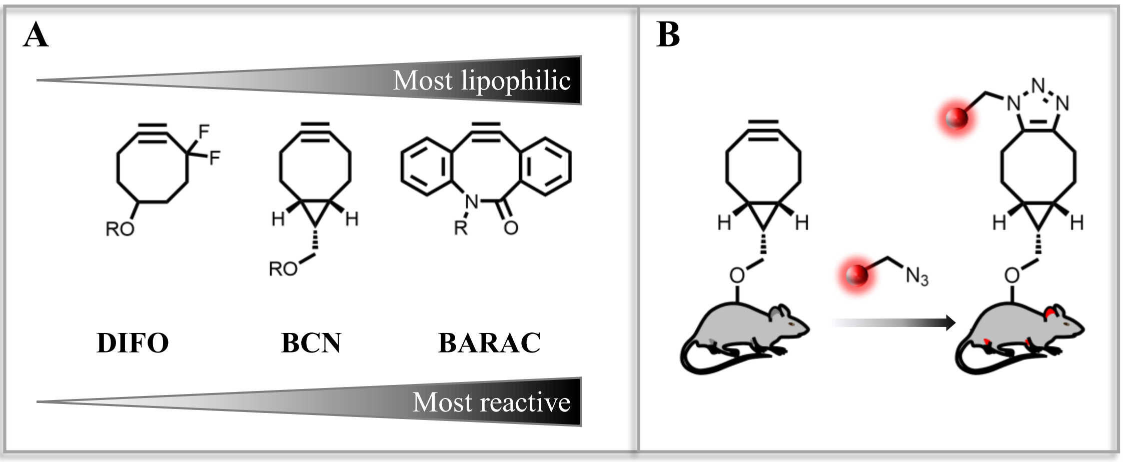

Figure 3: A: Examples of strained cyclooctyne derivatives for SPAAC. Difluorocyclooctyne (DIFO), bicyclononyne (BCN) and biarylazacyclooctyne (BARAC), arranged according to their reactivity and lipophilicity. B: Simplified application of a BCN-modified building block and an azide-modified fluorescent dye for SPAAC bioorthogonal labelling in mice.

Synthetically easier accessible starting materials are provided in the iEDDA (Figure 2, bright green), which requires the use of 1,2,4,5-tetrazines and strained alkenes.[25] This reaction is a modified version of the Diels-Alder reaction, presented by *Otto Diels* and *Kurt Alder* almost a century ago.[44] Their discovery provides one of the most versatile synthetic tools for forming carbon-carbon bonds and was therefore awarded the Nobel Prize in Chemistry in 1950.[45] In cycloadditions, two reaction partners form a transition state that involves the reorganisation of π-electrons and formation of two new σ-bonds.[46]

This results in a ring-type structure whose number of members depends on the initial reaction partners. Cycloadditions are classified in *i.e.*, [2+2], [4+2] or [4+4] cycloadditions, depending on the number of π-electrons of one of the two reaction partners. Mechanistically, both the Diels-Alder and the iEDDA reaction are a [4+2] cycloaddition of a conjugated diene with a dienophile but differ in the energetic positions of the molecular orbitals involved.[47] In a Diels-Alder reaction with normal electron demand, the energy gap between the highest occupied molecular orbital (HOMO) of the diene and the lowest unoccupied molecular orbital (LUMO) of the dienophile is the smallest, in contrast to the iEDDA reaction which is based on the small energy gap between the LUMO of the diene and the HOMO of the dienophile.[44, 47]

Initially applied for the synthesis of pyridazines and first published by *Carboni* and *Lindsey* in 1959,[48] the iEDDA was introduced as a bioorthogonal reaction technique almost simultaneously by the groups of *Hilderbrand* and *Fox* in 2008.[49]

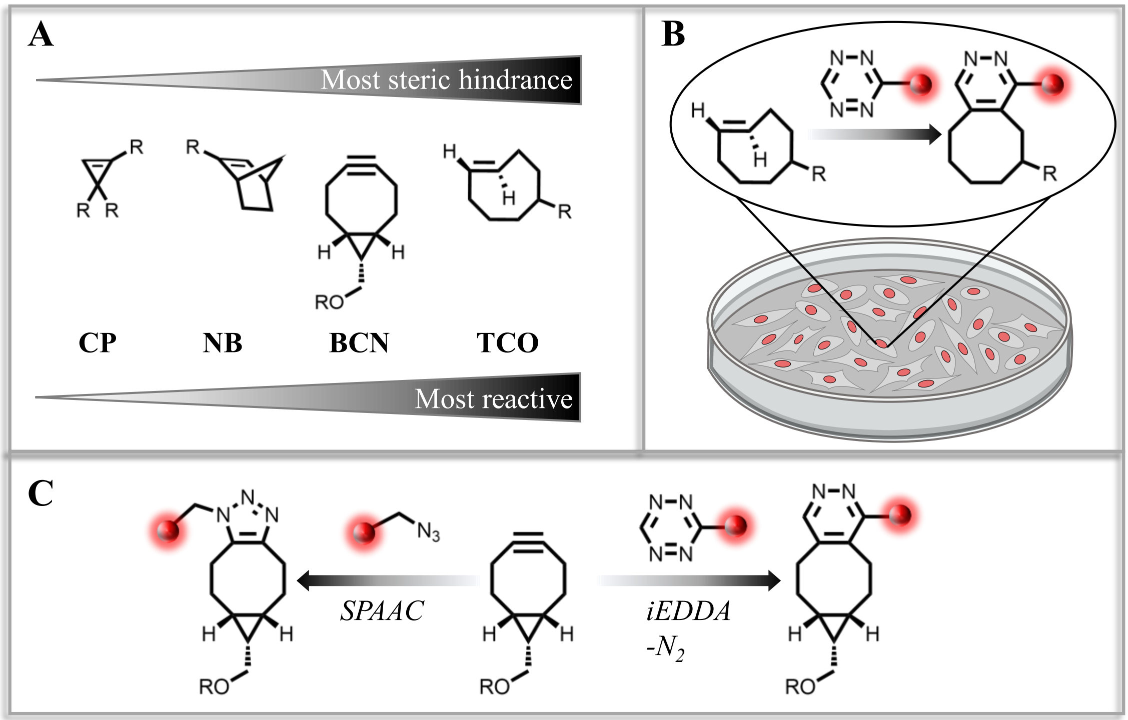

Figure 4: A: Most commonly used dienophiles for iEDDA: Cyclopropene (CP), norbonene (NB), bicyclononyne (BCN) and trans-cyclooctene (TCO), organised according to their reactivity and steric hindrance. B: Simplified application of a TCO-modified building block and a tetrazine-modified fluorescent dye for iEDDA bioorthogonal labelling in *HeLa* cells. C: Orthogonal SPAAC or iEDDA click chemistry using BCN as mutual starting material.

The most commonly used dienophils (Figure 4A) are cyclopropenes (CPs),[50] norbonenes (NBs),[51] bicyclonynes (BCNs)[52] and *trans*-cyclooctenes (TCOs)[53] in combination with 1,2,4,5-tetrazines as dienes. The latter pair shows the highest reaction rate constant ($k_2 = 2 \cdot 10^4$ $M^{-1}s^{-1}$) to date. In the meantime, the iEDDA reaction is not only exploited in a bioorthogonal manner in biomolecules (*e.g.*, genetic encoding[54] or *in cellulo* imaging[55] (Figure 4B)), but also in materials and polymer science as ligation tool.[56] One of the most appealing features of the iEDDA is the mutual orthogonality with azide-alkyne click chemistry. The combination of BCN with either azides as SPAAC acceptor or 1,2,4,5-tetrazines as iEDDA acceptor allow for a copper-free, mutually orthogonal and bioorthogonal labelling protocol (Figure 4C).[57] However, these two reactions cannot be performed simultaneously and do not adhere to the strict orthogonal click criteria as cross-reactivity of tetrazines and azides with species present in physiological environments, such as thiols cannot fully be excluded.[58]

The main disadvantage of the three previously mentioned methods is that they do not offer spatial and well-defined temporal control over the ligation and visualisation process. Spatio-temporal control enables the on-demand, remote and spatially addressable labelling of biological processes in highly dynamic living systems. One solution to this problem is the use of light to induce the desired reaction due to the precise control over both position and dose.[59] Photochemical reactions, such as photoclick reactions[27] (Figure 2, dark green) provide critical control of both time and position, thus regulating the initiation and progress of the reaction through variation of light wavelength and intensity. Regarding the relevance to this work, light-induced bioorthogonal reactions will be discussed in further detail in the following section.

2.2 Light-Induced Bioorthogonal Reactions

2.2.1 Photoclick Reactions

Organic photochemistry has been of key interest for more than one century, however it has only been employed for bioorthogonal labelling for the past decades.

The most common type of light-activated bioorthogonal reactions is the nitrile imine-mediated tetrazole-ene cycloaddition (NITEC)[60] or photoclick reaction.[61] The underlying mechanism dates back to the research of *Huisgen* and coworkers in 1967.[60] Through irradiation of a 2,5-diaryltetrazole, a nitrile imine is generated that reacts with an electron-deficient alkene to a fluorescent pyrazoline product (Figure 5).[60]

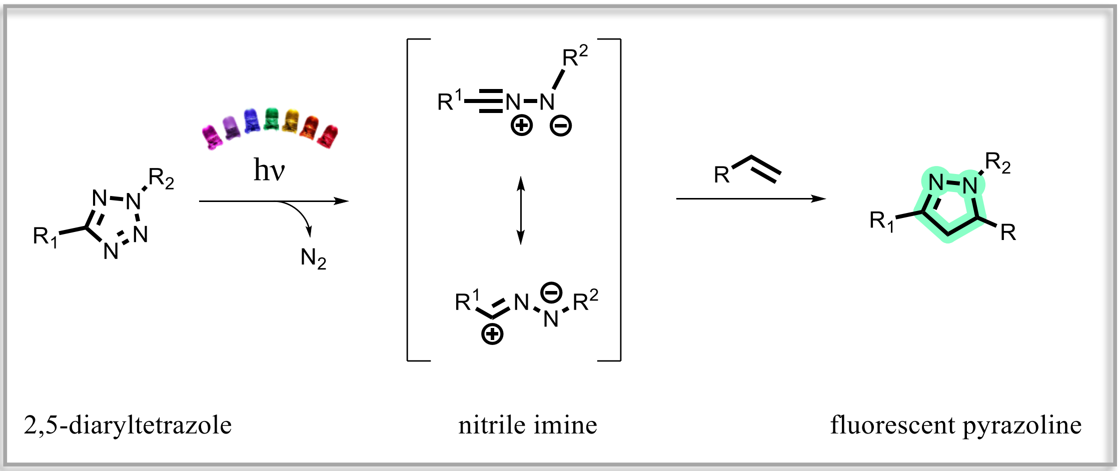

Figure 5: Mechanism of the nitrile imine / alkene photoclick reaction: After irradiation of a 2,5-diaryltetrazole, nitrogen is released to generate a highly reactive nitrile imine that results in building a fluorescent pyrazoline product through reaction with an electron-deficient alkene.

However, the reaction needed elevated temperatures (T = 150 °C) or UV-C light irradiation (λ = 280 nm, high pressure mercury lamp) to proceed[60] which made it unsuitable for bioorthogonal labelling until its improvement by the group of *Lin* in 2008.[62] They synthesised several methylbenzoate-functionalised diaryltetrazole derivatives and managed to induce the photoclick reaction with a simple hand-held UV lamp (λ = 302 nm).[63] Through further functionalisation of the diaryltetrazole, visualisation of biomolecules and live cell imaging of Z-domain protein encoding O-allyl-tyrosine in *E.coli* by means of photoclick chemistry was achieved.[62a]

The labelling is accomplished without employing further fluorescent markers as the photoclick reaction forms an intrinsically fluorescent pyrazoline (Figure 5). Ever since, this reaction is regularly employed for the labelling of proteins[64] but only rarely for nucleic acids. About ten years ago, the *Wagenknecht* group was one of the first to expand the research and application of photoclick reactions to the labelling of oligonucleotides. Here, a DNA building block bearing a diaryltetrazole moiety was incorporated into a DNA strand and successfully labelled with a sulfo-Cy3 maleimide dye upon irradiation with a 365 nm LED.[65]A few years later, the light-initiated labelling was further extended to RNA strands.[66] Apart from attaching the tetrazole moiety to the oligonucleotide, the incorporation of the alkene moiety opened new avenues for the labelling of nucleic acids as recently demonstrated by several groups. Here, a DNA base is modified with a vinyl group and incorporated into cellular DNA by a metabolic pathway. The groups of *Zhang* and *Xing* performed the successful photoclick reaction with a water-soluble coumarin-fused tetrazole (λ = 350 nm), leading to selective fluorescence imaging of cellular DNA in zebrafish.[67]

Photoclick reactions do not only have the advantage of spatiotemporal controllability, but also show comparably high reaction rate constants (k_2 = 4.6 to 58 $M^{-1}s^{-1}$) in relation to SPAAC (up to two orders of magnitude faster). The majority of reported light-induced bioorthogonal reactions employ wavelengths comprise between 305 nm and 405 nm (UV or violet light) as the trigger which can be harmful to living cells[68] while featuring low penetration depths in tissue.[69] To achieve effective and mild bioorthogonal labelling without potential damage to biological environments, the use of low-energy, long wavelength light is needed. The activation wavelengths of photoclick reactions can be further red-shifted by modifications of the tetrazole moiety, as recently exemplified by the groups of *Barner-Kowollik* and *Wagenknecht* which is based on an earlier visible light-induced variant by the *Barner-Kowollik* team.[70] Both teams employed an (*N,N*-dimethyl)aminopyrene aryl tetrazole, finding applications in polymer chemistry (Figure 6, left arrow) through irradiation with a green LED (λ = 515 nm)[71] or in the successful visualisation of genomic DNA in fixed *HeLa* cells (Figure 6, right arrow), using blue light irradiation (λ = 450 nm).[72]

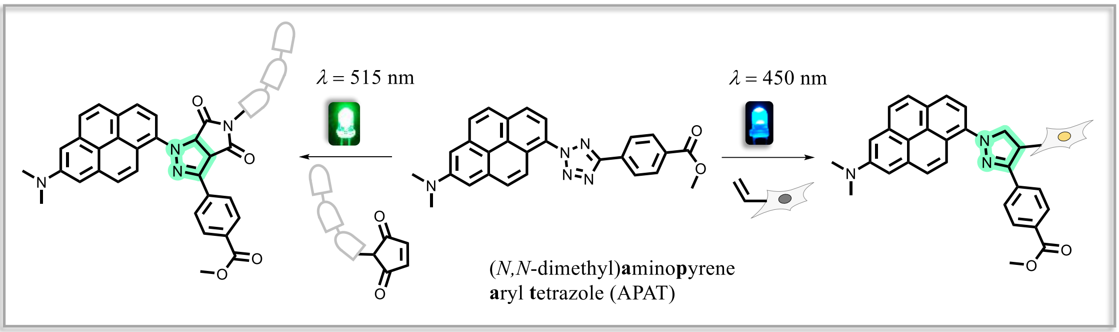

Figure 6: Synthetic routes for photoinduced NITEC reactions of (*N*,*N*-dimethyl)aminopyrene aryl tetrazole (APAT). Left arrow: Polymer end-group modification using a 515 nm LED and a maleimide-functionalised polymer. Right arrow: Metabolic labelling of fixed *HeLa* cells, incubated with vinyl-deoxyuridine prior to irradiation with a 450 nm LED.

Nevertheless, the highly reactive nitrile imine[73] which is formed upon irradiation does not adhere to the strict click criteria[74] as it shows undesired cross-reactivity[27] with moieties that are present in cellular environments, including water,[75] amines, thiols and carboxylic acids.[64c] Further, an often-occurring side reaction of the nitrile imine is the dimerization (Figure 7).

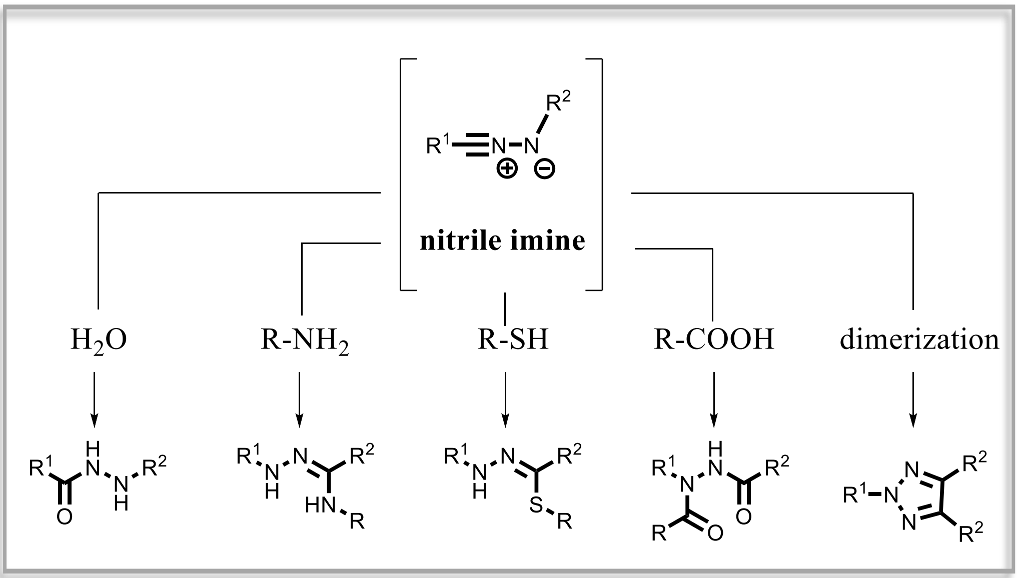

Figure 7: The highly reactive nitrile imine species shows cross-reactivity with moieties present in physiological environments, including water, amines, thiols and carboxylic acids as well as a dimerization as side reaction.

Thus, research needs to be shifted towards the development of new labelling techniques that show no side reactivity with naturally occurring functionalities in biological systems.

Ideally, the new strategies involve longer wavelength light activation, such as green light, as this shows better cell penetration[76] and is more desirable than blue or violet light. Promising candidates for this type of research are photoinduced bond forming reactions.

2.2.2 Light-Triggered Bond Forming Reactions

As mentioned in the previous section, several of the catalyst-free bioorthogonal reactions have already been applied for the labelling of biotargets in cells or even mice models. To provide typical bond-forming reactions the preferred strategy is the introduction of a photoexcitable functionality that reacts with its partner after an external light stimulus leading to one single ligation product. However, most of the photoreactions proceed via photoinduced electron transfer (PET) executed by highly reactive radical species which are formed upon irradiation. Radicals cannot only result in DNA damage but also usually form complex mixtures of products. A solution to this is provided by cycloadditions, which can photochemically occur between chemically distinct or identical π-systems.[77] In a [2+2] cycloaddition for example, two double bonds are combined upon irradiation and form a non-aromatic cyclobutan structure. Further, the starting materials can technically be restored by employing short wavelength light as a trigger. However, depending on the symmetry of the starting materials, some cycloreversion reactions lead to new compounds that differ from the initial composition (Figure 8).

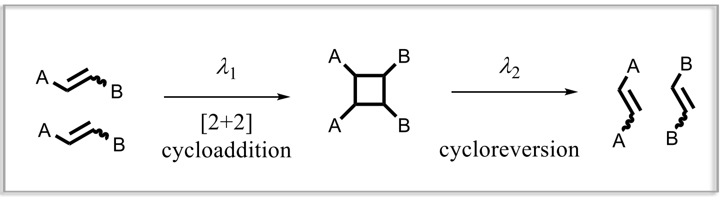

Figure 8: [2+2] photocycloaddition of unsymmetrically substituted double bonds that form a non-aromatic cyclobutan structure. Subsequent irradiation with short wavelength light may lead to cleavage into different monomers.

Although [2+2] cycloadditions have already found a widespread application in synthetic chemistry and material science, their use in complex biological systems is - so far - limited as both the PET process of high-energy excited states and the radical species need to be controlled under physiological conditions.[78] To overcome this challenge, *Zhang* and coworkers introduced a UV light-driven (λ = 360 nm) bioorthogonal [4+2] cyclo-addition between 9,10-phenanthrenequinone (PQ) and an electron-rich alkene, such as a dione vinylether (Figure 9A).[79] The reaction proceeds rapidly under physiological conditions without observable cross-reactions with water or other previously mentioned nucleophilic species.

In 2020, *Fu* and coworkers presented bioorthogonal ligations via mild and selective reactions of chloroquinoxalines (CQs) and *ortho*-dithiophenols (DTs), in which double nucleophilic substitutions of the DTs to the CQs provided the corresponding conjugates containing tetracyclic benzo[5,6][1,4]dithiino[2,3-*b*]quinoxalines with strong built-in fluorescence (Figure 9B).[80]

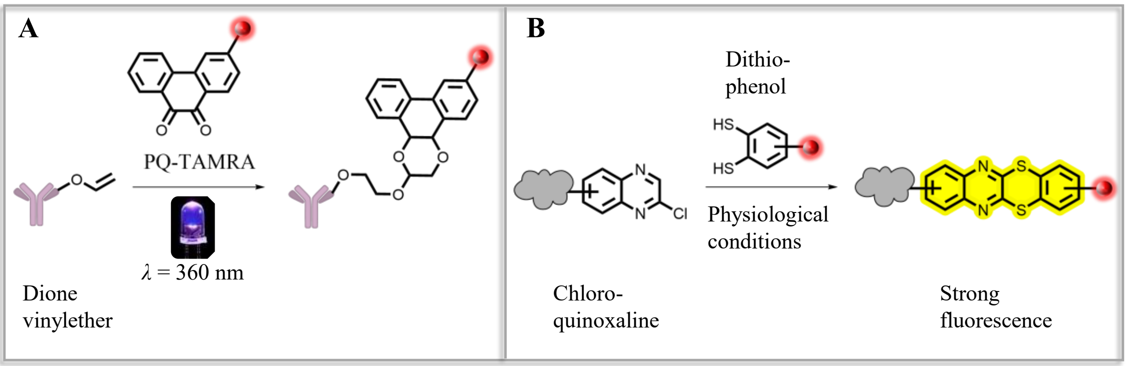

Figure 9: A: Visible light-driven bioorthogonal [4+2] photocycloaddition reaction between dione vinylethers and phenanthrenequinones (PQs). B: Ligation strategy via double nucleophilic substitution of chloroquinoxalines (CQs) and *ortho*-dithiophenols (DTs).

The CQ-DT conjugates were successfully applied for the bioorthogonal ligation, cleavage and trans-tagging of proteins. They are highly stable and show strong fluorescence under physiological conditions. Furthermore, this method provides several advantages including the readily accessible unnatural chloroquinoxaline-groups and appealing reaction kinetics ($k_2 \approx 1.3\ \mathrm{M^{-1}s^{-1}}$) as well as excellent yields.[80] Nevertheless, this system lacks the spatial and well-defined temporal control over the ligation process as this reaction proceeds without employing light as the trigger.

Therefore, *Barner-Kowollik* and coworkers recently expanded the quinoxaline toolbox and broke new ground by introducing a photoinduced [2+2] cycloaddition of a halochromic system, precisely a poly(ethylene glycol) (PEG) styrylquinoxaline (SQ) moiety that can be activated by green light (λ up to 550 nm, Figure 10A).[81]

Moreover, the photoreactivity can be switched on and off by adjusting the pH of the system, opening the door for developing advanced smart mechanisms for biomaterials engineering and extending applications of photocycloadditions in a biological setting. PEG significantly enhances the solubility of the compound in a wide range of solvents and distinguishes itself by its wide applicability in biomaterials design.[82] In comparison to all alkene derivatives performing [2+2] cycloadditions to date, the absorption of the PEG-SQ is significantly red-shifted, employing 510 nm as the longest activation wavelength so far in catalyst-free photocycloaddition.[83]

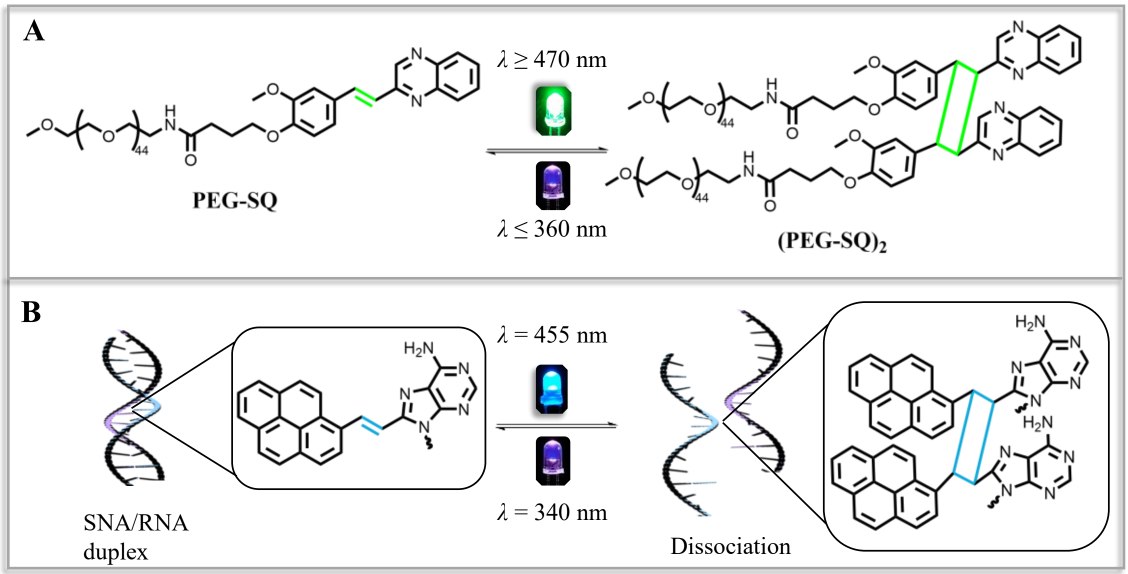

Figure 10: A: [2+2] Photocycloaddition of PEG-Styrylquinoxaline (PEG-SQ). B: Photocontrol of duplex formation between artificial serinol nucleic acid (SNA) and target RNA using 8-pyrenylvinyl adenine as photoresponsive nucleobase.

Concurrently, the group of *Asanuma* expanded the application of [2+2] photocycloadditions to nucleic acid research. Here, styrylpyrenes as well as pyrenylvinyl adenines were successfully employed for the crosslinking of DNA duplexes[84] as well as duplex formation between artificial serinol nucleic acid and RNA (Figure 10B).[85] Within the toolbox of light-induced ligation, [2+2] photocycloadditions offer key advantages, such as highly selective reactivity, generating one specific reaction product,[86] λ-orthogonal reversibility[87] and regioselectivity.[88] However, pyrene moieties have low solubility in water[89] due to their bulky and hydrophobic characteristic and may induce ROS during light irradiation, resulting in DNA damage.[36]

In terms of photochemical reactions, they have commonly been induced by broadly emitting light sources, such as mercury and halogen lamps, or just sunlight.[90] The excitation power of these irradiation sources was drastically reduced with the use of monochromators. With the advent of energy-saving light-emitting diodes (LEDs), fluorescent tubes or advanced monochromatic light amplification by stimulated emission of radiation (laser) setups, wavelength-gated processes have been made accessible.[59a] LEDs offer the advantages of being inexpensive and having reliability lifetimes of up to 10^8 h.[91] Nevertheless, their broad spectral width (60-100 nm)[91] and low output power[91] disqualify them for an intricate control over the photochemical process.

2.3 Laser Systems

In comparison to conventional light sources, lasers come with a unique set of advantages. A laser beam has a very narrow spectral width (0.1 to 0.5 nm) and does not broaden over long distances, resulting in the light being spatially and temporally coherent. Further, laser pulses can be very short (femtoseconds, 10^{-15}s or even attoseconds, 10^{-18}s),[92] reach extremely high intensities[93] and laser light is polarized.[91] Laser systems were first mentioned theoretically ("stimulated emission") by *Albert Einstein* about a century ago.[94] This term was then adopted for amplification of microwave radiation by *Gordon, Zeiger* and *Townes*.[95] In the 1960s, *Maiman* succeeded in shifting the wavelengths into the visible light region,[96] laying the foundation stone for a precision revolution in photochemistry. The pendantic control over photochemical processes can only be achieved employing a (tuneable) monochromatic laser setup. In addition to their important role as advanced research tool for analytical chemistry, biology and astronomy, lasers have become an integral part of modern life. Their widespread industrial applications include *e.g.,* laser pointers,[97] laser cutting,[98] and laser surgery.[99]

To construct a laser, three fundamental components are needed: A pump source, an active laser medium and a resonator (Figure 11).[100] The pump source is the primary source of energy and excites the active laser medium into an excited state. The active laser medium is placed in a resonator, consisting of two opposing mirrors of defined distance. A photon forms stationary waves within the resonator and is self-amplified as it passes through the inversely populated active laser medium, where it generates a second photon through stimulated emission. Newly generated photons match the incident ones in phase, polarisation, and direction, and can then generate new photons. As soon as the amplification is higher than the cavity loss (due to *e.g.,* absorption or scattering), the photons exit through a semi-transparent mirror as spatially and temporally coherent, polarised light beam (Figure 11).

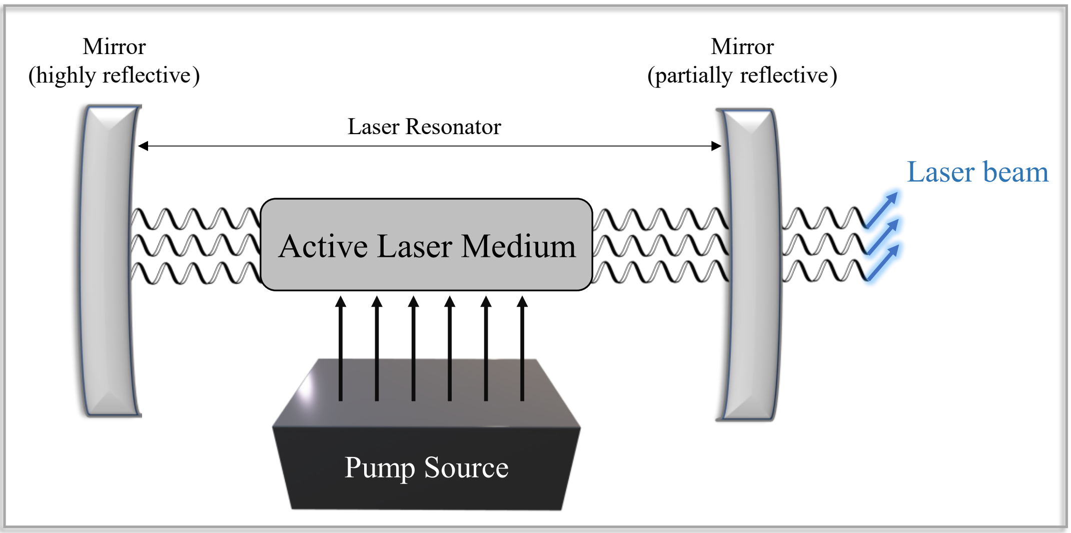
Mirror
(highly reflective)
Mirror
(partially reflective)
Laser Resonator
Laser beam
Active Laser Medium
Pump Source

Figure 11: Simplified schematic illustration of the interaction of the three main components of a laser: pump source, active laser medium and resonator. The laser action begins as soon as the number of amplified photons is higher than the cavity loss and the photons are exiting through a partially reflective mirror as a spatiotemporally coherent, polarised laser beam.

Laser devices generally emit only one wavelength. However, many spectroscopic applications require the application of tuneable laser systems. Their operation priciple is based on the conversion of the output wavelength of an Nd:YAG laser (λ = 1064 nm) into a wide and precise range of wavelengths in the UV, visible and infrared through nonlinear optical processes. With the help of such tuneable laser systems, the group of *Barner-Kowollik* has developed the so-called photochemical action plot methodology over the last decade which probes the efficiency of photochemical processes in a wavelength-resolved fashion.

2.4 Photochemical Action Plots

Approximately ten years ago, the *Barner-Kowollik* team discovered that the reactivity of a light-responsive unit, *i.e.*, at which wavelength it reacts most efficiently, can be significantly different from its absorption profile.[101] This fundamental mismatch between photochemical reactivity and absorptivity is contrary to common expectations and several theories have been proposed to explain the observations.[101] The concept of action plots – also termed “action spectra” earlier[102] – has a substantial and enduring history since the late 19th century in photobiological research, playing a critical role in identifying the key chromophores responsible for biological processes, such as chlorophyll’s role in plant growth[103] or unravelling the key wavelengths leading to skin cancer.[104] The method involved measuring a biological effect (*e.g.*, carbon fixation) as a function of wavelength, offering valuable insights into the underlying mechanisms. In the late 20th century, action spectra resurged as a critical tool to determine the photocurrent efficiency at various wavelengths, employing broad-band lamps coupled to a diffraction grating.[102] The information obtained in these studies has been vital in developing new materials[105] (*e.g.*, photovoltaics[106]) to enhance the capture and utilisation of solar energy. With regard to photochemistry, action spectra have been primarily limited to photodissociation studies, where a laser is coupled to a mass spectrometer and the wavelength-dependent dissociation of ions in the gaseous phase is recorded.[102] The evaluation of photochemical covalent bond forming and cleavage reactions with action plots, however, was only made possible about ten years ago by the group of *Barner-Kowollik* based on the accessibility of tuneable nanosecond pulsed lasers.[107] The most important driver behind recording the first modern day photochemical action plot was the availability of optical parametric oscillators (OPOs) which enable the precise adjustment of light intensity across a wide range of wavelengths from the deep-UV to near-infrared. One of the key criteria for the successful recording of an action plot is that identical aliquots of a reaction mixture are irradiated with an identical number of photons at each distinct wavelength. The quantity of photons, denoted as n_P, present in a monochromatic laser pulse can be determined using the *Plank-Einstein* relation:

$$n_P = \frac{E_{Pulse} \cdot \lambda}{h \cdot N_A \cdot c}$$

Where E_{Pulse} is the measured pulse energy, λ is the wavelength of the incident radiation, h is the *Planck*'s constant, N_A the *Avogadro*'s constant and c is the speed of light. [108]

Irradiation is followed by careful quantitative determination of the conversion of the probed chromophore as a function of irradiation wavelength. The result is a highly wavelength-resolved image of a specific photochemical process from a defined starting material to a defined reaction product.

Using the action plot methodology, a wide range of photochemical processes with emphasis on bond forming reactions has been mapped over the past few years.[109] Just recently, *Feist et al*. pioneered a wavelength-gated synthesis route to phenalene diimides which are applied in organic light-emitting diodes or organic photovoltaic devices as they facilitate charge transportation.[110] By careful choice of substrate and wavelength, the construction of the phenalene diimide scaffolds was stepwisely enabled, resulting in a faster and more efficient synthesis of the desired compounds.[110] In general, action plots provide valuable insights into the optimal activation wavelength to trigger a specific photochemical reaction. However, the methodology can also be translated to photoactive materials science,[111] including surface coating and 3D printing photoresists[112] as well as biomaterials engineering.[113]

Concerning the latter, photochemical action plots already found broad application for the design of advanced hydrogel materials[71, 81, 114] as recently exemplified by *Truong et al.*[115] Here, the wavelength-orthogonal crosslinking of hydrogel networks employing styrylpyrido[2,3-b]pyrazines (SPPs) and acrylpyrenes (APs) was introduced (Figure 12A).[87] With the help of photochemical action plots, it was possible to find the specific wavelength at which covalent bond formation is most efficient (Figure 12B). This opened further avenues in engineering of hydrogel systems with precise elastic moduli, simply by irradiation with discrete colours of light. Surprisingly, nearly all of action plots recorded for bond-forming reactions show a marked red-shift in photoreactivity in comparison to the UV/Vis absorption bands of the chromophore, often inspiring the use of biologically benign visible light (λ = up to 500 nm), where the molar absorptivity of the chromophores is extremely low.

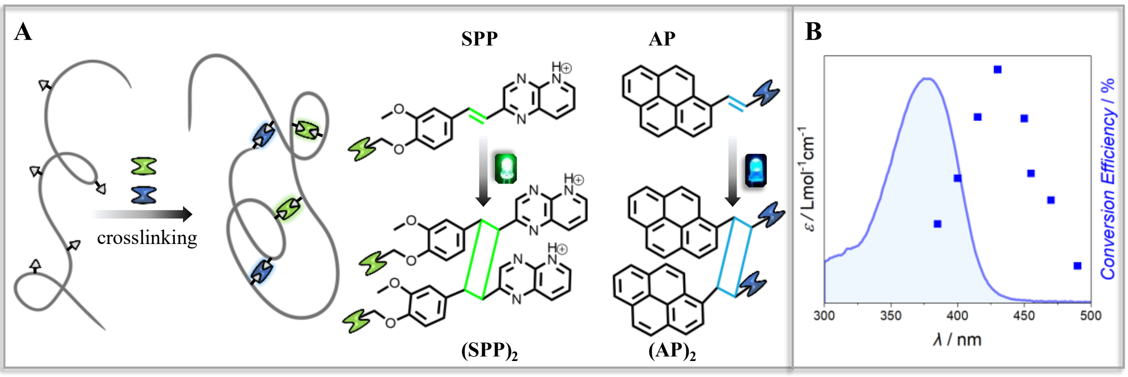

Figure 12: A: Simplified scheme of wavelength-orthogonal crosslinking of hydrogel networks using styrylpyrido[2,3-b]pyrazines (SPPs) and acrylpyrenes (APs). B: Example of an action plot with random red-shifted reactivity of the chromophore in comparison to its UV/Vis absorption band.

While bond-forming reactions have been studied excessively using the introduced action plot methodology, less attention was placed on photocleavages. To date, only the photofragmentation of radical initiators for free radical polymerization[107] and selected classical photodeprotection reactions have been studied, such as *o*-nitrobenzenes[116] and bimanes.[117]

2.5 Photocleavage Reactions

Photocaging and -uncaging of compounds and thus transferring them from an inactive state into an active one is currently a highly sought-after approach to enable non-invasive spatiotemporal photochemical control over the release of species of interest.[118]

Photoprotective groups (PPGs), such as nitrobenzyl-, coumarin-, perylene- or BODIPY-modified compounds (Figure 13) have already found broad application in *e.g.*, orthogonally uncaging DNA[119] or mRNA[120] in cells for optical control of transcription and translation processes[121] or in controlled light-responsive drug release.[122]

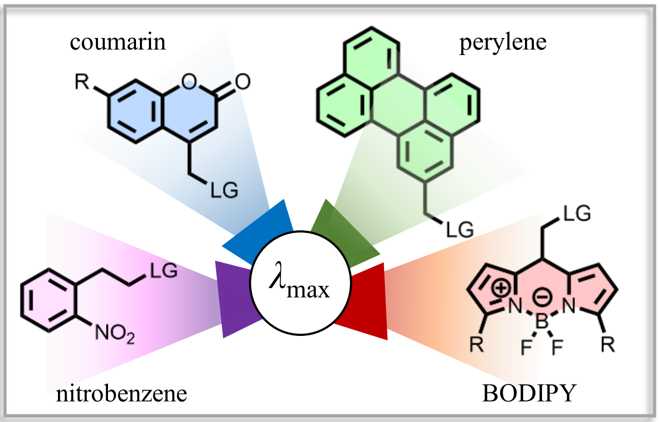

Figure 13: Overview over commonly used photoprotective groups (PPGs) and their respective cleavage wavelengths: nitrobenzenes (λ = 300-360 nm), coumarin (λ = 405-470 nm), perylenes (λ = 480-530 nm) and BODIPY ($\lambda \geq$ 540 nm). LG = Leaving group.

The latter example is an important aspect of modern pharmaceutical research as stimuli-responsive delivery systems enable better solubility and chemical stability of the substances, an increase in pharmacological activity and a reduction of potential side reactions.[123] Besides employing light to activate the release reaction, various other triggers can be used, either naturally occurring or externally applied. Examples of endogenous triggers include pH sensitivity,[124] redox sensitivity[125] or enzyme sensitivity.[126] Exogenous triggers, on the other hand, involve methods such as light[125] or temperature manipulation.[127] However, as already highlighted in preceding sections, light-triggered reactions stand out due to their non-invasive manner, high spatiotemporal and energetic precision, and the possibility of performing reactions at ambient temperatures.[128] Due to the precise control over both position and dose, light-triggered reactions further allow the widespread application in photothermal therapy,[129] *i.e.*, treating cancer metastasis with nanotherapeutics.[130] When compounds are embedded into or conjugated with carriers, the carrier materials become the main component, resulting in low drug loading and excess parenteral excipients. Further, photocaged substrates, especially drugs, offer therapeutic advantages, such as longer circulation time, improved bioavailability of active parent molecules, and reduced side-effects due to the precise spatial control of the release. Cleavage reactions usually employ photoprotective groups (PPGs) and were first introduced in organic synthesis in 1962 – at the same time as cycloadditions – by *Barltrop,*[131] *Barton,*[132] *Woodward,*[133] and *Sheehan*.[134] A few years later, *Engels*[135] and *Kaplan*[136] deciphered the application of PPGs in biology, photocaging adenosine triphosphates (ATPs) with cyclic 3,5-phosphate benzyl triesters. The caged ATP provided a stable source of ATP as it was unmetabolisable by intracellular ATPases until its release upon irradiation with a 340 nm mercury lamp.[136] PPGs are usually covalently bound to the active center of a biologically active substance to suppress its (re)activity. An effective PPG should rapidly and efficiently reveal the active species upon photolytic conversion.[137] As light can be directed and modulated in time and amplitude, it is possible to finely tune the uncaging process, allowing for spatiotemporal control over the release in the sub-micrometer and microsecond range.[138] Advances in synthetic chemistry further expanded the variety of PPGs and offer the possibility to virtually photocage any type of therapeutic or biologically active compound.

Coumarin derivatives are one of the most common used types of photoremovable groups and were first introduced by the group of *Givens*.[139] In their pioneer work 30 years ago, they discovered that the (coumarin-4-yl)methyl group displays photoreactivity, allowing for the release of phosphate esters.[139] Ever since, the applications of coumarin-based PPGs range from drug delivery,[140] *e.g.*, pharmacotherapy of breast cancer[141] to preparation of photoresponsive polymers,[142] such as functional latex nanoparticles.[143] Coumarin-functionalised PPGs offer numerous advantages, including high molar absorption coefficients at wavelengths above 350 nm, efficient and fast photorelease, stability in the dark and fast photolysis kinetics.

The mechanism for the photocleavage of coumarin-caged compounds (*e.g.*, carboxylic acids) involves several steps: (i) light absorption, (ii) relaxation to the lowest (π,π^*) excited singlet state, and (iii) heterolytic bond cleavage (Figure 14). The key intermediate in this process is proposed to be the tight ion pair (TIP),[144] consisting of the coumarinylmethyl cation, and leaving group as conjugated base.[118] The coumarinmethyl cation in this pair could potentially react directly with the adventitious nucleophiles or solvents to produce new stable coumarinmethyl products as suggested by *Bendig* and coworkers.[145]

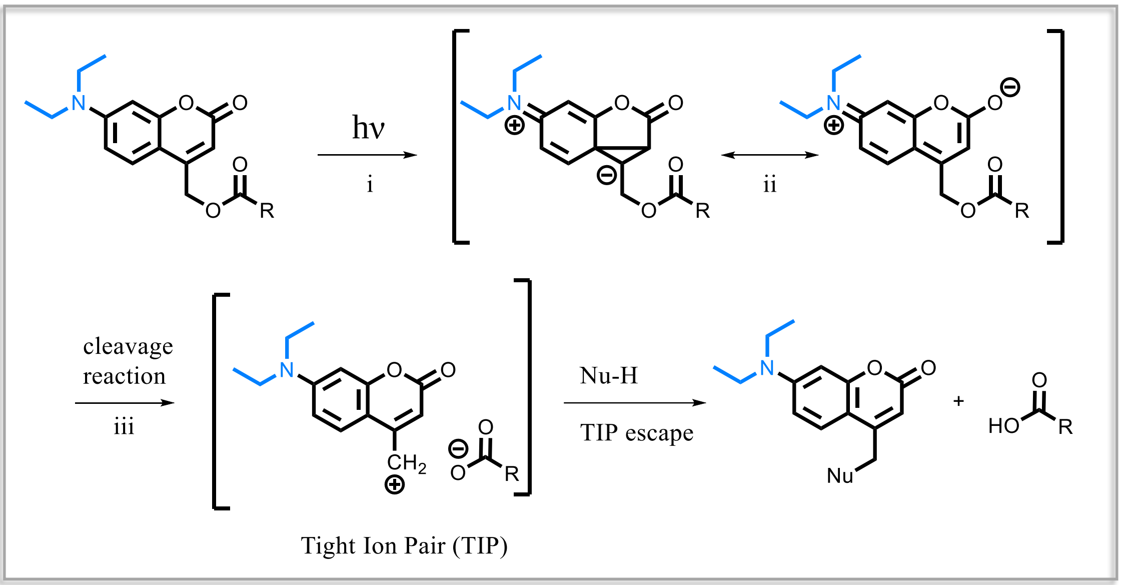

Figure 14: Assumed mechanism of coumarin-photocaged carboxylic acids. After light absorption and excitation (i), the photocaged substrate relaxes into the lowest $(\pi,\pi)^*$ excited single state, which is stabilised by the push-pull-system between the amine and the carbonyl group (ii). A heterocyclic bond cleavage follows, leading to the tight ion pair (TIP). The reaction with a nucleophile results in the formation of the free coumarin derivate and the uncaged carboxylic acid.[118]

The spectroscopic and chemical properties as well as solubility[146] of coumarins can easily be adjusted by altering the substituent on the coumarin ring. For example, the introduction of an electron-donating group, *i.e.*, a 7-diethylamino (NEt_2) substituent (Figure 14, highlighted in blue) enhances the intramolecular charge transfer character of the molecule, leading to a greater bathochromic shift of the peak absorbing wavelength.[147] The photorelease quantum yields for 7-(NEt_2)-modified coumarins are about two times faster than those for all other known coumarin derivatives due to greater stabilisation of the coumarinmethyl carbocation by the electron-donating dialkylamino substituents.[148]

To date, a wide range of molecules has been photocaged, such as active pharmaceutical ingredients,[149] amino acids,[150] peptides,[151] hormones[152] and fatty acids.[153] However, most of these publications cover the regulation of one process in a complex environment whereas the selective regulation of multiple processes within one system remains challenging.

2.5.1 Photoorthogonal Cleavage Reactions

Over the years, numerous attempts have been undertaken to develop strategies for the selective control of independent chemical reactions within one single system. In the field of physics, the term "orthogonality" has long been used to describe wave functions that do not overlap.[154] In chemistry, *Merrifield* first introduced the term "orthogonal" in 1977 in his innovative peptide synthesis[155] approach that was awarded with the Nobel Prize in Chemistry ten years later.[156] Here, orthogonality described the selective introduction and removal of protecting groups by varying the reaction conditions.[155] In a biological context, "bioorthogonal reactions" find broad application as described in detail in section 2.1.

To achieve simultaneous and independent control over chemical reactions within a single system, it is critical to apply external effects, such as light that activate specific reaction pathways without affecting other components. Based on the nature of the light-responsive chromophores, it is possible to achieve orthogonal control by utilising different wavelengths of light. Indeed, multiwavelength-controlled cleavages have been almost achieved in a λ-selective manner, *i.e.*, longer wavelength activation for the first photo-induced release, followed by shorter wavelengths for subsequent photouncaging.[121, 157] The ability of molecules to absorb light at specific wavelengths and trigger intra- or intermolecular photochemical reactions is determined by their chemical structure. By strategically selecting combinations of chromophores, it becomes possible to independently activate different photochemical reactions, as recently shown by

Rentmeister and coworkers.[158] Here, a coumarin-based as well as a nitrobenzene-based 5'-cap analogue was synthesised and incorporated into mRNA. After irradiation by light of different wavelengths, translation of multiple mRNAs was activated (Figure 15).[158]

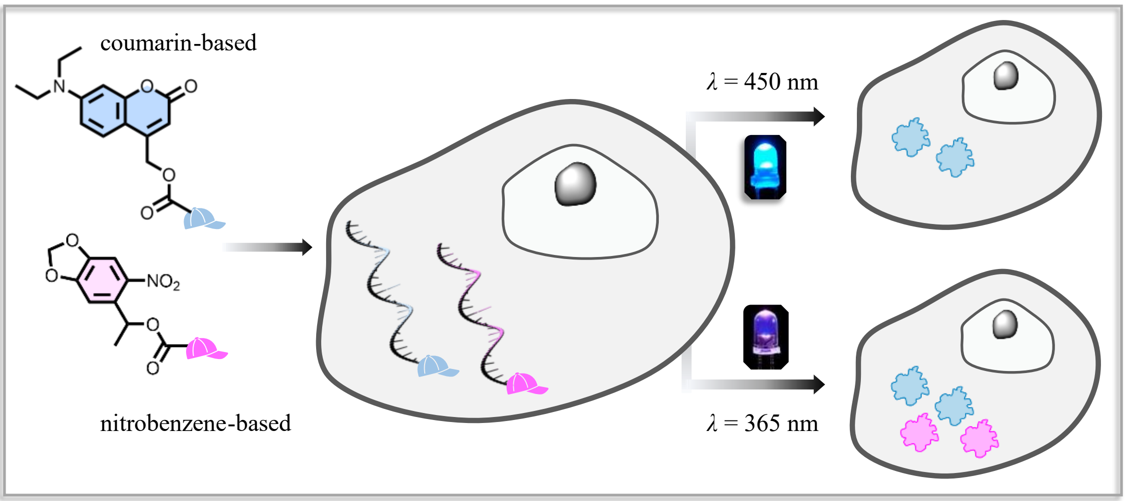

Figure 15: Simplified concept for multiplexed photocleavage to trigger translation of different mRNAs by irradiation with two different wavelengths. The translation is inhibited for both mRNAs until the photocleavable groups are removed separately by irradiation with either blue or violet light.

Concerning biomaterials, the team of *Barner-Kowollik* developed a photoresponsive hydrogel that degrades wavelength-selectively upon irradiation with three different colours of light.[117] The photolabile material crosslinkers are based on nitrobenzene derivatives and were just recently expanded with ruthenium polypyridyl derivatives by the group of *DeForest*, shifting the activation wavelength to low-energy visible light (λ = 500-610 nm).[159]

However, the dual uncaging of drugs remains largely elusive and only a few examples are found in literature.[160] Possible reasons could either be the requirement of exclusively addressing one photoactive species, while the other component remains unaffected or the challenging introduction of different photoresponsive protective groups. The synthesis of these molecules often requires multi-step protection group chemistry with low overall yield. Nevertheless, this can be remedied by "multicomponent reactions" (MCRs)[161] due to their ability to rapidly generate complex molecular architectures in one single step.

2.6 Multicomponent Reactions

MCRs[161-162] involve the simultaneous combination of multiple reactants, leading to the formation of multiple bonds and the creaction of diverse chemical structures.[163] In comparison to traditional stepwise synthesis approaches, MCRs offer increased efficiency, reduced reaction times and improved atom economy. Further, they contribute to the development of sustainable and environmentally friendly processes by minimising waste production and energy consumption.[162a]

Among the various types of MCRs, isocyanide-based reactions, such as *Ugi*[162a] or *Passerini*[162b] reactions, have gained significant attention in recent years. Isocyanides are versatile building blocks that exhibit a wide range of reactivity and compatibility with different functional groups.[161] They enable the construction of complex molecules, often with high levels of chemo-, regio- and stereoselectivity, which makes them especially attractive for the synthesis of biologically relevant natural products.[164]

The *Passerini* reaction is a three-component reaction and involves the combination of an aldehyde (Figure 16, black), a carboxylic acid (Figure 16, orange) and an isocyanide (Figure 16, green).[162b] Although being discovered more than a century ago, the *Passerini* reaction still harbours uncertainties regarding its precise mechanism. Two mechanisms have been proposed: an “open chain mechanism”, involving the formation of a nitrilium ion as a key intermediate (Figure 16, top),[165] and a “concerted mechanism” where no nitrilium ion is formed (Figure 16, bottom).[166] According to common textbooks of organic chemistry, the course of the reaction is dependent on the solvent.[166] In polar solvents (*i.e.*, H_2O or MeOH), the “open chain mechanism” is favoured. In the first step, the carbonyl component of the aldehyde is protonated, followed by nucleophilic additions of the isocyanide and carboxylate residue. The resulting nitrilium ion is subjected to an acyl group transfer, leading to the formation of an α-acyloxyamide. Afterwards, a Mumm-like rearrangement is considered to lead to the *Passerini* product.[165] Conversely, in non-polar solvents (*i.e.*, hexane, benzene or diethyl ether), the reaction is proposed to proceed via the “concerted mechanism”. This mechanism entails a trimolecular reaction between the carboxylic acid, isocyanide, and carbonyl group through a sequence of nucleophilic additions. The transition state is proposed to be a five-membered ring, equally leading to the *Passerini* product after a Mumm-like rearrangement.[166]

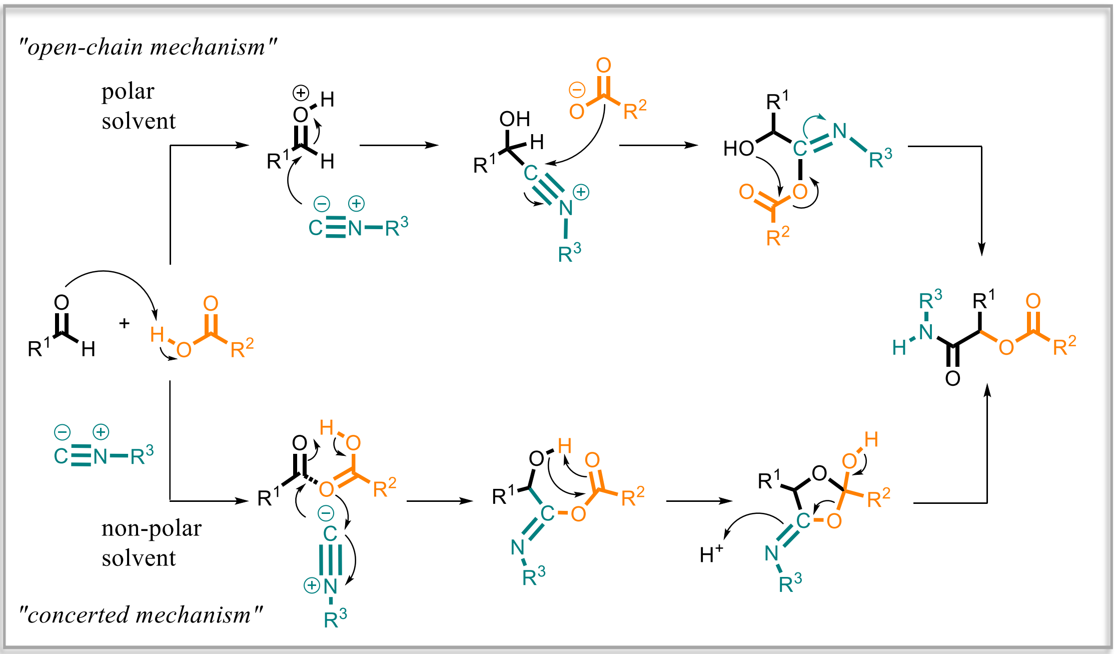

Figure 16: Possible mechanisms for the *Passerini* three component reaction employing aldehydes (black), carboxylic acids (orange) and isocyanides (green). Top: “open-chain mechanism”. After protonation of the carbonyl component of the aldehyde, nucleophilic additions of the isocyanide and carboxylate residue take place. The resulting nitrilium ion is the key intermediate and is subjected to an acyl group transfer, leading to the *Passerini* product after a Mumm-like rearrangement. Bottom: “concerted mechanism”. The three components undergo a sequence of nucleophilic additions to a five-membered ring, following Mumm-like rearrangements eventually lead to the *Passerini* product.

Due to their one-pot nature and simple feasibility, MCRs find various application especially in high-throughput synthesis as recently demonstrated by the groups of *Dömling*[167] and *Levkin*.[168] The simplicity in synthesis allows for the facile introduction of multiple photoprotective groups in one molecule, combining the aforementioned concepts of a light-responsive stimuli with wavelength-orthogonal cleavage.

3 DNA Labelling in Live Cells via [2+2] Photocycloaddition

As described in detail in section 2.1, bioorthogonal coupling reactions have become an indispensable and essential tool for the labelling of biological macromolecules. Albeit including many well-established click reactions, *e.g.*, SPAAC or iEDDA, all these lack spatial and well-defined temporal control over the ligation process. Spatio-temporal control can only be established employing light as the trigger, as exemplified by using photoinduced cycloadditions between tetrazoles and alkenes ("photoclick reactions"). However, most of the light-triggered ligation reactions found in literature employ potentially cytotoxic UV or violet light (λ_{max} = 405 nm) or undergo undesired side reactions with species present in cellular environments.

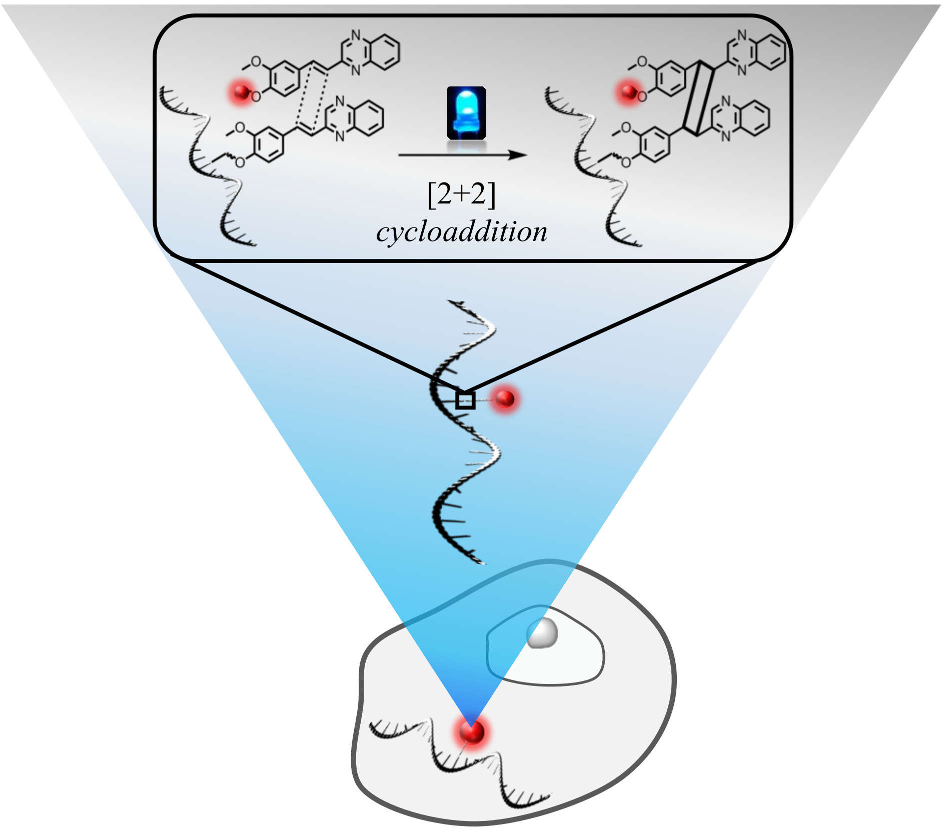

Figure 17: Visible light-induced orthogonal labelling in live cells, employing styrylquinoxaline (SQ)-modified DNA and an SQ-modified Atto655 dye (red sphere). Figure reproduced from ref.[169] with permission from the Royal Society of Chemistry.

To overcome these challenges, the aim of the current PhD project was to develop and apply a new light-induced and highly selective bioorthogonal labelling strategy for DNA in live cells. Since photoinduced [2+2] cycloadditions stand out due to their ability of generating only one specific reaction product, it was decided to employ a styrylquinoxaline (SQ) moiety (Figure 17). The SQ unit undergoes a dimerization through a [2+2] cycloaddition upon biological benign visible light irradiation (λ up to 500 nm), making it a suitable candidate for combining the highly selective reactivity of photocycloadditions with the concept of bioorthogonal reactions. As previously investigated by the group of *Barner-Kowollik*, the SQ moiety reacts selectively in water,[81] enabling further application of the potential bioorthogonal labelling strategy *in cellulo*. Based on a synthetic protocol by the group of *Wagenknecht*,[22b] the SQ moiety was incorporated centrally into an oligonucleotide, employing an NHS-ester amine coupling approach. The SQ-modified DNA can subsequently be tagged with an SQ-containing Atto dye upon visible light irradiation. The successful labelling of the DNA strand was validated via UV/Vis spectrosocpy, HPLC analysis and gel electrophoresis and further conducted in living *HeLa* cells to investigate the bioorthogonality of the newly developed photoinduced ligation approach.

Parts of the current chapter and the associated supplementary information have already been published:

DNA Labelling in Live Cells via Visible Light-Induced [2+2] Photocycloaddition

R. T. Michenfelder, L. Delafresnaye, V. X. Truong, C. Barner-Kowollik, H.-A. Wagenknecht, *Chem. Commun.* **2023**, *59*, 4012-4015.

DOI: 10.1039/D3CC00817G.[169]

3.1 Synthesis of SQ-Modified DNA and SQ-Modified Atto655 Dye

To attach the SQ moiety to DNA and the dye, the reaction of an NHS ester with a primary amine was chosen due to its easy modular interchange of coupling partners and feasibility. Thus, the SQ-NHS ester **7** was synthesised as precursor (Figure 18).

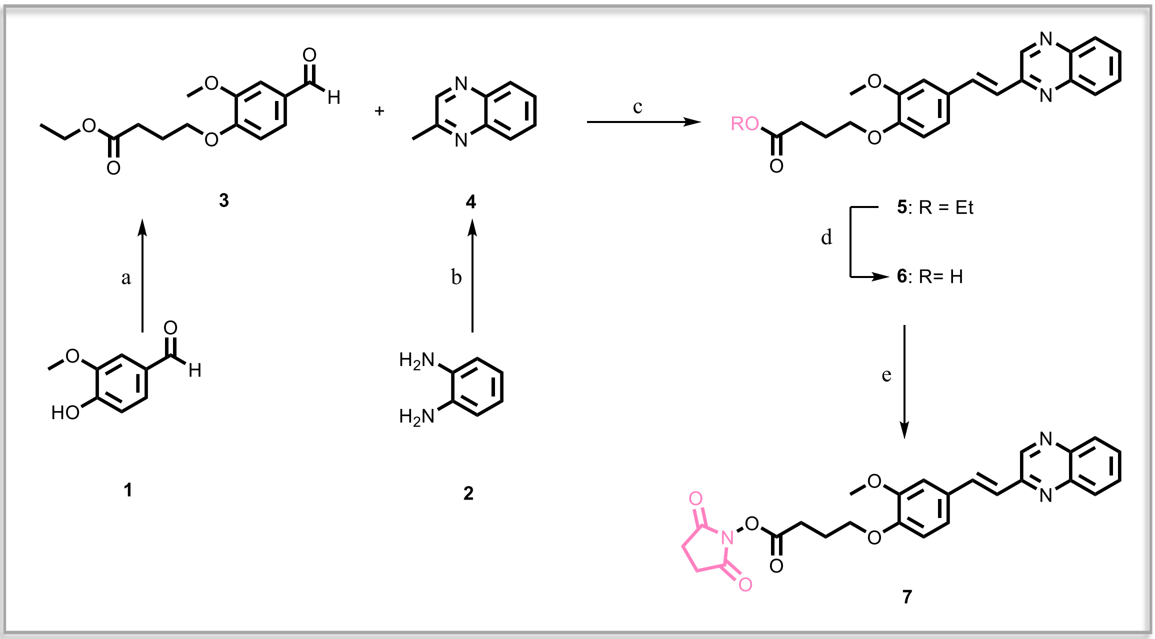

Figure 18: Synthesis of SQ-NHS ester **7**: a) Ethyl-4-bromobutyrate, K_2CO_3, DMF, 50 °C, 2 h, 82%; b) Methylglyoxal, ZnI_2, EtOH / H_2O, 80 °C, 1 h, 61%; c) Piperidine, acetic acid, toluene, 115 °C, 48 h, 71%; d) LiOH, THF, r.t., 1 h, 81%; e) NHS·HCl, DMF, r.t., 6 h, 82 %.

As a first step towards the SQ-NHS ester **7**, the two precursors formylmethoxyphenoxy butanoate (**3**) and methylquinoxaline (**4**) were synthesised according to literature by an S_N2 reaction of vanillin (**1**) with ethyl 4-bromobutyrate and a condensation reaction of benzene-diamine (**2**) and methylglyoxal.[81, 170] Both precursors were subjected to a condensation reaction prior to two consecutive transesterifications.[81] The final SQ-modified NHS ester was obtained via an acid-catalysed esterification in 82% yield (47% overall yield).[81]

Simultaneously, aminopropyl-modified phosphoramidite **13** was synthesised (Figure 19) for subsequent incorporation into **DNA1** by standard and automated solid-phase DNA synthesis.

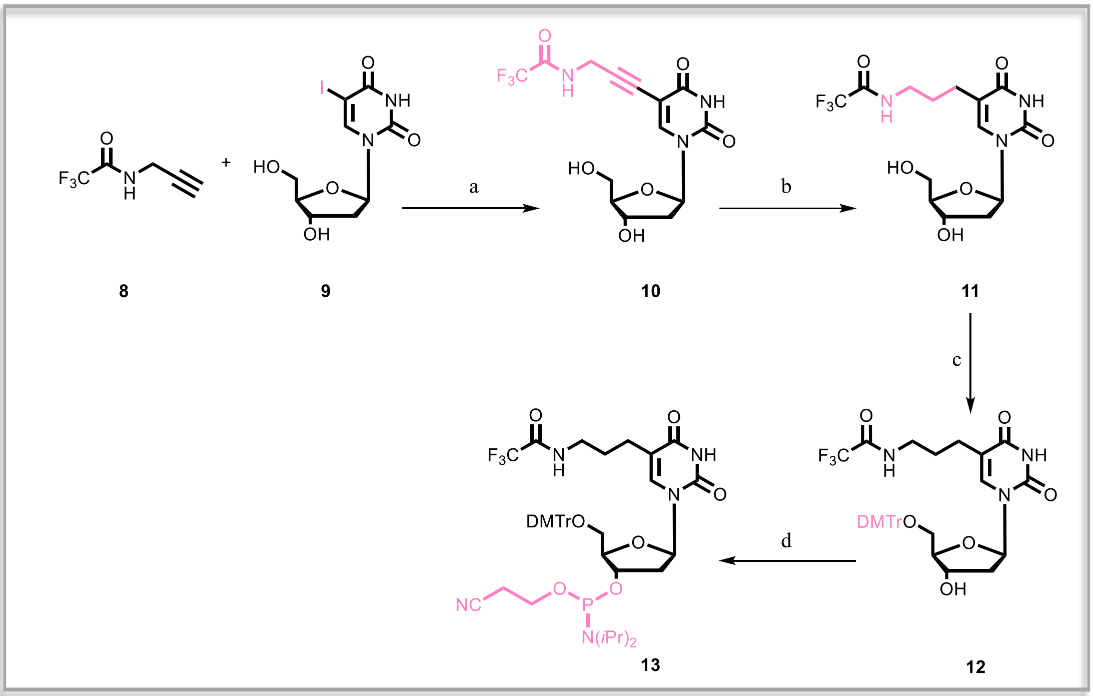

Figure 19: Synthesis of phosphoramidite **13**: a) Copper(I) iodide, tetrakis(triphenylphosphine)-palladium(0), triethylamine, DMF, 50 °C, 5 h, 55%; b) Hydrogen, Pd/C, MeOH, r.t., 6 h, 80%; c) 4,4‘-dimethoxytrityl chloride, silver(I) nitrate, pyridine, r.t., 16 h, 60%; d) 2-cyanoethyl *N*,*N*-diisopropyl-chlorophosphoramidite, DIPEA, DCM, r.t., 2 h, 63%.

Trifluoroacetyl (TFAc)-protected propargylamine (**8**) was reacted according to literature with 5-iodo-2’-deoxyuridine (**9**) to nucleoside **10** by a *Sonogashira* cross coupling.[171] After hydrogenation of the triple bond by employing hydrogen with palladium on charcoal as catalyst, the 5’-position of nucleoside **11** was protected with 4,4’-dimethoxytrityl chloride and silver(I) nitrate as a catalyst.[172] As the final step, a phosphoramidite group was introduced as a precursor for later oxidation to a phosphate at the 3’-position via nucleophilic substitution with 2-cyanoethyl *N*,*N*-diisopropylchloro-phosphoramidite, leading to DNA building block **13** in 63% yield (38% yield over four steps).[22b] Afterwards, phosphoramidite **13** was incorporated internally into DNA sequence **DNA1** using standard solid-phase DNA synthesis protocol. The TFAc group was subsequently removed using aqueous ammonium hydroxide, resulting in the oligonucleotide bearing a free amine group (Figure 20a). The oligonucleotide was cleaved off from the solid support and the SQ moiety was introduced postsynthetically into **DNA1** by reaction with the previously synthesised SQ-NHS ester **7** via an NHS ester-amine coupling protocol, yielding **DNA2** (Figure 20b).

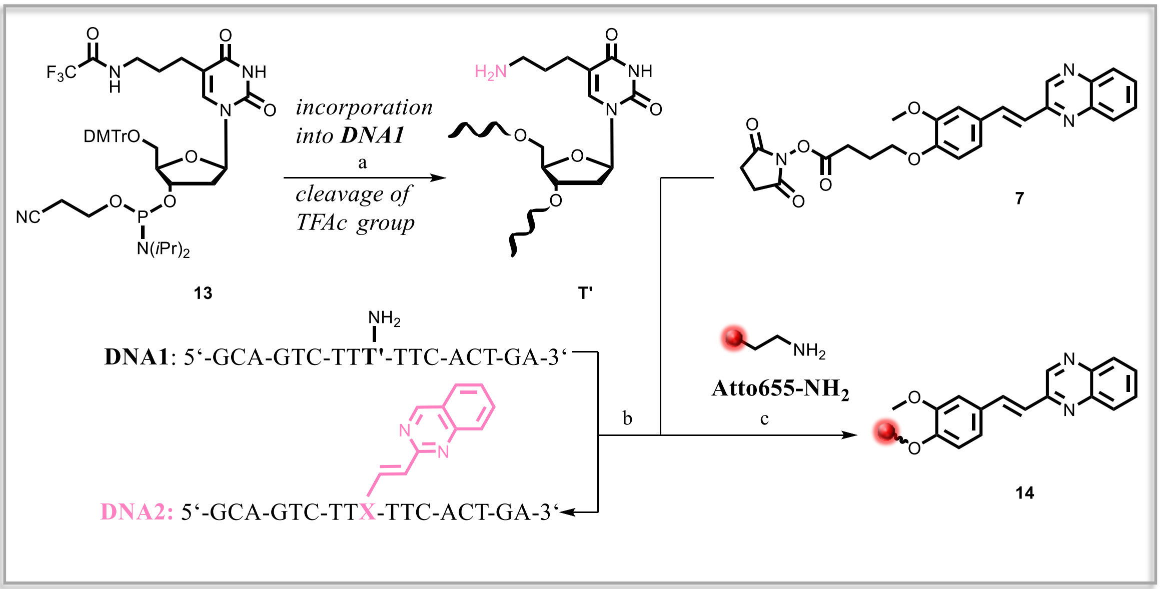
13
incorporation into DNA1
a
cleavage of TFAc group
T'
7
DNA1: 5'-GCA-GTC-TTT'-TTC-ACT-GA-3'
DNA2: 5'-GCA-GTC-TTX-TTC-ACT-GA-3'
b
Atto655-NH$_2$
c
14

Figure 20: a) Synthesis of **DNA1**: Incorporation of **13** into **DNA1** via DNA synthesiser, followed by cleavage of the TFAc group with 25% NH_4OH, 55 °C, 16 h; b) Synthesis of **DNA2**: **7**, DIPEA, DMF, r.t., 48 h; c) Synthesis of SQ-modified Atto655 dye **14**: DIPEA, DMF, r.t., 16 h, 69%.

The DNA strand design features a central attachment of the reactive unit as the middle position is the most sterically hindered and therefore inert position. Further, an SQ-modified Atto655 dye (**14**) was synthesised in 69% yield, employing commercially available Atto655-NH_2 dye and the SQ-NHS ester **7** (Figure 20c).

Both modified DNA strands (**DNA1** and **DNA2**) were purified via HPLC, and the success of the reaction confirmed by MALDI-ToF MS analysis (Table 1).

Table 1: Theoretical and experimental *m/z* values of oligonucleotides **DNA1** and **DNA2** after purification via HPLC.

Sequence	**Theoretical *m/z***	**Experimental *m/z***
DNA1	5191.9 [M^+]	5193.7 [M^+]
DNA2	5539.4 [M^+]	5540.0 [M^+]

Furthermore, **DNA2** was quantified photometrically and characterised by UV/Vis spectroscopy (Figure 21). Apart from the DNA absorbance maximum at λ_1 = 260 nm, the oligonucleotide shows a distinct band at λ_2 = 396 nm that can be assigned to the SQ moiety.

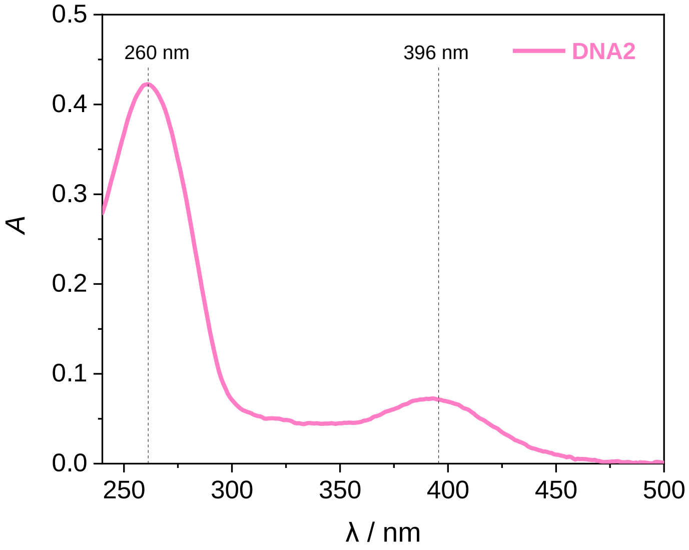

Figure 21: UV/Vis absorbance of **DNA2**: 2.50 µM solution in 10 mM Na-P$_i$ buffer with 250 mM NaCl at pH 7 at 20 °C.

3.2 Irradiation Experiments

In the following step, [2+2] photocycloaddition with the synthesised **DNA2** was performed using a 450 nm LED (refer to section 5.2.1 for LED emission spectra) to obtain insight regarding the proposed highly selective reactivity of two SQ moieties in water (homo-dimerization, Figure 22). To specifically highlight the linkage of two SQ-modified DNA strands, the irradiation experiments of **DNA2** to **(DNA2)$_2$** were performed on two non-complementary sequences as they would never fuse without a (light-driven) ligation reaction.

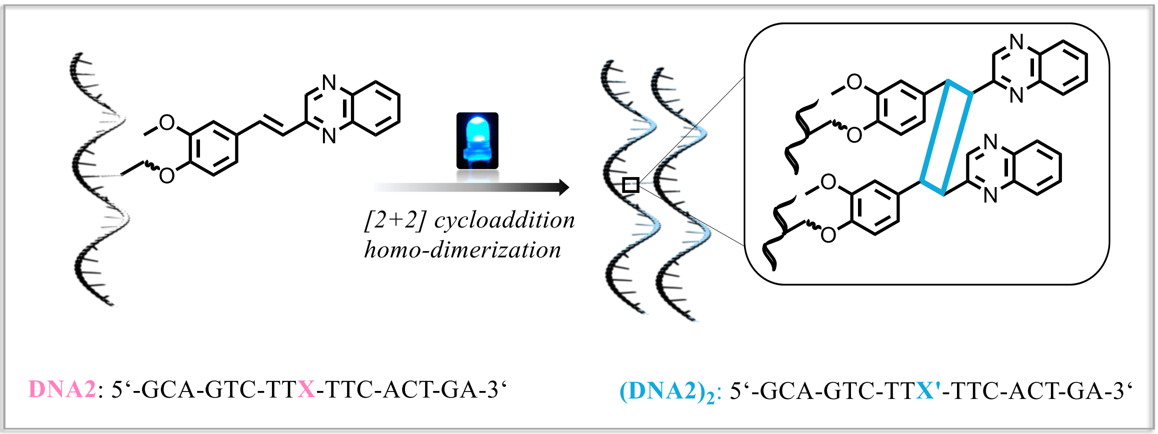
[2+2] cycloaddition
homo-dimerization
DNA2: 5'-GCA-GTC-TTX-TTC-ACT-GA-3'
(DNA2)$_2$: 5'-GCA-GTC-TTX'-TTC-ACT-GA-3'

Figure 22: Fusion of two non-complementarty **DNA2** strands via [2+2] cycloaddition to homo-dimerized **(DNA2)$_2$** through irradiation of 50 µM **DNA2** in H_2O, 10 mM Na-P_i buffer, 250 mM NaCl, pH 7 at 20 °C with a 450 nm LED for 24 h in total.

The reaction was followed by UV/Vis spectroscopy at defined times for 24 h in total. Pre-irradiation, **DNA2** shows two distinctive maxima at λ_{max1} = 260 nm and λ_{max2} = 397 nm (Figure 23 left, dark green line). λ_{max1} is assigned to the DNA absorbance and λ_{max2} is associated with the SQ-moiety. During irradiation, the DNA absorbance maximum as well as the SQ bands decrease (Figure 23 left, red line), whereas one new maximum is emerging at λ = 325 nm. This indicates successful homo-dimerization to **(DNA2)$_2$** as a similar change in the absorbance of the SQ moiety, attached to PEG, has previously been reported.[81] The decrease at λ = 260 nm can be explained by stacking of the chromophores leading to hyperchromicity due to forced interactions between the two DNA strands after successful ligation of two SQ moieties.

On closer inspection, the absorbance spectra indicate that the reaction to the dimer is complete after 5 h of irradiation, when the peak intensity reaches its maximum at λ = 325 nm (Figure 23 left, orange line). Nevertheless, the increase of the new maximum is not as significant as noted in literature.[81] Thus, to further support the suggested homo-dimerization of **DNA2** to **(DNA2)$_2$**, analytical HPLC analysis was performed.

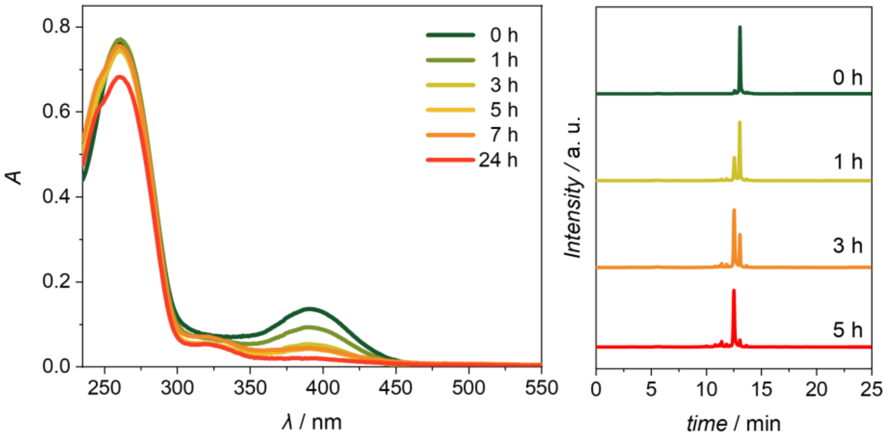

Figure 23: Left: UV/Vis spectroscopic changes and right: RP-HPLC analyses ($\lambda_{detection}$ = 260 nm) of 50 µM **DNA2** in H_2O, 10 mM Na-P$_i$ buffer, 250 mM NaCl, pH 7 at 20 °C over 24 h of irradiation at 20 °C with a 450 nm LED.

According to the maximum absorption of DNA, the detection wavelength for the HPLC analyses was set to λ = 260 nm. Since after 5 h of irradiation no further changes in the HPLC chromatograms were visible, only four chromatograms are presented (Figure 23 right). Pre-irradiation, the chromatogram of **DNA2** shows one significant peak at t_R = 13.1 min (dark green line). During irradiation, the peak decreases while a new peak at t_R = 12.6 min is formed (red line). The peak at t_R = 13.2 min retention time disappears completely over the course of irradiation, further supporting homo-dimerization of **DNA2**.

However, mass spectrometric analyses (MALDI-ToF, ESI-HRMS and ESI-LCMS) do not confirm the formation of **(DNA2)$_2$**. The dimerized oligonucleotide might be challenging to ionise during mass spectroscopic analyses and the high mass of **(DNA2)$_2$** exceeds the capabilities of the spectrometer. To overcome the analytical problems, agarose gel electrophoresis was performed as an alternative.

The agarose gel shows three lanes in total (Figure 24). In lane 1, the commercially available DNA marker is applied, lane 2 displays non-irradiated starting oligonucleotide **DNA2** and lane 3 is filled with **DNA2** after 5 h of irradiation with a 450 nm LED. The gel sieves the DNA fragments by their size, whereby smaller molecules move faster. After successful homo-dimerization of **DNA2**, **(DNA2)$_2$** is expected to feature double the mass and thus a slower electrophoretic mobility since the strands are connected through successful [2+2] cycloaddition between two SQ moieties. The band of **(DNA2)$_2$** is located between 15 bp and 20 bp in comparison to the ladder in lane 1, confirming the homo-dimerization of **DNA2** to **(DNA2)$_2$** after 5 h of irradiation with a 450 nm LED.

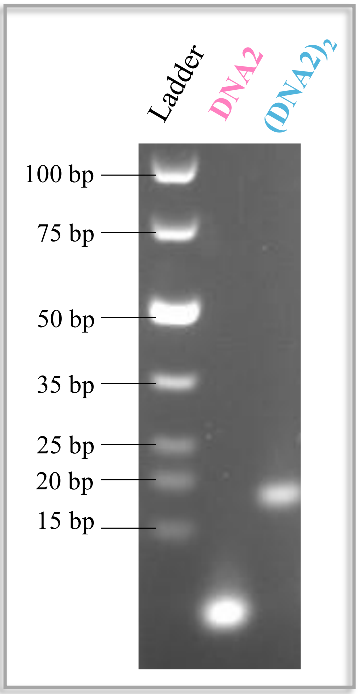

Figure 24: Agarose gel electrophoretic analysis of **(DNA2)$_2$** after irradiation of 50 µM **DNA2** at 20 °C with a 450 nm LED for 5 h in aqueous solution containing 10 mM Na-P$_i$ buffer and 250 mM NaCl in a total volume of 600 µL in a crimp vial. Staining was performed using SybrGreen™, followed by visualisation under UV light (λ_{exc} = 312 nm).

3.3 Labelling Experiments

After confirmation of homo-dimerization of **DNA2** to **(DNA2)**$_2$ employing spectroscopic, HPLC and gel electrophoretic analysis, the hetero-dimerization of SQ-modified **DNA2** with synthesised SQ-modified Atto655 dye **14** to **DNA3** was investigated (Figure 25).

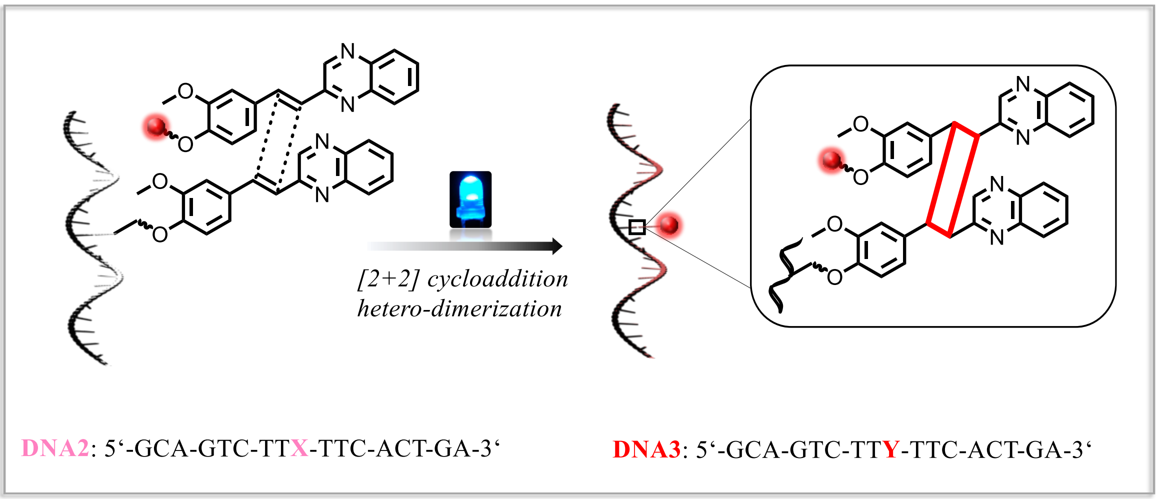
[2+2] cycloaddition
hetero-dimerization
N
O
DNA2: 5'-GCA-GTC-TTX-TTC-ACT-GA-3'
DNA3: 5'-GCA-GTC-TTY-TTC-ACT-GA-3'

Figure 25: Synthesis of **DNA3** through [2+2] cycloaddition of **DNA2** and SQ-modified Atto655 dye **14** in H_2O, 10 mM Na-P_i buffer, 250 mM NaCl, pH 7 at 20 °C through irradiation with a 450 nm LED for 5 h.

Initial experiments were carried out using 50 µM **DNA2** and 50 µM SQ-modified Atto655 dye **14** (1:1 equivalents) by irradiation with a 450 nm LED for 5 h in aqueous solution, collecting a sample at predefined times. As UV/Vis spectroscopy and HPLC analysis initially showed inconclusive results (refer to section 7.1, Figure A1 and Figure A2), agarose gel electrophoresis was selected as key analysis method. However, the agarose gel merely displayed homo-dimerization to **(DNA2)**$_2$ (refer to section 7.1, Figure A3). Therefore, denaturing polyacrylamide gel electrophoresis (PAGE) was performed as a more sensitive method.

The PAGE shows three lanes in total (Figure 26). Lane 1 displays non-irradiated **DNA2**, whereas lanes 2 and 3 show **(DNA2)$_2$** and **DNA3** after 5 h of irradiation with a 450 nm LED. As stated by the supplier of the ladder, double stranded ladders are not recommended for denaturing electrophoresis as they may form an atypical pattern. Lane 1 displays one gel band with the smallest size of all three lanes. **(DNA2)$_2$** in lane 2 shows two gel bands, one in the same position as lane 2 and one located at the upper end of the gel. After the successful reaction of **DNA2** with SQ-modified Atto655 dye **14, DNA3** (m/z_{theo} = 6456.5) features a mass between **DNA2** (m/z_{theo} = 5539.4) and **(DNA2)$_2$** (m/z_{theo} = 11 078.8) and is therefore expected to lead to a band between these two fragments. The smaller sized fragment is assigned to the starting material **DNA2**, whereas the larger sized fragment is associated with the dimerization product of **DNA2** to **(DNA2)$_2$**. Lane 3 displays the same two fragments as lane 2 but also a faint new band between **DNA2** and **(DNA2)$_2$**, indicating successful conversion of **DNA2** to **DNA3**. However, homo-dimerization seems to be favoured as the band at the upper end of the gel is more intense as the **DNA3** band.

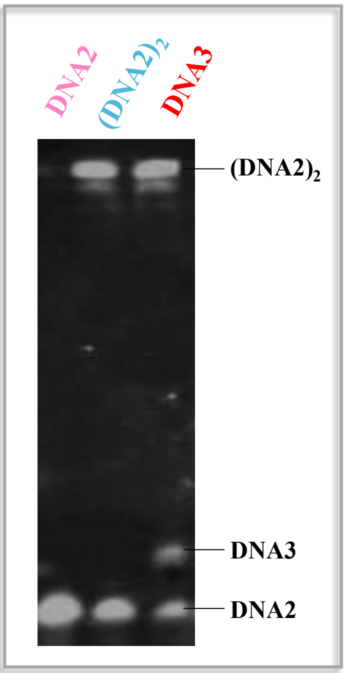

Figure 26: Denaturing PAGE analysis of **DNA3** after irradiation of **DNA2** and SQ-modified Atto655 dye **14** (1:1 equivalents) at 20 °C with a 450 nm LED for 5 h in aqueous solution containing 5% DMF, 10 mM Na-P$_i$ buffer and 250 mM NaCl in a total volume of 600 µL in a crimp vial. Staining was performed using SybrGreen™, followed by visualisation under UV light (λ_{exc} = 312 nm).

In addition, there is evidence of homo-dimerization between two SQ-modified Atto655 dyes (refer to section 7.1, Figure A4 and Figure A5). As this reaction is not interfering with the DNA strands, it is of minor concern and will further be disregarded.

To drive the reaction towards the formation of **DNA3** instead of **(DNA2)$_2$**, the experiment was repeated using 50 µM **DNA2** and 250 µM SQ-modified Atto655 dye **14** (1:5 equivalents). Again, UV/Vis absorbance and HPLC analysis of **DNA3** initially showed inconclusive results (refer to section 7.1, Figure A6 and Figure A7). Thus, agarose gel electrophoresis was selected as key method to investigate the ligation of **DNA2** to **DNA3**. The agarose gel (Figure 27A) shows four lanes in total with the commercially available DNA marker applied in lane 1. Lane 2 displays the non-irradiated starting oligonucleotide **DNA2** and lane 3 is filled with the previously confirmed **(DNA2)$_2$** homo-dimer. **DNA3** in lane 4 displays a fragment sized between **DNA2** and **(DNA2)$_2$**, confirming the full conversion of **DNA2** to **DNA3** after 5 h of irradiation.

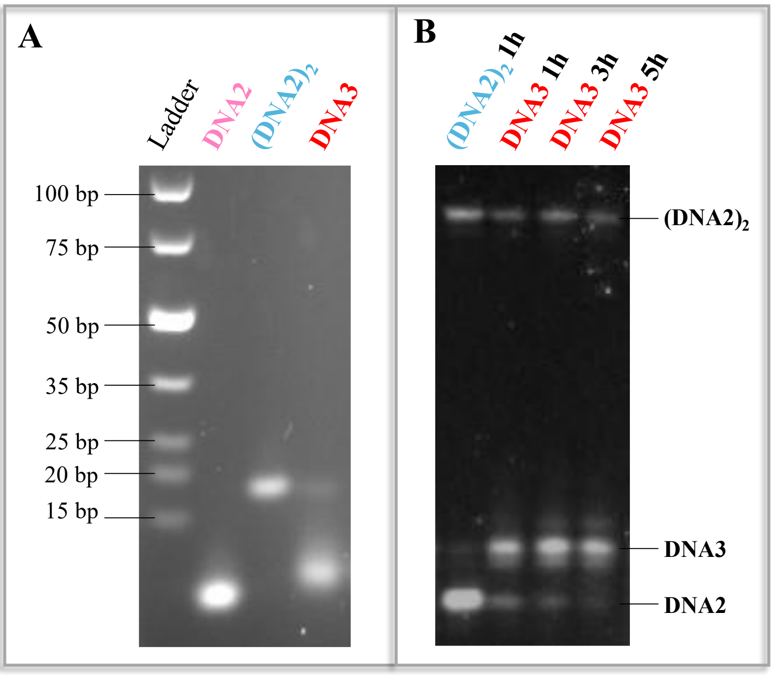

Figure 27: A: Agarose gel electrophoretic analysis and B: PAGE analysis of **DNA3** after irradiation of 50 µM **DNA2** and 250 µM SQ-modified Atto655 dye **14** at 20 °C with a 450 nm LED for 5 h in aqueous solution containing 5% DMF, 10 mM Na-P$_i$ buffer and 250 mM NaCl in a total volume of 600 µL in a crimp vial. Staining was performed with SybrGreen™ followed by visualisation under UV light (λ_{exc} = 312 nm).

Additionally, denaturing PAGE (Figure 27B) was performed to further confirm **DNA3** formation and to calculate the yield.

The yield of **DNA3** was determined through comparison of gel band intensities, calculating the percentage of integrated peak areas. For completeness, all collected samples were assembled on one gel. Lane 1 shows **DNA2** after 1 h of irradiation time, leading to homo-dimerization to **(DNA2)$_2$**. Lanes 2 to 4 show **DNA3** after 1 h, 3 h and 5 h irradiation time. The PAGE shows equal results as the agarose gel, clearly confirming the formation of **DNA3** as an intense new band between **DNA2** and **(DNA2)$_2$**. On closer inspection of the **DNA3** pockets, both gels show a faint fragment moving as far through the gel as **(DNA2)$_2$**, suggesting homo-dimerization of two **DNA2** strands as a competing reaction. However, due to the fivefold excess of the Atto655 dye **14**, the reaction is rather driven towards the formation of **DNA3** as confirmed by the band intensities in the gels. Further, by comparison of 1 h irradiation time to 5 h irradiation time in the PAGE gel, it is clearly visible that 1 h of irradiation time is sufficient to build **DNA3** as the band intensities are similar. This qualitative assumption is further confirmed by the yield calculation. The software determined similar conversion of **DNA2** to **DNA3** (58%) after 1 h of irradiation as well as after 5 h of irradiation (refer to section 7.1, Figure A8 and Table A1), allowing shorter reaction times in the following application in living cells.

3.4 Labelling Experiments in Live Cells

Next, the results of the successful formation of **DNA3** were transferred to live *HeLa* cells to highlight the bioorthogonality of the visible light-induced ligation *in cellulo*. *HeLa* cells were transfected with 75 ng of oligonucleotide **DNA2** using transfection reagent *ScreenFect A* and incubated for 24 h. Subsequently, the cells were incubated for 16 h with 20 µM of synthesised SQ-modified Atto655 dye **14**, followed by a careful washing step of the cells with PBS buffer. The *HeLa* cells were then irradiated with a 450 nm LED for 30 min at 37 °C to induce Atto655-labelling to **DNA3.** Success of the labelling reaction was investigated by confocal fluorescence microscopy imaging of the live cells (Figure 28). As a negative control, *HeLa* cells were incubated with 20 µM Atto655 dye **14** without prior transfection of **DNA2.** Initial experiments confirmed strong intrinsic fluorescence of the SQ-modified Atto655 dye **14**. As both images display the same red fluorescence staining inside the cytosol of the cells, a clear distinction between a successful [2+2] cycloaddition and the negative control is impossible.

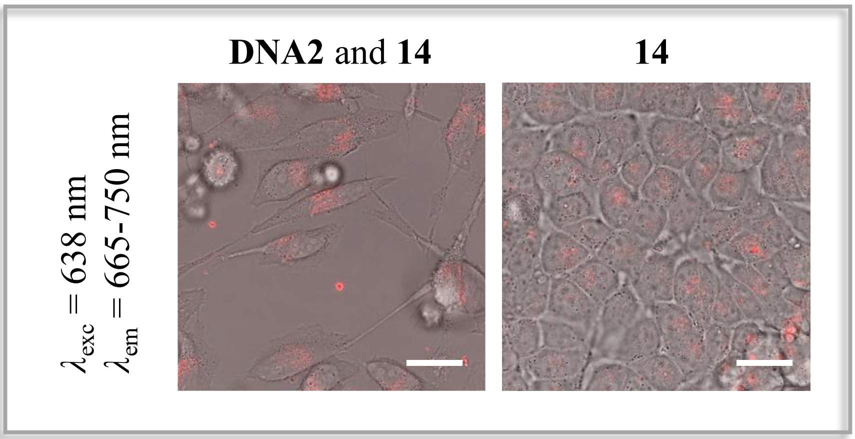

Figure 28: Confocal laser microscopy images of living *HeLa* cells. Left: *HeLa* cells were transfected for 24 h with 75 ng **DNA2**, followed by incubation for 16 h with 20 µM Atto655 dye **14**. Right: As a negative control, *HeLa* cells were incubated with 20 µM Atto655 dye **14** without prior transfection of **DNA2**. All cells were irradiated for 30 min at 37 °C with a 450 nm LED, followed by imaging at λ_{exc} = 638 nm and λ_{em} = 665-750 nm. Scale bar: 10 µm.

Thus, it was decided to exploit Förster Resonance Energy Transfer (FRET) to confirm the successful labelling of DNA in live cells. SQ- and Atto520-modified oligonucleotide **DNA6** was prepared as FRET-donor sequence via the following three-step synthesis (Figure 29).

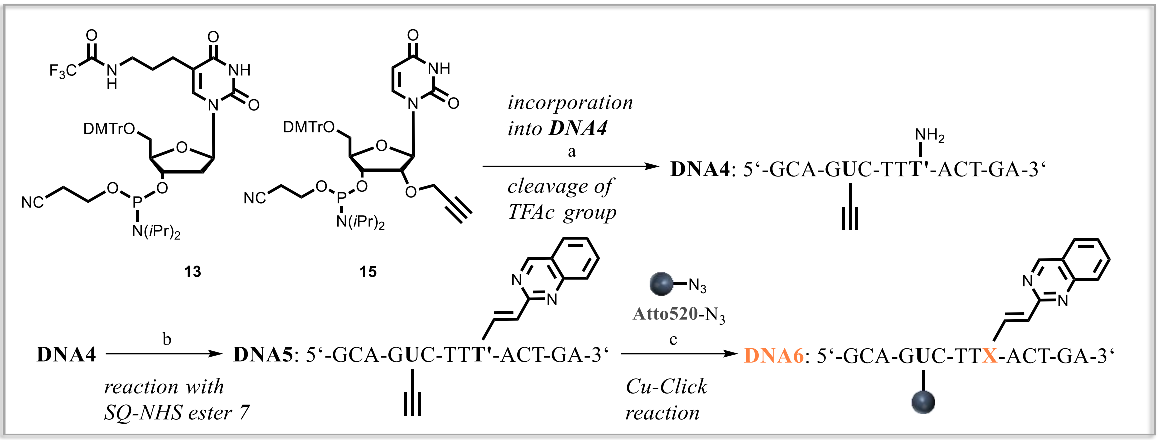
13
15
incorporation into DNA4
a
cleavage of TFAc group
DNA4: 5‘-GCA-GUC-TTT'-ACT-GA-3‘
DNA4
b
reaction with SQ-NHS ester 7
DNA5: 5‘-GCA-GUC-TTT'-ACT-GA-3‘
Atto520-N3
c
Cu-Click reaction
DNA6: 5‘-GCA-GUC-TTX-ACT-GA-3‘

Figure 29: Synthesis of **DNA6:** a) Synthesis of **DNA4**: incorporation of **13** and **15** into **DNA4** via DNA synthesiser, followed by cleavage of the TFAc group with 25% NH_4OH, 55 °C, 16 h; b) Synthesis of **DNA5**: **7**, DIPEA, DMF, r.t., 48 h; c) Synthesis of **DNA6** through Cu(I)-Click reaction with commercially available Atto520-N_3.

In the first step, previously synthesised phosphoramidite **13** and commercially available phosphoramidite **15** were incorporated internally into **DNA4** by standard and automated solid-phase DNA synthesis. The TFAc group was removed using aqueous ammonium hydroxide, followed by cleavage of **DNA4** from solid support (Figure 29a). Afterwards, the SQ moiety was introduced postsynthetically into **DNA5**, employing the previously established SQ-NHS ester-free amine coupling protocol (Figure 29b). In the last step, **DNA6** was obtained via copper(I)-catalysed alkyne-azide cycloaddition of the introduced alkyne moiety and a commercially available azide-modified Atto520 dye (Figure 29c).

All modified oligonucleotides (**DNA4** to **DNA6**) were purified via HPLC and the success of the reaction confirmed by MALDI-ToF MS analysis (Table 2).

Table 2: Theoretical and experimental *m/z* values of oligonucleotides **DNA4** to **DNA6** after purification via HPLC.

Sequence	**Theoretical *m/z***	**Experimental *m/z***
DNA4	4334.2 $[M^+]$	4329.9 $[M^+]$
DNA5	4681.5 $[M^+]$	4678.9 $[M^+]$
DNA6	5257.7 $[M^+]$	5256.1 $[M^+]$

Furthermore, **DNA6** was quantified photometrically and characterised by UV/Vis absorbance and emission spectroscopy (Figure 30). Apart from the DNA absorbance maximum at λ_{max1} = 260 nm, the oligonucleotide displays the distinct SQ band at

λ_{max2} = 397 nm. Also, **DNA6** shows a third absorbance maximum at λ_{max3} = 532 nm, which corresponds to the excitation maximum of the introduced Atto520 dye. In addition, **DNA6** displays an emission maximum at λ_{em} = 580 nm when excited at λ_{exc} = 488 nm (Figure 30, orange line).

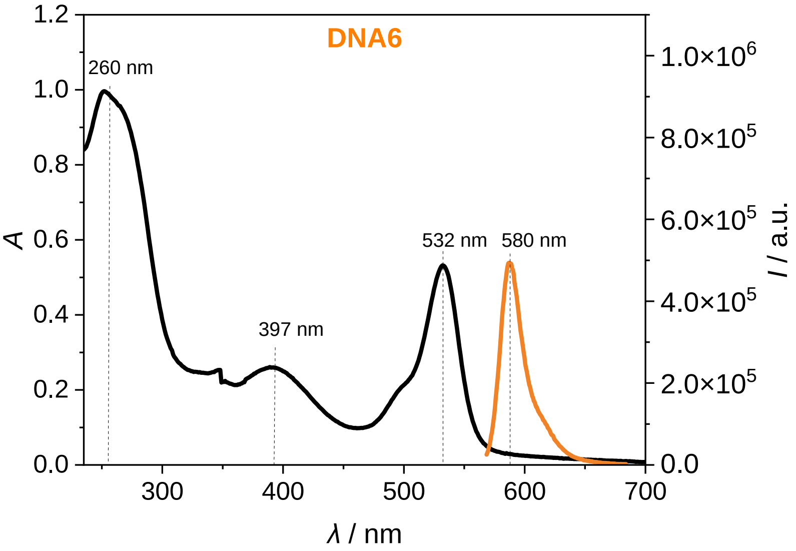

Figure 30: UV/Vis absorbance (black) and emission spectra (orange) of **DNA6**: 5 µM solution in ddH_2O at 20 °C.

Subsequently, *HeLa* cells were transfected with 75 ng of **DNA6** using transfection reagent *ScreenFect A* and incubated for 24 h (Figure 31a). Afterwards, the cells were incubated for 16 h with 20 µM of synthesised SQ-modified Atto655 dye **14** (Figure 31b), followed by a careful washing step of the cells with PBS buffer. The *HeLa* cells were then irradiated with a 450 nm LED for 30 min at 37 °C to induce Atto655-labelling to **DNA7** (Figure 31c). Success of the labelling reaction was confirmed by confocal fluorescence microscopy imaging of the live cells using the FRET (Figure 31d). The Atto520 dye acts as donor (λ_{exc} = 488 nm) and the Atto655 dye functions as acceptor, showing fluorescence emission at λ_{em} = 665-750 nm when the [2+2] photocycloaddition and accompanying FRET is successful.

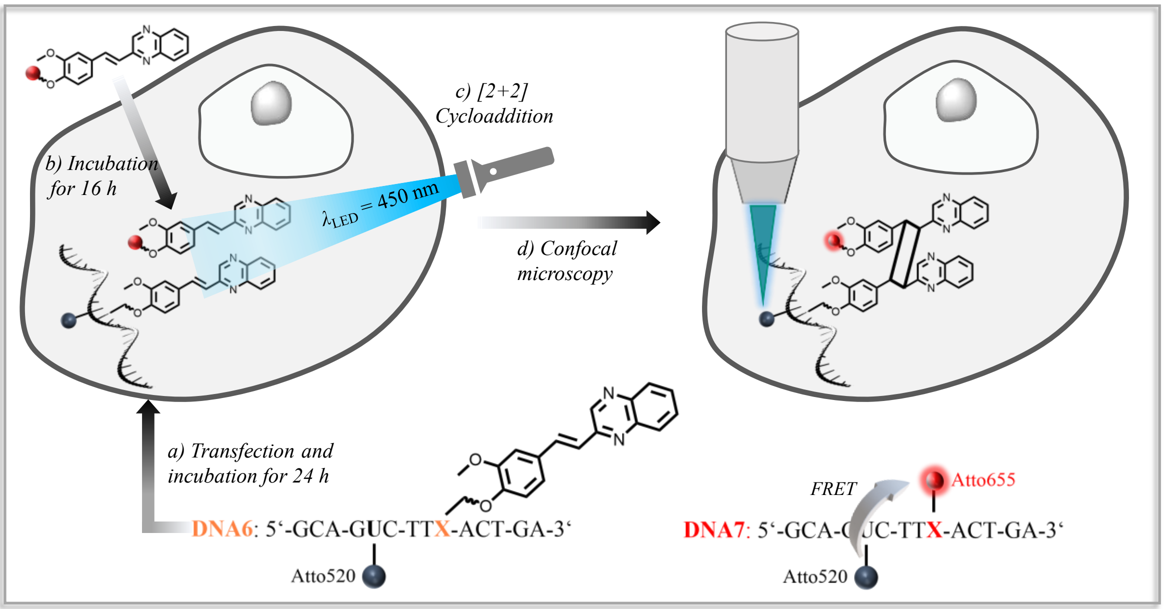
b) Incubation for 16 h
c) [2+2] Cycloaddition
λ_{LED} = 450 nm
d) Confocal microscopy
a) Transfection and incubation for 24 h
DNA6: 5'-GCA-GUC-TTX-ACT-GA-3'
Atto520
FRET
Atto655
DNA7: 5'-GCA-GUC-TTX-ACT-GA-3'
Atto520

Figure 31: Schematic overview of visible light-induced DNA labelling in living *HeLa* cells via [2+2] cycloaddition of SQ. a) Transfection of *HeLa* cells for 24 h with 75 ng SQ- and Atto520-modified **DNA6**; b) Incubation for 16 h with SQ-modified Atto655 dye **14**; c) Irradiation with a 450 nm LED for 30 min at 37 °C to form **DNA7**; d) Confirmation of the labelling reaction by confocal microscopy using the FRET, exciting donor Atto520 dye (λ_{exc} = 488 nm) and reading acceptor Atto655 dye (λ_{em} = 665-750 nm).

To evidence the concept for the following cell experiments, irradiation experiments with **DNA6** were initially performed *in vitro*. The successful reaction of **DNA6** to **DNA7** was confirmed via denaturing PAGE. For better comparison, samples of non-irradiated **DNA2**, homo-dimer **(DNA2)$_2$** and hetero-dimer **DNA3** were applied on the same gel.

The PAGE analysis shows six lanes in total (Figure 32). Gelelectrophoretic analysis of **DNA2** (lane 1), **(DNA2)$_2$** (lane 2) and **DNA3** (lanes 3 and 4) is discussed in detail in section 3.2 and 3.3. **DNA6** is expected to lead to a band with the fastest electrophoretic mobility as this sequence displays the lowest molecular weight (m/z_{theo} = 5257.7). This is validated through PAGE analysis, as lane 5 displays only one band on the bottom of the gel. After successful reaction of **DNA6** with SQ-modified Atto655 dye **14**, **DNA7** (m/z_{theo} = 6174.8) features a size between **DNA3** (m/z_{theo} = 6456.5) and **DNA6** (m/z_{theo} = 5257.7) and is therefore expected to lead to a band with an electrophoretic mobility between these two fragments. Lane 6 displays a fragment sized between **DNA3** and **DNA6**, confirming the formation of **DNA7**. Despite the significant band for **DNA7**, lane 6 also displays two faint bands – one with a higher and one with a lower electrophoretic mobility.

The lowest band can be assigned to starting material **DNA6**, whereas the other faint band shows homo-dimerization of **DNA6** to **(DNA6)$_2$**. Nevertheless, through 10-fold excess of Atto655 dye **2**, the reaction shows favourable reaction to hetero-dimerized **DNA7**. Furthermore, 30 min of irradiation time at 37 °C is sufficient to form the **DNA7** as FRET product, validating shorter reaction times in the following cell experiments.

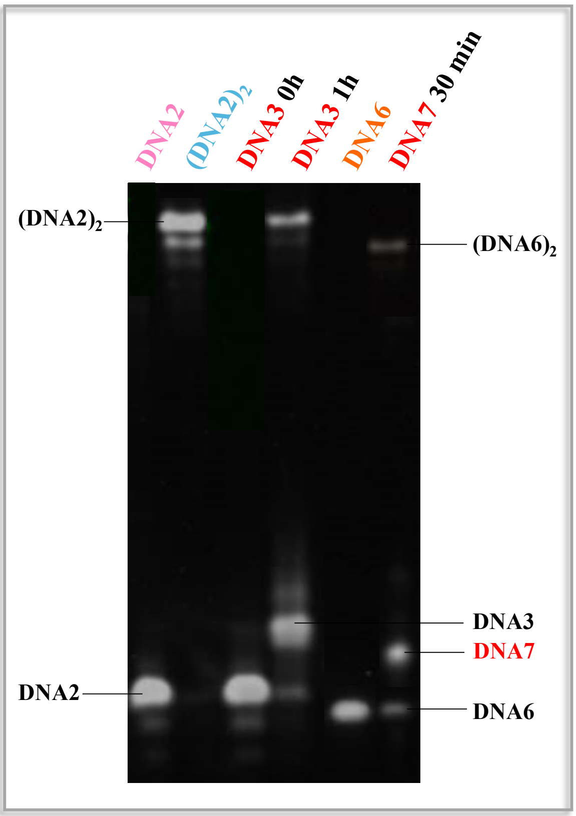

Figure 32: Denaturing PAGE analysis of **DNA7** after irradiation of 5 µM **DNA6** and 50 µM SQ-modified Atto655 dye **14** at λ_{max} = 450 nm in aqueous media containing 5% DMSO, 10 mM Na-P$_i$ buffer and 250 mM NaCl in a total volume of 500 µL in a crimp vial for 30 min at 37 °C. Staining was performed using SybrGreen™, followed by visualisation under UV light (λ_{exc} = 312 nm).

In the live cell FRET experiment, the *HeLa* cells were transfected with 75 ng Atto520- and SQ-modified **DNA6** and successfully labelled with 20 µM SQ-modified Atto655 dye **14** after irradiation with 450 nm LED for 30 min. The herein used transfection method is based on cationic non-liposomal lipids that interact with the negatively charged oligonucleotide, resulting in the formation of lipid complexes. These complexes enable the crossing of the cell membrane and uptake of the DNA strand by the endosomes of the *HeLa* cells, followed by their release into the cytosol.

Therefore, strong fluorescence staining of the Atto520 dye is expected and observed in the cytosol of the cells (Figure 33A$_1$) when excited in its respective excitation range (λ_{exc} = 488 nm, λ_{em} = 520-580 nm). Further, significant fluorescence staining in the endosomes and cytosol is clearly visible in the FRET wavelengths when the donor Atto520 is excited with a laser beam at λ_{exc} = 488 nm and emission of the acceptor Atto655 measured at λ_{em} = 665-750 nm (Figure 33A$_2$). The merge with the brightfield image shows orange fluorescence, exhibiting equal distribution of both dyes in the cell – one molecule Atto520 and one molecule Atto655 (Figure 33A$_3$), validating additionally the successful formation of **DNA7** and labelling in the live cells within 30 min irradiation time. In addition, less intense accumulation of the fluorophores in the nucleoplasm and nucleolus is visible, which can be attributed to templatisation of the Atto520 and Atto655 dye with oligonucleotides. Likewise, the point-like fluorescence signals in the cell can be attributed to endosomal vesicles.

As first negative FRET control, the cells were transfected with 75 ng **DNA6** without following incubation of SQ-modified Atto655 dye **14**. After irradiation with a 450 nm LED for 30 min, fluorescence staining is observed in the cytosol of the cell (Figure 33B$_1$) when the donor Atto520 dye is excited in its respective excitation range (λ_{exc} = 488 nm, λ_{em} = 520-580 nm), resulting from the uptake of the DNA by the endosomes followed by release into the cytosol. As the acceptor (SQ-modified Atto655 dye **14**) for successful FRET is missing, no [2+2] photocycloaddition and labelling of the cells with Atto655 dye **14** is expected. At λ_{exc} = 488 nm and λ_{em} = 665-750 nm no fluorescence is visible (Figure 33B$_2$), confirming anticipated results. The merge with the brightfield image exclusively displays presence of Atto520-modified **DNA6**, as solely green fluorescence is observed (Figure 33B$_3$).

As second negative control, the cells were incubated with 20 µM SQ-modified Atto655 dye **14** without prior transfection of **DNA6**, followed by irradiation with a 450 nm LED for 30 min. As the FRET-donor (**DNA6** with Atto520-modification) is missing, no fluorescence is expected and observed (Figure 33C$_1$) in the Atto520 excitation and emission wavelength (λ_{exc} = 488 nm, λ_{em} = 520-580 nm).

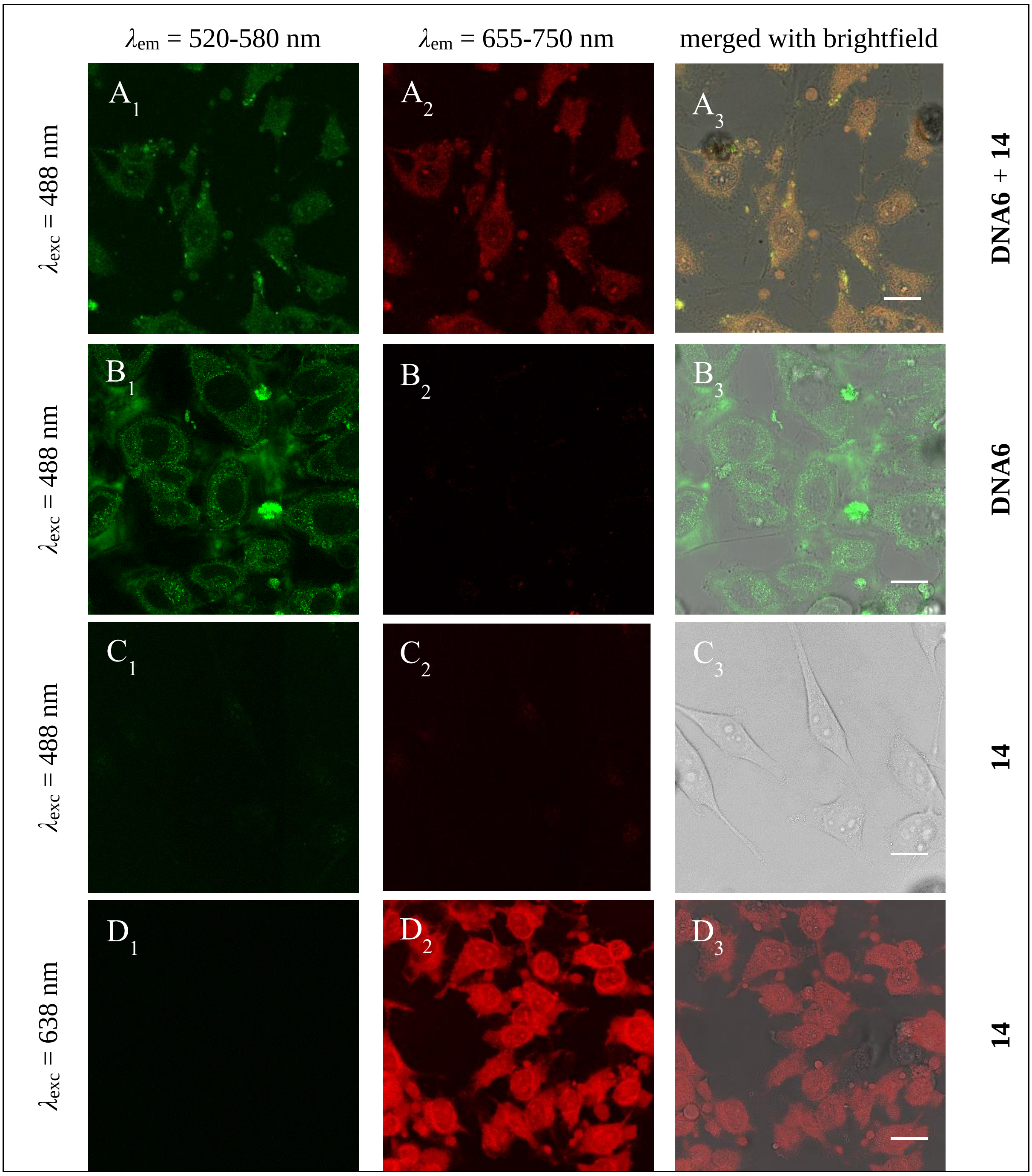
λ_{em} = 520-580 nm
λ_{em} = 655-750 nm
merged with brightfield
λ_{exc} = 488 nm
λ_{exc} = 488 nm
λ_{exc} = 488 nm
λ_{exc} = 638 nm
A_1
A_2
A_3
B_1
B_2
B_3
C_1
C_2
C_3
D_1
D_2
D_3
DNA6 + 14
DNA6
14
14

Figure 33: Confocal laser microscopy images of living *HeLa* cells. A: *HeLa* cells were transfected for 24 h with 75 ng **DNA6**, followed by incubation for 16 h with 20 µM Atto655 dye **14**. B: *HeLa* cells were transfected for 24 h with 75 ng **DNA6** without following incubation with Atto655 dye **14**. C and D: *HeLa* cells were incubated with 20 µM Atto655 **14** dye without prior transfection of **DNA6**. All cells were irradiated for 30 min with a 450 nm LED at 37 °C, followed by imaging at depicted excitation and emission wavelengths. The merge shows the combination of the pictures taken of direct excitation and the brightfield. Scale bar: 10 µm.

Most importantly, no fluorescence is visible in the FRET wavelengths (λ_{exc} = 488 nm, λ_{em} = 665-750 nm, Figure 33C$_2$, C$_3$), clearly validating that both **DNA6** *and* SQ-modified Atto655 dye **14** are needed to undergo a selective [2+2] cycloaddition with each other in a biological cell upon visible light irradiation. To confirm the uptake of the acceptor, the Atto655 dye was excited in its respective excitation range (λ_{exc} = 638 nm, λ_{em} = 665-750 nm) displaying intensive fluorescence staining in the cytoplasm (Figure 33D$_2$). It can be assumed that the synthesised Atto655 **14** can cross the cell membrane and enter the cytoplasm unhindered due to its positive charge. In the merge with the brightfield image, solely red fluorescence staining is observed (Figure 33D$_3$), indicating exclusively presence of Atto655 dye **14**. Further, the accumulation of the fluorophore in the nucleoplasm and nucleoli is observed, indicating templatisation of the dye with oligonucleotides.

In addition to the negative controls, a positive control was performed to further confirm the herein developed novel [2+2] photocycloaddition labelling strategy and FRET in the live cells. *HeLa* cells were transfected with 65 ng of **DNA3** using *ScreenFect A.*

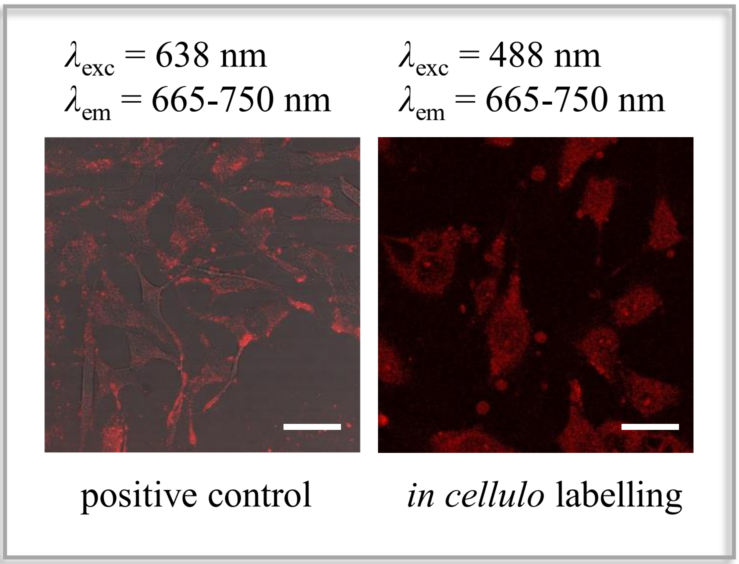
λ_{exc} = 638 nm
λ_{em} = 665-750 nm
λ_{exc} = 488 nm
λ_{em} = 665-750 nm

positive control *in cellulo* labelling

Figure 34: Confocal laser microscopy images of living *HeLa* cells. Left: *HeLa* cells were transfected for 24 h with 65 ng **DNA3** which was successfully labelled with the SQ-modified Atto655 dye **14** through [2+2] photocycloaddition prior to transfection. Imaging was performed at λ_{exc} = 638 nm and λ_{em} = 665-750 nm. Right: *HeLa* cells were transfected for 24 h with 75 ng SQ- and Atto520-modified **DNA6**, followed by incubation for 16 h with 20 µM Atto655 dye **14**. After irradiation for 30 min with a 450 nm LED, the success of the labelling reaction was confirmed using the FRET, exciting donor Atto520 at λ_{exc} = 488 nm and reading the acceptor Atto655 dye at λ_{em} = 665-750 nm. Scale bar: 10 µm.

In the positive control, **DNA3** was successfully labelled with the SQ-modified Atto655 dye **14** through visible light-induced [2+2] photocycloaddition prior to transfection. After incubation for 24 h, the cells were washed carefully with PBS, followed by confocal microscopy imaging by exciting the Atto655 dye **14** at λ_{exc} = 638 nm and reading emission at λ_{em} = 665-750 nm. Significant fluorescence staining is clearly visible in the cytosol and endosomes of the cells (Figure 34 left) due to uptake of the transfected DNA by the endosomes and following release into the cytosol. By comparing the positive control to the *in cellulo* FRET experiment (Figure 34 right), one notes that both exhibit the same fluorescence staining behaviour in the cytosol of the cells. This clearly confirms that DNA and dyes bearing the SQ tag undergo a selective [2+2] cycloaddition with each other in live *HeLa* cells.

Based on these results, the herein developed visible light-induced labelling strategy employing SQ as [2+2] reactive chromophore can be classified as bioorthogonal. The reaction between the two introduced SQ units proceeds highly selective under physiological conditions as there are no side reactions with naturally occurring biological compounds. Further, the starting materials and products are non-toxic and offer a high stability in the cellular environment which corresponds to the criteria of a bioorthogonal reaction.

3.5 Conclusion and Outlook

In the current PhD thesis, a new spatiotemporally controlled bioorthogonal labelling strategy for DNA in live cells was developed and applied. The herein employed styrylquinoxaline (SQ) moiety as photoreactive chromophore provides the first example of visible light-induced (λ_{max} = 450 nm) labelling of oligonucleotides by [2+2] photocycloaddition.

SQ-modified **DNA2** and SQ-modified Atto655 dye **14** were synthesised and successfully reacted to Atto655-labelled **DNA3** through irradiation with a 450 nm LED in initial *in vitro* experiments. The success of the [2+2] photoreactive labelling strategy was validated by UV/Vis spectroscopy, HPLC analysis and gel electrophoresis. In the following *in cellulo* experiments, the intrinsic fluorogenicity of the Atto655 dye did not display suitable readout to confirm the bioorthogonality of the newly introduced labelling approach. It was therefore decided to exploit Förster Resonance Energy Transfer (FRET) in the live *HeLa* cells. SQ- and Atto520-modified **DNA6** was successfully employed as donor in a FRET system with SQ-modified Atto655 dye **14** as an acceptor. The successful labelling of the DNA in the live cells using a [2+2] photocycloaddition demonstrates that styrylquinoxalines have a significant potential as versatile bioorthogonal tags as the following criteria were fulfilled: (i) highly selective reaction under physiological conditions (neutral pH, physiological temperature, aqueous medium); (ii) no side reactions with naturally occurring biological compounds; (iii) the SQ units as well as [2+2] photoreactive products are non-toxic and stable in the cellular environment and (iv) the reaction proceeds rapidly.

The current work presents the first example of visible light-induced labelling of oligonucleotides. As a next step, the irradiation wavelength to induce the [2+2] photocycloaddition should further be shifted to longer wavelengths, such as green or NIR light, allowing for even better tissue penetration. Red-shifted behaviour can possibly be obtained by attaching further substituents to the quinoxaline rings, *i.e.*, electron withdrawing groups or hetero atoms.

To further investigate and understand biological processes in living systems, the newly introduced bioorthogonal labelling strategy should be transferred to other biooligomers (*e.g.*, RNA, proteins or glycans). The herein introduced SQ-NHS ester-amine coupling protocol provides a synthetically easy access to the introduction of the SQ moieties into the mentioned biomacromolecules. SQ-modified RNA for example could be synthesised by incorporation of literature-known DMT- and phosphoramidite-protected 5-(3-amino)propyluridine[173] into RNA, followed by postsynthetic introduction of the SQ moiety. However, regarding proteins or glycans, multiple protection groups might be necessary to exclude undesired cross-reactivity of free amine groups in the biooligomers.

In the current work, the energy source to induce the photochemical labelling reaction was LED lights. Although providing a lot of advantages, such as specific wavelengths and spatiotemporal control, external light sources also bear critical disadvantages as they need a constant supply of energy in combination with advanced setups.

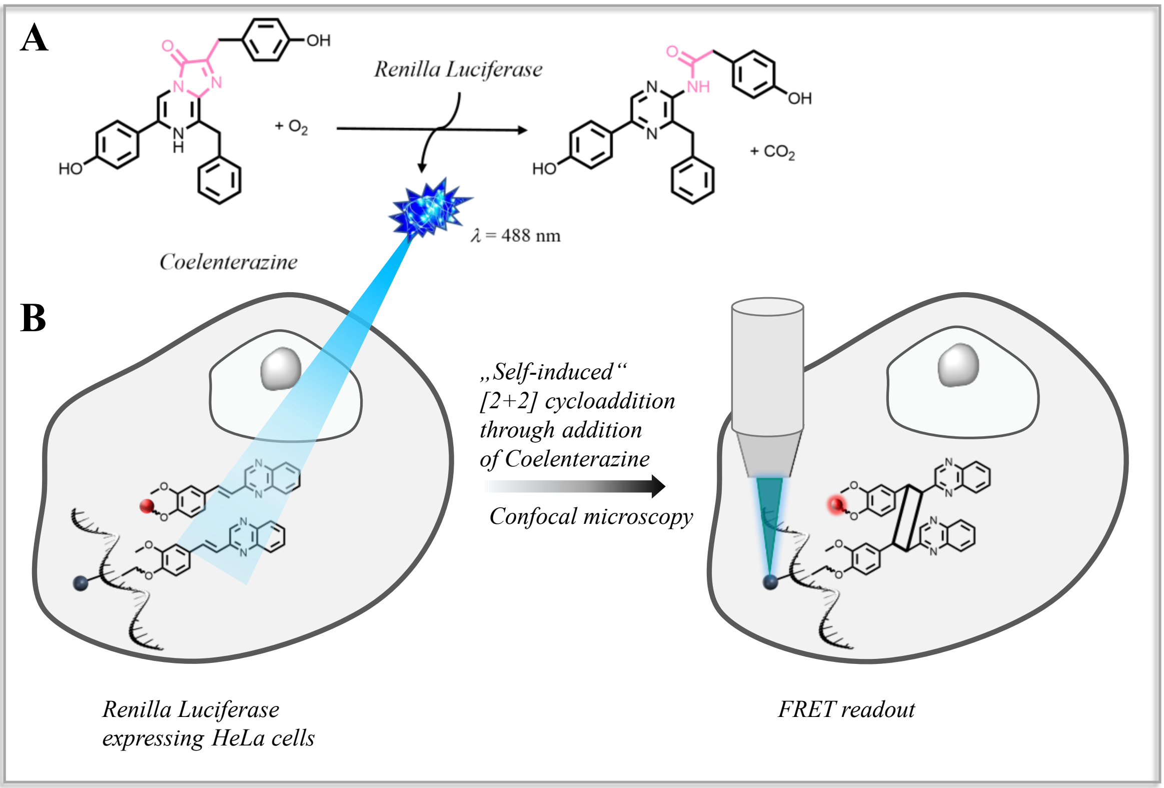
A
Renilla Luciferase
+ O₂
+ CO₂
HO
OH
λ = 488 nm
Coelenterazine
B
„Self-induced“
[2+2] cycloaddition
through addition
of Coelenterazine
Confocal microscopy
Renilla Luciferase
expressing HeLa cells
FRET readout

Figure 35: A: Coelenterazine and Renilla Luciferase as example of bioluminescence in the wild. The luciferase oxidises its complementary luciferin to yield photons of light in the blue wavelength region. B: Employment of renilla luciferase expressing *HeLa* cells in combination with the herein introduced transfection protocol and FRET readout.

A solution to overcome this problem could be provided by using bioluminescence as an internal light source as light is generated via chemical reactions within a living organism.

Photons generated by bioluminescence may be exploited to induce the [2+2] photocycloaddition in environments where external physical light sources cannot be applied while still maintaining spatiotemporal control over the ligation process. A promising bioluminescence pair to induce the herein developed SQ-driven labelling of biomacromolecules is provided by Coelenterazine as a substrate and Renilla Luciferase as an enzyme (Figure 35A). Their interaction leads to light with a wavelength of λ = 488 nm. The self-induced labelling in live cells could be realised employing Renilla Luciferase-expressing *HeLa* cells and the within this project established transfection protocol and FRET readout (Figure 35B). This would open the door for a new research field within bioorthogonal reactions as spatiotemporal control over the labelling process is accessed without the need of an external light trigger.

4 Action Plots for Photochemical Release Systems

As described in detail in section 2.4, photochemistry is currently undergoing a precision revolution. With the advent of tuneable laser systems, intricate control over photochemical processes in a wavelength-resolved fashion can be accessed. While light-driven chemical ligation processes have been studied for more than half a century,[28, 174] photochemically cleavage and release systems have only found widespread application since the last two decades.[158, 175] Photocaging and -uncaging of drugs and thus transferring them from an inactive state to an active one is an important aspect of modern pharmaceutical research due to the non-invasive manner, high spatiotemporal control and energetic precision light provides.[122, 176] However, multi wavelength-controlled cleavages are currently only achieved in a wavelength-selective manner, *i.e.*, longer wavelength activation for the first photoinduced release, followed by shorter wavelengths for the second release. Full λ-orthogonal pathway-independent drug release remains largely elusive as it requires exclusively addressing one photo-responsive species while the other component remains unaffected, and *vice versa*.

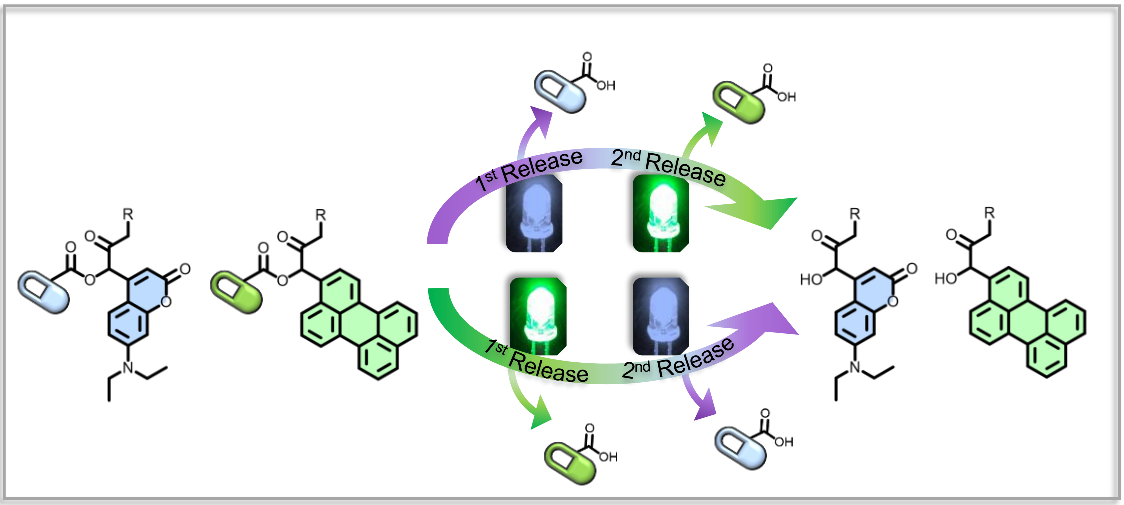

Figure 36: Simplified overview of the chromophores examined in this study alongside their proposed release mechanism. Based on the findings of a photochemical action plot analysis, pathway-independent and λ-orthgonal photochemical release was performed in a one-pot reaction.

To expand the toolbox of λ-orthogonal release, the aim of the current project was to develop and characterise a dual carrier system that allows for the sequential and fully wavelength-controlled release of cargo molecules (Figure 36). The absorbance spectra of 7-(diethylamino)-coumarin and 3-perylene are reasonably different, providing a sufficiently high chance that their wavelength-by-wavelength resolved reactivity is disparate, thus, making them suitable candidates for releasing two different cargo in a fully pathway-independent orthogonal fashion. Due to its one-pot nature and easy modular interchange of chromophores, it was decided to employ the *Passerini*[162b] three-component reaction. 7-(diethylamino)-coumarin- and 3-perylene-carboxaldehydes were introduced as photoprotecting groups (PPGs) into benzoic acid as model release entity and an isocyanide derivative based on a synthetic protocol by the group of *Meier*.[177] Post synthesis, initial LED experiments were carried out to understand the photochemical cleavage process which was validated by UV/Vis spectroscopy, LC-MS analysis and NMR spectroscopy. To determine the most suitable wavelengths for λ-orthogonality, photochemical action plots of the chromophores were recorded, followed by translation to LED irradiation to investigate the pathway-independent λ-orthogonal cleavage in a one-pot reaction.

Parts of the current chapter and the associated supplementary information have already been published:

Photochemical Action Plots Map Orthogonal Reactivity in Photochemical Release Systems

R. T. Michenfelder, F. Pashley-Johnson, V. Guschin, L. Delafresnaye, V. X. Truong, H.-A. Wagenknecht, C. Barner-Kowollik, *Adv. Sci.* **2024**, *11*, 2402011.

DOI: 10.1002/advs.202402011.[178]

4.1 Synthesis of the Chromophore Systems

The *Passerini* three-component reaction involves the combination of an aldehyde, a carboxylic acid, and an isocyanide (refer to section 2.6) and allows for the fast and efficient formation of multiple bonds and complex chemical structures.[162b, 166] As a first step towards the synthesis of the herein developed and characterised chromophore systems, isocyanide **20** was synthesised (Figure 37) as an overall precursor via an adapted literature procedure of the *Meier* group[177] for subsequent combination with 7-(diethylamino)-coumarin- and 3-perylene-carboxaldehydes as PPGs and commercially available acids.

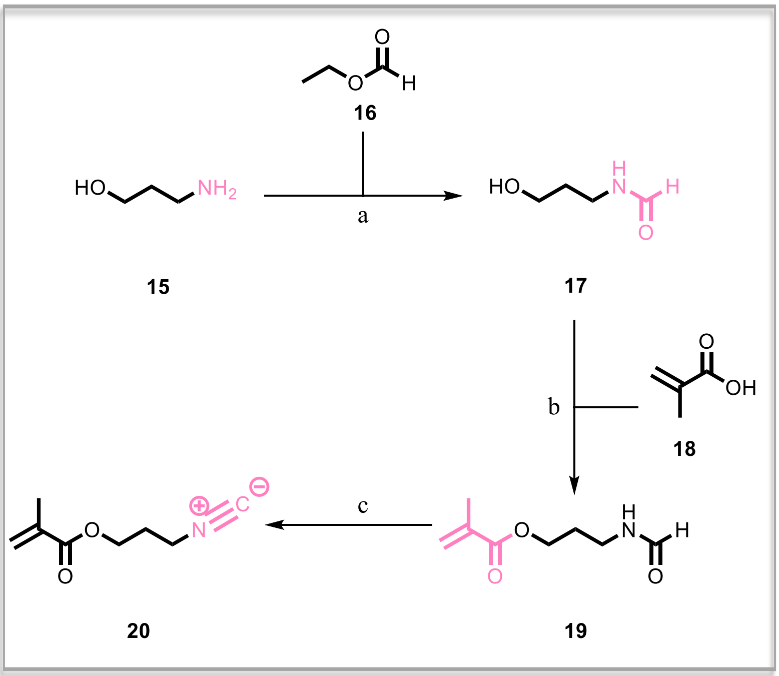

Figure 37: Synthesis of isocyanide **20**: a) MeOH, 50 °C, 2 h, quant.; b) EDC·HCl, DMAP, r.t., 16 h, 19%; c) Pyridine, *p*-TsCl, DCM, r.t., 2 h, 72%.

The first step was performed according to literature where the free electron pair on the aminopropanol (**15**) nucleophilic attacks the carbonyl bond of ethylformate (**16**) to obtain the formamide **17** in quantitative yield.[179] Due to its rapid decomposition upon storage, **17** was directly used in the next step.[180] A methacrylate functionality was introduced to enable a future incorporation into a polymeric backbone by radical or ionic polymerization. Under argon atmosphere, methacrylic acid (**18**) as well as EDC·HCl and

DMAP were added to a solution of **17** in dry DCM to undergo a condensation reaction to compound **19** in 19% yield. The low yield is most likely caused by a poor argon atmosphere. The solids were not dried before addition to the reaction mixture which could lead to interference via moisture. To compensate for these issues, a higher amount of both EDC·HCl (1.50 equiv.) and DMAP (1.50 equiv.) in comparison to literature (1.00 equiv. for EDC·HCl and catalytic amounts for DMAP) was used.[181] As the last step, the isocyanide **20** was obtained in 72% yield by dehydration of the formamide with the use of *para*-toluenesulfonyl chloride (*p*-TsCl).

Subsequently, commercially available 7-diethylamino-1-methylcoumarin (**21**) was oxidised via a *Riley*-like procedure according to literature to obtain coumarin carboxaldehyde **22** in 57% yield (Figure 38a).[175c] In the next step, isocyanide **20** and coumarin carboxaldehyde **22** were used in a *Passerini* reaction, introducing benzoic acid (**23**) as a model release entity in the photocaged compound **24** (Figure 38b).

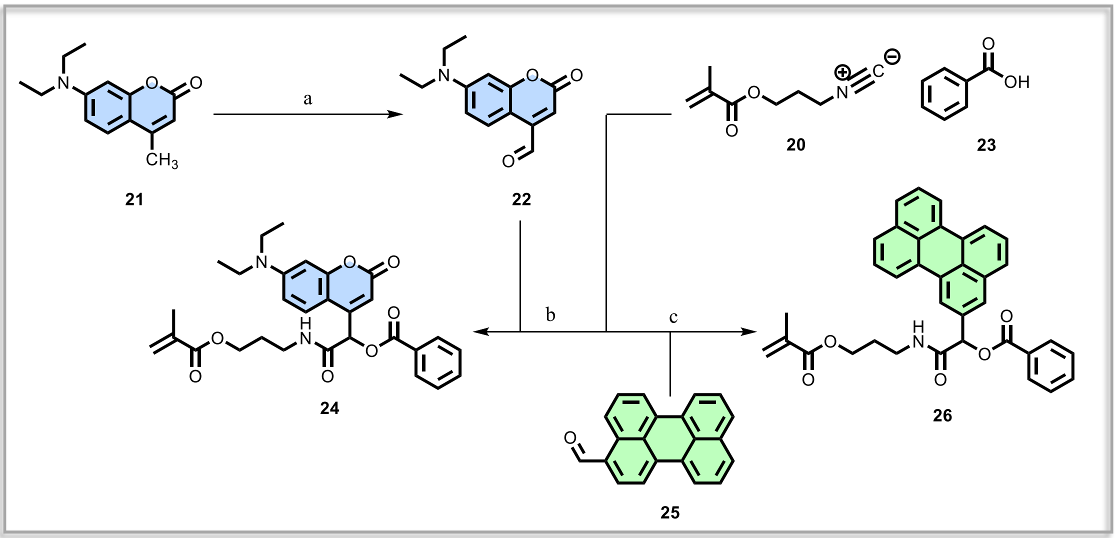

Figure 38: a) Synthesis of coumarin carboxaldehyde **22**: SeO_2, *o*-xylene, reflux, 5 h, 57%; b) Synthesis of photocaged coumarin-modified compound **24** via *Passerini* reaction: DCM, r.t., 16 h, 92%; c) Synthesis of photocaged perylene-modified compound **26**: $CHCl_3$ / toluene (3:1), r.t., 48 h, 3%.

As a second chromophore, commercially available 3-perylene carboxaldehyde (**25**) was selected and introduced into photocaged compound **26**, employing the same *Passerini* protocol with isocyanide **20** and benzoic acid (**23**) as model release entity (Figure 38c). Both *Passerini* reactions were initially carried out in DCM as solvent and the photocaged compounds isolated in yields up to 92%. However, due to poor solubility of the perylene-carboxaldehyde (**25**) in DCM, a mixture of $CHCl_3$ and toluene (3:1) as solvent as well as prolonged reaction times (48 h instead of 16 h) in comparison to coumarin-modified compound **24** were applied. Nevertheless, the solubility of **25** was only slightly improved. Over the course of time, different solvents were used (*e.g.*, acetone, Et_2O, DMF, DMSO, EtOAc, EtOH, MeOH, hexane and THF), yet none of them displayed sufficient solubility. To purify the perylene-modified compound **26**, two consecutive purification steps via column chromatography were needed, leading – in combination with the poor solubility of **25** – to a significant yield reduction and a low overall yield of 3% for **26**. In the interest of time and as sufficient material for the following irradiation experiments was available, further optimisation of the synthesis was not conducted. Nevertheless, as stated in literature, changing the solvent to water accelerates the *Passerini* reaction and leads to higher yields,[182] although the solubility of the highly non-polar 3-perylene-carboxaldehyde (**25**) in water is presumably not sufficient.

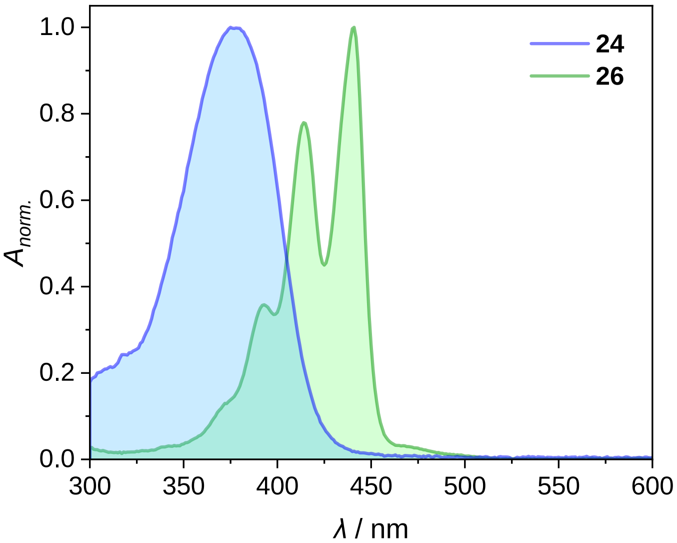

Figure 39: Normalised UV/Vis absorbance of coumarin photocaged compound **24** (147 µM in MeCN) and perylene photocaged compound **26** (72 µM in MeCN).

Both synthesised photocaged compounds **24** and **26** were analysed and characterised via NMR spectroscopy, LC-MS (refer to section 5.4.4) and UV/Vis spectroscopy (Figure 39).

The coumarin-modified compound **24** displays an absorbance maximum at $\lambda = 388$ nm, whereas the perylene-modified compound **26** shows three absorbance maxima in total: two local maxima at $\lambda_1 = 393$ nm and $\lambda_2 = 413$ nm as well as a global maximum at $\lambda_3 = 440$ nm.

4.2 LED Cleavage Experiments

To obtain insights regarding the cleavage of the benzoic acid, irradiation experiments with both synthesised photocaged compounds were performed using a 405 nm LED for the coumarin-modified substrate **24** and a 445 nm LED for the perylene-modified compound **26** (refer to section 5.2.1 for LED emission spectra). Despite the expected deviations of the absorption maximum from the reactivity maximum,[101-102] these experiments provide a preliminary indication of how the compound reacts during irradiation.

The LED irradiation of **24** was followed by UV/Vis spectroscopy at defined times for 2 h in total (Figure 40A). Pre-irradiation, **24** shows three distinctive maxima at λ_1 = 209 nm, λ_2 = 232 nm, and λ_3 = 388 nm. After 3 min of irradiation, the absorbance maxima decrease, and the formation of two isosbestic points at λ_1 = 342 nm and λ_2 = 425 nm is observed, indicating a clean reaction without intermediates (Figure 40A bright green line). The decrease of the absorption maximum can be explained by the decomposition of the compound into smaller parts as well as general photobleaching of the chromophore.

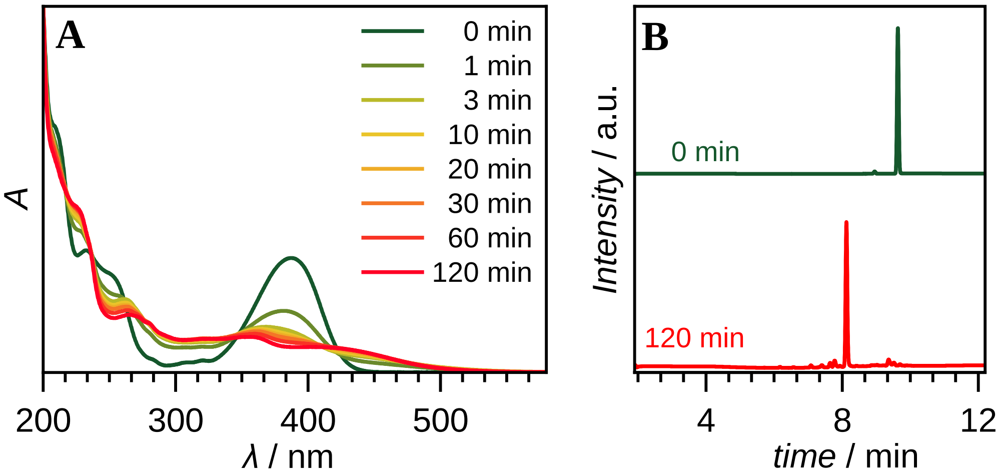

Figure 40: A: UV/Vis absorbance changes and B: HPLC results of 20 µM **24** over 2 h of irradiation at 20 °C with a 405 nm LED in MeCN.

With longer reaction times, the main signals are shifting, namely, the local maximum at λ = 232 nm undergoes a slight bathochromic shift to λ = 268 nm whereas the global maximum at λ = 388 nm is shifted hypsochromically to λ = 358 nm (Figure 40A orange and red lines).

To further evidence the cleavage mechanism, HPLC analysis was performed (Figure 40B). The cleavage mechanism follows similarly to that described by *Schade et al.* (refer to section 2.5, Figure 14),[145, 147] eventually resulting in the cleaved acid and a hydroxyl-functionalised partial *Passerini* adduct. The hydroxyl functionality increases the polarity of the molecule, leading to a shift to shorter elution times in the reverse-phase HPLC trace. Pre-irradiation, the chromatogram of **24** shows one significant peak at t_R = 9.67 min (Figure 40B dark green line). During irradiation, this peak decreases in intensity, while a new peak at t_R = 8.12 min is formed (Figure 40B red line), clearly confirming clean and successful scission of the benzoic acid. However, after light treatment the formation of two products (benzoic acid and the respective coumarin *Passerini* adduct) would be expected, yet there is only one peak recorded by the HPLC elugram. This can most likely be attributed to the much higher extinction coefficient of the coumarin in comparison to the benzoic acid, resulting in the benzoic acid peak not being visible as it is indistinguishable from the noise.

In addition, NMR analysis was performed and is further validating the cleavage of the acid. After 2 h of irradiation, a new resonance is arising at δ = 12.9 ppm (Figure 41 top, red line), confirming the release of a free acid group in comparison to the benzoic acid trace (Figure 41 top, grey line). Even though the NMR spectroscopic analysis showed almost full cleavage of the acid, the corresponding mass peak was not found in the LC-MS analysis. This is most likely traced back to the low *m/z* of the benzoic acid (m/z_{theo} = 122.0386) exceeding the capabilities of the spectrometer. However, the LC-MS data evidences the successful cleavage of the benzoic acid and formation of a hydroxyl-functionalised partial *Passerini* adduct (m/z_{theo} = 417.2026 for [(**24-cleaved**)+H]$^+$), as the peak in the red trace in Figure 40B indicates *m/z* values in very good agreement with a hydroxyl-functionalised coumarin derivative (Figure 41 bottom, m/z_{exp} = 417.2016 for [M+H]$^+$ and m/z_{exp} = 833.3960 for [2M+H]$^+$).

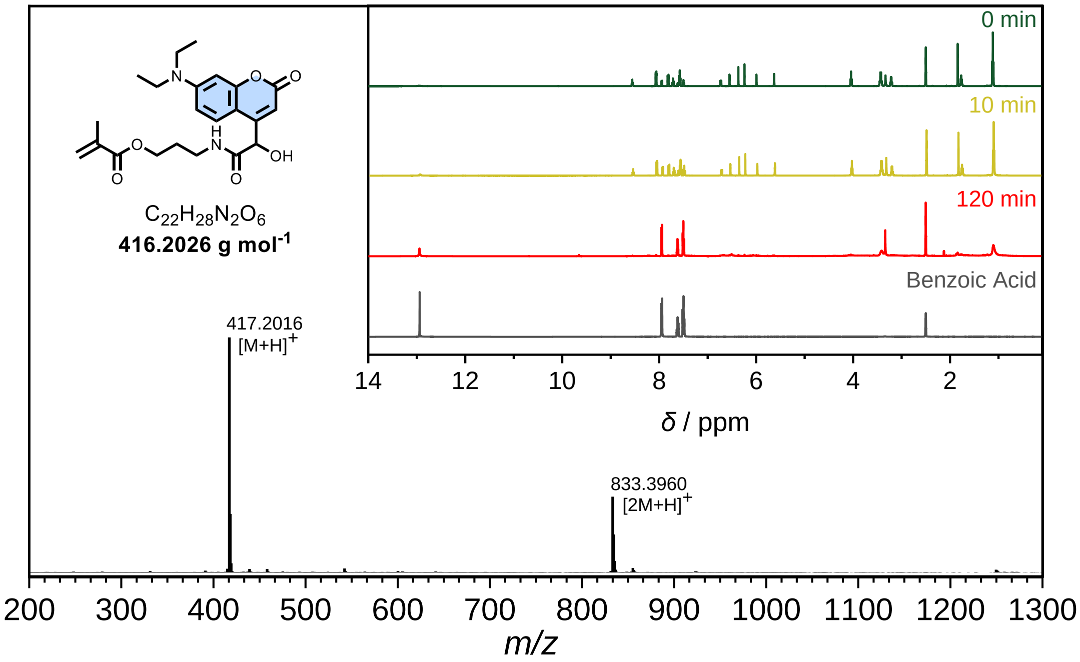

Figure 41: Top: NMR spectroscopic changes of 8 mg **24** over 2 h of irradiation at 20 °C with a 405 nm LED in 400 µL DMSO-d_6. Bottom: Mass spectrometric analysis of coumarin-modified compound **24** after irradiation for 2 h with a 405 nm LED: m/z_{theo} = 417.2026 for $[M+H]^+$ and 833.3979 for $[2M+H]^+$.

Simultaneously, cleavage experiments were performed with the perylene-modified compound **26**, employing 445 nm LED irradiation. The reaction was followed by UV/Vis spectroscopy, and LC-MS analysis. The UV/Vis spectra display similar changes of the maxima as coumarin-modified compound **24**. Pre-irradiation, **26** shows four distinctive maxima at λ_1 = 254 nm, λ_2 = 393 nm, λ_3 = 414 nm, and λ_4 = 440 nm (Figure 42A, dark green line). During irradiation, the absorbance maxima decrease and a new absorbance maximum at λ = 469 nm develops, indicating successful cleavage of the benzoic acid as the compound decomposes into smaller parts. Further, two isosbestic points develop over the course of irradiation at λ_1 = 373 nm and λ_2 = 455 nm (Figure 42A, red line). However, in comparison to the UV/Vis spectra of **24**, there is no significant hypsochromic or bathochromic shift of the maxima visible, and longer irradiation times are needed for the cleavage to occur.

The release of the benzoic acid was further confirmed via LC-MS. Pre-irradiation, the chromatogram of **26** shows one significant peak at t_R = 10.8 min (Figure 42B, dark green line) which decreases during irradiation, while a new peak at t_R = 9.44 min is formed (Figure 42B, red line).

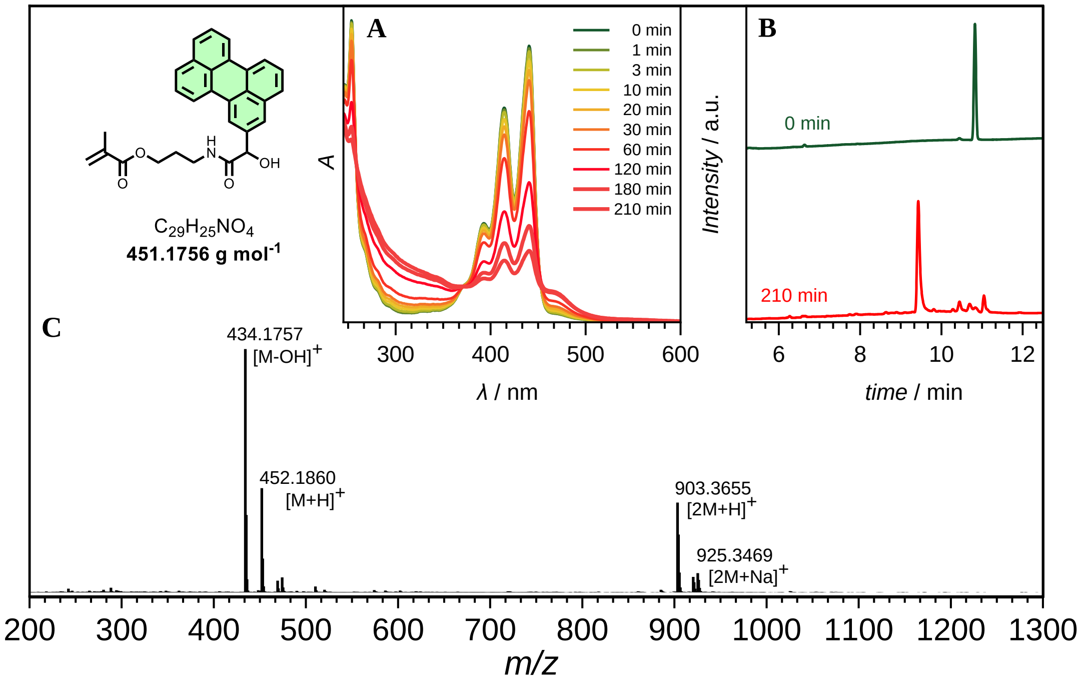

Figure 42: A: UV/Vis absorbance changes and B: HPLC results of 40 µM perylene-modified compound **26** over 3.5 h of irradiation at 20 °C with a 445 nm LED in MeCN. C: Mass spectrometric analysis of **26** after irradiation for 3.5 h with a 445 nm LED: m/z_{theo} = 434.1751 for $[M\text{-}OH]^+$, 452.1856 for $[M+H]^+$, 903.3640 for $[2M+H]^+$ and 925.3459 for $[2M+Na]^+$.

The increase in polarity and accompanying shorter elution time after 3.5 h of irradiation is in agreement with the results of coumarin photocaged compound **24** and supports the successful cleavage of the benzoic acid as well as the formation of the more polar hydroxyl-functionalised partial *Passerini* adduct (m/z_{theo} = 452.1856 for [(**26-cleaved**)+H]$^+$. Similar to **24**, the formation of the hydroxyl-functionalised *Passerini* adduct is evidenced by the LC-MS data as the peak in the red trace of Figure 42B has *m/z* values in very good agreement with the hydroxyl-functionalised perylene derivative (Figure 42C, m/z_{exp} = 434.1757 for $[M\text{-}OH]^+$, 452.1860 for $[M+H]^+$, 903.3655 for $[2M+H]^+$ and 925.3469 for $[2M+Na]^+$). As already discussed for the coumarin compound **24**, after light treatment the formation of two products (benzoic acid and the respective perylene *Passerini* adduct) would be expected, yet there is only one peak recorded by the HPLC elugram. This can most likely be attributed to the much higher extinction coefficient of the perylene in comparison to the benzoic acid, resulting in the benzoic acid peak not being visible as it is buried beneath the noise threshold.

In conclusion, all previously established analysis methods (UV/Vis spectroscopy and LC-MS analysis) showed equal results for the perylene photocaged compound **26** and the coumarin photocaged substrate **24**, and clearly confirmed the successful release of the benzoic acid after irradiation with a 405 nm LED or 445 nm LED respectively.

4.3 Action Plots of the Chromophore Systems

After having established the chromophore systems, action plots were recorded to determine the photochemical reactivity. As usual for action plots in cleavage systems, the chromophores' reactivity was followed by mapping the depletion of the starting material.[116-117] Prior to performing action plots measurements, the molar extinction coefficient ε is measured to determine the wavelength range of interest. In a next step, a kinetic analysis at the absorbance maximum is recorded to identify ideal light intensities required to achieve significant conversion of the starting material at a practical time period. Cleavage reactions typically follow first-order reaction kinetics and the progress of conversion approximates a linear trend at the beginning, and an exponential trend overall. To accurately compare the conversion at each indicated wavelength, it is recommended to stay within the linear regime, where the consumption of the starting materials is kept below 30%.[102] Therefore, the first step towards recording an action plot is the determination of the required number of photons to achieve 20-30% conversion, followed by measuring the actual action plot spectra in a wavelength resolved fashion. As explained in detail in section 2.4, identical aliquots of a reaction mixture are irradiated with the previously determined number of photons at each monochromatic light across the wavelength of interest (λ = 300-600 nm). Once the wavelength-dependent reactivity has been defined, a graph is plotted by overlaying the photochemical reactivity with the molar extinction spectrum, resulting in the chromophore's action plot.

4.3.1 Action Plot of the Coumarin-Modified Compound 24

Based on previous LED irradiation experiments and associated absorption measurements (refer to section 4.2), the coumarin-modified benzoic acid derivative **24** displays an absorption maximum at λ = 388 nm. After 3 min of irradiation with a 405 nm LED, the maximum intensity decreased by about 65%. Consequently, light exposure times for the kinetic measurements of **24** with the laser were adjusted to 30 s intervals up to the 5 min mark to ensure precise determination of the required number of photons to achieve 20-30% consumption of the starting material as it is recommended to stay within the linear regime that the initial progress of conversion approximates.[102] 8 identical samples of the coumarin derivative **24** with a concentration of 147 µM in MeCN (80 µg mL^{-1}) were irradiated at λ = 388 nm for various time intervals with an identical photon number (Figure 43 left). To determine the conversion of the starting material into the photodegradation product, UV/Vis spectroscopy was employed (refer to section 5.5.1 and Table A2 for detailed description of the method and further analysis).

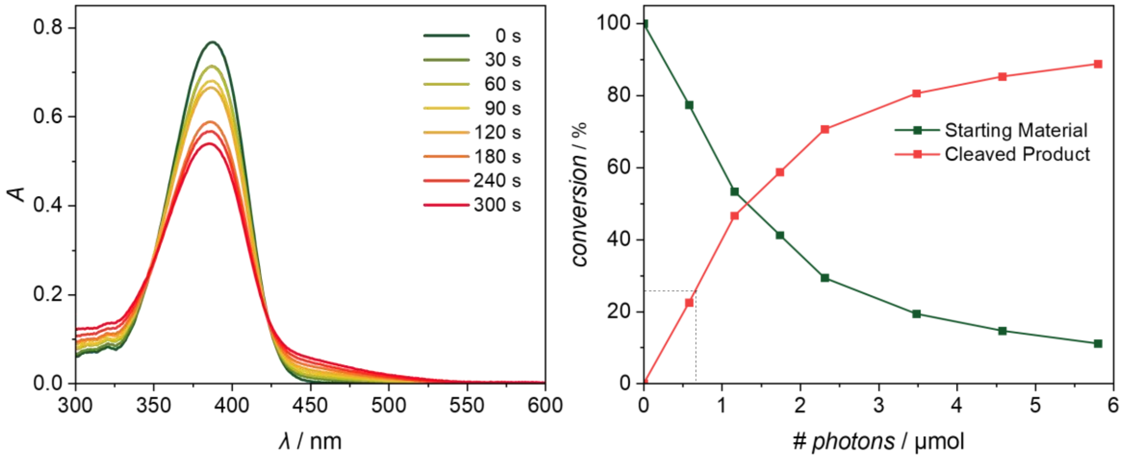

Figure 43: Left: UV/Vis absorbance of 8 identical samples of the coumarin derivative **24** after irradiation with monochromatic light at λ_{Laser} = 388 nm to determine the reaction kinetics. Right: Reaction kinetics of **24**. To obtain approximately 25% consumption of the starting material, 0.69 µmol photons should be deposited into the reaction system.

The kinetic studies (Figure 43 right) revealed that 0.69 µmol photons ($4.00 \cdot 10^{17}$ photons) should be deposited into the reaction system to obtain approximately 25% conversion. For the following measurement of the action plot spectra, coumarin photocaged compound **24** was prepared in a 147 µM stock solution (80 µg mL^{-1}) and identical aliquots irradiated with 0.69 µmol photons of monochromatic light at each indicated wavelength. The photochemical reactivity was probed in a 15 nm resolution, employing 15 different wavelengths ranging from 310 nm to 520 nm. Each wavelength was measured in triplicates to reduce the influence of sample preparation and minimise deviations in laser power which can occur for long laser runtimes.

The coumarin derivative's (**24**) action plot clearly shows higher reactivity outside of the absorption maximum (λ = 388 nm) on both sides (Figure 44). Interestingly, there are two reactive maxima at λ_1 = 350 nm and λ_2 = 400 nm, revealing an hypsochromic as well as a bathochromic shift in reactivity.

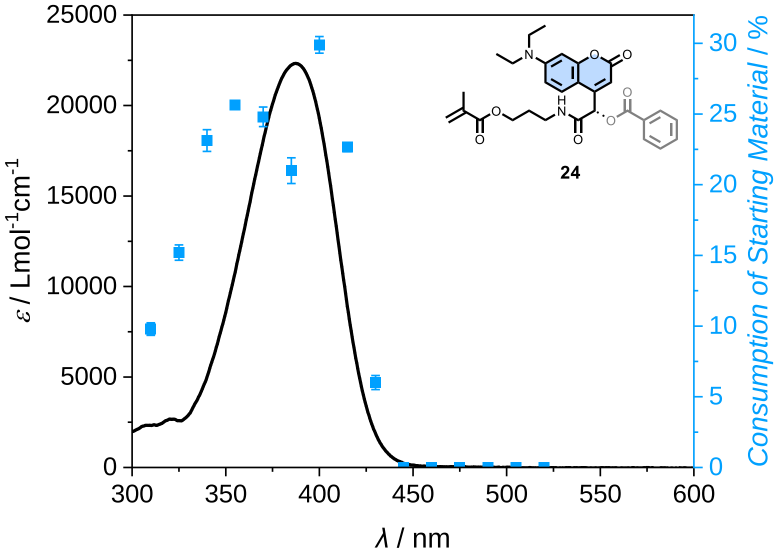

Figure 44: Molar extinction of **24** overlayed with the action plot consumption of the starting material (c = 147 µM in MeCN). For each indicated wavelength, 0.69 µmol photons were deposited into the reaction system.

Cleavage of the benzoic acid is already occurring in the UV-B wavelength region (*e.g.*, λ = 310 nm), where the molar absorptivity of the chromophore is reduced. Further, there is still some reactivity (6%) observed at λ = 430 nm, although the UV/Vis absorption is relatively low. The action plot indicates that coumarin-modified compound **24** should be irradiated with a wavelength of λ = 400 nm to achieve most efficient cleavage of the benzoic acid.

4.3.2 Action Plot of the Perylene-Modified Compound 26

Subsequently, the action plot for the perylene-modified compound **26** was recorded. The initial progress of conversion approximates a linear trend for first-order kinetics, and it is recommended to stay within this linear regime to accurately compare the conversion under different conditions.[102] Therefore, prior to performing the action plot measurements, a kinetic analysis of **26** was conducted. The LED irradiation and associated absorption measurements of the perylene-modified benzoic acid derivative **26** displayed a global absorption maximum at λ = 440 nm. 7 identical samples with a concentration of 72 µM in MeCN (40 µg mL^{-1}) were irradiated at λ = 440 nm for predefined time intervals with an identical photon number (Figure 45 left) to ensure precise determination of the required number of photons to achieve 20-30% consumption of the starting material. To determine the yield of the cleavage reaction, LC-MS with benzene as an internal standard was employed (refer to section 5.5.2 and Table A3 for detailed description of the method and further analysis).

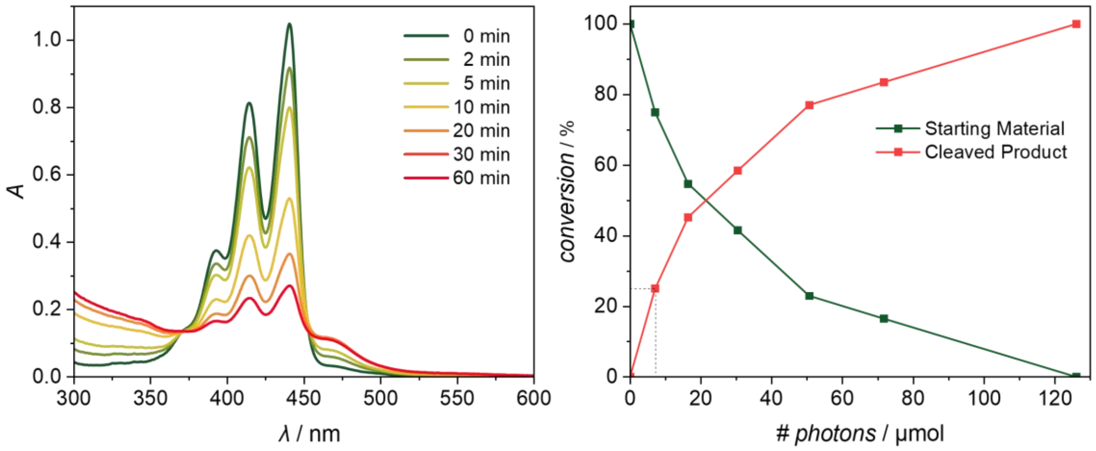

Figure 45: Left: UV/Vis absorbance of 7 identical samples of the perylene derivative **26** after irradiation with monochromatic light at $\lambda_{\text{Laser}} = 440$ nm to determine the reaction kinetics. Right: Reaction kinetics of **26**. To obtain approximately 25% consumption of the starting material, 7.09 µmol photons need to be deposited into the reaction system.

The kinetic studies (Figure 45 right) revealed that 7.09 µmol photons ($4.27 \cdot 10^{18}$ photons) should be deposited into the reaction system to obtain approximately 25% consumption of the starting material **26**. In comparison to the kinetic studies for the coumarin-modified compound **24**, ten times the photon flux is needed to achieve similar cleavage yields for **26**, confirming that the release reaction with the coumarin photocage proceeds faster than the cleavage reaction with the perylene photocage.

For measurement of the action plot spectra, identical aliquots of perylene photocaged compound **26** were prepared in a 72 µM solution (40 µg mL^{-1}) and irradiated with 7.09 µmol photons of monochromatic light across the wavelength region of interest (310 nm to 595 nm) in a 15 nm resolution and triplicates for each of the 20 analysed wavelengths. The perylene derivative's (**26**) action plot shows conversion far outside the absorption maxima ($\lambda_{\text{max1}} = 413$ nm and $\lambda_{\text{max2}} = 440$ nm) and strong, blue-shifted reactivity (Figure 46). The highest photochemical reactivity occurs at $\lambda = 370$ nm and in the UV light region in general ($\lambda = 310$-380 nm) where the molar extinction of the chromophore is strongly reduced. Interestingly, the action plot displays only little conversion of the starting material at *λ* = 445 nm (16%) although the UV/Vis absorbance is comparably high.

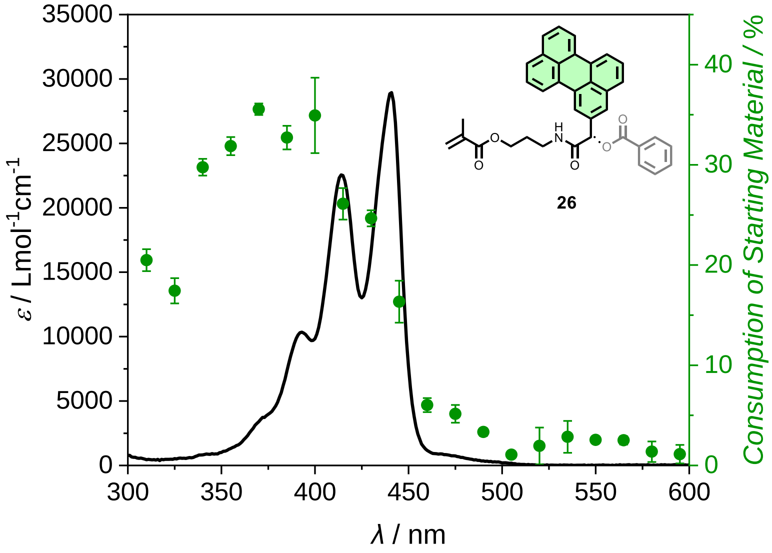

Figure 46: Molar extinction of **26** overlayed with the action plot consumption of the starting material (*c* = 72 µM in MeCN). For each indicated wavelength, 7.09 µmol photons were deposited into the reaction system.

Furthermore, there is still significant reactivity at longer wavelengths (*λ* = 470-580 nm), offering the possibility to shift the uncaging wavelength for the perylene photocage to a biological benign visible light region (*i.e.*, green light). However, to achieve most efficient release of the benzoic acid, the perylene-modified compound **26** should be irradiated at *λ* = 370 nm.

4.4 Pathway-Independent λ-Orthogonal Cleavage

In the next step, the laser experiments were translated to LED irradiation to demonstrate the applicability of the system in an easy-to-operate setup using widely available and low-priced irradiation sources. Pathway-independent orthogonal release of photocaged compounds offers the main advantage of spatiotemporal control over multiple cleavage reactions in a one-pot mixture by simply switching the colour of light. The overlay of both previously recorded action plots in a dual chromophore graph aimed to determine a reactivity window where both chromophores can independently cleave off the acid (Figure 47). Therefore, wavelength-orthogonal cleavage of the acids from a one-pot mixture containing both chromophores as starting material can be achieved. However, as both photocaged compounds show reactivity in the high energy wavelength region (λ = 300-425 nm), there appears to be no immediate avenue to achieve orthogonality by colour alone. Concerning the low energy wavelength region ($\lambda \geq 450$ nm), only the perylene-modified compound **26** cleaves off the benzoic acid whereas the coumarin-modified substrate **24** remains unaffected (Figure 47A).

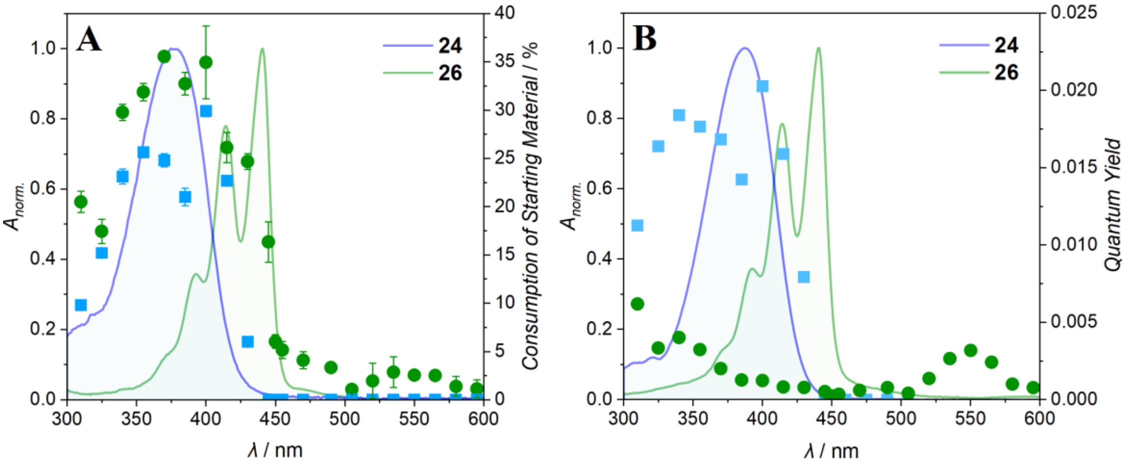

Figure 47: A: Dual chromophore action plot for **24** and **26** as well as their respective molar extinction (blue line for coumarin-modified substrate **24** and green line for perylene-modified compound **26**). The blue squares display the percentage consumption of the starting material of **24**, while the green dots present the percentage consumption of the starting material of **26**. B: Dual chromophore action plot for **24** and **26** as conversion per photon overlayed with their respective molar extinction.

Nevertheless, the reaction solution of **24** is converted faster than the solution of **26** because the reaction quantum yield is higher, confirmed by the number of photons that were needed to record the action plots (refer to section 4.3) which is further validated by plotting the quantum yield against the wavelength (Figure 47B).

Based on these findings, the wavelengths with the highest selectivity for pathway-independent orthogonality were set to 405 nm and 505 nm (Figure 48), using disparate numbers of photons. By employing either short irradiation times or low intensity of the violet-blue light (λ = 405 nm) only the coumarin-modified substrate **24** should cleave off the benzoic acid due to its faster reaction kinetics. With green light (λ = 505 nm), only the perylene-modified compound **26** releases the acid as indicated by the action plot.

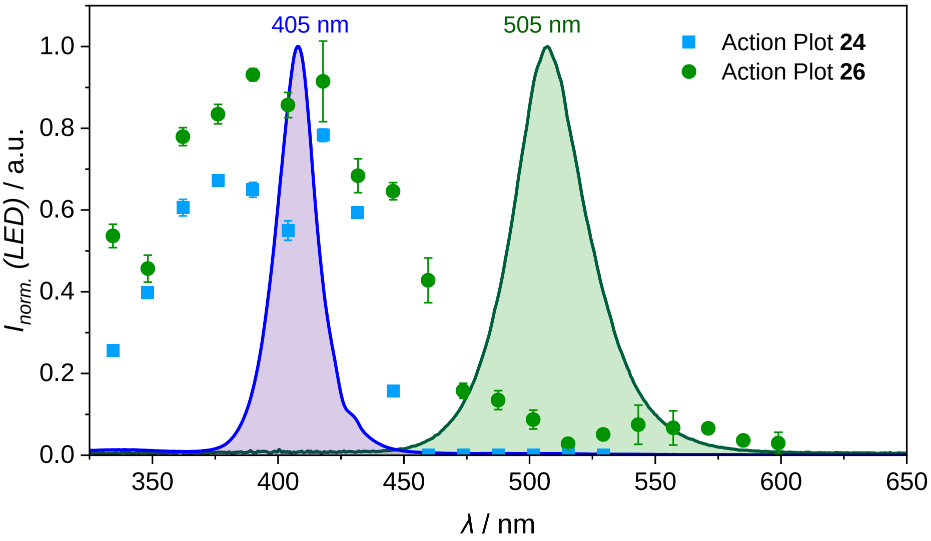

Figure 48: Normalised emission of the employed LEDs (405 nm, 0.20 mW and 505 nm, 40 mW) overlayed with the action plots of both photoreactive chromophores **24** and **26**.

A crimp vial was equipped with a stir bar and a solution of both photocaged compounds (147 µM **24** and 72 µM **26**) in MeCN. To perform the release of the acid from the coumarin-modified compound **24**, a 0.20 mW LED centered around 405 nm was employed, whereas a 40 mW LED, centered around 505 nm was used to cleave the acid from the perylene-modified substrate **26** (refer to section 5.6 for detailed description of the sample preparation and irradiation setup). The LED setup differs from the previously conducted laser experiments (benchtop experiment for LEDs vs. permanently installed OPO tuneable laser system; refer to section 5.2 for detailed description of the irradiation setups) and the LEDs present different output powers (405 nm LED: 0.20 mW; 505 nm LED: 40 mW) which is why the irradiation times need to be longer and may vary compared to each other. The irradiation pathway includes both possible pathways (high energy to low energy, low energy to high energy) as well as a dark period to confirm the sequence independence of the system. The high energy to low energy sequence was initially assessed, starting irradiation with the 405 nm LED. The lower output of the 405 nm LED led to the deposition of significantly fewer photons per unit into the reaction system. The duration of the first violet-blue light irradiation interval was set to 80 min with samples taken every 20 min.

The conversion plot (Figure 49) shows 45% cleavage of the coumarin-modified compound **24** and only 5% release from the perylene-modified substrate **26** after a combined 80 min irradiation with the 405 nm LED. Due to longer reaction times and the higher number of photons required, samples were taken every 30 min after switching to the 505 nm LED. The perylene-modified compound **26** continued cleaving the benzoic acid, reaching 30% release after a total irradiation time of 90 min, while the amount of **24** remained unaffected. In the following 45 min of dark period, neither compound reacted.

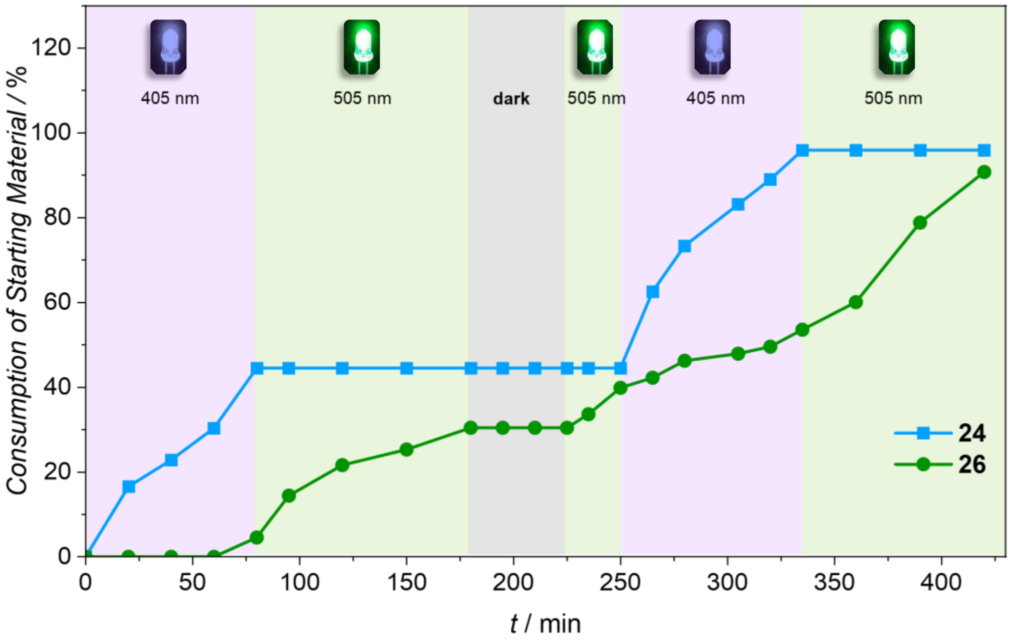

Figure 49: Consumption of the starting material of coumarin-modified substrate **24** and perylene-modified compound **26** after sequential irradiation with LEDs at two disparate wavelengths (λ_1 = 405 nm, 0.20 mW and λ_2 = 505 nm, 40 mW). Between the two possible reaction pathways (high energy to low energy, low energy to high energy), a dark period of 45 min was added. Upon 405 nm irradiation, almost exclusively **24** releases the benzoic acid, while **26** only releases the acid when exposed to 505 nm light.

Subsequently, the low energy to high energy irradiation sequence was executed, starting with 505 nm LED irradiation. Upon green light irradiation for 60 min in total, the perylene-modified compound **26** continued releasing the benzoic acid, finally affording 40% conversion. Again, the coumarin-modified substrate **24** remained photochemically silent until the setup was once more switched to the 405 nm LED. After violet-blue light irradiation for 75 min in total again, **24** displayed an overall cleavage yield of 95%, yet also 13% more of **26** was cleaved off due to the slower but still existing reactivity of the perylene-modified compound in the lower wavelength range. In a last step, irradiation was reverted back to 505 nm, leading to a final cleavage of 90% for **26**, whereas **24** did not react.

These results clearly demonstrate that the release of the benzoic acid of the coumarin photocaged compound **24** and the perylene photocaged compound **26** can be addressed almost fully pathway-independent in a one-pot reaction, simply by switching the colour of the incident light. Widely available LEDs were employed as light sources in a simple benchtop setup, opening an avenue for releasing two different molecular cargo with mild visible wavelengths in a fully orthogonal fashion.

4.5 Drug Release by Visible Light Irradiation

After having established the chromophore systems and confirmed light-induced release of a model release entity in a near fully wavelength orthogonal fashion, a further coumarin-modified compound (**28**) was synthesised. This molecule bears commercially available valproic acid (**27**) as release entity to evidence that the cleavage reaction and reactivity is only dependent on the chromophore, but independent of the attached acid. Further, it should be investigated whether the herein employed chromophore systems could potentially find application in light-induced and λ-orthogonal drug release. The therapeutic uses of valproic acid include epilepsy treatment, bipolar disorder management, and migraine prophylaxis.[183] The synthesis of the molecule was carried out in 22% yield using the previously established *Passerini* protocol, employing synthesised isocyanide **20**, coumarin carboxaldehyde **22** and commercially available valproic acid **27** (Figure 50). Due to an excess of valproic acid in the reaction mixture, two consecutive purification steps via column chromatography as well as additional washing steps with water and saturated Na_2CO_3-solution were needed to obtain the pure compound **28**, resulting in a significantly lower final yield in comparison to compound **24.**

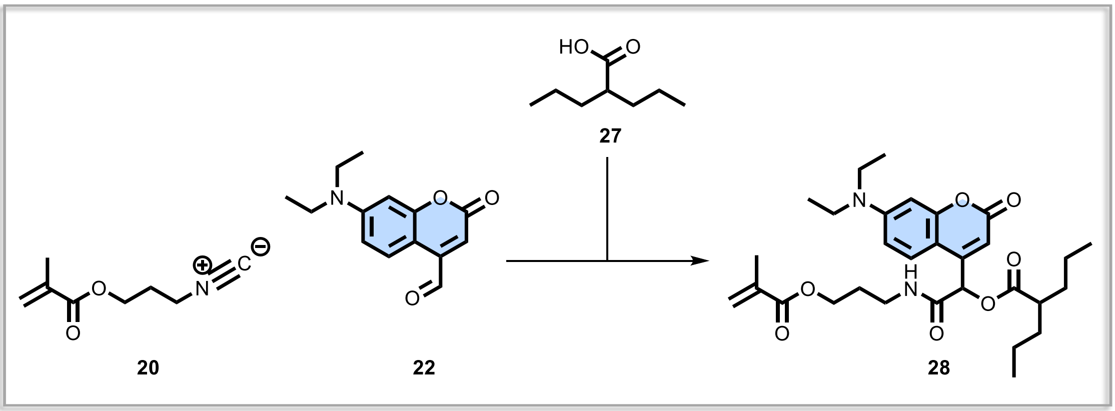

Figure 50: Synthesis of photocaged valproic acid-modified compound **28**: DCM, r.t., 16 h, 22%.

The best way to compare the reactivity of both coumarin-modified compounds (**24** and **28**) is provided by action plots as they allow the wavelength-resolved determination of photochemical release efficiency. Prior to the recording of the action plot, initial irradiation experiments were carried out using a 385 nm LED (refer to section 5.2.1 for

LED emission spectra) and were followed by UV/Vis spectroscopy to obtain insights regarding the cleavage of the valproic acid. Absorbance spectra of **28** display similar changes as absorbance spectra of **24** and indicate successful cleavage of the valproic acid as the three maxima at λ_1 = 208 nm, λ_2 = 252 nm and λ_3 = 385 nm decrease and shift bathochromically to λ = 269 nm and hypsochromically to λ = 359 nm and two isosbestic points develop at λ_1 = 334 nm and λ_2 = 425 nm during 10 min irradiation (Figure 51).

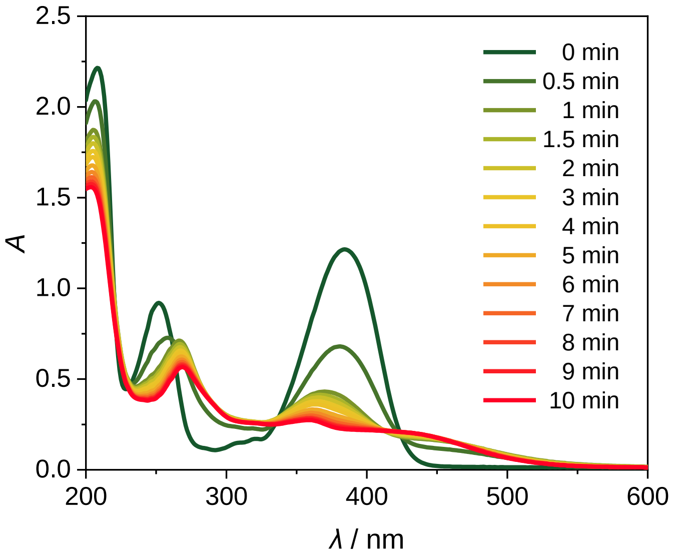

Figure 51: UV/Vis absorbance changes of 50 µM valproic acid-modified compound **28** over 10 min of irradiation at 20 °C with a 385 nm LED in MeCN.

Prior to the recording of the action plot measurements for **28**, a kinetic analysis at the absorbance maximum (λ = 385 nm) was conducted. 11 identical samples of **28** with a concentration of 150 µM (80 µg mL^{-1}) were irradiated for various time intervals with an identical photon number to ensure the precise determination of the required number of photons to achieve 20-30% consumption of the starting material, following the recommendation to stay within the linear regime that the initial progress of conversion approximates.[102] To determine the yield of the cleavage reaction, LC-MS with benzene as an internal standard was used (refer to section 5.5.3 for detailed description of the method). The kinetic studies of **28** revealed that 1.93 µmol photons ($1.16\cdot10^{18}$ photons) need to be deposited into the reaction system to obtain approximately 25% conversion of the starting material (refer to section 7.2, Figure A9 and Table A4).

For the following action plot measurement, coumarin photocaged compound **28** was prepared in a 150 µM stock solution (80 µg mL^{-1}) and identical aliquots irradiated with 1.93 µmol photons of monochromatic light across the wavelength region of interest (Figure 52A). The photochemical reactivity was probed in a 15 nm resolution, employing 15 different wavelengths ranging from 310 nm to 520 nm. Each wavelength was measured in triplicates.

Prior to recording of the action plot, it was surprising that one third more photons are needed (0.69 µmol for **24**, 1.93 µmol for **28**) to achieve similar cleavage yields using the same chromophore. However, as revealed by the action plot of **28** (Figure 52A), the consumption of the starting material of **28** at λ = 385 nm – the selected wavelength for the kinetic measurements – is not equal to 25%. Due to the lack of replicated control samples for the reaction kinetics, no averaging pipette imprecision was conducted. This may explain the higher number of photons and associated deviation from expected 25% conversion. Nevertheless, this fact was further disregarded as a trend in the action plot is still observable, and the values are used relatively to each other.

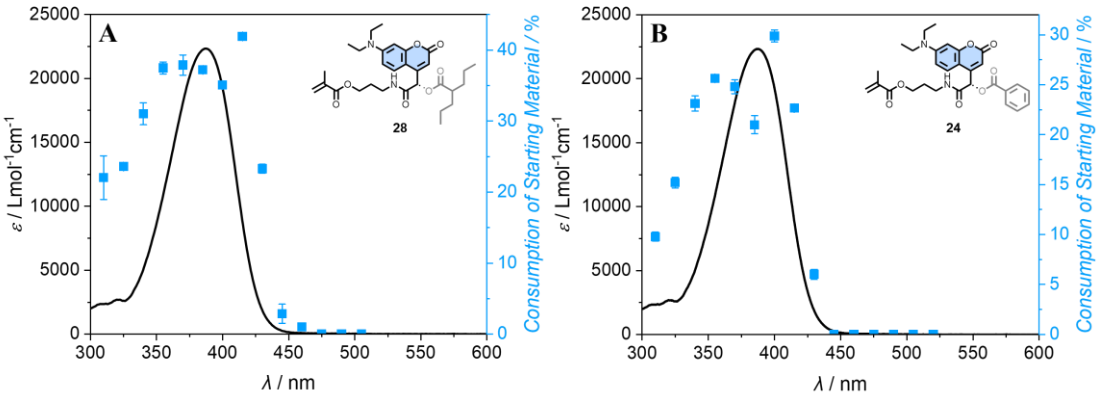

Figure 52: A: Molar extinction of **28** overlayed with the action plot consumption of the starting material (c = 150 µM in MeCN). For each indicated wavelength, 1.93 µmol photons were deposited into the reaction system. B: Molar extinction of **24** overlayed with the action plot consumption of the starting material (c = 147 µM in MeCN). For each indicated wavelength, 0.69 µmol photons were deposited into the reaction system.

The action plot of **28** (Figure 52A) clearly reveals likewise reactivity outside of the absorption maximum (λ_{max} = 385 nm) as the action plot of **26** (Figure 52B). Both action plots display an hysochromic as well as bathochromic shift of the reactivity maxima in comparison to the absorbance maximum, with the highest conversions for **28** reached at

λ_1 = 370 nm (blue-shift) and λ_2 = 415 nm (red-shift). Further, there is reactivity at λ = 430 nm (6% for **24**, 23% for **28**), although the molar extinction is negligibly low. The deviation can be traced back to the disparate number of photons that were used for the recording of the action plots.

The similar shape and reactivity of the action plots provide strong evidence that the reactivity is only dependent on the employed chromophore, but independent of the acid and employed laser instrument (refer to section 5.5 for detailed description of the used laser instruments), offering critical potential for photochemical delivery applications exploiting the herein introduced and analysed chromophores.

4.6 Conclusion and Outlook

Herein, a dual carrier system that allows for the sequential and fully wavelength-controlled release of cargo molecules was developed and characterised, employing 7-(diethylamino)-coumarin and 3-perylene photocaged compounds. Their wavelength-by-wavelength resolved photocleavage was investigated by the recording of action plots and further applied in a λ-orthogonal delivery system.

Three photocaged compounds (**24**, **26** and **28**) were successfully synthesised, employing a *Passerini* approach to combine either coumarin or perylene carboxaldehydes photo-protecting groups with carboxylic acids as model release entity and an isocyanide derivative. Post synthesis, the general feasibility of the light-induced cleavage of the acid was investigated in initial LED irradiation experiments and successful cleavage confirmed by UV/Vis spectroscopy, LC-MS analysis and NMR spectroscopy. To determine the most suitable wavelengths for λ-orthogonality, photochemical action plots were recorded and uncovered a high photoreactivity outside the chromophores' respective molar extinction maxima. Under the same photon number, the perylene-modified compound displayed slower reaction kinetics compared to the coumarin photoprotected substrate. This resulted in a near pathway-independent λ-orthogonal release of two different molecular cargo employing widely available LEDs (λ_{LED1} = 405 nm, λ_{LED2} = 505 nm) in a simple benchtop experiment, although both chromophores showed reactivity in the shorter wavelength' region. The reactivity is independent of the release entity, demonstrating that the herein analysed chromophores offer critical potential for multi-wavelength-controlled delivery applications, such as light-responsive drug release or photolabile hydrogels.

Concerning the anticipated photochemical delivery applications within biological systems, the herein developed and introduced compounds need further investigation regarding physiological conditions, *i.e.*, different pH, physiological temperature and aqueous solvents. Therefore, the action plots of each compound could be re-recorded while changing one parameter at a time to determine the most efficient release of the cargo molecule.

Besides the herein investigated valproic acid as cargo, chlorambucil (**29**) or ciprofloxacin (**30**) could be introduced to further analyse the wavelength-orthogonal drug release (Figure 53 left). Chlorambucil is a chemotherapy medication, finding application in the treatment of chronic lymphocytic leukemia,[184] whereas ciprofloxacin is an antibiotic used to treat bone and joint infections as well as complicated intra-abdominal infections.[185] Both drugs are commercially available and could be readily introduced employing the herein established *Passerini* approach as it allows for an easy modular interchange of both the carboxylic acids and the chromophores.

The introduction of different chromophores, such as nitroaryles (**31**), quinoxalines (**32**) or BODIPY derivatives (**33**) further expands the toolbox of λ-orthogonal cleavage reactions, achieving potentially full orthogonal release of selected drugs simply by switching the colour of light (Figure 53 right). Regarding their employment in the *Passerini* protocol, various literature-known procedures could be used, providing a synthetically easy access to the chromophore carboxaldehydes.[186]

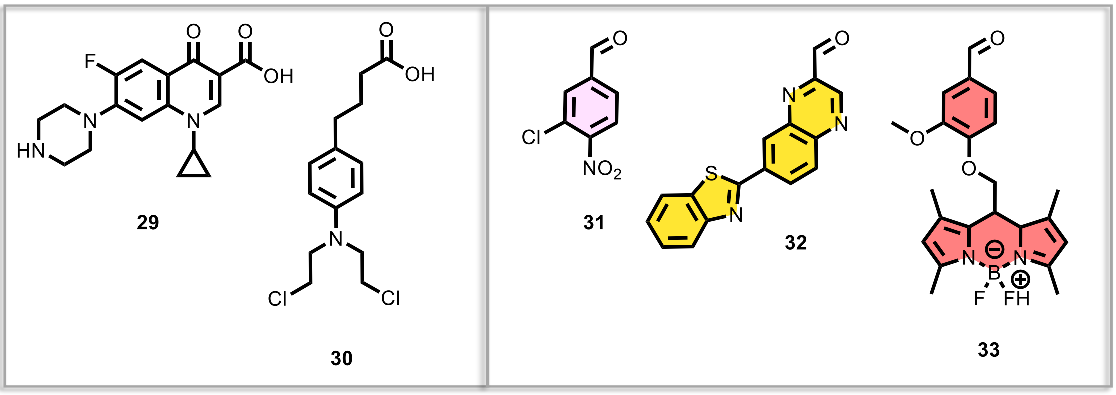

Figure 53: Left: Structures of chlorambucil (**29**) and ciprofloxacin (**30**), bearing carboxylic acids and right: Structures of possible carboxaldehyde-modified chromophores to be potentially further investigated in λ-orthogonal drug release.

A blue-shifted peak reactivity of the nitroaryles in comparison to the herein introduced coumarin and perylene photoprotective groups would be expected, whereas for the quinoxalines or BODIPY photoprotective groups a red-shifted photoreactivity would be anticipated. However, only the recording of wavelength-resolved photochemical action plots allows for the design of wavelength orthogonal systems as the inspection of UV/Vis absorption alone is not sufficient.

Following the herein presented successful *in vitro* experiments, it would further be interesting to transfer the wavelength-orthogonal release of different cargo to applications *in cellulo*, *i.e.*, light-responsive drug release in *HeLa* cells or photodynamic therapy in mice.

The methacrylate functionality in the herein introduced *Passerini* system offers the possibility to incorporate the chromophores combined with their release entities into a polymeric backbone by radical or ionic polymerization. This provides scaffolds for further application in 3D printing of *e.g.*, pharmaceuticals and miniaturisation of drug delivery systems, enabling fast and efficient analysis of various combinations of different photoprotected compounds.

5 Experimental Section

5.1 Materials and Methods

All reactions were either performed under a dry argon environment or under inert atmosphere, as detailed for each reaction in section 5.4. All solvents and reagents were commercially purchased at *ABCR, ACROS Organics, ALFA Aesar, Carl Roth, Chem Supply, CombiBlocks, Merck, Sigma Aldrich, ThermoFisher Scientific* and *VWR*. Unless stated otherwise, all chemicals were used as received without further purification. Anhydrous solvents were purchased at *ACROS Organics* and stored under argon. HPLC grade solvents were acquired at *ThermoFisher Scientific*, deuterated solvents for NMR spectroscopy were purchased at *Eurisotop*. Water was deionised using a *Merck* Millipore-Q8. Concerning reactions under inert conditions, flasks and other glassware were heated with a heat gun and dried in high vacuum, followed by flooding with argon (99.999% purity). Room temperature refers to ambient temperature (20-22 °C). The silica gel for flash chromatography (pore size 60 Å, particle size 40-63 µM) was purchased at *Sigma Aldrich*. The crude product was either dissolved in the solvent system or adsorbed onto silica before purification. Pressure was applied to the column using an air pump. Reactions were monitored by Thin Layer Chromatography (TLC) using silica gel 60 F_{254} coated aluminum plates by *Merck*. For detection, λ = 254 nm (fluorescence deletion) or λ = 366 nm (fluorescence excitation) was used. For staining, 5 % H_2SO_4 in MeOH, $KMnO_4$ solution (1.50 $KMnO_4$, 10.0 g K_2CO_3, 1.85 mL 10 % NaOH and 200 mL H_2O) or 0.5 % Ninhydrin in Butan-1-ol (spray reagent) were used.

Spectroscopy

UV/Vis spectroscopy

Samples were prepared using 1 cm quartz glass cuvettes (*Starna*) with either a sample volume of 500 µL or 1 mL at 25 °C. Molar absorption coefficients were determined by measuring spectra at different concentrations and applying *Beer-Lambert*'s law to calculate a linear fit, $A = \varepsilon c d$. UV/Vis absorbance spectra were either recorded on a *Varian* Cary100 Scan UV/Vis spectrometer or a *Shimadzu* UV-2700 spectrometer.

NMR spectroscopy

NMR spectroscopic data were either recorded on a *Bruker* Ascend LH spectrometer (^{1}H: 600.13 MHz, ^{13}C: 150.90 MHz) or a *Bruker* Avance 400 MHz spectrometer (^{1}H: 400.13 MHz, ^{13}C: 100.90 MHz) at ambient temperature. 10 mg of compound was dissolved in 400 µL deuterated solvent. The chemical shifts are reported in δ units, parts per million (ppm) downfield from TMS. Coupling constants (J) are given in Hertz (Hz) and multiplicities are abbreviated as following: s (singlet), d (doublet), dd (doublet of doublets), ddd (doublet of doublet of doublets), t (triplet), td (triplet of doublets), tt (triplet of triplets), p (pentet), m (multiplet), b (broad). Various 2D technique experiments were used to establish the structures and to assign the signals.

Mass Spectrometry

MALDI-ToF

Matrix-assisted laser desorption ionization (MALDI) mass spectrometry was performed on a *Shimadzu* Axima Confidence in reflectron (nucleosides and other small molecules) or linear negative (oligonucleotides) mode. As matrices, THAP (6-Aza-2-thiothymine, saturated in MeCN) and 2,4,6-trihydroxyacetophenone (0.3 M in EtOH) or ATT (3-Hydroxypicolinic acid, saturated in MeCN / H_2O 1:1/ di-ammonium hydrogen citrate (0.44 M in H_2O) 9:1) were used.

LC-MS

QUT: Liquid-chromatography coupled mass spectrometry (LC-MS) measurements were performed on an Ultimate 3000 UHPLC System by *Dionex* consisting of a pump (LPG 3400SZ), autosampler (WPS 3000TSL) and a temperature-controlled column compartment (TCC 3000). Separation was performed on a C_{18} column (Phenomenex Luna 5 µm, 100 Å, 250 x 2.0 mm), operating at 40 °C. A Gradient of MeCN / H_2O 5:95 to 100:0 (v/v) during 7 min at a flow rate of 1.0 mL min^{-1} was applied. The flow was split in a 9:1 ratio, where 90 % of the eluent was directed through a DAD UV-Detector (VWD 3400, *Dionex*) and 10 % was injected into the electrospray source. Spectra were recorded on a LTQ Orbitrap Elite mass spectrometer (*ThermoFisher Scientific*) equipped with a HESI II probe. The instrument was calibrated in the *m*/*z* range between 74-1822 using premixed calibration solutions (*ThermoFisher Scientific*). A constant spray voltage of 3.5 kV was applied, and the capillary temperature set to 300 °C. Unless stated otherwise, samples were prepared in a concentration of 0.5 mg mL^{-1} in MeCN and filtered through 0.22 µm PTFE membrane filters prior to injection.

KIT: LC-MS measurements were performed on an *Agilent* 1260 Infinity II system consisting of a quarternary pump (GB7111B), autosampler (G7129A, 100 µL sample loop), a temperature-controlled column oven (G7114A) and a variable UV/Vis detector (G7114A, VWD, flow cell G7114A 018, d = 10 mm, V = 14 µL). Separation was performed on a C_{18} HPLC column (*Agilent* Poroshell 120 EC-C18, 4.6·100 mm, 2.7 µm) operating at 40 °C. A gradient of MeCN / H_2O 10:90 to 80:20 (v/v) (additive 10 mmol L^{-1} $NH_4CH_3CO_2$) at a flow rate of 1 mL min^{-1} during 15 min was used as the eluting solvent. The flow was directed into an *Agilent* MSD (G613BA, AP-ESI ion source). The instrument was calibrated in the *m*/*z* range 118-2121 in positive mode and 113-2233 in the negative mode, using a premixed calibration solution (*Agilent*). The following parameters were used: spray chamber flow: 12 L min^{-1}, drying temperature: 350 K, Capillary Voltage: 3000 V, Fragmentor Voltage: 100 V.

Oligonucleotide Synthesis

Oligonucleotide synthesis was performed on a H-6 synthesizer by *K&A Laborgeräte*. After cleavage, the oligonucleotides were purified on a semi-preparative reversed-phase HPLC *ThermoFisher* system (RP-C_{18} column, A: NH_4OAc buffer, B: MeCN). The purified oligonucleotide strands were quantified photometrically using a NanoDrop ND-1000 spectrometer.

Freeze Drying

For removal of water or ammonium hydroxide from the oligonucleotide samples, a *Christ* Alpha RVC vacuum centrifuge was used in either of the following settings: 35 min, 35 °C, 100 mbar (ammonium hydroxide) or 16 h, 25 °C, 0.100 mbar (water).

HPLC

HPLC separation was performed on a *ThermoFisher Scientific* UltiMate™ 3000 system. For DNA purification, a *VDSpher* OptiBio Pur 300 S18-SE column (250·10 mm, 5 µm) was employed using a flow rate of 2.50 mL min^{-1}. Elution of the product was executed through 0-20% MeCN in NH_4OAc buffer at 40 °C in 30 min, followed by 10 min hold. Analytical separations were performed using a *VDSpher* OptiBio Pur 300 S_{18}-SE column (250·4.6 mm, 5 µm) with a flow rate of 1.00 mL min^{-1}. Elution of the product was executed through 0-50 % MeCN in NH_4OAc buffer at 40 °C in 30 min, followed by 10 min hold.

Gel Electrophoresis

Agarose gel electrophoresis

Agarose gel electrophoresis was performed using a PerfectBlue gel system (Mini L) by *VWR Peqlab* (120 V, max. 500 mA, 3 h). 8.00 g agarose was diluted in 200 mL TAE buffer (40 mM tris base, 20 mM acetate and 1 mM EDTA) in a microwave until no air bubbles and smears were visible. 15 µL SybrGreen™ Nucleic Acid Gel Stain was added to the gel mixture and mixed thoroughly. The gel was poured into the gel chamber and allowed to polymerize for 1 h. Subsequently, samples were prepared using 2 µL 25 µM DNA, 8 µL ddH_2O and 2 µL loading dye (14 mM EDTA, 63 mM tris base, 63 mM boronic acid, 2.8% ficoll, 0.07% bromphenol blue, 0.01% xylene cyano FF, 5M urea). The whole mixture was filled into the gel pockets, prior to running the gel for 3 h (120 V, max. 500 mA). Imaging was performed using a UV-light table (*Raytest* Bioimaging, λ_{exc} = 312 nm).

PAGE

Denaturing polyacrylamide / urea gel electrophoresis (PAGE) was conducted using a *Sequi/Gen GT* sequencing cell (21·40 cm) with a PowerPac HV. 50 mL polyacrylamide gel (12.5%), containing 16 mL acrylamide/bisacrylamide (19:1) gel mixture (*Carl Roth*), 25 g urea, 5 mL ddH_2O, 89 mM tris base, 89 mM boronic acid and 20 µL TEMED were polymerized for 45 min upon addition of 425 µL ammonium persulfate (APS) solution (100 mg APS in 900 µL ddH_2O) as a radical source. A freshly prepared TBE buffer (89 mM tris base, 89 mM boronic acid, 2 mM EDTA, pH 8.0) was used as electrolyte. For sample preparation, 10 µL of a 50 µM DNA solution were thinned in 10 µL ddH_2O and mixed thoroughly with 20 µL loading dye (14 mM EDTA, 63 mM tris base, 63 mM boronic acid, 2.8% ficoll, 0.07% bromphenol blue, 0.01% xylene cyano FF, 5M urea). 10 µL of the sample were filled into the gel pockets. After running the gel for 90 min at 50 °C (U = 3000 V, P = 50 W), the power source was turned off and the gel stained with SybrGreen™ Nucleic Acid Gel Stain according to the protocol supplied by the manufacturer (*ThermoFisher Scientific*): a mixture of 200 mg EDTA, 1.40 g boronic acid, 3.00 g tris base and 25 µL SybrGreen™ concentrate in 500 mL ddH_2O. The gel was incubated with the SybrGreen™ mixture for 30 min prior to fluorescence measurement with a Stella 830 *Raytest* spectrofluorometer containing LEDs radiating with a wavelength of 470 ± 10 nm or using a UV table (Raytest Bioimaging, λ_{exc} = 312 nm).

5.2 Irradiation Setups

5.2.1 LED Irradiation

All LEDs used within this work were purchased at *Roithner* Laser Technik GmbH (385 nm: LED385-03, 405 nm: 5P4FCA, 445 nm: VL440-5-15, 450 nm: LED450-03 and 505 nm: B5B-433-B505, Figure S1A). LED irradiation experiments were conducted in a benchtop setup which was designed and manufactured by the University of Regensburg and the workshop of the Institute for Physical Chemistry at KIT. The in-house built photoreactor contains a magnetic stirrer, a customised sample holder, which could be placed on top of the LED and a *Lauda* Alpha R8-thermostat to provide cooling of the LEDs and sample holder (Figure S1B). All reaction mixtures were irradiated in a distance of 10 mm between the LED and the bottom of the vial.

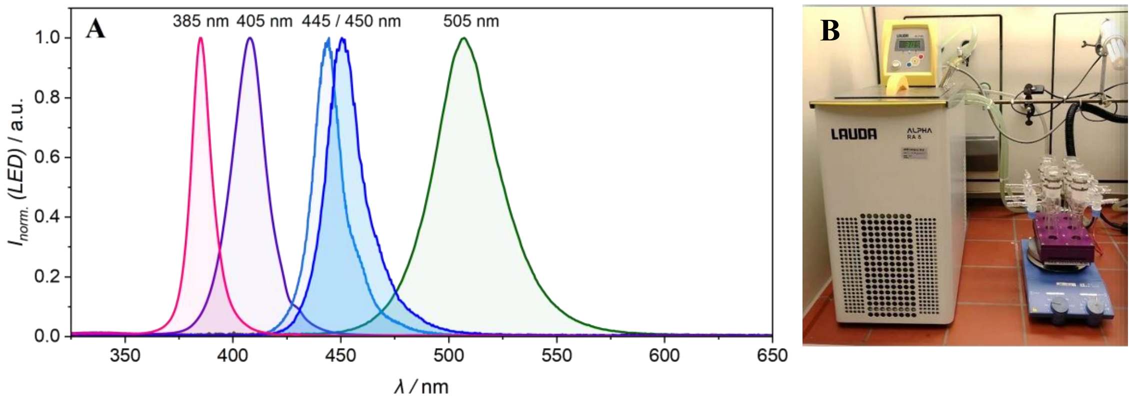

Figure S1: A: Normalised emission spectra of the used LEDs (385 nm, 20 mW; 405 nm, 0.20 mW; 445 nm, 40 mW, 450 nm, 20 mW, 505 nm, 40 mW). B: In-house build LED irradiation setup with thermostat, magnetic stirrer, and customised sample holder for crimp vials.

5.2.2 20 Hz Tuneable Laser System

Laser experiments for the kinetic and action plot measurements of molecules **24**, **26** and **28** were carried out according to procedures pulished by the team of *Barner-Kowollik*.[102, 109c, 187] The experiments were either conducted using a Coherent *Opolette* 355 OPO tuneable laser system (QUT) or an *Innolas* SpitLight 600 OPO tuneable laser system (KIT), operated at wavelengths between 300 nm and 650 nm with a full width half maximum of 7 ns and a repetition rate of 20 Hz. The emitted pulse has a flat-top spatial profile was expanded to 6 mm diameter to cover the entire sample volume, using focusing lenses and directed onto the sample from below using a prism. The spectral linewidth (FWHM) of the beam is 4-6 cm^{-1}. The energy of the laser pulses was downregulated by an attenuator (polarizer). The beam was redirected into the vertical cylindrical hole of a custom-made sample holder, which contains the sample during the experiments (Figure S2). For the irradiation experiments, all samples (300 µL degassed solution in MeCN) were prepared in 0.7 mL crimped glass vials by Supelco, *Merck* (Product Number: 24738-U). Since these glass vials were discontinued at *Merck*, the supplier was changed to *ThermoFisher* (Clear Glass Vial, 7·40 mm, Flat Bottom, Product Number: C4008-741). The energy of the incident laser pulses was measured by an Energy Max OC power meter (*Coherent*) directly above the sample holder (immediately before each sample was suspended into the samples holder). Prism and sample holder are positioned such that the complete diameter of the hole of the sample holder was covered by the incident laser beam.

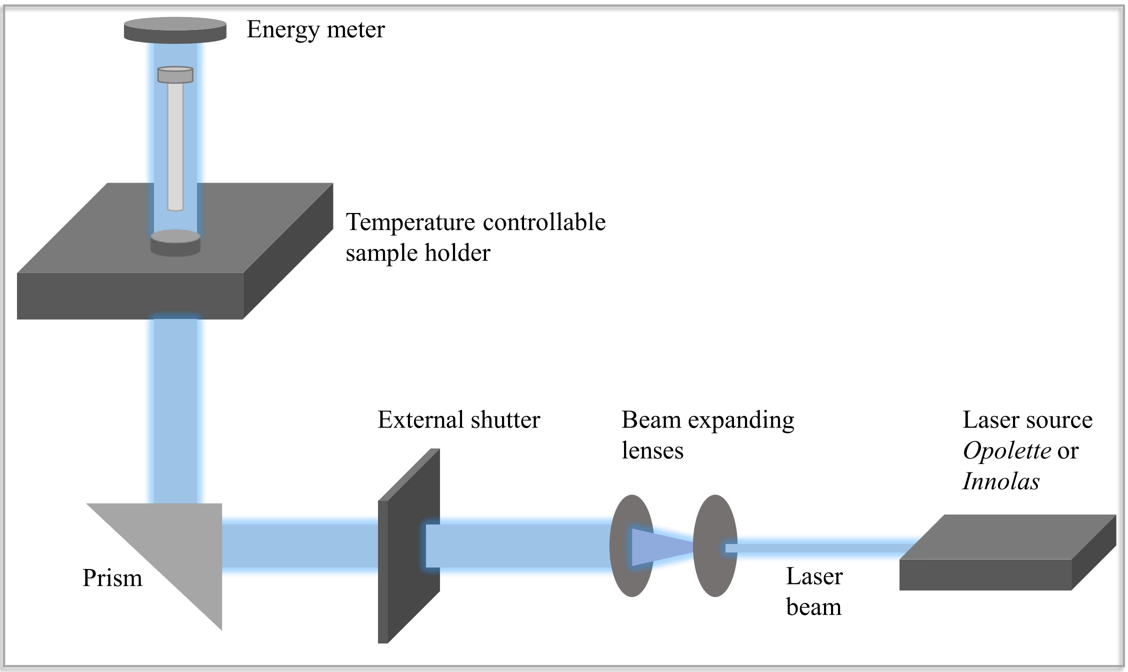
Energy meter
Temperature controllable sample holder
External shutter
Beam expanding lenses
Laser source *Opolette* or *Innolas*
Prism
Laser beam

Figure S2: Experimental setup of the herein used 20 Hz tuneable laser system. Light from a monochromatic light source is expanded, passed through an external, mechanical shutter and directed upwards using a prism. The sample is inserted in a custom-made aluminium block, and the energy delivered to the sample is monitored using an energy meter.

Control over incident photon number

The number of photons n_P ($[n_P]$ = mol) that a monochromatic laser pulse contains was determined from the laser pulse energy using the *Planck-Einstein* relation:

$$n_P = \frac{E_{Pulse} \cdot f_{rep} \cdot \lambda \cdot t}{h \cdot c \cdot [T_\lambda / 100]}$$

Where E_{Pulse} is the measured pulse energy above the aluminum block, λ is the wavelength of the incident radiation, f_{rep} is the laser repetition rate, t is the irradiation time, h is Planck's constant, c is the speed of light and T_λ is the wavelength dependent glass transmittance presented in Figure S3.

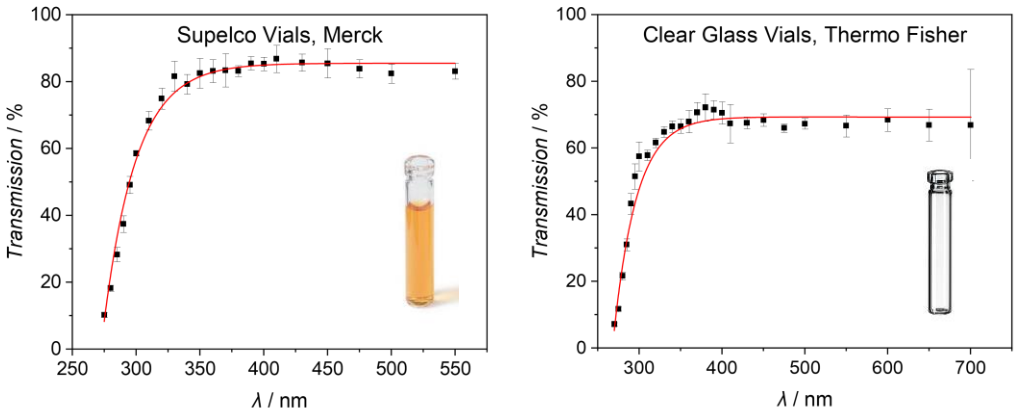

Figure S3: Left: Calibration of the glass vial transmittance of the Supelco Vials, commercially available at *Merck* including a fit to obtain values that were not determined experimentally. Right: Calibration of the glass vial transmittance of the Clear Glass Vials, purchased at *ThermoFisher* including a fit to obtain values that were not determined experimentally.

The wavelength dependent transmittance of the glass vials was determined experimentally using the above setup and following a procedure described by the group of *Barner-Kowollik*.[188] Three glass vials were randomly selected as calibration vials. For varying wavelengths and in each case at a constant power output of the laser, the energy was measured both with and without the calibration vials fitted into the sample holder. The measured energy per pulse without a calibration vial in the sample holder is denoted as E_0 and the measured energy per pulse with a calibration vial in the sample holder as E_n. The transmittance was calculated as the ratio of E_n to E_0. The average transmittance over the measurements of the three vials (T_λ) was plotted together with the respective error (Figure S3), as well as a fit to obtain values that were not determined experimentally.

5.3 Cell Experiments

Human cervix carcinoma (*HeLa*) cells were bought from *ATCC* (Manassas Virginia) and cultured in Dulbecco's modified Eagle Medium (DMEM) containing 10% fetal calf serum and 1% penicillin / streptomycin (100 µg/mL at 37 °C / 5% CO_2). For subculturing, the cells were detached with 0.25% trypsin-EDTA solution. For transfection, $4 \cdot 10^4$ cells per well were seeded into *Ibidi* 8-well µ-slides with ibiTreat surface. For cells that were only treated with SQ-modified Atto655 dye **14** and not transfected, $1 \cdot 10^4$ cells per well were seeded into *Ibidi* 8-well µ-slides with ibiTreat surface.

After seeding of the cells and incubation for 24 h, they were transfected with 75 ng **DNA6** per well using *Screenfect A* according to the protocol supplied by the manufacturer: Per transfected well, 1.40 µL *Screenfect A* reagent was diluted with 38.6 µL dilution buffer. 1 µL **DNA6** (25.6 µM solution in water) was diluted with 39 µL dilution buffer. Both solutions were combined and incubated for 5 h to allow lipoplex formation. Subsequently, lipoplexes were diluted with 120 µL DMEM and the whole solution was added to the well. After incubation for 24 h, the cells were washed carefully with PBS, followed by incubation for 16 h with 20 µM SQ-modified Atto655 dye **14** (4.41 mM stock solution in DMSO) in DMEM. Afterwards, the cells were washed carefullywith PBS, covered with DMEM and irradiated with a 450 nm LED for 30 min at 37 °C.

Visualisation of Atto520 (**DNA6**) and Atto655 dye (**14**) was performed with a *Leica* DMi8, TCS SP8 confocal microscope with a 60x oil objective. Image acquisition was conducted at a resolution of 1024·1024 pixels and 8-bit depth using LAS X 3.5.7.23225 software. For Atto520 detection, the excitation wavelength was set to λ_{exc} = 488 nm (OPSL 488 laser, 20% laser power) and emission detected at λ_{em} = 520-580 nm. Atto655 was excited at λ_{exc} = 638 nm (OPSL 638 laser, 20% laser power) and emission measured at λ_{em} = 665-750 nm, 20% laser power). For FRET detection, excitation wavelength was set to λ_{exc} = 488 nm (OPSL 488 nm laser, 20% laser power) and emission detected at λ_{em} = 665-750 nm. Fluorescence settings were complemented with a transmission channel, detected with a PMT detector.

5.4 Synthetic Procedures

5.4.1 DNA Building Blocks and SQ-modified Atto655 dye

Compound **3**

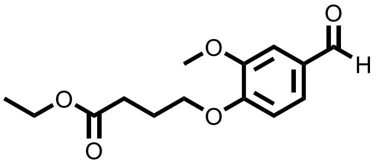

$C_{14}H_{18}O_5$
266.2930 g mol^{-1}

4.40 mL ethyl-4-bromobutyrate (6.00 g, 30.8 mmol, 1.00 equiv.) and 4.68 g vanillin (30.8 mmol, 1.00 equiv.) were dissolved in 50 mL DMF. 6.81 g K_2CO_3 (49.3 mmol, 1.60 equiv.) was added and the mixture heated to 50 °C under stirring for 2 h. Subsequently, the mixture was filtered, diluted with 50 mL water and extracted with 100 mL ethyl acetate. The organic extract was twice washed with 100 mL water, 100 mL brine, dried over Na_2SO_4 and concentrated in vacuo to give 6.72 g product (82%, 25.2 mmol) as a white solid.

R*f* (DCM) = 0.63 – The product was stained using $KMnO_4$-solution.

^{1}H-NMR (400 MHz, $CDCl_3$): δ (ppm) = 9.84 (s, 1H, C*H*O), 7.42 (dd, *J* = 8.2, 1.7 Hz, 1H, Ar-*H*), 7.40 (d, *J* = 1.7 Hz, 1H, Ar-*H*), 6.98 (d, *J* = 8.2 Hz, 1H, Ar-*H*), 4.15 (t, *J* = 7.2 Hz, 2H, $OCH_2CH_2CH_2CO$), 4.12 (d, *J* = 7.2 Hz, 2H, OCH_2CH_3), 3.92 (s, 3H, OCH_3), 2.54 (t, *J* = 7.2 Hz, 2H, $OCH_2CH_2CH_2CO$), 2.19 (p, *J* = 7.2 Hz, 2H, $OCH_2CH_2CH_2CO$), 1.26 (t, *J* = 7.2 Hz, 3H, OCH_2CH_3).

The spectroscopic data is in agreement with literature.[170]

Compound **4**

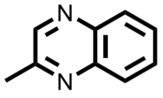

$C_9H_8N_2$
144.1770 g mol^{-1}

4.62 mL methylglyoxal (40% in H_2O, 5.40 g, 74.9 mmol, 2.00 equiv.) was added to a solution of 4.05 g benzene-1,2-diamine (37.5 mmol, 1.00 equiv.) and 1.20 g ZnI_2 (3.75 mmol, 0.10 equiv.) in 40 mL ethanol/water (1:1 v/v) and the solution was heated at 80 °C for 1 h. The solution was then partially concentrated in vacuo, 2x extracted with 50 mL CH_2Cl_2, dried over Na_2SO_4 and concentrated in vacuo. The crude product was purified by column chromatography (*n*-Hex / EtOAc 7:3) to give 3.30 g product (61%, 22.9 mmol) as a yellow liquid.

R*f* (*n*-Hex / EtOAc 7:3) = 0.41.

^{1}H-NMR (400 MHz, $CDCl_3$): δ (ppm) = 8.74 (s, 1H, N-C*H*), 8.07-8.02 (m, 2H, 2x C*H*-Ar), 7.76-7.67 (m, 2H, 2x C*H*-Ar), 2.77 (s, 3H, CH_3).

The spectroscopic data is in agreement with literature.[81]

Compound **5**

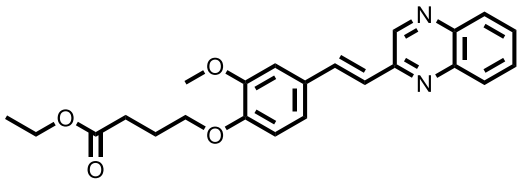

$C_{23}H_{24}N_2O_4$
392.4550 g mol^{-1}

To a mixture of 3.26 g **3** (12.2 mmol, 1.00 equiv.) and 2.11 g **4** (14.6 mmol, 1.20 equiv.) was added 604 µL piperidine (519 mg, 6.10 mmol, 0.50 equiv.), 523 µL acetic acid (550 mg, 9.15 mmol, 0.75 equiv.) and 5 mL dry toluene. The mixture was purged with argon, sealed and heated at 115 °C for 48 h. The resultant solution was concentrated in vacuo and absorbed onto silica gel. Column chromatography (*n*-Hex / EtOAc 2:1) delivered 3.40 g product (71%, 8.66 mmol) as yellow solid.

R*f* (*n*-Hex / EtOAc 2:1) = 0.38.

^{1}H-NMR (400 MHz, $CDCl_3$): *δ* (ppm) = 9.09 (s, 1H, N-*H*), 8.09 (td, *J* = 7.9, 7.3, 1.6 Hz, 2H, Ar-*H*), 7.85 (d, *J* = 16.4 Hz, 1H, Ar-*H*-OCH_3), 7.78-7.71 (m, 2H, Ar-*H*), 7.31 (d, *J* = 5.0 Hz, 1H, C*H*), 7.28 – 7.18 (m, 2H, Ar-*H*), 6.96(d, *J* = 8.3 Hz, 1H, C*H*), 4.22-4.15 (m, 4H, 2x C*H*$_2$), 3.98 (s, 3H, OC*H*$_3$), 2.59 (t, *J* = 7.2 Hz, 2H, C*H*$_2$), 2.23 (p, *J* = 7.2 Hz, 2H, C*H*$_2$), 1.30 (t, *J* = 7.2 Hz, 3H, C*H*$_3$).

The spectroscopic data is in agreement with literature.[81]

Compound **6**

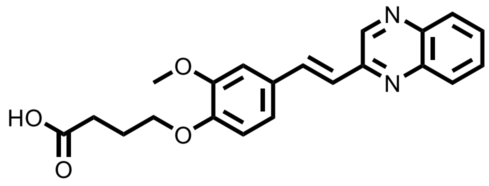

$C_{21}H_{20}N_2O_4$
364.4010 g mol^{-1}

716 mg **5** (1.82 mmol, 1.00 equiv.) was dissolved in 10 mL THF. To this solution was added a suspension of 87.4 mg LiOH (3.65 mmol, 2.00 equiv.) in 10 mL water and the solution was stirred at ambient temperature for 1 h. The solution was partially concentrated in vacuo and pH was adjusted to 6 using 3 mL 1M HCl solution. The solution was further diluted with 100 mL water, filtered, and dried in vacuo to give 536 mg (81%, 1.47 mmol) product as yellow solid.

^{1}H-NMR (400 MHz, DMSO-d_6): δ (ppm) = 12.18 (bs, 1H, O*H*), 9.21 (s, 1H, N-*H*), 8.03 (t, *J* = 9.2 Hz, 2H, Ar-*H*), 7.95 (d, *J* = 16.3 Hz, 1H, Ar-*H*-OCH$_3$), 7.80 (dt, *J* = 24.8, 7.3 Hz, 2H, Ar-*H*), 7.48 (d, *J* = 16.3 Hz, 1H, C*H*), 7.27 (dd, *J* = 8.3, 1.9 Hz, 1H, Ar-*H*), 7.02 (d, *J* = 8.3 Hz, 1H, C*H*), 4.03 (t, *J* = 6.4 Hz, 2H, C*H*$_2$), 3.87 (s, 3H, OC*H*$_3$), 2.40 (t, *J* = 7.3 Hz, 2H, C*H*$_2$), 1.96 (p, *J* = 6.9 Hz, 2H, C*H*$_2$).

The spectroscopic data is in agreement with literature.[81]

Compound **7**

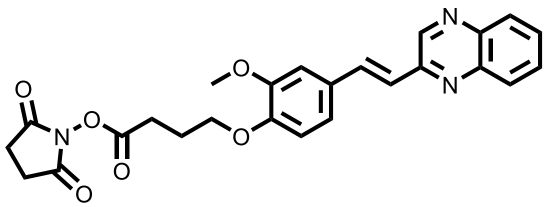

$C_{25}H_{23}N_3O_6$
461.4703 g mol^{-1}

200 mg **6** (549 µmol, 1.00 equiv.) was dissolved in 5 mL DMF. To this solution, 158 mg N-(3-dimethylaminopropyl)-N'-ethylcarbodiimide hydrochloride (EDC·HCl, 824 µmol, 1.50 equiv.) and 94.8 mg N-hydroxysuccinimide (824 µmol, 1.50 equiv.) were added and the solution was stirred at ambient temperature for 6 h. DMF was concentrated in vacuo and the residue was absorbed onto silica gel (ca. 500 mg). Column chromatography (*n*-Hex / EtOAc = 3:7) delivered 208 mg SQ-NHS ester **1** (82%, 450 µmol) as a yellow solid.

R*f* (*n*-Hex / EtOAc 3:7) = 0.48.

^{1}H-NMR (400 MHz, $CDCl_3$): *δ* (ppm) = 9.06 (s, 1H, N-*H*), 8.06 (ddd, *J* = 8.2, 3.1, 1.5 Hz, 2H, Ar-*H*), 7.81 (d, *J* = 16.3 Hz, 1H, Ar-*H*-OCH_3), 7.73 (dddd, *J* = 23.7, 8.3 6.9, 1.5 Hz, 2H, Ar-*H*), 7.30 – 7.25 (m, 1H, C*H*), 7.23 – 7.18 (m, 2H, Ar-*H*), 6.94 (d, *J* = 8.2 Hz, 1H, C*H*), 4.17 (t, *J* = 6.1 Hz, 2H, CH_2), 3.95 (s, 3H, OCH_3), 2.91 (t, *J* = 7.3 Hz, 2H, CH_2), 2.84 (bs, 4H, 2x CH_2), 2.29 (t, *J* = 6.7 Hz, 2H, CH_2).

The spectroscopic data is in agreement with literature.[81]

Compound **8**

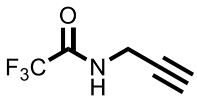

$C_5H_4F_3NO$
151.0982 g mol^{-1}

4.50 mL ethyl trifluoroacetate (5.33 g, 38.0 mmol, 1.20 equiv.) were slowly added to an ice-cold solution of 2.00 mL propargylamine (1.72 g, 31.00 mmol, 1.00 equiv.) in 30 mL MeOH. After stirring for 24 h at ambient temperature, the solvent was removed under reduced pressure, followed by diluting the residue in 50 mL DCM. Saturated $NaHCO_3$ solution was added to the residue and the aqueous phase was extracted 3x with 100 mL DCM. The combined organic layers were dried over sodium sulfate, filtered and the solvent was removed under reduced pressure. Column chromatography (DCM) delivered 2.84 g (60%, 18.8 mmol) of the amide as yellow liquid.

R_f (DCM) = 0.80 – The product was visualized using $KMnO_4$-solution.

^{1}H-NMR (400 MHz, $CDCl_3$): δ (ppm) = 6.57 (bs, 1H, N*H*), 4.16 (dd, *J* = 5.5, 2.5 Hz, 2H, C*H*$_2$), 2.33 (t, *J* = 2.6 Hz, 1H, C*H*).

The spectroscopic data is in agreement with literature.[171]

Compound **10**

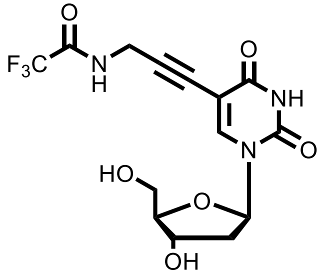

$C_{14}H_{14}F_3N_3O_6$
377.2896 g mol^{-1}

Under an argon atmosphere, 2.33 g 5-iodo-2’-deoxyuridine (**9**) (6.60 mmol, 1.00 equiv.) was dissolved in 25 mL anhydrous DMF. 251 mg copper(I) iodide (1.32 mmol, 0.20 equiv.) and 2.20 µL **8** (2.84 g, 19.8 mmol, 3.00 equiv.) were added. The reaction was degassed by bubbling with argon gas for 15 min. 763 mg tetrakis(triphenyl-phosphine)palladium(0) (660 µmol, 0.10 equiv.) and 1.82 mL triethylamine (1.34 mg, 13.2 mmol, 2.00 equiv.) were added and the reaction stirred for 16 h at ambient temperature. The solvent was removed under reduced pressure and the crude product dissolved in 100 mL MeOH/DCM 1:1 (v/v). Two teaspoons of freshly prepared AMBERLITE® *IRA-402* (bicarbonate form) were added and the resulting suspension stirred for 15 min. After filtration, the solvent was removed under reduced pressure and the crude product purified via column chromatography (DCM / MeOH 10:1). The product was obtained as a brown foam (1.37 g, 55%, 3.63 mmol).

R_f (DCM / MeOH 10:1) = 0.23 – The product was stained using 5% H_2SO_4 solution.

^{1}H-NMR (400 MHz, DMSO-d_6): δ (ppm) = 11.63 (s, 1H, 3-N*H*), 10.06 (d, J = 5.6 Hz, 1H, N*H*), 8.19 (s, 1H, 6-C*H*), 6.10 (t, J = 6.7 Hz, 1H, 1’-C*H*), 5.23 (d, J = 4.3 Hz, 1H, 3’-O*H*), 5.08 (t, J = 5.1 Hz, 1H, 5’-O*H*), 4.23 (d, J = 4.7 Hz, 3H, 3’-CH, CH_2), 3.79 (q, J = 3.4 Hz, 1H, 4’-C*H*), 3.58 (ddd, J = 10.5, 5.1, 3.5 Hz, 2H, 5’-CH_2), 2.13 - 2.10 (m, 2H, 2’-CH_2).

The spectroscopic data is in agreement with literature.[172a]

Compound **11**

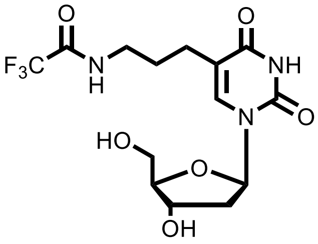

$C_{14}H_{18}F_3N_3O_6$

381.3168 g mol^{-1}

730 mg nucleoside **10** (1.93 mmol, 1.00 equiv.) and 309 mg Pd/C (10% Pd, 290 µmol, 0.15 equiv.) were dissolved in 25 mL anhydrous MeOH. Hydrogen (approx. 3 L balloon) was bubbled through the suspension for 5 h. The reaction mixture was filtered over a plug of CELITE®, followed by removal of the solvent under reduced pressure. 589 mg (80%, 1.54 mmol) of the product were obtained as a light brown foam.

R*f* (DCM / MeOH 10:1) = 0.18 – The product was stained using 5% H_2SO_4 solution.

^{1}H-NMR (400 MHz, DMSO-*d*$_6$): *δ* (ppm) = 11.29 (s, 1H, 3-N*H*), 9.40 (t, *J* = 5.2 Hz, 1H, N*H*), 7.68 (s, 1H, 6-C*H*), 6.16 (t, *J* = 6.8, 1H, 1'-C*H*), 5.22 (d, *J* = 4.2 Hz, 1H, 3'-O*H*), 5.00 (t, *J* = 5.2 Hz, 1H, 5'-O*H*), 4.23 (td, *J* = 6.1, 5.2, 3.1 Hz, 1H, 3'-C*H*), 3.76 (q, *J* = 3.7 Hz, 1H, 4'-C*H*), 3.56 (pt, *J* = 9.1, 4.9 Hz, 2H, 5'-C*H*$_2$), 3.17 (dd, *J* = 5.6, 2.7 Hz, 2H, C*H*$_2$), 2.20 (q, *J* = 7.2 Hz, 2H, C*H*$_2$), 2.10 – 2.07 (m, 2H, 2'-C*H*$_2$), 1.64 (qd, *J* = 7.2, 2.0 Hz, 2H, C*H*$_2$).

The spectroscopic data is in agreement with literature.[172b]

Compound **12**

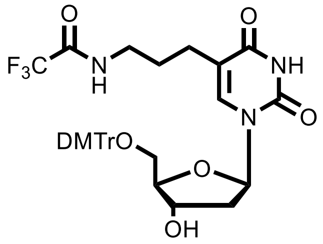

$C_{35}H_{36}F_3N_3O_8$
683.6897 g mol^{-1}

Under an argon atmosphere, 600 mg **11** (1.58 mmol, 1.00 equiv.) were dissolved in 12 mL anhydrous pyridine. 322 mg silver(I) nitrate (1.90 mmol, 1.20 equiv.) and 644 mg 4,4’-dimethoxytrityl chloride (1.57 mmol, 1.20 equiv.) were added and the reaction mixture stirred for 6 h. The crude mixture was diluted with 50 mL DCM, filtered and washed 3x with 50 mL saturated $NaHCO_3$ solution. The solvent was removed under reduced pressure. Column chromatography (DCM / MeOH 40:1 to 20:1) and following lyophilisation from benzene delivered 648 mg (60%, 948 µmol) of a brown / beige foam.

R*f* (DCM / MeOH 10:1) = 0.65 – The product was stained using 5% H_2SO_4 solution.

^{1}H-NMR (400 MHz, DMSO-d_6): δ (ppm) = 11.37 (s, 1H, 3-N*H*), 9.34 (t, *J* = 5.5 Hz, 1H, N*H*), 7.41 (s, 1H, 6-C*H*), 7.39 – 7.37 (m, 2H, C*H*$_{ar}$), 7.32 – 7.22 (m, 7H, C*H*$_{Ar}$), 6.88 (dd, 4H, *J* = 8.9, 1.7 Hz, C*H*$_{Ar}$), 6.19 (t, *J* = 6.8 Hz, 1H, 1’-C*H*), 5.32 (d, *J* = 4.6 Hz, 1H, 3’-O*H*), 4.29 (dq, *J* = 8.2, 4.1 Hz, 1H, 3’-C*H*), 3.87 (q, *J* = 4.0 Hz, 1H, 4’-C*H*), 3.73 (s, 6H, 2x OC*H*$_3$), 3.18 (ddt, *J* = 13.4, 10.4, 4.1 Hz, 2H, 5’-C*H*$_2$), 2.97 (q, *J* = 6.8 Hz, 2H, C*H*$_2$), 2.26 (dt, *J* = 13.6, 6.9 Hz, 1H, 2’-C*H*$_2$), 2.15 (ddd, *J* = 13.4, 6.6, 3.8 Hz, 1H, 2’-C*H*$_2$), 1.91 (q, *J* = 6.7 Hz, 2H, C*H*$_2$), 1.47 (dq, *J* = 14.3, 6.5 Hz, 2H, C*H*$_2$).

The spectroscopic data is in agreement with literature.[22b]

Compound **13**

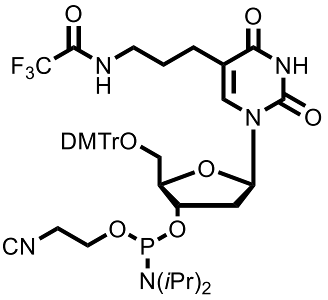

$C_{35}H_{36}F_3N_3O_8$
683.6897 g mol^{-1}

75.0 mg **12** (110 µmol, 1.00 equiv.) were lyophilized from 5 mL benzene and dissolved in 3 mL anhydrous DCM. 56 µL DIPEA (42.5 mg, 329 µmol, 3.00 equiv.) and 37 µL 2-cyano-ethyl-*N*,*N*-diisopropylchlorophosphoramidite (39.1 mg, 165 µmol, 1.50 equiv.) were added and the reaction mixture stirred for 4 h. The crude product was purified via column chromatography (DCM / Acetone 3:1), yielding 61.3 mg product (63%, 69.3 µmol) as light beige foam.

R_f (DCM / Acetone 3:1) = 0.73 – The product was stained using 5% H_2SO_4 solution.

^{1}H-NMR (400 MHz, DMSO-d_6): δ (ppm) = 11.38 (s, 1H, 3-N*H*), 9.34 (t, *J* = 5.5 Hz, 1H, N*H*), 7.41 (s, 1H, 6-C*H*), 7.39 – 7.37 (m, 2H, CH_{Ar}), 7.32 – 7.22 (m, 7H, CH_{Ar}), 6.88 (dd, 4H, *J* = 8.9, 1.7 Hz, CH_{Ar}), 6.19 (t, *J* = 6.8 Hz, 1H, 1'-C*H*), 4.52 (ddt, *J* = 15.2, 10.8, 4.1 Hz, 1H, 3'-C*H*), 4.01 (dq, *J* = 20.5, 4.3 Hz, 1 H, 4'-C*H*), 3.73 (d, *J* = 2.5 Hz, 6H, 2 x OCH_3), 3.61 – 3.43 (m, 4H, 2x CH_2), 3.24 (dt, *J* = 11.2, 2.4 Hz, 2H, 5'-CH_2), 2.99 (p, *J* = 6.6 Hz, 2H, CH_2), 2.76 (t, *J* = 5.9 Hz, 1H, C*H*), 2.62 (t, *J* = 5.9 Hz, 1H, C*H*), 2.42 – 2.24 (m, 2H, 2'-CH_2), 1.95 (dd, *J* = 16.1, 8.1 Hz, 2H, CH_2), 1.54 – 1.44 (m, 2H, CH_2)., 1.23 – 1.06 (m, 12 H, 4x CH_3).

The spectroscopic data is in agreement with literature.[22b]

Compound **14**

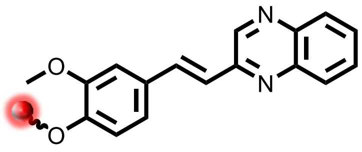

$C_{50}H_{58}N_7O_8S^+$
917.4062 g mol^{-1}

5.00 mg Atto655-NH$_2$ (8.76 µmol, 1.00 equiv.) and 6 µL DIPEA (4.53 mg, 35.0 µmol, 4.00 equiv.) was dissolved in 2 mL anhydrous DMF. To this solution was slowly added a solution of 7.85 mg **7** (17.0 mmol, 1.00 equiv.) in 2 mL anhydrous DMF. The reaction mixture was stirred for 16 h at ambient temperature, followed by removal of the solvent under reduced pressure. The crude product was lyophilised from benzene / MeOH (5:4) solution, affording 5.54 mg SQ-modified Atto655 dye **2** (69%, 6.04 µmol) as a blue-green solid.

R*f* (DCM / MeOH 10:1) = 0.45.

The resulting product was characterised via **ESI-HRMS** (Figure S4).

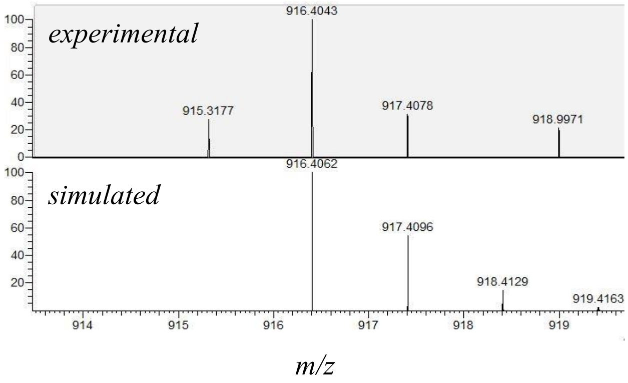

Figure S4: ESI-HRMS analysis of compound **14**: m/z_{theo} = 916.4062 for $[C_{50}H_{58}N_7O_8S]^-$, m/z_{exp} = 916.4043 $[C_{50}H_{58}N_7O_8S]^-$.

5.4.2 SQ-modified DNA2

Phosphoramidite-modified DNA building block **13** was incorporated into **DNA1** using a H-6 DNA/RNA Synthesiser from *K&A Laborgeräte*. CPG (1 µmol, 500 Å), phosphoramidites, reagents, solvents and columns which were used in DNA synthesis were purchased from *ChemGenes*, *GlenResearch* and *Sigma Aldrich*. Oligonucleotides were synthesized DMT-on. Conventional monomers were incorporated using standard conditions. Phosphoramidite **13** was used as 100 mM solution in MeCN with extended coupling time. Once dissolved, the solution of the phosphoramidite is only stable for 24 h. After cleavage from the CPG (25% NH_4OH, 55 °C, 16 h) the oligonucleotides were purified by Glen-Pak™ DNA purification cartridge. Freeze drying gave **DNA1** as white powder.

For the synthesis of **DNA2**, approximately 1 µmol **DNA1** (1.00 equiv.) was dissolved in 100 µL ddH_2O and diluted in 100 µL anhydrous DMF. To this solution was added 10 µL DIPEA, followed by slow addition of a solution of 1.38 mg SQ-NHS ester **7** (3 µmol, 3.00 equiv.) in 200 µL anhydrous DMF. The mixtures was stirred at ambient temperature for 48 h. After removal of the solvent by “Freeze Drying” (refer to section 5.1), the oligonucleotide was purified by HPLC. **DNA2** was detected by a DAD-3000 diode array detector at 260 nm and 290 nm (DNA absorbance) and 383 nm (SQ moiety absorbance) and obtained as a yellow powder.

LED irradiation experiments of **DNA2** to homo-dimerized **(DNA2)$_2$** were performed using a 450 nm LED and a solution of 50 µM **DNA2** in H_2O, 10 mM Na-P_i buffer and 250 mM NaCl in a total volume of 600 µL in a crimp vial.

5.4.3 SQ-modified DNA6 and DNA7

SQ- and Atto520-modified **DNA6** was synthesised via a three-step procedure, starting with the simultaneous incorporation of modified phosphoramidite building block **13** and commercially available phosphoramidite **15** into **DNA4**, employing standard and automated DNA synthesis protocol**.** Phosphoramidites **13** and **15** were each used as 100 mM solution in MeCN (the solution of each phosphoramidite is only stable for 24 h) with extended coupling time. After cleavage from the CPG (25% NH_4OH, 55 °C, 16 h) the oligonucleotides were purified by Glen-Pak™ DNA purification cartridge. After freeze drying, **DNA4** was obtained as white powder.

For synthesis of SQ-modified **DNA5**, approximately 5 µmol **DNA5** (1.00 equiv.) were dissolved in 200 µL ddH_2O and diluted in 200 µL anhydrous DMF. 20 µL DIPEA and a solution of 6.92 mg SQ-NHS ester **7** (15 µmol, 3.00 equiv.) in 500 µL anhydrous DMF was added and the mixture was stirred at ambient temperature for 48 h. After removal of the solvent by "Freeze Drying", the oligonucleotide was purified by HPLC. **DNA6** was detected by a DAD-3000 diode array detector at 260 nm and 290 nm (DNA absorbance) and 383 nm (SQ moiety absorbance) and obtained as a yellow powder.

DNA6 was synthesised via a copper(I)-catalysed azide-alkyne cycloaddition: **DNA5** was dissolved in 50 µL ddH_2O and 57 µL of the azide-dye (10 mM in DMSO/^{t}BuOH 3:1), followed by addition of 34 µL tris-[(1-benzyl-1*H*-1,2,3-triazol-4-yl)methyl]amine (TBTA, 100 mM in DMSO / ^{t}BuOH 3:1), 17 µL tetrakis(acetonitrile)copper(I)-hexafluorophosphate (100 mM in DMSO / ^{t}BuOH 3:1) and 25 µL sodium ascorbate solution (400 mM in ddH_2O). The reaction mixture was incubated for 2 h at 60 °C using a heating block, followed by cooling down to ambient temperature and transfer into a 15 mL centrifuge tube. 450 µL sodium acetate (300 mM in ddH_2O) and 150 µL EDTA (50 mM in ddH_2O) were added and the conical centrifuge tube filled with 100% EtOH to a total volume of 10 mL. The solution was mixed on a vortex mixer and stored at -32 °C for 60 h. Subsequently, the solution was centrifuged for 10 min at 4000 rpm, followed by decantation of the supernatant. The remaining DNA pellet was washed 3x with 1 mL 80% EtOH by centrifugation for 10 min at 4000 rpm. The pellet was freeze dried prior to purification by HPLC. **DNA6** was detected by a DAD-3000 diode array detector at 260 nm and

290 nm (DNA absorbance), 383 nm (SQ moiety absorbance) and 520 nm (Atto520 absorbance) and obtained as a purple powder.

To synthesise **DNA7** for the PAGE analysis**,** 5 µM **DNA6** and 50 µM SQ-modified Atto655 dye **14** in aqueous solution, containing 5% DMSO, 10 mM Na-P_i buffer and 250 mM NaCl in a total volume of 500 µL in a crimp vial were irradiated with a 450 nm LED for 30 min at 37 °C. Afterwards, the samples were freeze dried over night and analysed via denaturing PAGE.

5.4.4 Photocaged Compounds

Compound **17**

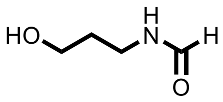

$C_4H_9NO_2$
103.1210 g mol^{-1}

1.00 mL 3-aminopropan-1-ol (**15**) (1.00 g, 13.3 mmol, 1.00 equiv.) was dissolved in 10 mL MeOH and cooled with an ice bath. 1.08 mL ethylformate (**16**) (985 mg, 13.3 mmol, 1.00 equiv.) was added portion-wise to the stirred solution over a period of 15 min. Subsequently, the solution was removed from the ice bath and heated at 50 °C for 2 h. The solvent was removed under reduced pressure to afford 1.35 g (99%, 13.2 mmol) of the desired product as a colourless oil. This compound decomposes upon storage and was immediately used in the next step.

R*f* (DCM / MeOH 10:1) = 0.23 – The product was stained using $KMnO_4$-solution.

^{1}H-NMR (600 MHz, DMSO-d_6): δ (ppm) = 7.98-7.95 (m, 1H, C*H*O), 4.29 (bs, 1H, O*H*), 3.41 (t, *J* = 6.3 Hz, 2H, CH_2), 3.12 (td, *J* = 7.1, 5.6 Hz, 2H, CH_2), 1.55 (p, *J* = 6.6 Hz, 2 H, CH_2).

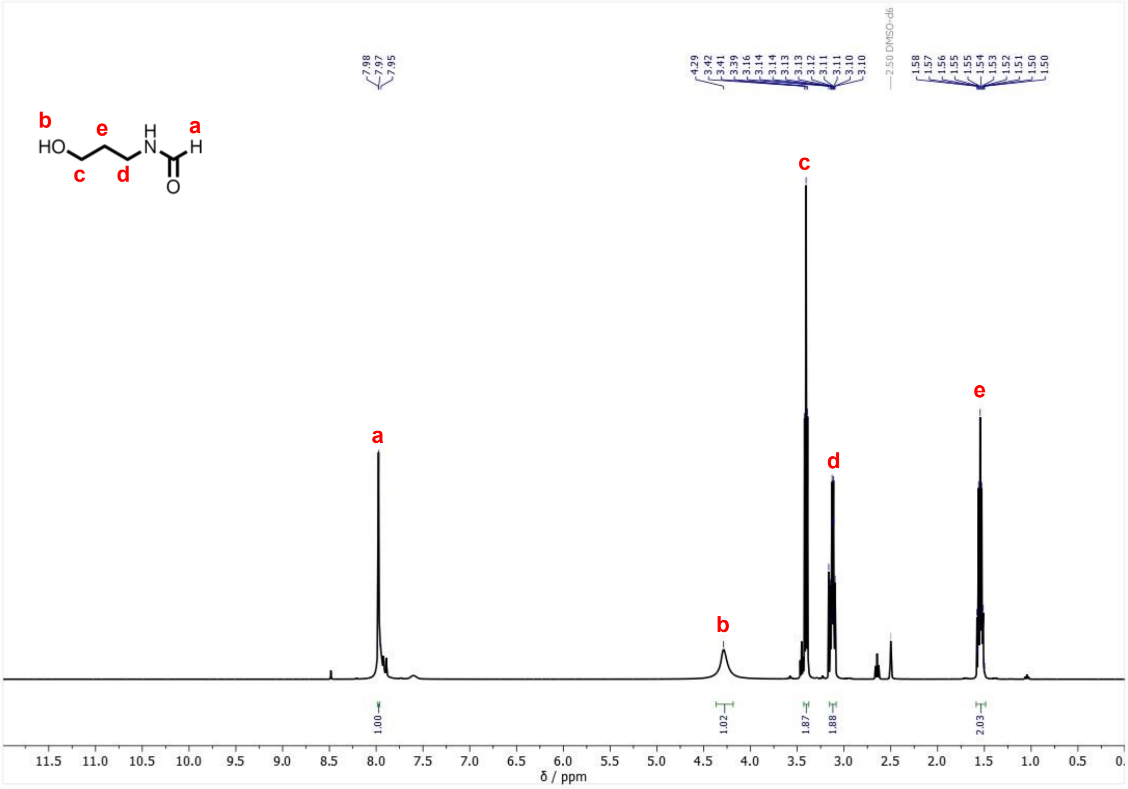

Figure S5: ^{1}H-NMR spectrum of compound **17** (DMSO-d_6, 600 MHz).

^{13}C-NMR (151 MHz, DMSO-d_6): δ (ppm) = 161.2 (s, 1C, *C*HO), 58.5 (s, 1C, *C*H_2), 34.5 (s, 1C, *C*H_2), 32.3 (s, 1C, *C*H_2).

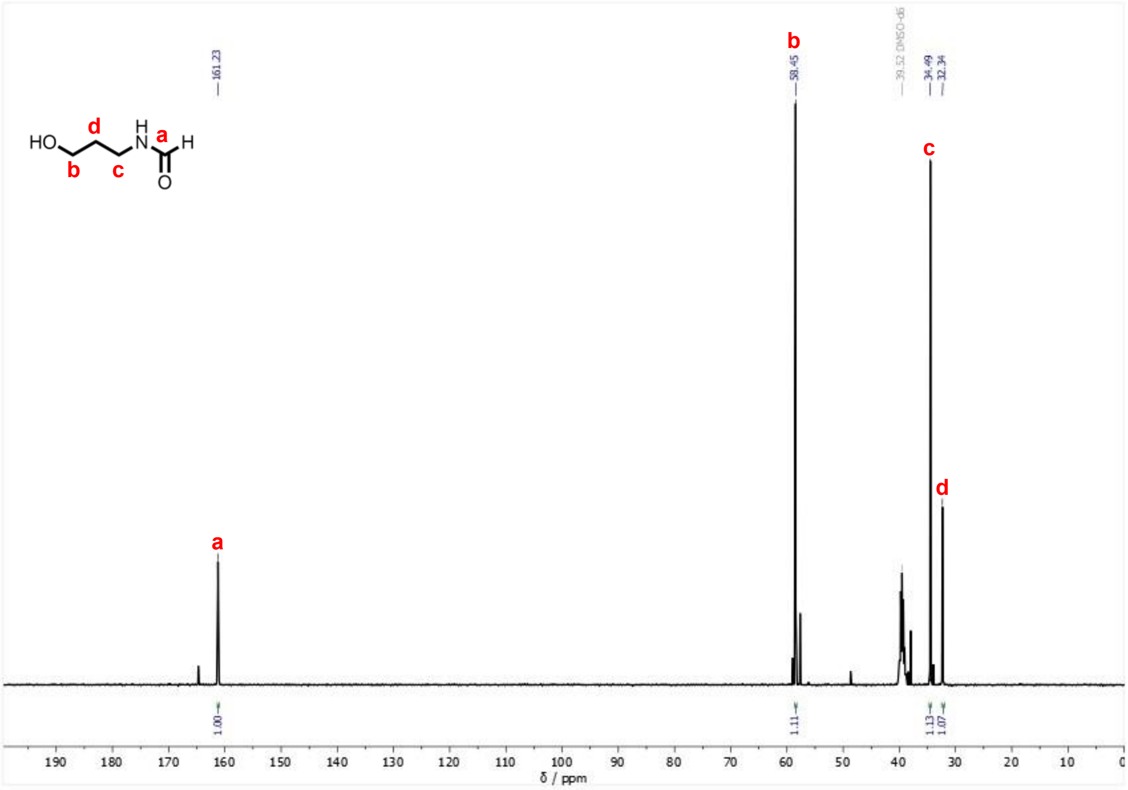

Figure S6: ^{13}C-NMR spectrum of compound **17** (DMSO-d_6, 151 MHz).

Compound **19**

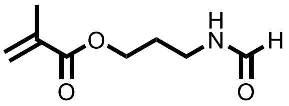

$C_8H_{13}NO_3$
171.1960 g mol^{-1}

3.80 g EDC·HCl (19.9 mmol, 1.50 equiv.) and 1.50 mL methacrylic acid (**18**) (1.39 g, 13.3 mmol, 1.00 equiv.) were dissolved in 40 mL dry DCM under argon atmosphere and stirred for 30 min at ambient temperature. 1.35 g **17** (13.3 mmol, 1.00 equiv.) and 2.43 g DMAP (19.9 mmol, 1.50 equiv.) was added, and the reaction mixture stirred for 16 h at ambient temperature. 20 mL DCM was added, and the organic phase was extracted with brine (4 x 30 mL) and water (4 x 30 mL). The organic phase was dried over Na_2SO_4 and the solvent removed under reduced pressure. Column chromatography (DCM / MeOH 10:1) delivered 426 mg product (19%, 2.50 mmol) as colourless oil.

R*f* (5% MeOH in DCM) = 0.33 – The product was stained using $KMnO_4$-solution.

^{1}H-NMR (600 MHz, DMSO-d_6): δ (ppm) = 8.05 (bs, 1H, NH), 8.01 (s, 1H, CHO), 6.03 (s, 1H, CH), 5.67 (t, J = 1.6 Hz, 1H, CH), 4.10 (t, J = 6.4 Hz, 2H, CH_2), 3.17 (q, J = 6.5 Hz, 2H, CH_2), 1.88 (s, 3H, CH_3), 1.77 (p, J = 6.6 Hz, 2H, CH_2).

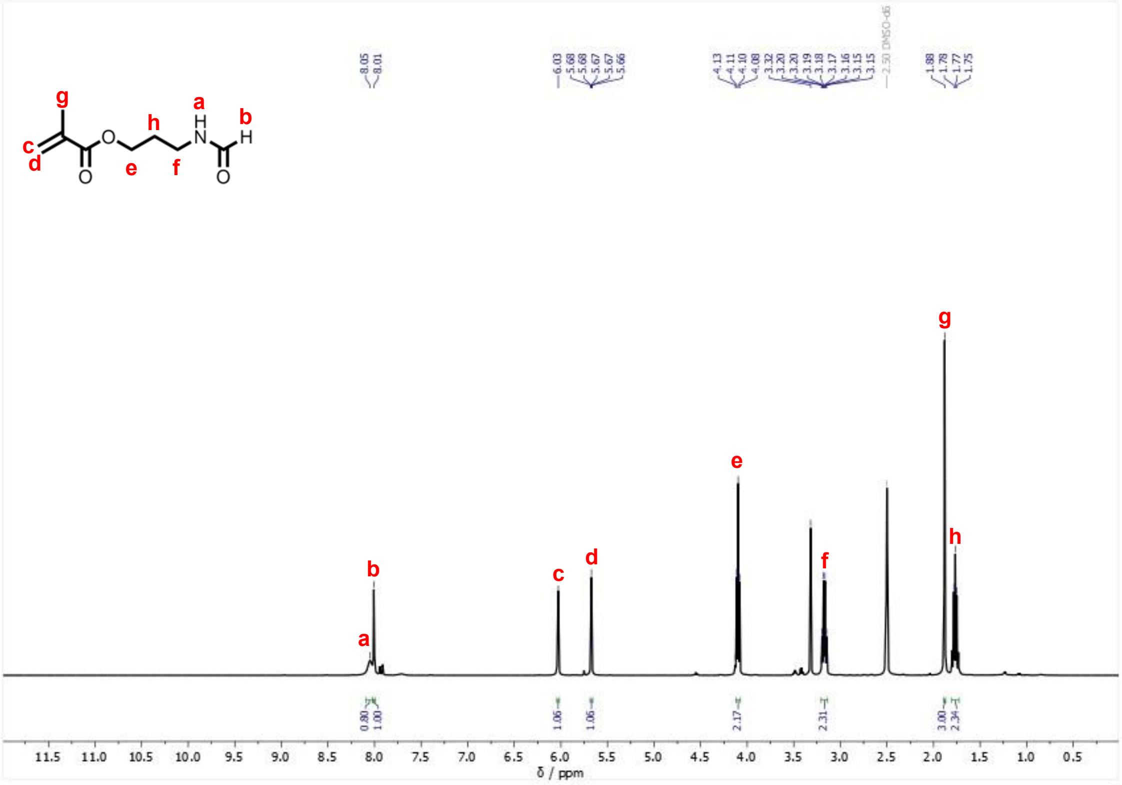

Figure S7: ^{1}H-NMR spectrum of compound **19** (DMSO-d_6, 600 MHz).

^{13}C-NMR (151 MHz, DMSO-d_6): δ (ppm) = 166.5 (s, 1C, *C*HO), 161.1 (s, 1C, *C*HO), 135.9 (s, 1C, *C*H$_2$), 125.6 (s, 1C, *C*H$_2$), 62.0 (s, 1C, *C*H$_2$), 34.0 (s, 1C, *C*H$_2$), 28.2 (s, 1C, *C*H$_2$), 17.9 (s, 1C, *C*H$_3$).

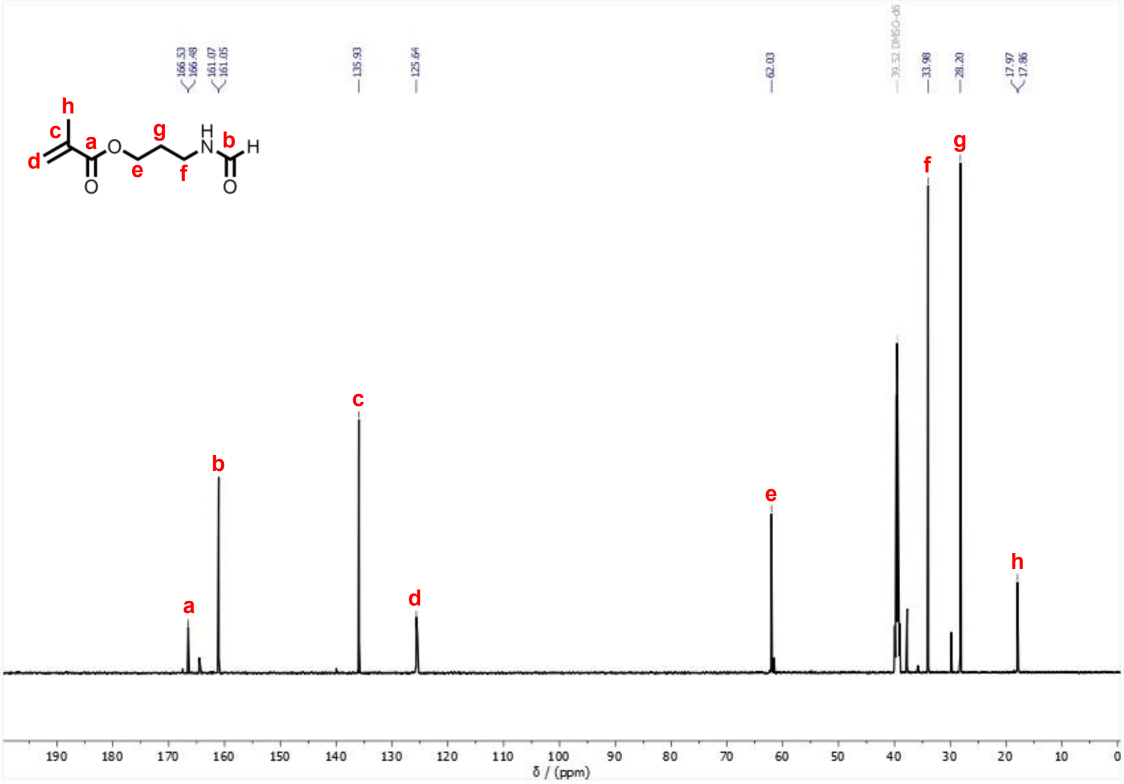

Figure S8: ^{13}C-NMR spectrum of compound **19** (DMSO-d_6, 151 MHz).

ESI-HRMS: *m/z*$_{theo}$ for [$C_8H_{14}NO_3$], [M+H]$^+$ = 172.0984, *m/z*$_{exp}$ = 172.0966.

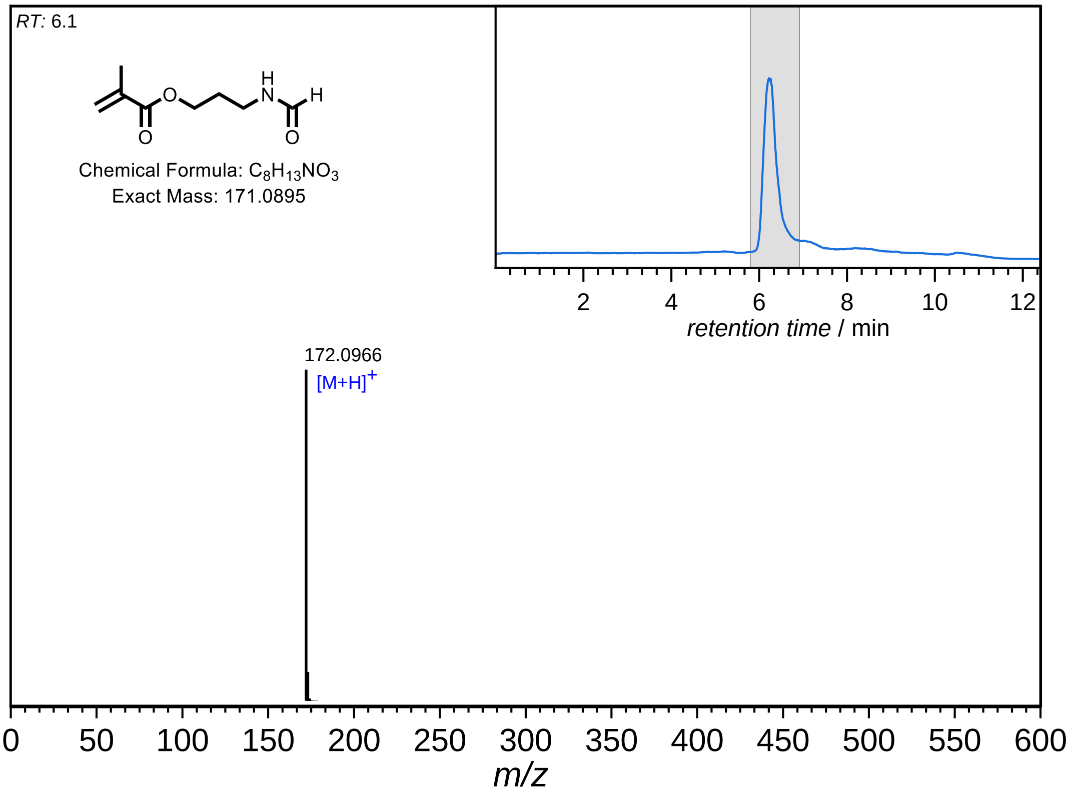

Figure S9: LC-MS analysis of compound **19**: *m/z*$_{theo}$ for [$C_8H_{14}NO_3$], [M+H]$^+$ = 172.0984, *m/z*$_{exp}$ = 172.0966.

Compound **20**

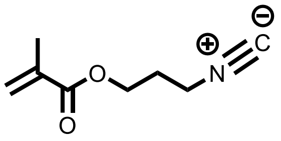

$C_8H_{11}NO_2$
153.1810 g mol^{-1}

365 mg **19** (2.13 mmol, 1.00 equiv.) was dissolved in 15 mL DCM and 515 µL pyridine (505 mg, 1.75 mmol, 3.00 equiv.) was added. Subsequently, 167 mg *p*-TsCl (876 µmol, 1.50 equiv.) was added under cooling with an ice bath. Cooling was removed and the reaction mixture stirred until full conversion (monitored via TLC, average reaction time of 2 h) was observed. Subsequently, 10 mL aqueous Na_2SO_4-solution (20 wt%) was added and the biphasic mixture stirred for another 30 min. 10 mL water and 10 mL DCM were added and the organic phase was separated. The aqueous phase was extracted with DCM (3 x 10 mL), the organic extracts were combined and washed with water (3 x 10 mL) and brine (2 x 10 mL). The organic extract was dried over Na_2SO_4, filtered and the solvent was removed under reduced pressure. The crude product was purified via column chromatography (1% MeOH in DCM) to obtain 235 mg of the isocyanide (72%, 1.53 mmol) as a pale-yellow oil with a distinct smell.

R_f (DCM) = 0.65 – The product was stained using $KMnO_4$-solution.

^{1}H-NMR (600 MHz, DMSO-d_6): δ (ppm) = 6.07 (dq, J = 1.9, 1.0 Hz, 1H, CH), 5.69 (q, J = 1.6 Hz, 1H, CH), 4.18 (t, J = 6.1 Hz, 2H, CH_2), 3.61 (ddd, J = 8.6, 5.2 Hz, 2.0 Hz, 2H, CH_2), 1.97 (ttd, J = 11.0, 6.3, 5.5 Hz, 2.4 Hz, 2H, CH_2), 1.89 (dd, J = 1.6, 1.0 Hz, 3H, CH_3).

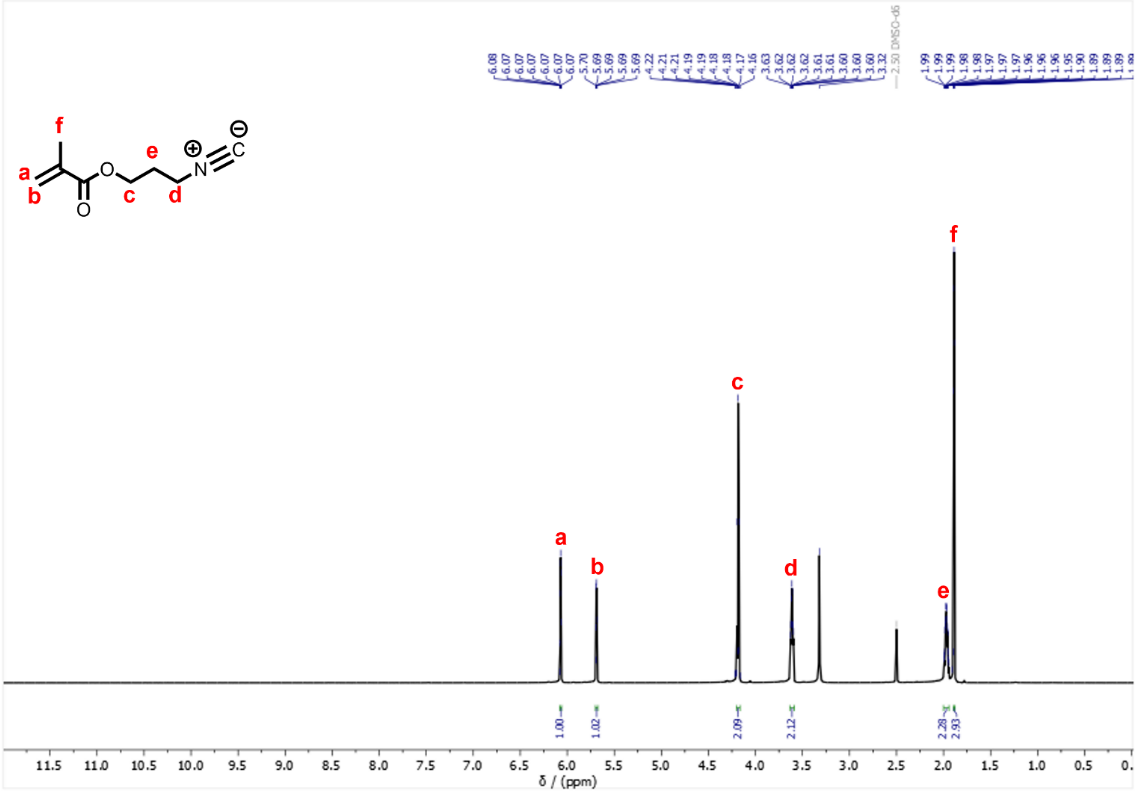

Figure S10: ^{1}H-NMR spectrum of compound **20** (DMSO-d_6, 600 MHz).

^{13}C-NMR (151 MHz, DMSO-*d*$_6$): *δ* (ppm) = 166.4 (s, 1C, *C*N), 156.1 (s, 1C, *C*HO), 135.7 (s, 1C, *C*H$_2$), 126.0 (s, 1C, *C*H$_2$), 61.2 (s, 1C, *C*H$_2$), 38.5 (s, 1C, *C*H$_2$), 27.7 (s, 1C, *C*H$_2$), 18.0 (s, 1C, *C*H$_3$).

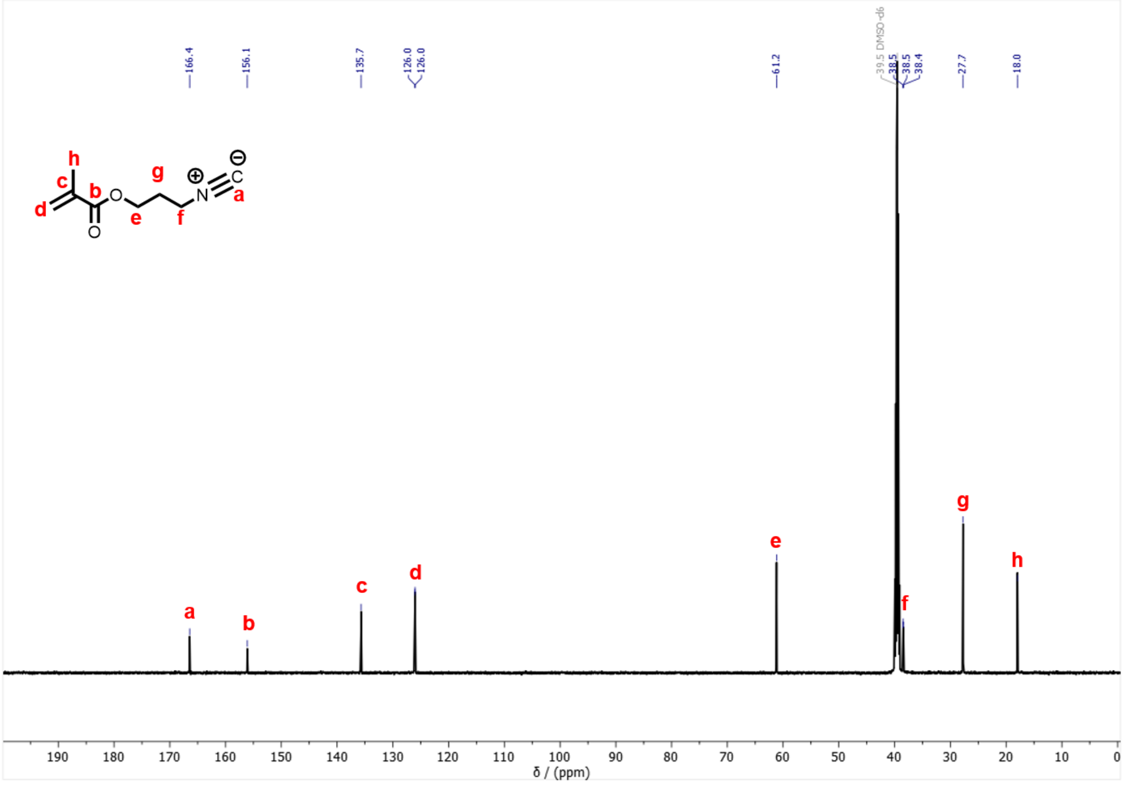

Figure S11: ^{13}C-NMR spectrum of compound **20** (DMSO-*d*$_6$, 151 MHz).

Compound **22**

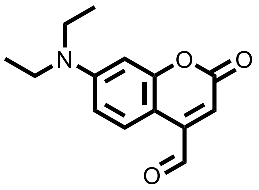

$C_{14}H_{15}NO_3$
245.2780 g mol^{-1}

2.30 g 7-diethylamine-1-methylcoumarin (**21**) (10.0 mmol, 1.00 equiv.) and 1.66 g SeO_2 (15.0 mmol, 1.50 equiv.) was dissolved in 60 mL *o*-xylene and the mixture heated at 130 °C under refluxing conditions for 5 h. The solution was filtered when hot and the filtrate was concentrated in vacuo. The crude product was purified via column chromatography on silica gel running with *n*-Hex / EtOAc (3:1) to give 1.39 g of the product (57%, 5.67 mmol) as a red solid.

$\mathbf{R}_f$ (*n*-Hex / EtOAc 3:1) = 0.42.

^{1}H-NMR (400 MHz, DMSO-d_6): δ (ppm) = 10.07 (s, 1H, C*H*O), 8.19 (d, *J* = 9.2 Hz, 1H, Ar-*H*), 7.88 (d, *J* = 9.0 Hz, 1H, Ar-*H*), 6.77-5.58 (m, 1H, Ar-*H*), 6.49 (d, *J* = 2.5 Hz, 1H, Ar-*H*), 5.92 (d, *J* = 1.4 Hz, 1H, Ar-*H*), 3.46-3.39 (m, 4H, 2x CH_2),1.12 (td, *J* = 1.2 Hz, 6H, 2x CH_3).

The spectroscopic data is in agreement with literature.[175c]

Compound **24**

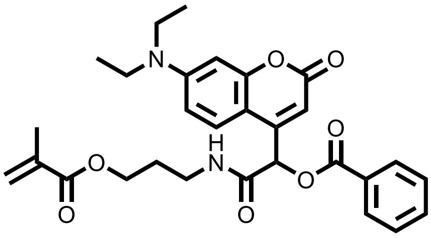

$C_{29}H_{32}N_2O_7$
520.5820 g mol^{-1}

130 mg **20** (848 µmol, 1.00 equiv.) was dissolved in 10 mL DCM. 245 mg **22** (1.02 mmol, 1.20 equiv.), 125 mg benzoic acid (**23**) (1.02 mmol, 1.20 equiv.) was added, and the reaction mixture was stirred for 16 h at ambient temperature. Subsequently, the solvent was removed under reduced pressure and the crude product purified via column chromatography (2% MeOH in DCM) to obtain 404 mg of the desired compound (92%, 777 µmol) as a yellow, fluffy solid.

R_f (2% MeOH in DCM) = 0.13.

^{1}H-NMR (600 MHz, DMSO-*d*$_6$): *δ* (ppm) = 8.55 (t, *J* = 5.8 Hz, 1H, N*H*), 8.07-8.05 (m, 2H, Ar-*H*), 7.81 (d, *J* = 9.0 Hz, 1H, Ar-*H*), 7.58 (t, *J* = 7.9 Hz, 2H, Ar-*H*), 7.50 (t, *J* = 7.8 Hz, 1H, Ar-*H*), 6.67 (dd, *J* = 9.2, 2.6 Hz, 1H, Ar-*H*), 6.55 (d, *J* = 2.5 Hz, 1H, Ar-*H*), 6.36 (s, 1H, C*H*), 6.24 (s, 1H, Ar-*H*), 5.99 (d, *J* = 1.9 Hz, 1H, C*H*), 5.63 (s, 1H, C*H*), 4.07-4.01 (m, 2H, C*H*$_2$), 3.43 (qd, *J* = 7.2, 2.4 Hz, 4H, 2x C*H*$_2$), 3.21 (q, *J* = 6.6. Hz, 2H, C*H*$_2$), 1.84 (d, *J* = 1.4 Hz, 3H, C*H*$_3$), 1.77 (p, *J* = 6.7 Hz, 2H, C*H*$_2$), 1.12 (t, *J* = 7.0 Hz, 6H, 2x C*H*$_3$).

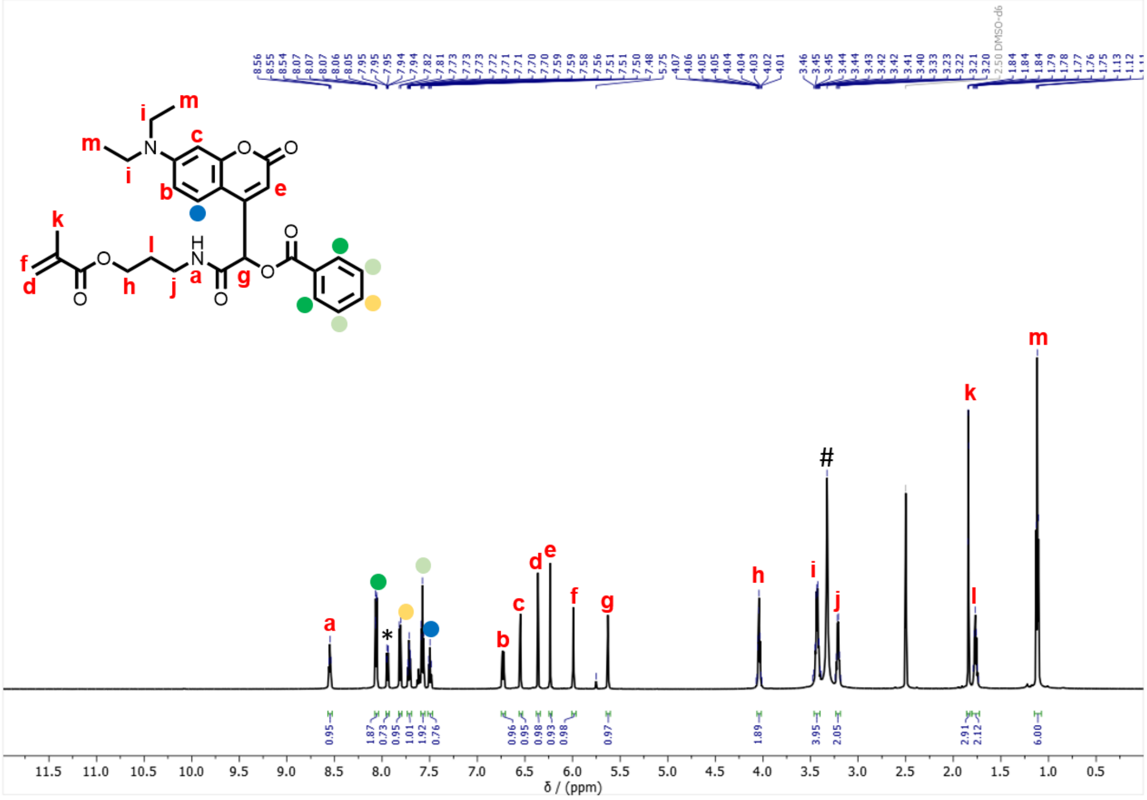

Figure S12: ^{1}H-NMR spectrum of compound **24** (DMSO-*d*$_6$, 600 MHz, *: DMF, #: water).

^{13}C-NMR (151 MHz, DMSO-*d*$_6$): *δ* (ppm) = 166.5 (s, 1C, *C*O), 165.7 (s, 1C, *C*O), 164.4 (s, 1C, *C*O), 160.6 (s, 1C, *C*O), 156.2 (s, 1C, *C*H), 150.5 (s, 1C, *C*H$_{Ar}$), 149.5 (s, 1C, *C*H$_{Ar}$), 135.8 (s, 1C, *C*H), 134.0 (s, 1C, *C*H$_{Ar}$), 129.3 (s, 2C, *C*H$_{Ar}$), 128.9 (s, 2C, *C*H$_{Ar}$), 128.5 (s, 1C, *C*H$_{Ar}$), 125.6 (s, 1C, *C*H$_2$), 108.8 (s, 1C, *C*H$_{Ar}$), 107.6 (s, 1C, *C*H$_{Ar}$), 105.3 (s, 1C, *C*H$_{Ar}$), 96.9 (s, 1C, *C*H$_{Ar}$), 72.8 (s, 1C, *C*H), 61.9 (s, 1C, *C*H$_2$), 44.0 (s, 2C, 2x *C*H$_2$), 35.8 (s, 1C, *C*H$_2$), 28.0 (s, 1C, *C*H$_2$), 18.0 (s, 1C, *C*H$_3$), 12.3 (s, 2C, 2x *C*H$_3$).

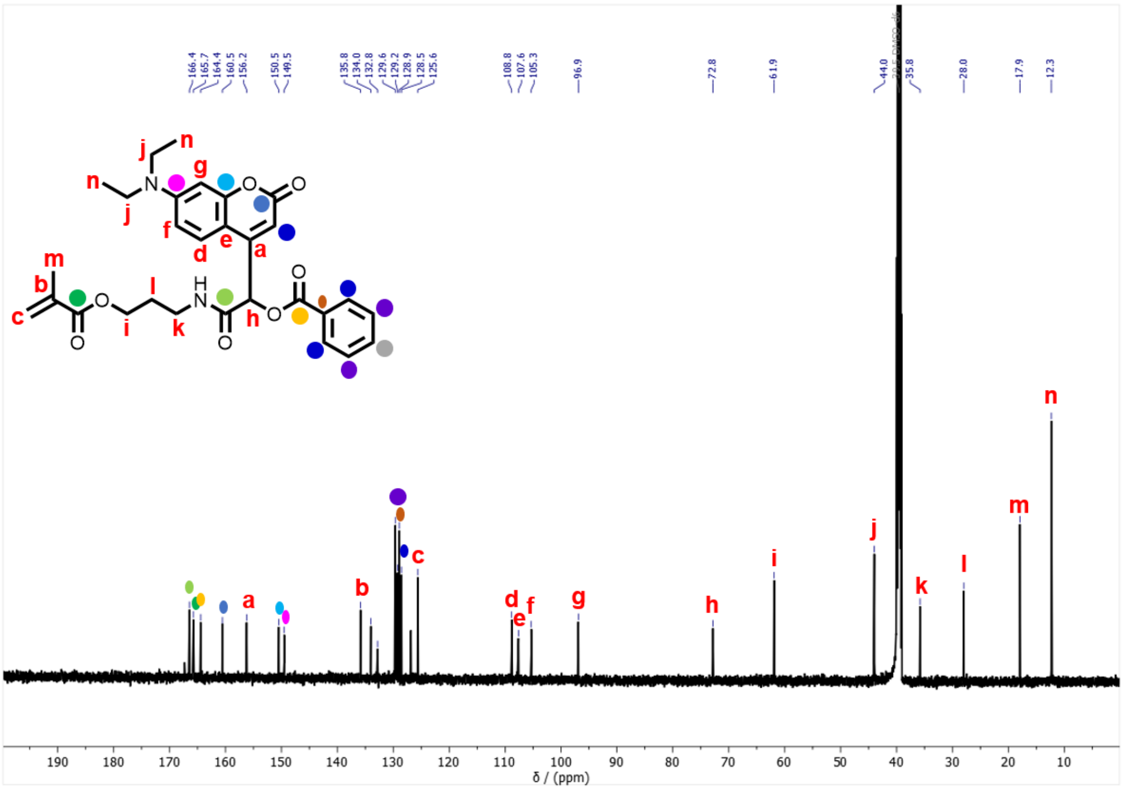

Figure S13: ^{13}C-NMR spectrum of compound **24** (DMSO-*d*$_6$, 151 MHz).

ESI-HRMS: *m/z*$_{theo}$ for [$C_{29}H_{33}N_2O_7$], [M+H]$^+$ = 521.2210, *m/z*$_{exp}$ = 521.2276.

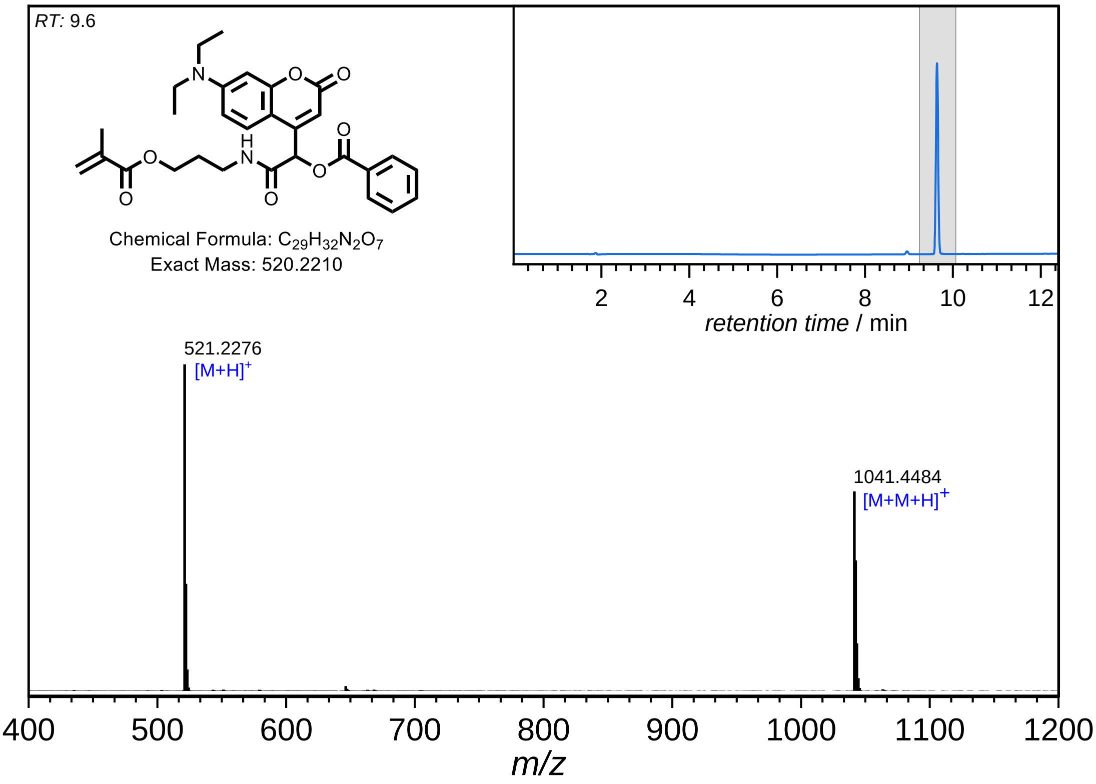

Figure S14: LC-MS analysis of compound **24:** *m/z*$_{theo}$ for [$C_{29}H_{33}N_2O_7$], [M+H]$^+$ = 521.2210, *m/z*$_{exp}$ = 521.2276.

Compound **26**

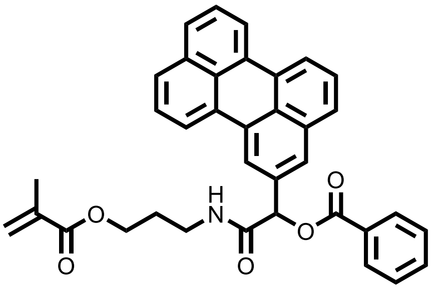

$C_{36}H_{29}NO_5$
555.6300 g mol^{-1}

196 mg perylenecarboxaldehyde (**25**) (700 µmol, 1.20 equiv.) and 85.4 mg benzoic acid (**23**) (700 µmol, 1.20 equiv.) was dissolved in 300 mL $CHCl_3$ in an amber flask. 90.0 mg **20** (583 µmol, 1.00 equiv.) was added and the reaction mixture stirred for 16 h at ambient temperature. The solvent was removed under reduced pressure and the crude product purified via two consecutive column chromatographic runs (first column: 1% MeOH in DCM, second column: 3% MeOH in DCM) to afford 9.00 mg of the desired product (16.2 mmol, 3%) as a fluffy, orange solid.

R_f (first column: 1% MeOH in DCM) = 0.23.

R_f (second column: 3% MeOH in DCM) = 0.75.

^{1}**H-NMR** (600 MHz, DMSO-d_6): δ (ppm) = 8.51 (t, J = 5.8 Hz, 1H, NH), 8.44-8.40 (m, 4H, 4x Perylene-H), 8.18-8.16 (m, 1H, 1x Perylene-H), 8.05-8.03 (m, 2H, 2x Ar-H), 7.80 (t, J = 7.5 Hz, 2H, 2x Ar-H), 7.75 (d, J = 7.9 Hz, 1H, 1x Ar-H), 7.68 (ddt, J = 7.7, 7.1, 1.3 Hz, 1H, 1x Perylene-H), 7.64 (dd, J = 8.5, 7.5 Hz, 1H, 1x Perylene-H), 7.59-7.53 (m, 4H, 4x Perylene-H), 6.74 (s, 1H, CH), 6.00 (dq, J = 2.0, 1.0 Hz, 1H, CH), 5.63 (p, J = 1.6 Hz, 1H, CH), 4.06 (t, J = 6.4 Hz, 2H, CH_2), 3.28-3.22 (m, 2H, CH_2), 1.84 (dd, J = 1.6, 1.0 Hz, 3H, CH_3), 1.79 (p, J = 6.7 Hz, 2H, CH_2).

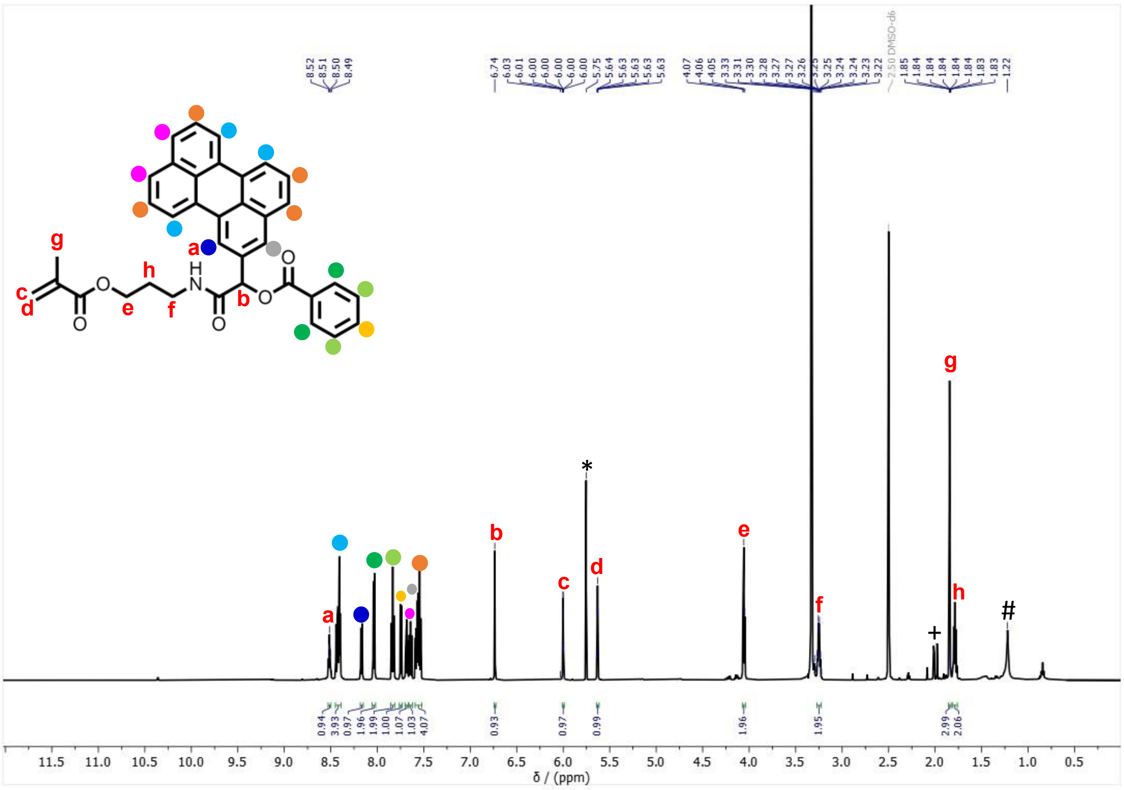

Figure S15: ^{1}H-NMR spectrum of compound **26** (DMSO-d_6, 600 MHz, *: DCM, +: acetone, #: silicon grease).

^{13}C-NMR (151 MHz, CDCl$_3$): *δ* (ppm) = 168.7 (s, 1C, *C*HO), 167.8 (s, 1C, *C*HO), 165.5 (s, 1C, *C*HO), 136.2 (s, 1C, *C*H), 134.7 (s, 1C, *C*H), 133.7 (s, 2C, Perylene-*C*H), 133.1 (s, 1C, Perylene-*C*), 132.9 (s, 1C, Perylene-*C*), 132.0 (s, 1C, Perylene-*C*), 131.0 (s, 1C, Benzoic Acid-*C*H), 130.2 (s, 2C, 2x Benzoic Acid-*C*H), 129.4 (s, 2C, 2x Benzoic Acid-*C*H), 128.7 (s, 4C, 3x Perylene-*C*, 1x *C*H$_2$), 128.2 (s, 1C, Perylene-*C*H), 126.8 (s, 1C, Perylene-*C*H), 123.8 (s, 1C, Perylene-*C*), 120.7 (s, 1C, Perylene-*C*), 119.8 (s, 1C, Perylene-*C*), 74.4 (s, 1C, *C*H), 61.9 (s, 1C, *C*H$_2$), 36.4 (s, 1C, *C*H$_2$), 28.9 (s, 1C, *C*H$_2$), 18.4 (s, 1C, *C*H$_3$).

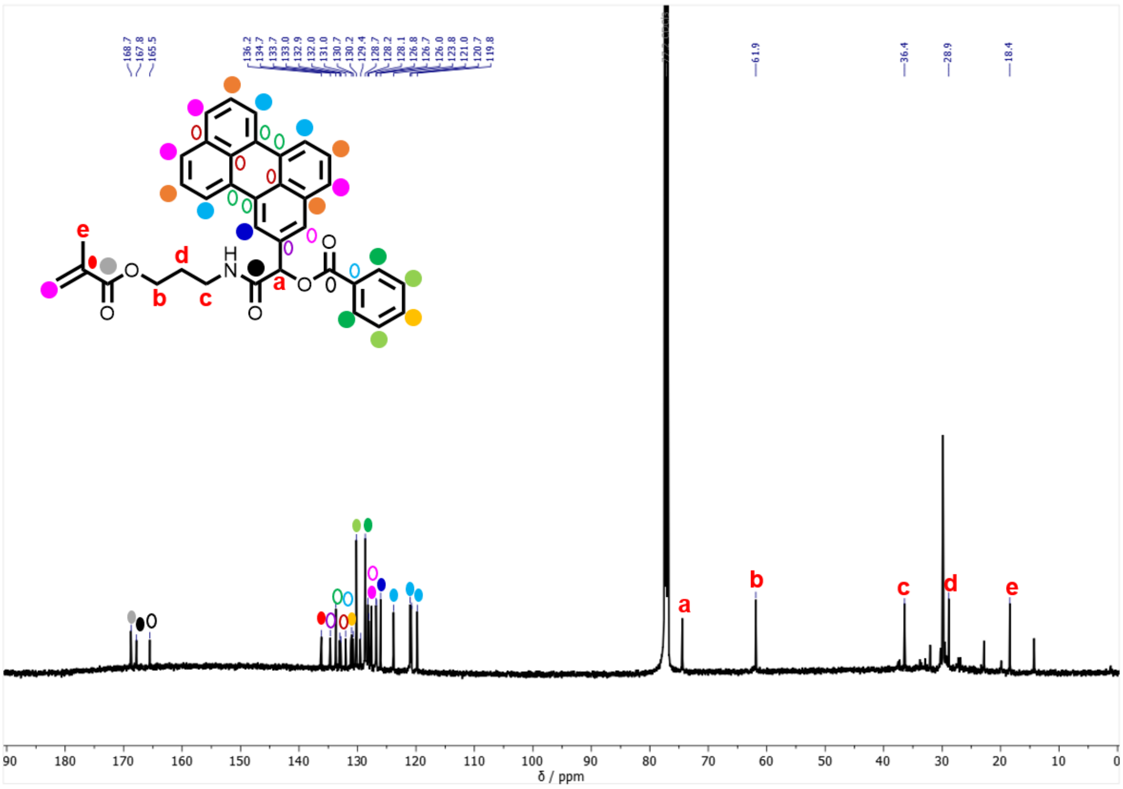

Figure S16: ^{13}C-NMR spectrum of compound **26** (CDCl$_3$, 151 MHz).

ESI-HRMS: m/z_{theo} for [$C_{72}H_{62}N_3O_{10}$], [$2M+NH_4]^+$ = 1128.4483, m/z_{exp} = 1128.4430.

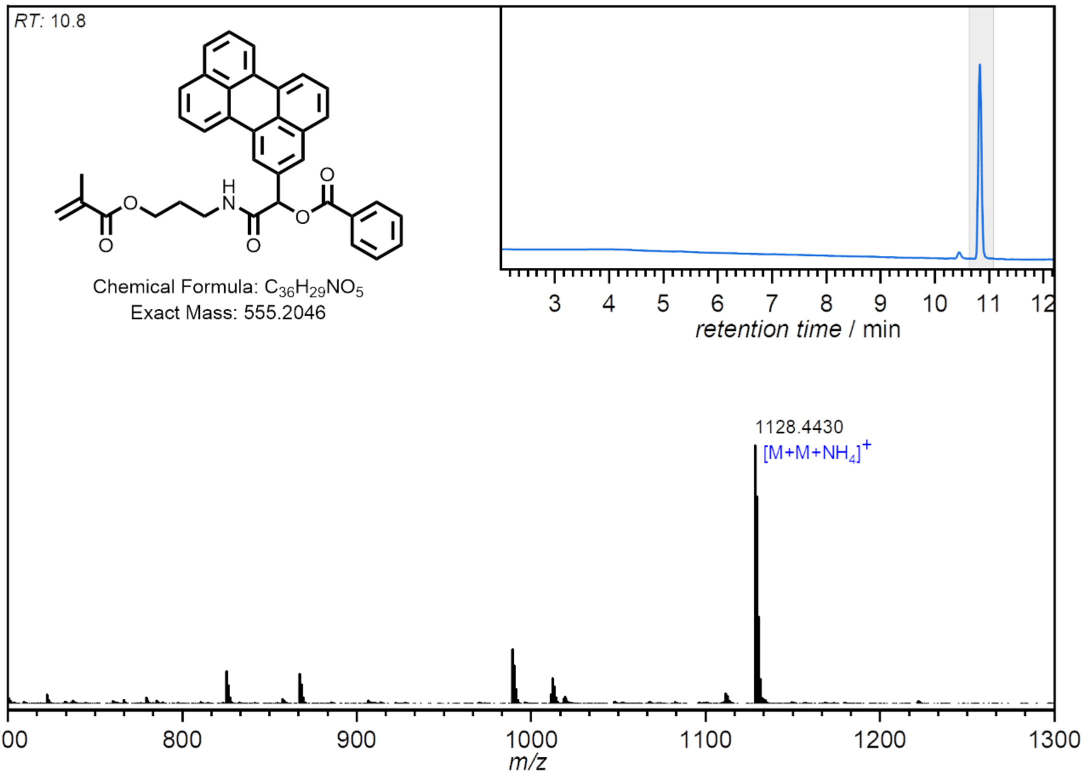

Figure S17: LC-MS analysis of compound **26**: m/z_{theo} for [$C_{72}H_{62}N_3O_{10}$], [$2M+NH_4]^+$ = 1128.4483, m/z_{exp} = 1128.4430.

Compound **28**

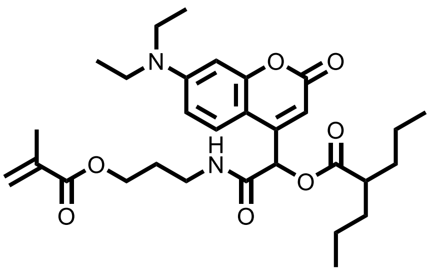

$C_{30}H_{42}N_2O_7$
542.6730 g mol^{-1}

90 µL valproic acid (**27**) (81.4 mg, 564 µmol, 1.10 equiv.) and 153 mg **22** (624 µmol, 1.20 equiv.) was dissolved in 20 mL DCM in an amber flask. 78.9 mg of **20** (515 µmol, 1.00 equiv.) was added and the reaction mixture stirred for 16 h at ambient temperature. Subsequently, the reaction mixture was washed with water (2 x 10 mL), saturated NaHCO3 solution (3 x 10 mL) and water (3 x 10 mL), followed by removal of the solvent under reduced pressure. The crude product was purified twice via column chromatography (first column: 1% MeOH in DCM, second column: 2% MeOH in DCM) to obtain 61.5 mg of the desired compound (113 µmol, 22%) as a highly viscose, yellow oil.

R_f (first column: 1% MeOH in DCM) = 0.19 – The product was stained using $KMnO_4$- solution.

R_f (second column: 2% MeOH in DCM) = 0.18 – The product was stained using $KMnO_4$-solution.

^{1}H-NMR (400 MHz, DMSO-d_6): δ (ppm) = 8.41 (t, J = 5.7 Hz, 1H, NH), 7.70 (d, J = 9.2 Hz, 1H, Ar-H), 6.68 (dd, J = 9.2, 2.6 Hz, 1H, Ar-H), 6.53 (d, J = 5.53 Hz, 1H, Ar-H), 6.11 (d, J = 10.3 Hz, 2H, CH_2), 6.00 (dd, J = 1.9, 1.0 Hz, 1H, Ar-H), 5.64 (p, J = 1.7 Hz, 1H, Ar-H), 4.02 (t, J = 6.4 Hz, 2H, CH_2), 3.43 (q, J = 7.0 Hz, 4H, 2x CH_2), 3.18 (q, J = 6.5 Hz, 2H, CH_2), 2.54 (s, 1H), 1.85 (t, J = 1.3 Hz, 3H, CH_3), 1.74 (p, J = 6.6. Hz, 2H, CH_2), 1.62-1.49 (m, 2H, CH_2), 1.43 (dddd, J = 12.9, 10.8, 6.2, 3.3 Hz, 2H, CH_2), 1.34-1.21 (m, 4H, 2x CH_2), 1.11 (t, J = 7.0 Hz, 6H, 2x CH_3), 0.83 (dt, J = 15.8, 7.3 Hz, 6H, 2x CH_3).

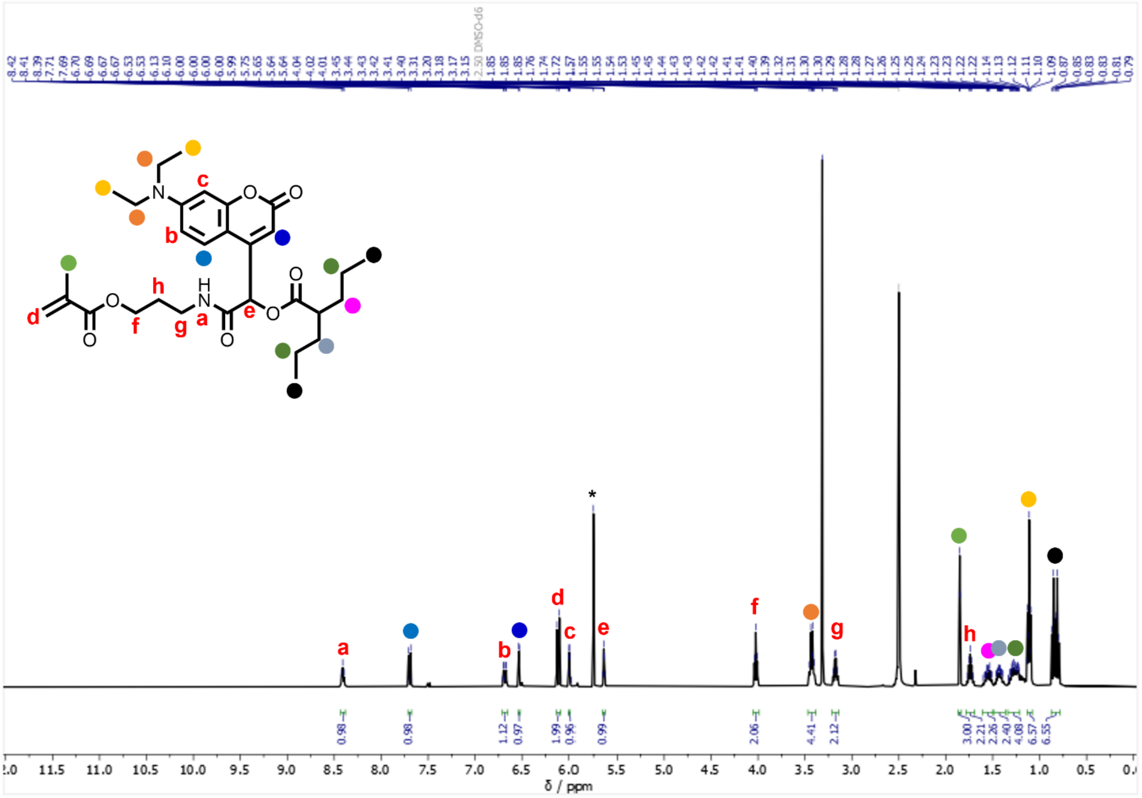

Figure S18: ^{1}H-NMR spectrum of compound **28** (DMSO-d_6, 400 MHz, *: DCM).

^{13}C-NMR (101 MHz, CDCl$_3$): *δ* (ppm) = 174.4 (s, 1C, *C*HO), 167.8 (s, 1C, *C*HO), 166.5 (s, 1C, *C*HO), 162.0 (s, 1C, *C*HO), 151.0 (s, 1C, *C*H), 150.20 (s, 1C, *C*H), 136.1 (s, 1C, *C*H), 126.8 (d, 1C, Coumarin-*C*H), 126.1 (s, 1C, Coumarin-*C*H), 109.0 (s, 1C, Coumarin-*C*), 106.7 (s, 1C, Coumarin-*C*H), 106.3 (s, 1C, Coumarin-*C*H), 97.7 (s, 1C, *C*H), 71.1 (s, 1C, *C*H$_2$), 61.6 (s, 1C, *C*H$_2$), 45.2 (s, 2C, 2x *C*H$_2$), 36.2 (s, 1C, *C*H), 34.4 (s, 2C, 2x C*H*$_2$), 28.8 (s, 1C, *C*H$_2$), 20.7 (s, 1C, *C*H$_2$), 20.6 (s, 1C, *C*H$_3$), 18.4 (s, 1C, *C*H$_3$), 14.0 (s, 2C, 2x *C*H$_3$), 12.6 (s, 2C, 2x *C*H$_3$).

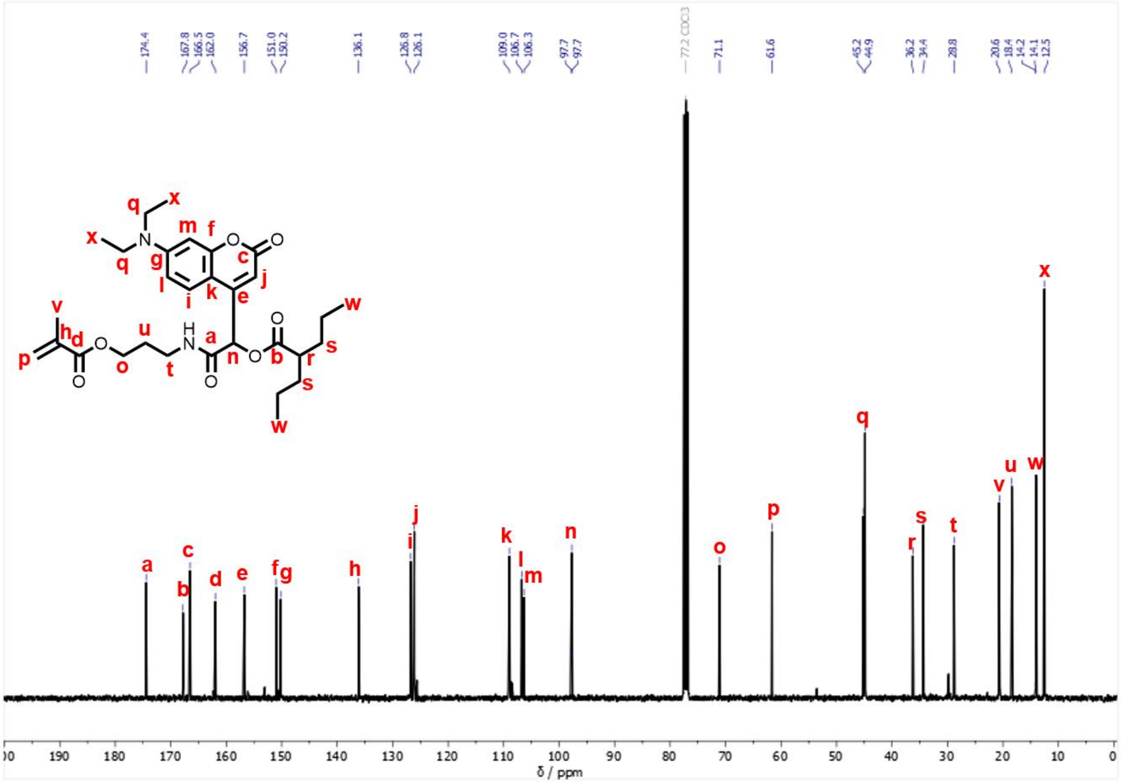

Figure S19: ^{13}C-NMR spectrum of compound **28** (CDCl$_3$, 101 MHz).

ESI-HRMS: *m/z*$_{\text{theo}}$ for [$C_{30}H_{43}N_2O_{10}$], $[M+H]^+$ = 543.3065, *m/z*$_{\text{exp}}$ = 543.3050.

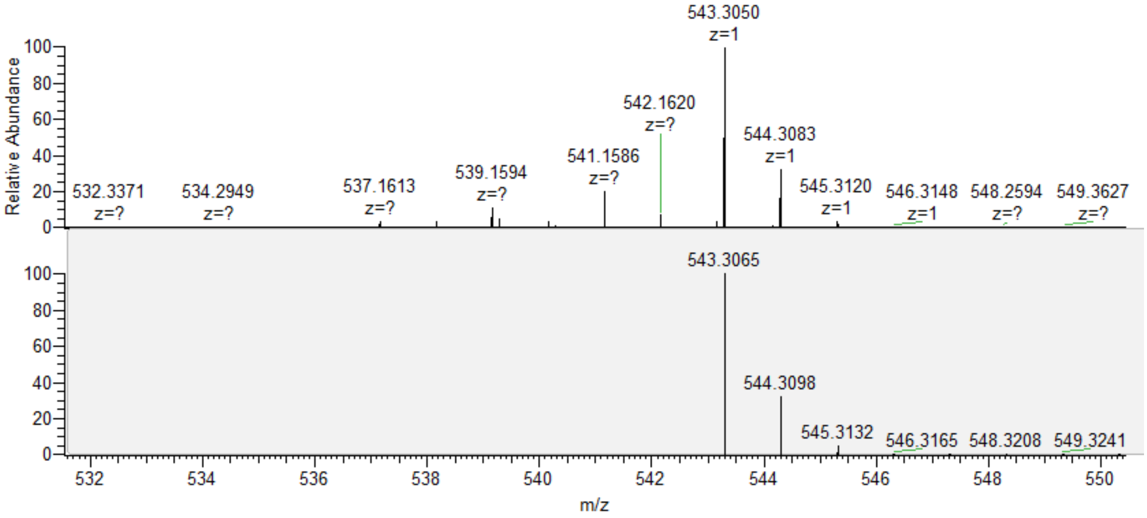

Figure S20: ESI-HRMS analysis of compound **28**: *m/z*$_{\text{theo}}$ for [$C_{30}H_{43}N_2O_{10}$], $[M+H]^+$ = 543.3065, *m/z*$_{\text{exp}}$ = 543.3050.

5.5 Kinetic and Action Plot Measurements

5.5.1 Coumarin-Modified Compound 24

The determination of the irradiation conditions was performed as described previously by our group.[102] Prior to the recording of an action plot, a kinetic analysis of the **24** at the absorbance maximum (λ_{max} = 388 nm) of the chromophore was performed. Specifically, the coumarin derivative **24** was dissolved in MeCN at a concentration of 80 µg mL^{-1} (147 µM). The stock solution was prepared and bubbled with N_2 gas for 15 min, then 300 µL were withdrawn and added to capped laser vials (Supelco Vials, *Merck*) that had previously been flushed with N_2 for 5 min. Sample solutions were freshly prepared every day and not kept overnight. For the kinetic analysis of **24**, 8 identical samples were irradiated for various time intervals with an identical photon flux, using the in section 5.2.2 described Coherent *Opolette* tuneable laser system (QUT). To determine the conversion of the starting material into the photodegradation product, UV/Vis spectroscopy was used. After irradiation, each sample was diluted with 800 µL MeCN followed by recording of the absorbance spectra.

First, the molar extinction coefficients of both the starting material (Figure S21 left) and the photodegradation product (Figure S21 right) – isolated by preparative thin layer chromatography – were determined by obtaining the average (Figure S22) of a dilution series using the *Beer Lambert*'s law.

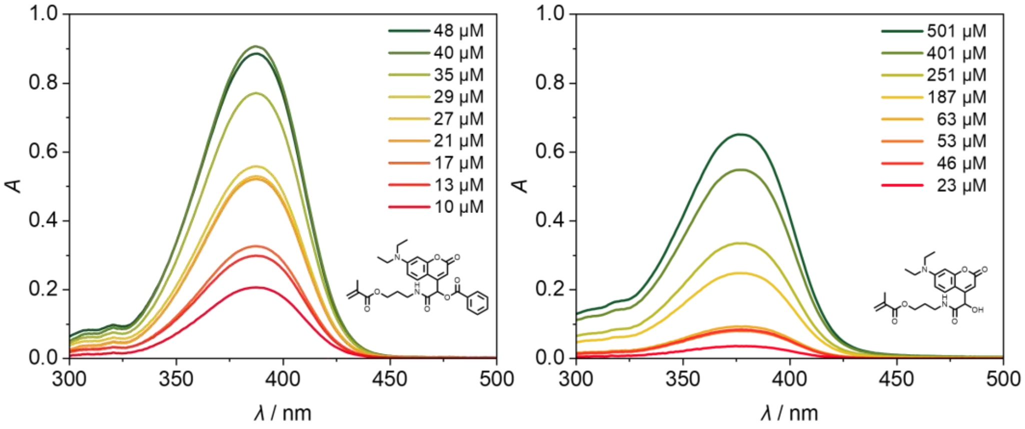

Figure S21: Extinction coefficient spectra of the starting material **24** (left) and of the photodegradation product (right).

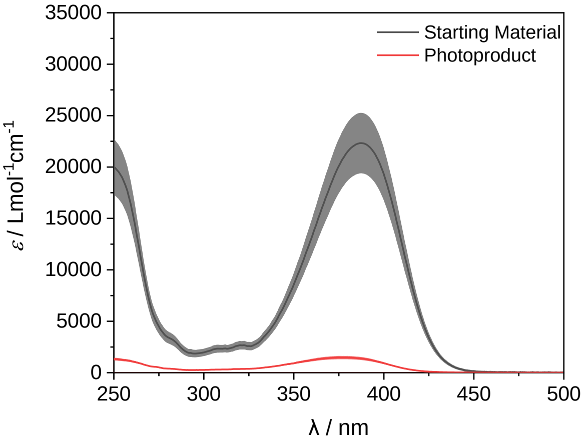

Figure S22: Molar extinction coefficient spectra for both the starting material and the photoproduct. Solid lines show the average calculated from a serial dilution, with the shaded area showing the error.

Given that the measured absorbance A, spectrum at a given time t, in the reaction of the starting material (SM) to the photoproduct (PP) can be deconvoluted in the equation:

$$A(t) = A_{\mathrm{SM}}(t) + A_{\mathrm{PP}}(t)$$

and that the absorbance A is given by:

$$A = \varepsilon c l$$

where ε is molar extinction coefficient, c is the concentration of the solution, and l is the path length of the solution, which is 1 cm in all of the experiments, the following equation was derived:

$$A(t) = c_{\mathrm{SM}}\varepsilon_{\mathrm{SM}} + c_{\mathrm{PP}}\varepsilon_{\mathrm{PP}}$$

Thus, the concentration of each of the species present at time *t* can be calculated by fitting the measured spectrum to a linear combination of the two measured extinction coefficients. Due to the significant blue shift observed upon formation of the photoproduct in this region as well as the large difference in molar extinction coefficient between SM and PP, the wavelength region between 300-500 nm was selected to improve the reliability of the fit.

A solver tool using Microsoft Excel was developed, of which a screenshot is shown in Figure S23 taking the molar extinction coefficient at each wavelength for the SM and PP (column B and C respectively), and combining them using cells C2 and C3 as scaling variables to afford the fit (column F). The error between the fit and the measured absorbance is subsequently assessed for each wavelength by taking the absolute value of the difference between the measured absorbance and the fit (column G), which is then summated in cell F2.

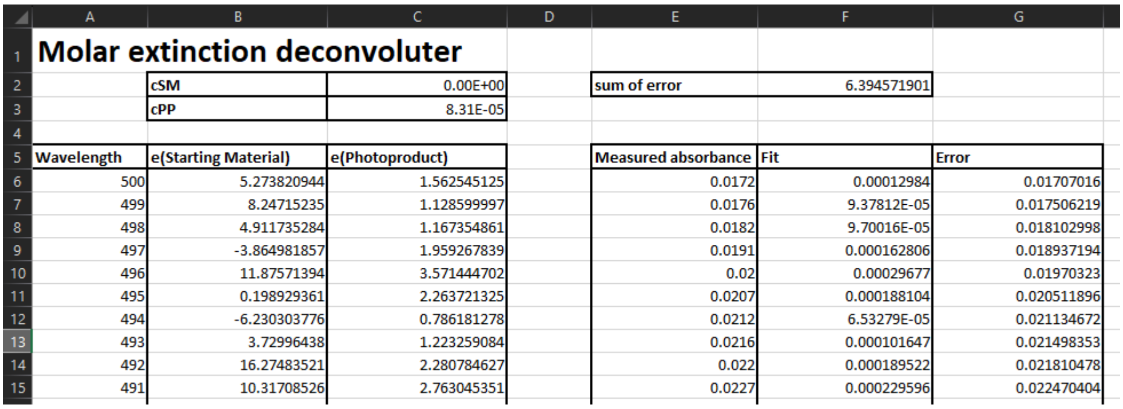

	A	B	C	D	E	F	G
1	**Molar extinction deconvoluter**						
2		cSM	0.00E+00		sum of error	6.394571901	
3		cPP	8.31E-05				
4							
5	Wavelength	e(Starting Material)	e(Photoproduct)		Measured absorbance	Fit	Error
6	500	5.273820944	1.562545125		0.0172	0.00012984	0.01707016
7	499	8.24715235	1.128599997		0.0176	9.37812E-05	0.017506219
8	498	4.911735284	1.167354861		0.0182	9.70016E-05	0.018102998
9	497	-3.864981857	1.959267839		0.0191	0.000162806	0.018937194
10	496	11.87571394	3.571444702		0.02	0.00029677	0.01970323
11	495	0.198929361	2.263721325		0.0207	0.000188104	0.020511896
12	494	-6.230303776	0.786181278		0.0212	6.53279E-05	0.021134672
13	493	3.72996438	1.223259084		0.0216	0.000101647	0.021498353
14	492	16.27483521	2.280784627		0.022	0.000189522	0.021810478
15	491	10.31708526	2.763045351		0.0227	0.000229596	0.022470404

Figure S23: Screenshot from the excel sheet used to deconvolte the absorption spectra after irradiation.

The data is fitted using a Generalised Reduced Gradient (GRG) non-linear algorithm with a convergence value of 0.0001 using the excel solver add-on. The cell F2 is set to be minimised by changing the values in C2 and C3 (concentration of SM and PP), which were each set at $10 \cdot 10^{-6}$ mol dm^{-3} as a starting point. Once optimised, the concentrations can be extracted, and the conversion of starting material into photoproduct is given by the following equation,

$$\mathit{conversion} \,/\, \% = 100 - \frac{100 \cdot c_{\mathrm{SM}}}{c_{\mathrm{SM}} + c_{\mathrm{SM}}}$$

which is then directly plotted in the reaction kinetics and later action plot.

The kinetic experiments revealed that for each indicated wavelength, 0.69 µmol of photons should be deposited in the reaction system (refer to section 4.3.1). For action plot measurements, compound **24** was dissolved in MeCN at a concentration of 80 µg mL^{-1} (147 µM). After preparation of the stock solution, it was bubbled with N_2 for 15 min prior to withdrawal of 300 µL into capped laser vials (Supelco Vials, Merck) that had previously been flushed with N_2 for 5 min. Sample solutions were freshly prepared every day and not kept overnight. For each indicated wavelength, three samples à 300 µL were irradiated with the in section 5.2.2 described Coherent *Opolette* tuneable laser system (QUT), followed by dilution in 800 µL MeCN and analysis via UV/Vis spectroscopy to calculate the consumption of the starting material (Table S1) via the previous introduced solver function in excel.

Table S1: Detailed specifications of the laser parameters and the calculations for the action plot of coumarin-modified compound **24**.

	λ / nm	***E* / µJ**	**t_{irr} / s**	**Consumption of SM / %**	**Error / %**
1	310	148	130	9.79	
2	310	147	132	9.86	
3	310	148	131	9.54	0.446
4	325	212	77	15.2	
5	325	210	78	15.7	
6	325	208	78	15.9	0.540
7	340	220	67	23.1	
8	340	219	67	23.9	
9	340	228	64	23.6	0.773
10	355	176	77	25.6	
11	355	183	75	25.6	
12	355	179	76	25.7	0.0521
13	370	227	63	24.8	
14	370	64	64	25.0	
15	370	64	64	24.0	0.694
16	385	194	76	21.0	
17	385	191	80	21.1	

	λ / nm	***E* / µJ**	**t_{irr} / s**	**Consumption of SM / %**	**Error / %**
18	385	191	80	20.9	0.908
19	400	154	56	29.9	
20	400	146	58	29.5	
21	400	146	57	29.2	0.589
22	415	365	31	22.7	
23	415	343	33	22.8	
24	415	341	33	22.9	0.335
25	430	363	30	6.00	
26	430	334	32	6.25	
27	430	336	32	5.99	0.496
28	445	380	28	0	-
29	445	384	28	0	-
30	445	377	28	0	-
31	460	434	23	0	-
32	460	430	23	0	-
33	460	427	24	0	-
34	475	368	27	0	-
35	475	355	28	0	-
36	475	354	28	0	-
37	490	423	22	0	-
38	490	412	23	0	-
39	490	405	23	0	-
40	505	410	22	0	-
41	505	422	22	0	-
42	505	427	22	0	-
43	520	415	22	0	-
44	520	417	21	0	-
45	520	420	21	0	-

5.5.2 Perylene-Modified Compound 26

The kinetic analysis of the perylene-modified compound **26** was likewise performed at the absorbance maximum (λ_{max} = 440 nm) prior to the recording of the action plot. **26** was dissolved in MeCN at concentration of 40 µg mL^{-1} (72 µM). The stock solution was prepared and bubbled with Ar for 15 min, then 300 µL were withdrawn and added to capped laser vials (Clear Glass Vials, *ThermoFisher*) that had previously been flushed with N_2 for 5 min. Sample solutions were freshly prepared every day and not kept overnight. For the kinetic measurements, 7 identical samples were irradiated for various time intervals with an identical photon flux, using the in section 5.2.2 described Coherent *Innolas* tuneable laser system (KIT). To determine the consumption of the starting material, LC-MS analysis was used. After irradiation of each sample for the respective time, they were filtered and 50 µL withdrawn into an LC-MS vial. Prior to analysis, 50 µL of benzene (c = 1 mg mL^{-1} in MeCN) was added as internal standard to determine the reaction kinetics via comparison of the ratio of the peak integrals of the starting material and the internal standard.

The kinetic experiments revealed that for each indicated wavelength, 7.09 µmol of photons should be deposited in the reaction system (refer to section 4.3.2). For action plot measurements, compound **26** was dissolved in MeCN with the total concentration being 40 µg mL^{-1} (72 µM). Sample solutions were freshly prepared every day and not kept overnight. The stock solution was prepared and bubbled with N_2 for 15 min, then 300 µL were withdrawn and added to capped laser vials (Clear Glass Vials, *ThermoFisher*) that had previously been flushed with N_2 for 5 min. For each indicated wavelength, three samples à 300 µL were irradiated with the in section 5.2.2 described Coherent *Innolas* tuneable laser system (KIT), followed by filtration. 50 µL of the irradiation sample were mixed with 50 µL benzene (c = 1 mg mL^{-1} in MeCN) and analysed via LC-MS to calculate the consumption of the starting material (Table S2).

Table S2: Detailed specifications of the laser parameters and the calculations for the action plot of perylene-modified compound **26**.

	λ / nm	**E / µJ**	**t_{irr} / min**	**Consumption of SM / %**	**Error / %**
1	310	853	04:02 s	20.5	
2	310	797	04:19 s	19.4	
3	310	815	04:13 s	21.6	1.096
4	325	870	03:20 s	17.4	
5	325	914	03:10 s	18.9	
6	325	898	03:13 s	19.6	1.259
7	340	846	03:04 s	29.8	
8	340	846	03:04 s	28.7	
9	340	800	03:15 s	30.7	0.839
10	355	1000	02:25 s	31.8	
11	355	1000	02:25 s	30.7	
12	355	984	02:27 s	32.1	0.904
13	370	858	02:39 s	35.5	
14	370	867	02:38 s	34.9	
15	370	883	02:35 s	36.3	0.572
16	385	600	03:37 s	32.7	
17	385	687	03:10 s	31.3	
18	385	717	03:02 s	34.2	1.173
19	400	550	03:47 s	34.9	
20	400	611	03:24 s	30.8	
21	400	592	03:31 s	39.9	3.767
22	415	1100	01:49 s	26.6	
23	415	1020	01:59 s	27.7	
24	415	1090	01:50 s	29.5	1.576
25	430	1080	01:47 s	24.7	
26	430	1120	01:43 s	23.9	
27	430	1120	01:43 s	25.5	0.802

	λ / nm	***E* / µJ**	**t_{irr} / min**	**Consumption of SM / %**	**Error / %**
28	445	1180	01:35 s	16.3	
29	445	1220	01:32 s	18.4	
30	445	1190	01:34 s	14.2	2.095
31	460	1010	01:47 s	10.02	
32	460	1070	01:41 s	9.37	
33	460	1140	01:35 s	11.2	0.698
34	475	1110	01:34 s	4.08	
35	475	1140	01:32 s	6.19	
36	475	1130	01:32 s	7.21	0.886
37	490	1140	01:29 s	3.33	
38	490	1130	01:30 s	4.09	38
39	490	1090	01:33 s	3.98	0.371
40	505	992	01:39 s	1.06	
41	505	995	01:39 s	1.89	
42	505	991	01:39 s	2.09	0.151
43	520	1010	01:34 s	1.94	
44	520	1050	01:31 s	3.02	
45	520	1070	01:29 s	1.70	1.83
46	535	1080	01:26 s	2.85	
47	535	1100	01:24 s	2.55	
48	535	1070	01:26 s	4.37	1.59
49	550	1070	01:24 s	2.55	
50	550	1080	01:23 s	2.22	
51	550	1070	01:24 s	2.96	0.331
52	565	1050	01:24 s	2.50	
53	565	1090	01:21 s	1.98	
54	565	1020	01:26 s	0.894	0.411
55	580	1020	01:24 s	1.37	
56	580	1040	01:23 s	0.756	

	λ / nm	***E* / µJ**	**t_{irr} / min**	**Consumption of SM / %**	**Error / %**
57	580	1020	01:24 s	2.66	1.02
58	595	996	01:28 s	1.13	
59	595	993	01:28 s	2.06	
60	595	996	01:28 s	0.896	0.924

5.5.3 Coumarin-Modified Compound 28

Similar to compounds **24** and **26**, the kinetic analysis of compound **28** at the absorbance maximum (λ_{max} = 384 nm) was performed prior to the recording of the action plot. **28** was dissolved in MeCN with the total concentration being 80 µg mL^{-1} (150 µM). The stock solution was prepared and bubbled with N_2 for 15 min, then 300 µL were withdrawn and added to capped laser vials (Supelco Vials, *Merck*) that had previously been flushed with N_2 for 5 min. Sample solutions were freshly prepared every day and not kept overnight. For the kinetic measurements, 12 identical samples were irradiated for various time intervals with an identical photon flux, using the in section 5.2.2 described Coherent *Innolas* tuneable laser system (KIT). To determine the consumption of the starting material, LC-MS analysis was employed. After irradiation of each sample for the respective time, they were filtered and 50 µL withdrawn into an LC-MS vial. Prior to analysis, 50 µL benzene (c = 1 mg mL^{-1} in MeCN) was added as internal standard to determine the reaction kinetics via comparison of the ratio of the peak integrals of the starting material and the internal standard.

The kinetic experiments determined that for each indicated wavelength, 1.93 µmol of photons should be deposited in the reaction system (refer to section 7.2). For the action plot measurements, compound **28** was dissolved in MeCN with the total concentration being 80 µg mL^{-1} (150 µM). The stock solution was prepared and bubbled with N_2 for 15 min, then 300 µL were withdrawn and added to capped laser vials (Supelco Vials, *Merck*) that had previously been flushed with N_2 for 5 min. Sample solutions were freshly prepared every day and not kept overnight. For each indicated wavelength, three samples à 300 µL were irradiated, followed by filtration. 50 µL of the irradiation sample were mixed with 50 µL benzene (c = 1 mg mL^{-1} in MeCN) and analysed via LC-MS to calculate the consumption of the starting material (Table S3).

Table S3: Detailed specifications of the laser parameters and the calculations for the action plot of coumarin-modified compound **28**.

	λ / nm	***E* / µJ**	**t_{irr} / min**	**Consumption of SM / %**	**Error / %**
1	310	600	02:35 s	18.9	
2	310	589	02:38 s	25.1	
3	310	623	02: 29 s	22.0	3.09
4	325	705	01:51 s	23.5	
5	325	749	01:45 s	23.7	
6	325	796	01:39 s	23.9	0.124
7	340	524	02:14 s	29.5	
8	340	530	02:13 s	32.6	
9	340	512	01:18 s	31.0	1.55
10	355	689	01:35 s	36.6	
11	355	712	01:32 s	37.0	
12	355	654	01:30 s	38.3	0.839
13	370	550	01:52 s	39.3	
14	370	573	01:48 s	36.5	
15	370	562	01:50 s	37.9	1.42
16	385	608	01:36 s	32.7	
17	385	592	01:39 s	31.3	
18	385	573	01:42 s	34.2	1.17
19	400	582	01:37 s	35.1	
20	400	555	01:41 s	34.7	
21	400	513	01:39 s	35.5	0.431
22	415	551	01:38 s	41.7	
23	415	520	01:40 s	42.1	
24	415	499	01:38 s	41.9	0.211
25	430	602	01:27 s	23.0	
26	430	610	01:25 s	22.7	
27	430	603	01:26 s	24.2	0.626

	λ / nm	**E / µJ**	**t_{irr} / min**	**Consumption of SM / %**	**Error / %**
28	445	589	01:25 s	1.54	
29	445	570	01:28 s	4.23	
30	445	566	01:29 s	2.89	1.34
31	460	486	01:40 s	1.42	
32	460	490	01:39 s	2.42	
33	460	468	01:44 s	1.92	0.498
34	475	492	01:36 s	1.58	
35	475	497	01:35 s	1.91	
36	475	481	01:38 s	1.76	0.167
37	490	449	01:42 s	0.548	
38	490	467	01:38 s	3.15	
39	490	438	01:40 s	1.85	1.30
40	505	583	01:17 s	0	
41	505	567	01:18 s	0	
42	505	541	01:22 s	0	0
43	520	427	01:41 s	0	
44	520	430	01:40 s	0	
45	520	422	01:42 s	0	0

5.6 Sequential LED Irradiation

The pathway-independent and sequential LED irradiation experiment (refer to section 4.4) was conducted using 72 µM **24** (80 µg mL^{-1}) and 147 µM **26** (40 µg mL^{-1}) in a total volume of 5 mL MeCN in a crimp vial. The solution was filtered, equipped with a stir bar, sealed and degassed with Ar for 15 minutes. Irradiation was carried out using the 405 nm (0.2 mW) and 505 nm (40 mW) LED (refer to section 5.2.1) from the bottom of the vial under continuous stirring and constant temperature of 20 °C. At each indicated time slot, 3 x 50 µL were taken out of the irradiated solution and analysed via LC-MS. Prior to analysis, 50 µL benzene (c = 1 mg mL^{-1} in MeCN) was added as an internal standard to determine the consumption of both starting materials via comparison of the ratio of the peak integrals of the starting material and the internal standard (Table S4).

Table S4: Results of the sequential LED experiment. The consumption of the starting materials was determined via LC-MS.

λ / nm	t_{irr} (total) / min	Consumption of 24 / %	Error / %	Consumption of 26 / %	Error / %
405	20	16.6	1.21	0	-
405	40	22.9	0.758	0	-
405	60	30.4	1.06	0	-
405	80	44.5	0.0867	4.56	0.908
505	95	44.5	0.0867	14.4	0.635
505	120	44.5	0.0867	21.6	0.302
505	150	44.5	0.0867	25.3	0.942
505	180	44.5	0.0867	30.4	0.290
Dark	195	44.5	0.0867	30.4	0.290
Dark	210	44.5	0.0867	30.4	0.290
Dark	225	44.5	0.0867	30.4	0.290
505	235	44.5	0.0867	33.6	1.36
505	250	44.5	0.0867	39.9	1.127
405	265	62.6	0.757	42.2	0.837
405	280	73.3	0.603	46.6	1.36

λ / nm	**t_{irr} (total) / min**	**Consumption of 24 / %**	**Error / %**	**Consumption of 26 / %**	**Error / %**
405	305	83.1	0.690	47.9	1.35
405	320	89.0	0.1477	49.6	0.141
405	335	95.9	0.1014	53.1	1.88
505	360	95.9	0.1014	60.1	1.75
505	390	95.9	0.1014	78.8	1.33
505	420	95.9	0.1014	90.8	1.26

6 References

[1] D. Wu, T. Wu, Q. Liu, Z. Yang, *Int. J. Infec. Dis.* **2020**, *94*, 44-48.

[2] D. S. Hui, E. I Azhar, T. A. Madani, F. Ntoumi, R. Kock, O. Dar, G. Ippolito, T. D. McHugh, Z. A. Memish, C. Drosten, A. Zumla, E. Petersen, *Int. J. Infec. Dis.* **2020**, *91*, 264-266.

[3] B. Hu, H. Guo, P. Zhou, Z.-L. Shi, *Nat. Rev. Microbiol.* **2021**, *19*, 141-154.

[4] aF. Krammer, *Nature* **2020**, *586*, 516-527; bY. Dong, T. Dai, Y. Wei, L. Zhang, M. Zheng, F. Zhou, *Signal Transduct. Target. Ther.* **2020**, *5*, 237; cA. Awadasseid, Y. Wu, Y. Tanaka, W. Zhang, *Int. J. Biol. Sci.* **2021**, *17*, 8-19.

[5] J. W. Park, P. N. P. Lagniton, Y. Liu, R.-H. Xu, *Int. J. Biol. Sci.* **2021**, *17*, 1446-1460.

[6] a) K. Karikó, M. Buckstein, H. Ni, D. Weissman, *Immunity* **2005**, *23*, 165-175; b) K. Karikó, H. Muramatsu, F. A. Welsh, J. Ludwig, H. Kato, S. Akira, D. Weissman, *Mol. Ther.* **2008**, *16*, 1833-1840; c) B. R. Anderson, H. Muramatsu, S. R. Nallagatla, P. C. Bevilacqua, L. H. Sansing, D. Weissman, K. Karikó, *Nucleic Acids Res.* **2010**, *38*, 5884-5892.

[7] Press Release Nobel Prize Medicine, **2023**; https://www.nobelprize.org/prizes/medicine/2023/press-release/ [accessed 02.01.25]

[8] a) H. Rinderknecht, *Nature* **1962**, *193*, 167-168; b) J. Lambris, M. Papamichail, P. Fessas, *J. Immunol. Methods* **1979**, *27*, 55-59; c) B. Albert Griffin, S. R. Adams, J. Jones, R. Y. Tsien, in *Methods in Enzymology, Vol. 327* (Eds.: J. Thorner, S. D. Emr, J. N. Abelson), Academic Press, **2000**, pp. 565-578; d) S. I. Reja, M. Minoshima, Y. Hori, K. Kikuchi, *Chem. Sci.* **2021**, *12*, 3437-3447.

[9] a) O. Shimomura, F. H. Johnson, Y. Saiga, *J. Cell. Physiol.* **1962**, *59*, 223-239; b) M. Chalfie, Y. Tu, G. Euskirchen, W. W. Ward, D. C. Prasher, *Science* **1994**, *263*, 802-805.

[10] a) D. J. Vocadlo, H. C. Hang, E.-J. Kim, J. A. Hanover, C. R. Bertozzi, *Proc. Natl. Acd. Sci. USA* **2003**, *100*, 9116-9121; b) H. C. Hang, C. Yu, D. L. Kato, C. R. Bertozzi, *Proc. Natl. Acd. Sci. USA* **2003**, *100*, 14846-14851; c) J. A. Prescher, D. H. Dube, C. R. Bertozzi, *Nature* **2004**, *430*, 873-877.

[11] a) J. A. Prescher, C. R. Bertozzi, *Nat. Chem. Biol.* **2005**, *1*, 13-21; b) J. M. Baskin, J. A. Prescher, S. T. Laughlin, N. J. Agard, P. V. Chang, I. A. Miller, A. Lo, J. A. Codelli, C. R. Bertozzi, *Proc. Natl. Acd. Sci. USA* **2007**, *104*, 16793-16797.

[12] a) E. M. Sletten, C. R. Bertozzi, *Angew. Chem. Int. Ed.* **2009**, *48*, 6974-6998; b) E. M. Sletten, C. R. Bertozzi, *Acc. Chem. Res.* **2011**, *44*, 666-676; c) P. V. Robinson, C.-t. Tsai, A. E. de Groot, J. L. McKechnie, C. R. Bertozzi, *J. Am. Chem. Soc.* **2016**, *138*, 10722-10725.

[13] H. C. Kolb, M. Finn, K. B. Sharpless, *Angew. Chem. Int. Ed.* **2001**, *40*, 2004-2021.

[14] C. W. Tornøe, C. Christensen, M. Meldal, *J. Org. Chem.* **2002**, *67*, 3057-3064.

[15] Press Release Nobel Prize Chemistry, **2022**; https://www.nobelprize.org/prizes/chemistry/2022/press-release/ [accessed 02.01.25]

[16] a) M. Handula, K.-T. Chen, Y. Seimbille, *Molecules* **2021**, *26*, 4640; b) Z. Liu, M. Sun, W. Zhang, J. Ren, X. Qu, *Angew. Chem. Int. Ed.* **2023**, *135*, e202308396.

[17] a) P. Tardi, N. Boman, P. Cullis, *J. Drug. Target.* **1996**, *4*, 129-140; b) Z. Ni, C. Yao, X. Zhu, C. Gong, Z. Xu, L. Wang, S. Li, C. Zou, S. Zhu, *Br. J. Cancer* **2017**, *117*, 1621-1630; c) J. Li, J. Liu, Z. Liang, F. He, L. Yang, P. Li, Y. Jiang, B. Wang, C. Zhou, Y. Wang, *Cell Death Dis.* **2017**, *8*, e2673-e2673.

[18] a) P. M. Gramlich, S. Warncke, J. Gierlich, T. Carell, *Angew. Chem. Int. Ed.* **2008**, *47*, 3442-3444; b) V. Borsenberger, S. Howorka, *Nucleic Acids Res.* **2009**, *37*, 1477-1485; c) U. Reisacher, D. Ploschik, F. Rönicke, G. B. Cserép, P. Kele, H.-A. Wagenknecht, *Chem. Sci.* **2019**, *10*, 4032-4037; d) D. Ganz, D. Harijan, H.-A. Wagenknecht, *RCS Chem. Bio.* **2020**, *1*, 86-97; e) H. Liu, Y. Wang, X. Zhou, *RCS Chem. Bio.* **2022**, *3*, 994-1007.

[19] A. Battigelli, B. Almeida, A. Shukla, *Bioconjugate Chem.* **2022**, *33*, 263-271.

[20] a) K. Lang, J. W. Chin, *ACS Chem. Biol.* **2014**, *9*, 16-20; b) Y. Gong, L. Pan, *Tetrahedron Lett.* **2015**, *56*, 2123-2132.

[21] a) P. V. Chang, J. A. Prescher, M. J. Hangauer, C. R. Bertozzi, *J. Am. Chem. Soc.* **2007**, *129*, 8400-8401; b) A. Niederwieser, A.-K. Späte, L. D. Nguyen, C. Jüngst, W. Reutter, V. Wittmann, *Angew.*

Chem. Int. Ed. **2013**, *52*, 4265-4268; c) A. Lopez Aguilar, J. G. Briard, L. Yang, B. Ovryn, M. S. Macauley, P. Wu, *ACS Chem. Biol.* **2017**, *12*, 611-621.

[22] a) N. Klöcker, F. P. Weissenboeck, A. Rentmeister, *Chem. Soc. Rev.* **2020**, *49*, 8749-8773; b) K. Krell, B. Pfeuffer, F. Rönicke, Z. S. Chinoy, C. Favre, F. Friscourt, H.-A. Wagenknecht, *Chem. Eur. J.* **2021**, *27*, 16093-16097.

[23] R. K. V. Lim, Q. Lin, *Chem. Commun.* **2010**, *46*, 1589-1600.

[24] Q. Wang, T. R. Chan, R. Hilgraf, V. V. Fokin, K. B. Sharpless, M. G. Finn, *J. Am. Chem. Soc.* **2003**, *125*, 3192-3193.

[25] W. Chen, D. Wang, C. Dai, D. Hamelberg, B. Wang, *Chem. Commun.* **2012**, *48*, 1736-1738.

[26] N. J. Agard, J. A. Prescher, C. R. Bertozzi, *J. Am. Chem. Soc.* **2004**, *126*, 15046-15047.

[27] Z. Li, L. Qian, L. Li, J. C. Bernhammer, H. V. Huynh, J.-S. Lee, S. Q. Yao, *Angew. Chem. Int. Ed.* **2016**, *55*, 2002-2006.

[28] R. Huisgen, L. Möbius, G. Müller, H. Stangl, G. Szeimies, J. M. Vernon, *Chem. Ber.* **1965**, *98*, 3992-4013.

[29] V. V. Rostovtsev, L. G. Green, V. V. Fokin, K. B. Sharpless, *Angew. Chem. Int. Ed.* **2002**, *41*, 2596-2599.

[30] P. M. E. Gramlich, C. T. Wirges, A. Manetto, T. Carell, *Angew. Chem. Int. Ed.* **2008**, *47*, 8350-8358.

[31] H. Jiang, T. Zheng, A. Lopez-Aguilar, L. Feng, F. Kopp, F. L. Marlow, P. Wu, *Bioconjugate Chem.* **2014**, *25*, 698-706.

[32] C. Uttamapinant, A. Tangpeerachaikul, S. Grecian, S. Clarke, U. Singh, P. Slade, K. R. Gee, A. Y. Ting, *Angew. Chem. Int. Ed.* **2012**, *51*, 5852-5856.

[33] C. F. Ancajas, T. J. Ricks, M. D. Best, *Chem. Phys. Lipids* **2020**, *232*, 104971.

[34] a) V. Hong, N. F. Steinmetz, M. Manchester, M. G. Finn, *Bioconjugate Chem.* **2010**, *21*, 1912-1916; b) S. Li, L. Wang, F. Yu, Z. Zhu, D. Shobaki, H. Chen, M. Wang, J. Wang, G. Qin, U. J. Erasquin, L. Ren, Y. Wang, C. Cai, *Chem. Sci.* **2017**, *8*, 2107-2114.

[35] D. C. Kennedy, C. S. McKay, M. C. B. Legault, D. C. Danielson, J. A. Blake, A. F. Pegoraro, A. Stolow, Z. Mester, J. P. Pezacki, *J. Am. Chem. Soc.* **2011**, *133*, 17993-18001.

[36] T.-W. Yu, D. Anderson, *Mutant. Res. - Fundam. Mol.* **1997**, *379*, 201-210.

[37] E. V. Stelmashook, N. K. Isaev, E. E. Genrikhs, G. A. Amelkina, L. G. Khaspekov, V. G. Skrebitsky, S. N. Illarioshkin, *Biochemistry* **2014**, *79*, 391-396.

[38] J. C. Jewett, E. M. Sletten, C. R. Bertozzi, *J. Am. Chem. Soc.* **2010**, *132*, 3688-3690.

[39] J. Dommerholt, S. Schmidt, R. Temming, L. J. A. Hendriks, F. P. J. T. Rutjes, J. C. M. van Hest, D. J. Lefeber, P. Friedl, F. L. van Delft, *Angew. Chem. Int. Ed.* **2010**, *49*, 9422-9425.

[40] P. Geng, E. List, F. Rönicke, H. A. Wagenknecht, *Chem. Eur. J.* **2023**, *29*, e202203156.

[41] X. Ren, A. H. El-Sagheer, T. Brown, *Nucleic Acids Res.* **2016**, *44*, e79-e79.

[42] I. Nikić, J. H. Kang, G. E. Girona, I. V. Aramburu, E. A. Lemke, *Nat. Protoc.* **2015**, *10*, 780-791.

[43] E. G. Chupakhin, M. Y. Krasavin, *Chem. Heterocycl. Compd.* **2018**, *54*, 483-501.

[44] O. Diels, *Chem. Ber.* **1929**, *62*, 554-562.

[45] O. Diels, K. Alder, *Liebigs Ann. Chem.* **1928**, *460*, 98-122.

[46] J. Sauer, *Angew. Chem. Int. Ed.* **1967**, *6*, 16-33.

[47] B. L. Oliveira, Z. Guo, G. J. L. Bernardes, *Chem. Soc. Rev.* **2017**, *46*, 4895-4950.

[48] R. Carboni, R. Lindsey Jr, *J. Am. Chem. Soc.* **1959**, *81*, 4342-4346.

[49] a) N. K. Devaraj, R. Weissleder, S. A. Hilderbrand, *Bioconjugate Chem.* **2008**, *19*, 2297-2299; b) M. L. Blackman, M. Royzen, J. M. Fox, *J. Am. Chem. Soc.* **2008**, *130*, 13518-13519.

[50] D. M. Patterson, L. A. Nazarova, B. Xie, D. N. Kamber, J. A. Prescher, *J. Am. Chem. Soc.* **2012**, *134*, 18638-18643.

[51] K. Lang, L. Davis, J. Torres-Kolbus, C. Chou, A. Deiters, J. W. Chin, *Nat. Chem.* **2012**, *4*, 298-304.

[52] D. Wang, W. Chen, Y. Zheng, C. Dai, K. Wang, B. Ke, B. Wang, *Org. Biomol. Chem.* **2014**, *12*, 3950-3955.

[53] A. Darko, S. Wallace, O. Dmitrenko, M. M. Machovina, R. A. Mehl, J. W. Chin, J. M. Fox, *Chem. Sci.* **2014**, *5*, 3770-3776.

[54] J. L. Seitchik, J. C. Peeler, M. T. Taylor, M. L. Blackman, T. W. Rhoads, R. B. Cooley, C. Refakis, J. M. Fox, R. A. Mehl, *J. Am. Chem. Soc.* **2012**, *134*, 2898-2901.

[55] a) Y. Deng, T. Shen, X. Yu, J. Li, P. Zou, Q. Gong, Y. Zheng, H. Sun, X. Liu, H. Wu, *Angew. Chem. Int. Ed.* **2024**, e202319853; b) V. T. Sterrenberg, D. Stalling, J. I. H. Knaack, T. K. Soh, J. B.

Bosse, C. Meier, *Angew. Chem. Int. Ed.* **2023**, *62*, e202308271; c) M. O. Loehr, N. W. Luedtke, *Angew. Chem. Int. Ed.* **2022**, *61*, e202112931.

[56] a) Z. M. Png, X. Y. D. Soo, J. X. D. Liew, M. H. Chua, S. Xiong, Q. Zhu, J. Xu, *Polymer Chem.* **2023**, *14*, 3347-3351; b) S. A. Busche, M. Traxler, A. Thomas, H. G. Börner, *ChemSusChem* **2024**, e202301045.

[57] Y. Liang, J. L. Mackey, S. A. Lopez, F. Liu, K. N. Houk, *J. Am. Chem. Soc.* **2012**, *134*, 17904-17907.

[58] a) J. C. Jewett, C. R. Bertozzi, *Chem. Soc. Rev.* **2010**, *39*, 1272-1279; b) A.-C. Knall, C. Slugovc, *Chem. Soc. Rev.* **2013**, *42*, 5131-5142.

[59] a) H. Frisch, D. E. Marschner, A. S. Goldmann, C. Barner-Kowollik, *Angew. Chem. Int. Ed.* **2018**, *57*, 2036-2045; b) V. M. Lechner, M. Nappi, P. J. Deneny, S. Folliet, J. C. K. Chu, M. J. Gaunt, *Chem. Rev.* **2022**, *122*, 1752-1829.

[60] J. S. Clovis, A. Eckell, R. Huisgen, R. Sustmann, G. Wallbillich, V. Weberndörfer, *Chem. Ber.* **1967**, *100*, 1593-1601.

[61] B. D. Fairbanks, L. J. Macdougall, S. Mavila, J. Sinha, B. E. Kirkpatrick, K. S. Anseth, C. N. Bowman, *Chem. Rev.* **2021**, *121*, 6915-6990.

[62] a) W. Song, Y. Wang, J. Qu, Q. Lin, *J. Am. Chem. Soc.* **2008**, *130*, 9654-9655; b) Y. Wang, W. J. Hu, W. Song, R. K. V. Lim, Q. Lin, *Org. Lett.* **2008**, *10*, 3725-3728.

[63] W. Song, Y. Wang, J. Qu, M. M. Madden, Q. Lin, *Angew. Chem. Int. Ed.* **2008**, *47*, 2832-2835.

[64] a) Z. Yu, L. Y. Ho, Q. Lin, *J. Am. Chem. Soc.* **2011**, *133*, 11912-11915; b) Z. Yu, T. Y. Ohulchanskyy, P. An, P. N. Prasad, Q. Lin, *J. Am. Chem. Soc.* **2013**, *135*, 16766-16769; c) S. Zhao, J. Dai, M. Hu, C. Liu, R. Meng, X. Liu, C. Wang, T. Luo, *Chem. Commun.* **2016**, *52*, 4702-4705.

[65] a) S. Arndt, H.-A. Wagenknecht, *Angew. Chem. Int. Ed.* **2014**, *53*, 14580-14582; b) B. Lehmann, H.-A. Wagenknecht, *Org. Biomol. Chem.* **2018**, *16*, 7579-7582.

[66] K. Krell, H.-A. Wagenknecht, *Biomolecules* **2020**, *10*, 480.

[67] Y. Wu, G. Guo, J. Zheng, D. Xing, T. Zhang, *ACS Sens.* **2019**, *4*, 44-51.

[68] H.-A. Wagenknecht, *ChemPhysChem* **2013**, *14*, 3197-3198.

[69] Y. Qi, S. Bai, T. Vogelmann, G. Heisler, *Proc. SPIE* **2003**, *5156*.

[70] P. Lederhose, K. N. R. Wüst, C. Barner-Kowollik, J. P. Blinco, *Chem. Commun.* **2016**, *52*, 5928-5931.

[71] P. W. Kamm, J. P. Blinco, A.-N. Unterreiner, C. Barner-Kowollik, *Chem. Commun.* **2021**, *57*, 3991-3994.

[72] L. Rieger, B. Pfeuffer, H.-A. Wagenknecht, *RCS Chem. Bio.* **2023**, *4*, 1037-1042.

[73] C. Jamieson, K. Livingstone, *Properties, Reactivity and Applications; Springer* **2020**.

[74] H. C. Kolb, M. G. Finn, K. B. Sharpless, *Angew. Chem. Int. Ed.* **2001**, *40*, 2004-2021.

[75] Y. Wang, W. Song, W. J. Hu, Q. Lin, *Angew. Chem. Int. Ed.* **2009**, *48*, 5330-5333.

[76] N. Umeda, H. Takahashi, M. Kamiya, T. Ueno, T. Komatsu, T. Terai, K. Hanaoka, T. Nagano, Y. Urano, *ACS Chem. Biol.* **2014**, *9*, 2242-2246.

[77] R. Huisgen, *Angew. Chem. Int. Ed.* **1968**, *7*, 321-328.

[78] J. Li, H. Kong, C. Zhu, Y. Zhang, *Chem. Sci.* **2020**, *11*, 3390-3396.

[79] J. Li, H. Kong, L. Huang, B. Cheng, K. Qin, M. Zheng, Z. Yan, Y. Zhang, *J. Am. Chem. Soc.* **2018**, *140*, 14542-14546.

[80] Y. Li, Z. Lou, H. Li, H. Yang, Y. Zhao, H. Fu, *Angew. Chem. Int. Ed.* **2020**, *59*, 3671-3677.

[81] K. Kalayci, H. Frisch, V. X. Truong, C. Barner-Kowollik, *Nat. Commun.* **2020**, *11*, 4193.

[82] a) L. C. Bahlmann, A. Fokina, M. S. Shoichet, *MRS Commun.* **2017**, *7*, 472-486; b) V. X. Truong, F. Li, F. Ercole, J. S. Forsythe, *ACS Macro Lett.* **2018**, *7*, 464-469.

[83] a) B. T. Tuten, S. Wiedbrauk, C. Barner-Kowollik, *Prog. Polym. Sci.* **2020**, *100*, 101183; b) J. T. Offenloch, M. Gernhardt, J. P. Blinco, H. Frisch, H. Mutlu, C. Barner-Kowollik, *Chem. Eur. J.* **2019**, *25*, 3700-3709.

[84] T. Doi, H. Kawai, K. Murayama, H. Kashida, H. Asanuma, *Chem. Eur. J.* **2016**, *22*, 10533-10538.

[85] K. Murayama, Y. Yamano, H. Asanuma, *J. Am. Chem. Soc.* **2019**, *141*, 9485-9489.

[86] S. Protti, D. Ravelli, M. Fagnoni, *Photochem. Photobiol. Sci.* **2019**, *18*, 2094-2101.

[87] V. X. Truong, J. Bachmann, A.-N. Unterreiner, J. P. Blinco, C. Barner-Kowollik, *Angew. Chem. Int. Ed.* **2022**, *61*, e202113076.

[88] O. A. Fedorova, A. E. Saifutiarova, E. N. Gulakova, E. O. Guskova, T. M. Aliyeu, N. E. Shepel, Y. V. Fedorov, *Photochem. Photobiol. Sci.* **2019**, *18*, 2208-2215.

[89] T. A. Andersson, K. M. Hartonen, M.-L. Riekkola, *J. Chem. Eng. Data* **2005**, *50*, 1177-1183.

[90] J. O. Mueller, N. K. Guimard, K. K. Oehlenschlaeger, F. G. Schmidt, C. Barner-Kowollik, *Polymer Chem.* **2014**, *5*, 1447-1456.

[91] M. Ott, *Internal NASA Parts and Packaging Publication* **1996**.

[92] a) A. H. Zewail, *J. Phys. Chem.* **1993**, *97*, 12427-12446; b) P. H. Bucksbaum, *Nature* **2003**, *421*, 593-594.

[93] A. Di Piazza, C. Müller, K. Hatsagortsyan, C. H. Keitel, *Rev. Mod. Phys.* **2012**, *84*, 1177.

[94] A. Einstein, *Zur quantentheorie der strahlung, Vol. 18*, Hirzel Leipzig, **1917**.

[95] J. P. Gordon, H. J. Zeiger, C. H. Townes, *Phys. Rev.* **1955**, *99*, 1264.

[96] T. H. Maiman, **1960**.

[97] J.-Y. Oh, W. Stuerzlinger, in *Graphics Interface, Vol. 2002*, **2002**, pp. 141-149.

[98] Naresh, P. Khatak, *Mater. Today* **2022**, *56*, 2484-2489.

[99] S. C.-M. Huang, H.-C. Chen, *Chang Gung Med. J.* **2008**, *31*, 237-252.

[100] W. Lauterborn, T. Kurz, *Coherent Optics: Fundamentals and Applications*, Springer Science & Business Media, **2003**.

[101] S. L. Walden, J. A. Carroll, A.-N. Unterreiner, C. Barner-Kowollik, *Adv. Sci.* **2024**, *11*, 2306014.

[102] I. M. Irshadeen, S. L. Walden, M. Wegener, V. X. Truong, H. Frisch, J. P. Blinco, C. Barner-Kowollik, *J. Am. Chem. Soc.* **2021**, *143*, 21113-21126.

[103] C. G. B. Daubeny, *Philos. Trans. R. Soc. Lond.* **1836**, 149-175.

[104] R. B. Setlow, E. Grist, K. Thompson, A. D. Woodhead, *Proc. Natl. Acd. Sci. USA* **1993**, *90*, 6666-6670.

[105] a) D. Kuang, S. Uchida, R. Humphry-Baker, S. M. Zakeeruddin, M. Grätzel, *Angew. Chem. Int. Ed.* **2008**, *47*, 1923-1927; b) S. K. Cushing, J. Li, F. Meng, T. R. Senty, S. Suri, M. Zhi, M. Li, A. D. Bristow, N. Wu, *J. Am. Chem. Soc.* **2012**, *134*, 15033-15041.

[106] P. K. Nayak, S. Mahesh, H. J. Snaith, D. Cahen, *Nat. Rev. Mater.* **2019**, *4*, 269-285.

[107] D. E. Fast, A. Lauer, J. P. Menzel, A.-M. Kelterer, G. Gescheidt, C. Barner-Kowollik, *Macromolecules* **2017**, *50*, 1815-1823.

[108] A. P. French, *An Introduction to Quantum Physics*, Routledge, **2018**.

[109] a) H. Frisch, J. P. Menzel, F. R. Bloesser, D. E. Marschner, K. Mundsinger, C. Barner-Kowollik, *J. Am. Chem. Soc.* **2018**, *140*, 9551-9557; b) D. E. Marschner, H. Frisch, J. T. Offenloch, B. T. Tuten, C. R. Becer, A. Walther, A. S. Goldmann, P. Tzvetkova, C. Barner-Kowollik, *Macromolecules* **2018**, *51*, 3802-3807; c) J. P. Menzel, B. B. Noble, J. P. Blinco, C. Barner-Kowollik, *Nat. Commun.* **2021**, *12*, 1691; d) I. M. Irshadeen, K. De Bruycker, A. S. Micallef, S. L. Walden, H. Frisch, C. Barner-Kowollik, *Polymer Chem.* **2021**, *12*, 4903-4909.

[110] F. Feist, S. L. Walden, J. Alves, S. V. Kunz, A. S. Micallef, A. J. Brock, J. C. McMurtrie, T. Weil, J. P. Blinco, C. Barner-Kowollik, *Angew. Chem. Int. Ed.* **2021**, *60*, 10402-10408.

[111] a) J. W. Halloran, *Annu. Rev. Mater. Res.* **2016**, *46*, 19-40; b) J. Z. Manapat, Q. Chen, P. Ye, R. C. Advincula, *Macromol. Mater. Eng.* **2017**, *302*, 1600553.

[112] L. Yang, F. Mayer, U. H. Bunz, E. Blasco, M. Wegener, *Adv. Manuf.* **2021**, *2*, 296-312.

[113] F. P. Melchels, J. Feijen, D. W. Grijpma, *Biomaterials* **2010**, *31*, 6121-6130.

[114] K. Kalayci, H. Frisch, C. Barner-Kowollik, V. X. Truong, *Adv. Funct. Mater.* **2020**, *30*, 1908171.

[115] V. X. Truong, J. Bachmann, A. N. Unterreiner, J. P. Blinco, C. Barner-Kowollik, *Angew. Chem. Int. Ed.* **2022**, *61*, e202113076.

[116] J. Bachmann, C. Petit, L. Michalek, Y. Catel, E. Blasco, J. P. Blinco, A.-N. Unterreiner, C. Barner-Kowollik, *ACS Macro Lett.* **2021**, *10*, 447-452.

[117] J. L. Pelloth, P. A. Tran, A. Walther, A. S. Goldmann, H. Frisch, V. X. Truong, C. Barner-Kowollik, *Adv. Mater.* **2021**, *33*, 2102184.

[118] R. Weinstain, T. Slanina, D. Kand, P. Klán, *Chem. Rev.* **2020**, *120*, 13135-13272.

[119] a) P. Seyfried, M. Heinz, G. Pintér, D.-P. Klötzner, Y. Becker, M. Bolte, H. R. A. Jonker, L. S. Stelzl, G. Hummer, H. Schwalbe, A. Heckel, *Chem. Eur. J.* **2018**, *24*, 17568-17576; b) W. Zhou, C. P. Hankinson, A. Deiters, *Chembiochem* **2020**, *21*, 1832-1836.

[120] M. Zhou, X. Liang, T. Mochizuki, H. Asanuma, *Angew. Chem. Int. Ed.* **2010**, *49*, 2167-2170.

[121] N. Klöcker, F. P. Weissenboeck, M. van Dülmen, P. Špaček, S. Hüwel, A. Rentmeister, *Nat. Chem.* **2022**, *14*, 905-913.

[122] P. A. Shaw, M. Klausen, M. Bradley, *Polymer Chem.* **2024**, *15*, 54-58.

[123] D. B. Kassel, *Curr. Opin. Chem. Biol.* **2004**, *8*, 339-345.

[124] M. Eing, B. Olshausen, K. E. Fairfull-Smith, U. Schepers, C. Barner-Kowollik, J. P. Blinco, *Polymer Chem.* **2018**, *9*, 499-505.

[125] Y. Chi, X. Yin, K. Sun, S. Feng, J. Liu, D. Chen, C. Guo, Z. Wu, *J. Control. Release* **2017**, *261*, 113-125.

[126] F. Fouladi, K. J. Steffen, S. Mallik, *Bioconjugate Chem.* **2017**, *28*, 857-868.

[127] M. A. Santos, D. E. Goertz, K. Hynynen, *Theranostics* **2017**, *7*, 2718.

[128] A. Goulet-Hanssens, F. Eisenreich, S. Hecht, *Adv. Mater.* **2020**, *32*, 1905966.

[129] D. Zhi, T. Yang, J. O'Hagan, S. Zhang, R. F. Donnelly, *J. Control. Release* **2020**, *325*, 52-71.

[130] L. Zou, H. Wang, B. He, L. Zeng, T. Tan, H. Cao, X. He, Z. Zhang, S. Guo, Y. Li, *Theranostics* **2016**, *6*, 762-772.

[131] J. A. Barltrop, P. Schofield, *Tetrahedron Lett.* **1962**, *3*, 697-699.

[132] D. H. R. Barton, Y. L. Chow, A. Cox, G. W. Kirby, *Tetrahedron Lett.* **1962**, *3*, 1055-1057.

[133] A. Patchornik, B. Amit, R. B. Woodward, *J. Am. Chem. Soc.* **1970**, *92*, 6333-6335.

[134] J. C. Sheehan, R. M. Wilson, *J. Am. Chem. Soc.* **1964**, *86*, 5277-5281.

[135] J. Engels, E. J. Schlaeger, *J. Med. Chem.* **1977**, *20*, 907-911.

[136] J. H. Kaplan, B. Forbush, III, J. F. Hoffman, *Biochemistry* **1978**, *17*, 1929-1935.

[137] G. C. Ellis-Davies, *Nat. Methods* **2007**, *4*, 619-628.

[138] A. Deiters, *Chembiochem* **2010**, *11*, 47-53.

[139] R. S. Givens, B. Matuszewski, P. S. Athey, M. R. Stoner, *J. Am. Chem. Soc.* **1990**, *112*, 6016-6021.

[140] a) S. Barman, J. Das, S. Biswas, T. K. Maiti, N. D. Pradeep Singh, *J. Mater. Chem. B.* **2017**, *5*, 3940-3944; b) B.-Y. Wang, Y.-C. Lin, Y.-T. Lai, J.-Y. Ou, W.-W. Chang, C.-C. Chu, *Bioorg. Chem.* **2020**, *100*, 103904.

[141] M. A. Musa, J. S. Cooperwood, M. O. F. Khan, *Curr. Med. Chem.* **2008**, *15*, 2664-2679.

[142] a) H. Li, J. Zhou, J. Zhao, *Appl. Surf. Sci.* **2023**, *614*, 156180; b) F. Sai, H. Zhang, J. Qu, J. Wang, X. Zhu, Y. Bai, P. Ye, *Appl. Surf. Sci.* **2022**, *573*, 151526.

[143] A. Abdollahi, B. Ghasemi, S. Nikzaban, N. Sardari, S. Jorjeisi, A. Dashti, *ACS Appl. Mater. Interfaces* **2023**, *15*, 7466-7484.

[144] A. M. Schulte, G. Alachouzos, W. Szymanski, B. L. Feringa, *Chem. Sci.* **2024**, *15*, 2062-2073.

[145] R. Schmidt, D. Geissler, V. Hagen, J. Bendig, *J. Phys. Chem.* **2007**, *111*, 5768-5774.

[146] N. Senda, A. Momotake, Y. Nishimura, T. Arai, *Bull. Chem. Soc.* **2006**, *79*, 1753-1757.

[147] B. Schade, V. Hagen, R. Schmidt, R. Herbrich, E. Krause, T. Eckardt, J. Bendig, *J. Org. Chem.* **1999**, *64*, 9109-9117.

[148] V. Hagen, J. Bendig, S. Frings, T. Eckardt, S. Helm, D. Reuter, U. B. Kaupp, *Angew. Chem. Int. Ed.* **2001**, *40*, 1045-1048.

[149] P. Kumari, A. Kulkarni, A. K. Sharma, H. Chakrapani, *ACS Omega* **2018**, *3*, 2155-2160.

[150] K. D. Philipson, J. P. Gallivan, G. S. Brandt, D. A. Dougherty, H. A. Lester, *Am. J. Physiol. Cell Physiol.* **2001**, *281*, C195-C206.

[151] S. Petersen, J. M. Alonso, A. Specht, P. Duodu, M. Goeldner, A. del Campo, *Angew. Chem. Int. Ed.* **2008**, *120*, 3236-3239.

[152] K. M. Schelkle, T. Griesbaum, D. Ollech, S. Becht, T. Buckup, M. Hamburger, R. Wombacher, *Angew. Chem. Int. Ed.* **2015**, *54*, 2825-2829.

[153] Y. A. Kim, D. M. C. Ramirez, W. J. Costain, L. J. Johnston, R. Bittman, *Chem. Commun.* **2011**, *47*, 9236-9238.

[154] G. Makey, Ö. Yavuz, D. K. Kesim, A. Turnalı, P. Elahi, S. Ilday, O. Tokel, F. Ö. Ilday, *Nat. Photon.* **2019**, *13*, 251-256.

[155] G. Barany, R. Merrifield, *J. Am. Chem. Soc.* **1977**, *99*, 7363-7365.

[156] R. B. Merrifield, *Angew. Chem. Int. Ed.* **1985**, *24*, 799-810.

[157] a) M. A. Azagarsamy, K. S. Anseth, *Angew. Chem. Int. Ed.* **2013**, *52*, 13803-13807; b) A. Rodrigues-Correia, X. M. M. Weyel, A. Heckel, *Org. Lett.* **2013**, *15*, 5500-5503.

[158] A. Bollu, N. Klöcker, P. Špaček, F. P. Weissenboeck, S. Hüwel, A. Rentmeister, *Angew. Chem. Int. Ed.* **2023**, *62*, e202209975.

[159] T. L. Rapp, C. A. DeForest, *Nat. Commun.* **2023**, *14*, 5250.

[160] a) J. A. Peterson, D. Yuan, A. H. Winter, *J. Org. Chem.* **2021**, *86*, 9781-9787; b) A. K. Singh, S. Banerjee, A. V. Nair, S. Ray, M. Ojha, A. Mondal, N. D. P. Singh, *ACS Appl. Bio Mater.* **2022**, *5*, 1202-1209.

[161] J. Zhu, H. Bienaymé, *Multicomponent Reactions*, John Wiley & Sons, **2006**.

[162] a) A. Dömling, I. Ugi, *Angew. Chem. Int. Ed.* **2000**, *39*, 3168-3210; b) M. Passerini, *Gazz. Chim. Ital.* **1921**, *51*, 181-189.

[163] Y. Huang, F. Yang, C. Zhu, *J. Am. Chem. Soc.* **2005**, *127*, 16386-16387.

[164] I. Akritopoulou-Zanze, *Curr. Opin. Chem. Biol.* **2008**, *12*, 324-331.

[165] R. Ramozzi, K. Morokuma, *J. Org. Chem.* **2015**, *80*, 5652-5657.

[166] J. J. Li, J. J. Li, *Collection of Detailed Mechanisms* **2021**, 424-426.

[167] F. Sutanto, S. Shaabani, R. Oerlemans, D. Eris, P. Patil, M. Hadian, M. Wang, M. E. Sharpe, M. R. Groves, A. Dömling, *Angew. Chem. Int. Ed.* **2021**, *60*, 18231-18239.

[168] Y. Tian, M. Seifermann, L. Bauer, C. Luchena, J. J. Wiedmann, S. Schmidt, A. Geisel, S. Afonin, J. Höpfner, M. Brehm, X. Liu, C. Hopf, A. A. Popova, P. A. Levkin, *Small* **2024**, 2307215.

[169] R. T. Michenfelder, L. Delafresnaye, V. X. Truong, C. Barner-Kowollik, H.-A. Wagenknecht, *Chem. Commun.* **2023**, *59*, 4012-4015.

[170] K. Wada, J.-Y. Lee, H.-Y. Hung, Q. Shi, L. Lin, Y. Zhao, M. Goto, P.-C. Yang, S.-C. Kuo, H.-W. Chen, *Bioorg. Med. Chem.* **2015**, *23*, 1507-1514.

[171] A. S. K. Hashmi, T. Häffner, W. Yang, S. Pankajakshan, S. Schäfer, L. Schultes, F. Rominger, W. Frey, *Chem. Eur. J.* **2012**, *18*, 10480-10486.

[172] a) T. R. Battersby, D. N. Ang, P. Burgstaller, S. C. Jurczyk, M. T. Bowser, D. D. Buchanan, R. T. Kennedy, S. A. Benner, *J. Am. Chem. Soc.* **1999**, *121*, 9781-9789; b) Á. Eördögh, J. Steinmeyer, K. Peewasan, U. Schepers, H.-A. Wagenknecht, P. Kele, *Bioconjugate Chem.* **2016**, *27*, 457-464.

[173] N. K. Vaish, A. W. Fraley, J. W. Szostak, L. W. McLaughlin, *Nucleic Acids Res.* **2000**, *28*, 3316-3322.

[174] H. D. Roth, *Angew. Chem. Int. Ed.* **1989**, *28*, 1193-1207.

[175] a) A. A. Holder, S. Swavey, K. J. Brewer, *Inorg. Chem.* **2004**, *43*, 303-308; b) A. Jana, K. S. P. Devi, T. K. Maiti, N. P. Singh, *J. Am. Chem. Soc.* **2012**, *134*, 7656-7659; c) V. X. Truong, F. Li, J. S. Forsythe, *ACS Appl. Mater. Interfaces* **2017**, *9*, 32441-32445.

[176] a) C. G. Dariva, J. F. J. Coelho, A. C. Serra, *J. Control. Release* **2019**, *294*, 337-354; b) J. Liu, W. Kang, W. Wang, *Photochem. Photobiol.* **2022**, *98*, 288-302.

[177] K. Waibel, R. Nickisch, N. Möhl, R. Seim, M. Meier, *Green Chem.* **2020**, *22*, 933-941.

[178] R. T. Michenfelder, F. Pashley-Johnson, V. Guschin, L. Delafresnaye, V. X. Truong, H.-A. Wagenknecht, C. Barner-Kowollik, *Adv. Sci.* **2024**, *11*, 2402011.

[179] C. Ausín, J. S. Kauffman, R. J. Duff, S. Shivaprasad, S. L. Beaucage, *Tetrahedron* **2010**, *66*, 68-79.

[180] J. Tu, M. Xu, S. Parvez, R. T. Peterson, R. M. Franzini, *J. Am. Chem. Soc.* **2018**, *140*, 8410-8414.

[181] R. Arshady, *Polymer* **1982**, *23*, 1099-1100.

[182] M. C. Pirrung, K. D. Sarma, *J. Am. Chem. Soc.* **2004**, *126*, 444-445.

[183] a) S. Kinze, M. Clauss, U. Reuter, T. Wolf, J. P. Dreier, K. M. Einhäupl, G. Arnold, *Headache* **2001**, *41*, 774-778; b) W. Löscher, *CNS Drugs* **2002**, *16*, 669-694.

[184] A. Begleiter, M. Mowat, L. G. Israels, J. B. Johnston, *Leuk. Lymphoma* **1996**, *23*, 187-201.

[185] D. J. Mason, E. G. Power, H. Talsania, I. Phillips, V. A. Gant, *J. Antimicrob. Chemother.* **1995**, *39*, 2752-2758.

[186] a) Y. Zhu, C. M. Pavlos, J. P. Toscano, T. M. Dore, *J. Am. Chem. Soc.* **2006**, *128*, 4267-4276; b) J. A. Peterson, L. J. Fischer, E. J. Gehrmann, P. Shrestha, D. Yuan, C. S. Wijesooriya, E. A. Smith, A. H. Winter, *J. Org. Chem.* **2020**, *85*, 5712-5717.

[187] J. P. Menzel, F. Feist, B. Tuten, T. Weil, J. P. Blinco, C. Barner-Kowollik, *Angew. Chem. Int. Ed.* **2019**, *58*, 7470-7474.

[188] J. P. Menzel, B. B. Noble, A. Lauer, M. L. Coote, J. P. Blinco, C. Barner-Kowollik, *J. Am. Chem. Soc.* **2017**, *139*, 15812-15820.

7 Appendix

7.1 DNA Labelling in Live Cells via [2+2] Cycloaddition

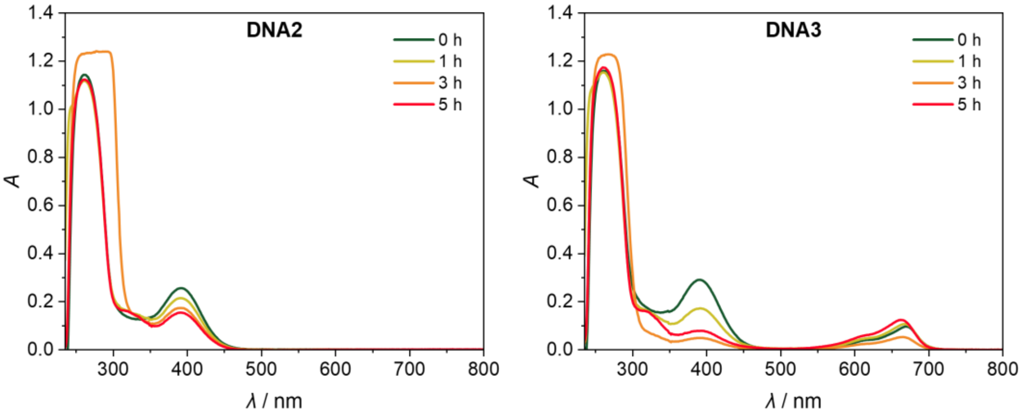

Figure A1: UV/Vis spectroscopic analysis of **DNA2** (left) and **DNA3** (right) after irradiation of 50 µM **DNA2** and 50 µM SQ-modified Atto655 dye **14** (1:1 equivalents) with a 450 nm LED in aqueous media containing 5% DMF, 10 mM Na-P$_i$ buffer and 250 mM NaCl in H_2O in a total volume of 600 µL in a crimp vial for 5 h at 20 °C. Pre-irradiation (dark green line), **DNA2** and **DNA3** both show two distinctive absorbance maxima at λ_{max1} = 260 nm, associated with the DNA absorbance and λ_{max2} = 397 nm, associated with the SQ moiety. Furthermore, **DNA3** shows a third maximum at λ_{max3} = 655 nm, that can be assigned to the Atto655 dye. During irradiation, one new maximum is emerging at λ = 325 nm whereas the assigned SQ maximum is decreasing (red line). Nevertheless, **DNA2** and **DNA3** predominantly show similar changes in absorbance after 5 h of irradiation, making clear differentiation and conclusion about the formation of **DNA3** challenging.

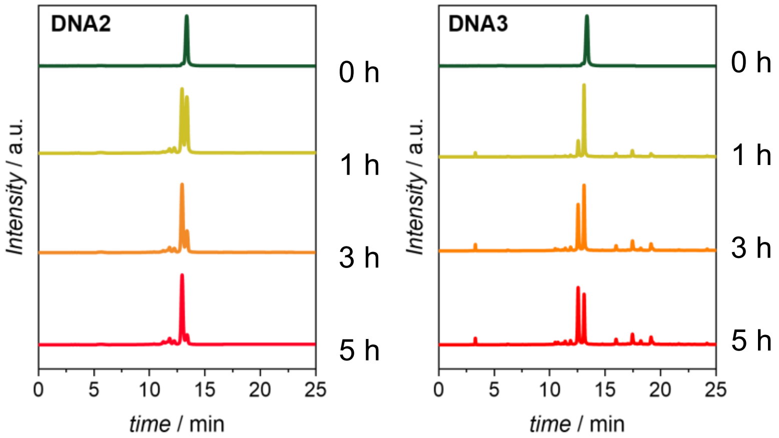

Figure A2: HPLC analysis ($\lambda_{detection}$ = 260 nm) of **DNA2** (left) and **DNA3** (right) after irradiation of 50 µM **DNA2** and 50 µM SQ-modified Atto655 dye **14** (1:1 equivalents) with a 450 nm LED in aqueous media containing 5% DMF, 10 mM Na-P_i buffer and 250 mM NaCl in H_2O in a total volume of 600 µL in a crimp vial for 5 h at 20 °C. Pre-irradiation (dark green line), the chromatograms of both **DNA2** and **DNA3** show one significant peak at t_R = 13.1 min. During irradiation, the peak decreases, and a new peak at t_R = 12.6 min (red line) is formed. The formation of the new peak in **DNA3** is not as significant as it is in **DNA2**, suggesting possible reaction of to **DNA3**. Nevertheless, clear confirmation of the formation of **DNA3** is not possible.

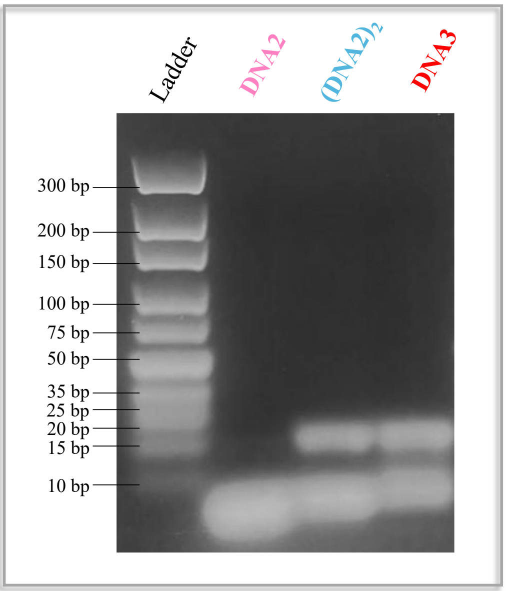

Figure A3: Agarose gel electrophoretic analysis of **DNA3** after irradiation of 50 µM **DNA2** and 50 µM SQ-modified Atto655 dye **14** (1:1 equivalents) with a 450 nm LED in aqueous media containing 5% DMF, 10 mM Na-P_i buffer and 250 mM NaCl in H_2O in a total volume of 600 µL in a crimp vial for 5 h at 20 °C. Staining was performed using SybrGreen™, followed by visualisation under UV light (λ_{exc} = 312 nm). Lane 1 shows the commercial DNA marker. Lane 2 displays **DNA2** (pre-irradiation) with one gel band with the smallest size of all three lanes. **(DNA2)₂** in lane 3 shows two gel bands, one in the same position as lane 2 and one located between 15 bp and 20 bp in comparison to the marker in lane 1. Therefore, the smaller sized fragment can be assigned to the starting material **DNA2** whereas the larger sized fragment describes the dimerization product of **DNA2** to **(DNA2)₂**. **DNA3** is expected to feature a band between **DNA2** and **(DNA2)₂**. However, lane 4 displays the same wo fragments as lane 3, indicating no reaction between **DNA2** and the SQ-modified Atto655 dye **14**, but favoured reaction to homo-dimerized **(DNA2)₂**.

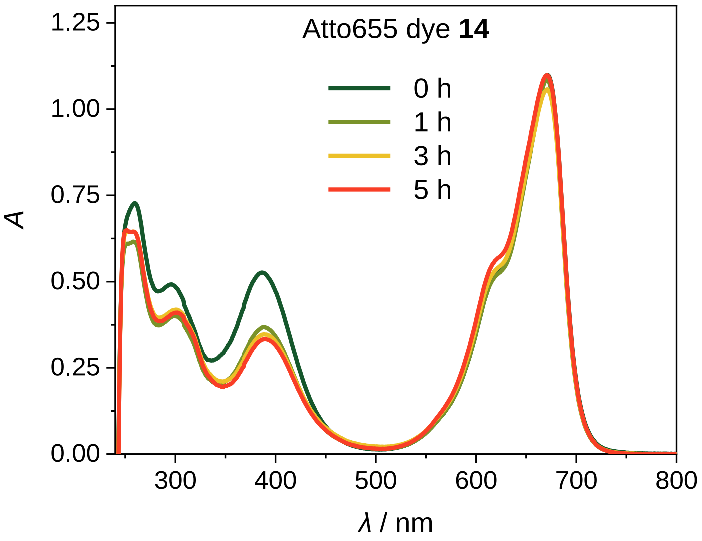

Figure A4: UV/Vis spectroscopic analysis of 50 µM SQ-modified Atto655 dye **14** after irradiation with a 450 nm LED in aqueous media containing 5% DMF, 10 mM Na-P_i buffer and 250 mM NaCl in H_2O in a total volume of 600 µL in a crimp vial for 5 h at 20 °C. Pre-irradiation (dark green line), the dye shows three distinctive absorbance maxima at λ_{max1} = 260 nm, λ_{max2} = 298 nm and λ_{max3} = 397 nm associated with the SQ moiety and λ_{max4} = 655 nm, which displays the excitation maximum of the Atto655 dye. During irradiation, one new maximum is emerging at λ = 325 nm, whereas the assigned SQ maximum at λ = 397 nm is decreasing (red line), suggesting homo-dimerization between two Atto655 dyes. The assigned Atto655 maximum at λ_{max4} = 655 nm remains unchanged, confirming the stability of the dye after 5 h of irradiation.

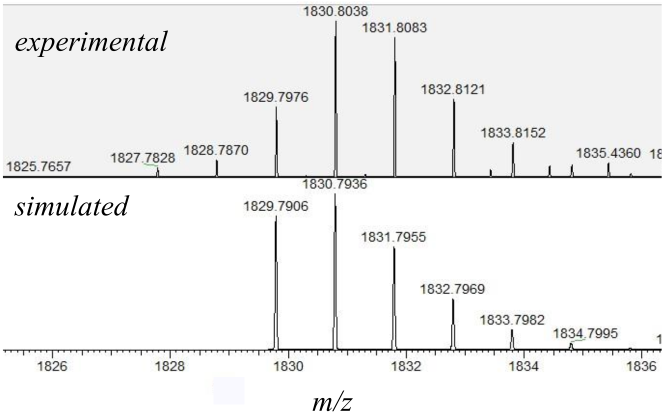

Figure A5: ESI-HRMS analysis of homo-dimerized Atto655 dye **(14)₂**: m/z_{theo} = 1829.7906 for $[C_{100}H_{113}N_{14}O_{16}S_2^-]$, m/z_{exp} = 1829.7976. After successful reaction of SQ-modified Atto655 dye **14** with itself to homo-dimerized Atto655 dye **(14)₂** through [2+2] cycloaddition of the two SQ moieties the resulting product features double the molecular weight. Although occurring as a competing reaction, the homo-dimerization between two fluorophore dyes was neither detectable though gel electrophoresis due to too low molecular weight nor distinguishable from hetero-dimerization of **DNA2** to **DNA3** in UV/Vis spectra. As this reaction is not interfering with the DNA strand itself, it is of minor concern.

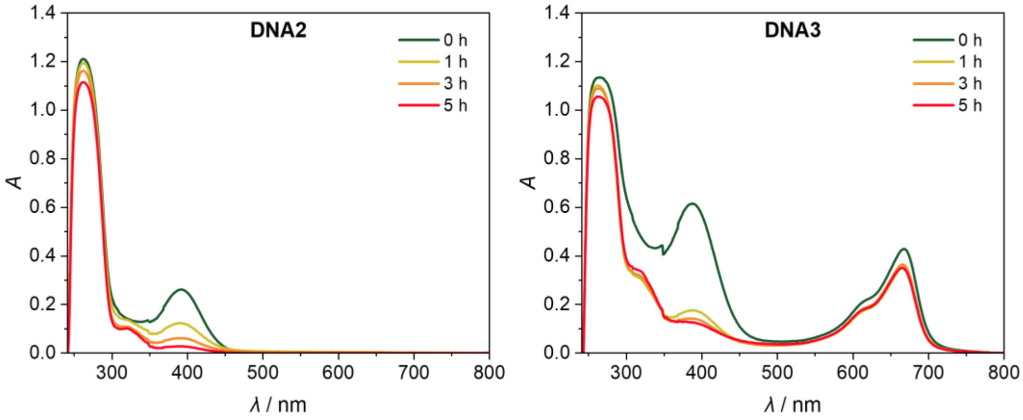

Figure A6: UV/Vis spectroscopic analysis of **DNA2** (left) and **DNA3** (right) after irradiation of 50 µM **DNA2** and 250 µM SQ-modified Atto655 dye **14** (1:5 equivalents) with a 450 nm LED in aqueous media containing 5% DMF, 10 mM Na-P$_i$ buffer and 250 mM NaCl in H_2O in a total volume of 600 µL in a crimp vial for 5 h at 20 °C. Pre-irradiation (dark green line), **DNA2** and **DNA3** both show two distinctive absorbance maxima at λ_{max1} = 260 nm, associated with the DNA absorbance and λ_{max2} = 397 nm, associated with the SQ moiety. Furthermore, **DNA3** shows a third maximum at λ_{max3} = 655 nm, that can be assigned to the Atto655 dye. During irradiation, one new maximum is emerging at λ = 325 nm whereas the assigned SQ maximum is decreasing (red line). Nevertheless, **DNA2** and **DNA3** predominantly show similar changes in absorbance after 5 h of irradiation, making clear differentiation and conclusion about the formation of **DNA3** challenging.

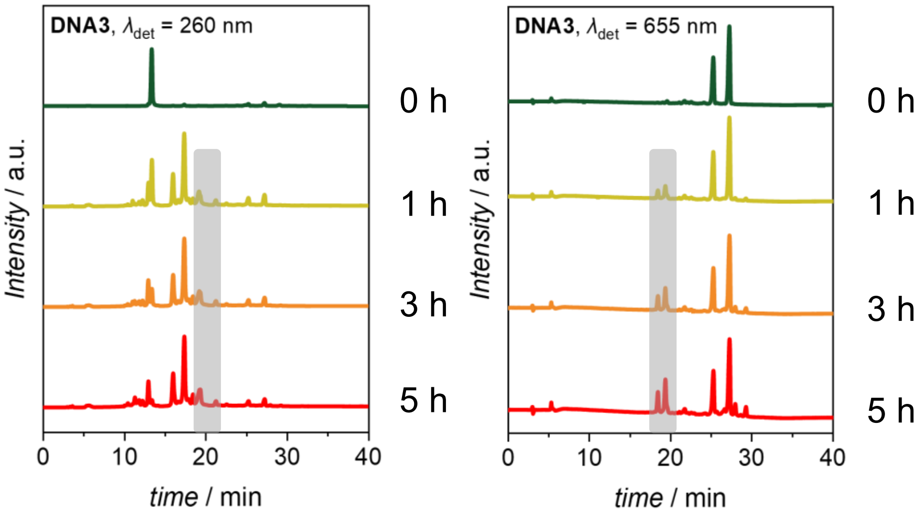

Figure A7: HPLC analysis with $\lambda_{detection}$ = 260 nm (left) and $\lambda_{detection}$ = 655 nm (right) of **DNA3** after irradiation of 50 µM **DNA2** and 250 µM SQ-modified Atto655 dye **14** (1:5 equivalents) with a 450 nm LED in aqueous media containing 5% DMF, 10 mM Na-P$_i$ buffer and 250 mM NaCl in H_2O in a total volume of 600 µL in a crimp vial for 5 h at 20 °C. The signals at t_R ~ 13 min represent **DNA2/(DNA2)$_2$**. Four new peaks are forming and increasing over the course of irradiation at t_R = 15.9, 17.4, 18.5 and 19.2 min. The last two peaks (t_R = 25 and 27 min) at $\lambda_{detection}$ = 655 nm (right) are assigned to the SQ-modified Atto655 dye. As two new peaks develop and increase at t_R = 18.5 and 19.2 min (gray shaded area), both showing absorbance at λ_1 = 260 nm and λ_2 = 655 nm, they suggest formation of **DNA3**. However, the HPLC results of **DNA3** are not as convincing as HPLC analyses of homo-dimerization to **(DNA2)$_2$**.

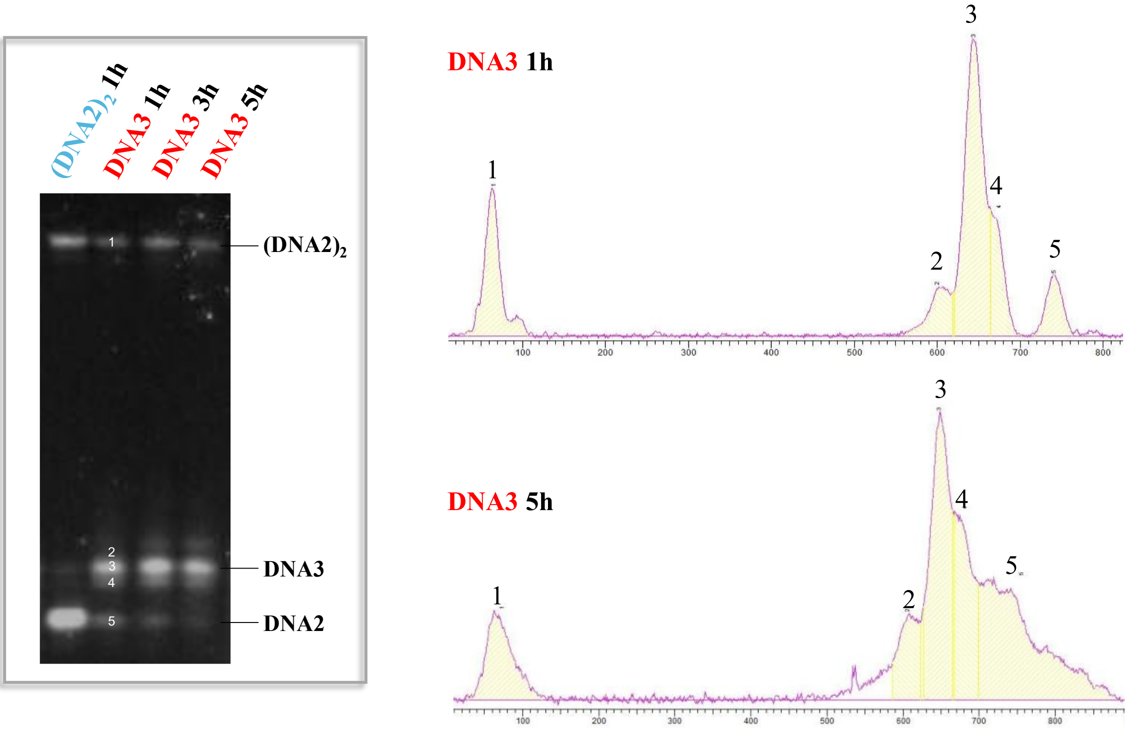

Figure A8: PAGE analysis (left) and yield determination (right) of **DNA3**. The software for the yield determination recognised five bands in total.

Table A1: Determined yields after irradiation of **DNA2** with fivefold excess of SQ-modified Atto655 dye **14** for 1 h and 5 h with a 450 nm LED.

Product	**Yield / % (t_{irr} = 1 h)**	**Yield / % (t_{irr} = 5 h)**
DNA2	24	7
DNA3	58	58
($DNA2)_2$	18	35

7.2 Action Plots for Photochemical Release Systems

Table A2: Detailed specifications of the laser and results of the kinetic experiments of coumarin-modified compound **24**.

	λ / nm	t_{irr} / s	E / µJ	# Photons	# Photons / µmol	Consumption / %
1	388	0	0	0	0	0
2	388	30	323	3.49×10^{17}	0.579	22.5
3	388	60	320	6.97×10^{17}	1.16	46.6
4	388	90	326	1.05×10^{18}	1.74	58.8
5	388	120	295	1.39×10^{18}	2.31	70.6
6	388	180	285	2.09×10^{18}	3.48	80.6
7	388	240	282	2.79×10^{18}	4.58	85.3
8	388	300	272	3.49×10^{18}	5.80	88.9

Table A3: Detailed specifications of the laser and results of the kinetic experiments of perylene-modified compound **26**.

	λ / nm	t_{irr} / min	E / µJ	# Photons	# Photons / µmol	Consumption / %
1	441	0	0	0	0	0
2	441	2	804	4.27×10^{18}	7.09	25.0
3	441	5	744	9.88×10^{18}	16.4	45.2
4	441	10	689	1.83×10^{19}	30.4	58.4
5	441	20	630	3.35×10^{19}	50.6	77.0
6	441	30	542	4.32×10^{19}	71.7	83.5
7	441	60	477	7.60×10^{19}	126	100

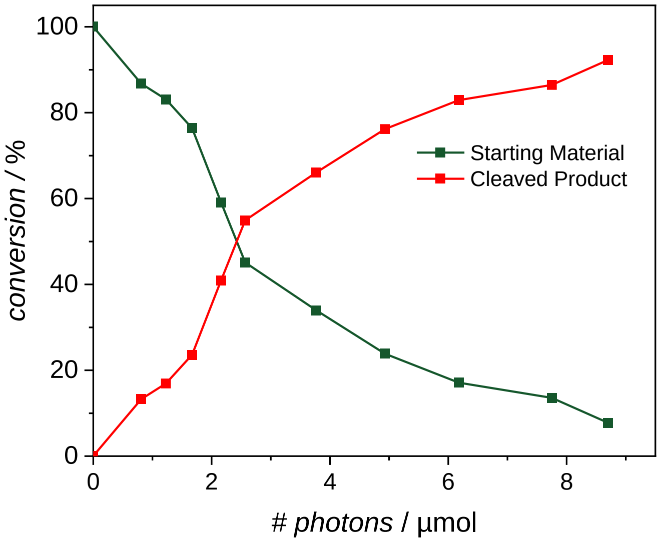

Figure A9: Reaction kinetics of compound **28**. To obtain approximately 25% consumption of the starting material, 1.93 µmol photons need to be deposited into the reaction system.

Table A4: Detailed specifications of the laser and results of the kinetic experiments of valproic acid-modified compound **28**.

	λ / nm	**t_{irr} / s**	**# Photons**	**# Photons / µmol**	**Consumption / %**
1	385	0	0	0	0
2	385	20	4.89×10^{17}	0.812	13.24
3	385	30	7.40×10^{17}	1.23	16.91
4	385	40	1.01×10^{18}	1.67	23.61
5	385	50	1.30×10^{18}	2.16	26.87
6	385	60	1.55×10^{18}	2.57	40.90
7	385	90	2.27×10^{18}	3.77	54.92
8	385	120	2.97×10^{18}	4.93	66.05
9	385	150	3.72×10^{18}	6.18	76.17
10	385	180	4.67×10^{18}	7.75	82.92
11	385	210	5.24×10^{18}	8.70	86.44
12	385	240	5.67×10^{18}	9.42	92.25

8 Acknowledgments

Eingangs möchte ich mich bei meinen Doktorvätern Prof. Dr. Hans-Achim Wagenknecht und Prof. Dr. Christopher Barner-Kowollik bedanken. Ich bedanke mich für die einmalige Chance, meine Doktorarbeit in Form einer Cotutelle-Vereinbarung in beiden Ihrer Labore durchzuführen, die unglaublich schöne Zeit, die ich daher in Karlsruhe und Brisbane verbringen durfte, Ihre Unterstützung und das motivierende Feedback. Herrn Wagenknecht, Ihnen danke ich besonders für den nötigen Freiraum und das entgegengebrachte Vertrauen bei jeder meiner wissenschaftlichen Entscheidungen sowie für das Kennenlernen Ihrer privateren Seite bei gemeinsamen AK-Feierabendbieren, Weihnachtsfeiern oder in Obergurgl. Christopher, dir danke ich für die herzliche Aufnahme in die Macroarc Gruppe, die enge Betreuung von nah und fern und den Versuch, doch noch eine Polymerchemikerin aus mir zu machen sowie für das Verständnis bei wissenschaftlichen und persönlichen Unsicherheiten. Danke, dass Sie beide mich nicht nur zu einer besseren Naturwissenschaftlerin gemacht, sondern maßgeblich zu meiner Persönlichkeitsentwicklung beigetragen haben.

Im Besonderen möchte ich mich bei folgenden Personen bedanken:

- Prof. Dr. Stefan Bräse für die Übernahme des Zweitgutachtens.
- Dr. Andreas Rapp für die Instandhaltung der NMR-Geräte und vor allem die Erreichbarkeit bei Tag und Nacht bei Problemen derselbigen.
- Annette Hochgesand für die schnelle Erledigung meiner (Sonder-)Bestellwünsche, die Messung meiner MALDI-Proben und deinen unermüdlichen Einsatz, wenn die Masse nicht gefunden wurde, sowie für die erfrischenden Gespräche zwischendurch.
- Claudia Sommer für die Unterstützung bei sämtlichen bürokratischen und organisatorischen Dingen und deinen positiven und selbstbewussten Charakter, von dem ich mir einiges abschauen konnte.
- Allen Kollegen aus den Arbeitskreisen Wagenknecht und Barner-Kowollik, die mich in jeder Hinsicht und in jeder Situation unterstützt haben – sei es im Labor, im Büro, beim Aperol-Trinken, beim Karaoke-Singen, beim Wandern, am Strand oder beim Feiern im „Beat“-Megaclub. Die großartigen Tage und Nächte, die wir zusammen verbracht haben, haben

wesentlich zum Erfolg und Spaß an dieser Arbeit beigetragen und für einen wunderbaren Ausgleich gesorgt.

- Florian Feist für die Erklärung des Lasers am INT, den Beistand bei wissenschaftlichen Problemen und die Hilfe bei der Messung meiner LC-MS Proben.
- Dem Origin-Template- und Import-Assistenten für die Veranschaulichung meiner Daten und Zeitersparnis bei der Analyse.
- Sämtlichen Malle-Interpreten und weiteren Musikern für ihre (kreativen) Hits, mit denen die Arbeit gleich doppelt so viel Spaß gemacht hat.
- Meinen beiden Vertieferstudenten Jan Kunzmann und Viktor Guschin für eure Mithilfe und das Interesse an meinen Forschungsprojekten und für euren aufgeschlossenen und humorvollen Charakter, der die Zusammenarbeit mit euch so angenehm gemacht hat.
- Kerstin Müller für die Hilfe am DNA-Synthesiser und deine ruhige, liebe Art sowie dein offenes Ohr.
- Anna-Lena Ruopp, Simon Heckmeier, Sebastian Häcker und Silas Leidenheimer für die zwar kurze, aber dennoch denkwürdige Zeit, die ich nach meiner Rückkehr aus Australien an sämtlichen Weihnachts- oder Doktorfeiern und Einständen im AKW mit euch verbringen konnte.
- Allen Kollegen aus Labor 203. Sven Klehenz, danke, dass die Bierkasse in dir einen mehr als würdigen Nachfolger gefunden hat – allein schon, weil plötzlich per PayPal gezahlt werden kann. Danke für die vielen Kaffeepausen und Feierabendbiere, die mir sehr dabei geholfen haben, mich im AKW wieder einzufinden und dafür, dass du mir Bangerz wie „Alarm“ und „For Those About To Rave“ gezeigt hast. Madeleine Giraud, danke für deinen Beistand beim TosoX-Workshop sowie deine mitfühlende und strukturierte Art und deine Organisationsbereitschaft, von der ich mir einiges abschauen müsste. Danke auch für deine Liebe zum Gossip und die vielen langen und witzigen Gespräche, die sich daraus entwickelten. Eileen List, danke, dass du jeden Tag aufs Neue beweist, dass schicke Kleidung und (Synthese)-Chemie sich nicht ausschließen und du mich so oft durch deine „Ketscher Dorfkind-Art“, die tief im Inneren in dir schlummert, so sehr zum Lachen gebracht hast! Danke auch für deine Hilfsbereitschaft und dafür, dass alles so entspannt und einfach mit dir ist.
- Allen Kollegen aus dem Nachbarlabor 204. Andreas Schmidt aka andreas.schmidt3, danke für die vielen Spaziergänge, unseren wunderbaren badischen Dialekt und deine liebens-

würdige, urdeutsche und lokal-patriotische Art. Danke für's Zuhören und dafür, dass wir stets sehr offen und ehrlich über alles reden können. Mathis Mitha (Mathis mit H), danke für deine unterhaltsamen Stories, die die ein oder andere unerwartete, aber auch fragwürdige Wendung genommen haben und deinen ehrlichen, norddeutschen Charakter. Danke für die ständigen Hinweise, wo man günstig (oder gar kostenlos!) Essen abgreifen kann und für deine Extrovertiertheit, sodass es in der Mittagspause nie still wurde. Lukas Frey danke ich für die überlegte und fleißige Art und für deine trockenen Sprüche, die mich öfter zum Schmunzeln gebracht haben. Jan Kunzmann, danke, dass du es immer mit Humor genommen hast, wenn wir Witze über deine nicht vorhandenen Computer-Skills gemacht haben. Was nicht ist, kann ja noch werden! Danke an Maren Schrödter, dafür dass du mir deine Nudeln mit Pesto à la Maren Spezial gezeigt hast sowie deine Kreativität und deine Zeichenkünste, durch die jede Geburtstagskarte so wunderschön und persönlich wurde. Danke auch für die Realisierung des AK-Wappens und die ständige Versorgung mit sehr gutem Prosecco! Nicola Seul, danke dafür, dass wir unsere Reise im AK Wagenknecht gemeinsam begonnen haben und auch gemeinsam abschließen werden und am Ende doch noch alles hingehauen hat – Ich bin genauso überrascht wie du! Danke für sämtliche gemeinsame Aperol- oder Lillet-Abende, Sportsessions und Kurzurlaube nach Konferenzen, bei denen du mir mit deiner entspannten und rationalen Art gezeigt hast, dass man nicht immer alles zerdenken muss. Danke für deine Freundschaft, die hoffentlich auch zukünftig bestehen bleibt.

- Meinen Laborkollegen aus Labor 205. Danke dir, Bastian Pfeuffer (Sebastian Pfeiffer), für die Einführung in die Welt des Deutsch-Raps, deine humorvolle, harmoniebedürftige Art und deine herzliche, ansteckende Lache! Danke für dein entgegengebrachtes Vertrauen und dafür, dass ich dir ausnahmslos alles erzählen kann. Danke für unser sehr gutes Verhältnis, das sich in den letzten drei Jahren richtig gefestigt hat und für sämtliche Aperoli, die wir zusammen gesippt haben. Lisa Rieger, danke, dass ich mich immer auf dich verlassen, dich zu jeder Tages- und Nachtzeit auch vom anderen Ende der Welt aus anrufen kann und du immer für mich da bist. Danke für deinen allemannischen Dialekt beim Reden mit Rolf und Claudia, deinen Humor, deinen herzlichen, starken Charakter und dafür, dass ich so unglaublich viele Sachen von dir lernen konnte, allen voran Kommunikation, Selbstwert und Ehrlichkeit. Danke, dass wir immer zusammenhalten – ich freue mich schon auf die kommenden Jahrzehnte mit dir. Wegen euch beiden bin ich die letzten drei Jahre immer mit einem Lächeln auf den Lippen ins Labor gelaufen und hätte mir keine besseren Laborpartner vorstellen können.

- Fabian Weick und Sven Schneider, danke euch für insgesamt zehn gemeinsame Jahre Chemiestudium inklusive Promotion am KIT. Fabi, danke für die Idee zum AK-Wappen und dafür, dass oftmals ein Bier ausgereicht hat, damit du in deinen charmanten Kurpfälzer-Dialekt abdriftest. Danke auch für den Fahrradunfall, der im Endeffekt dazu geführt hat, dass ich nun ein wesentlich besseres Fahrrad nutze und mich nicht mehr mit meinem alten Schrott-Rad abmühen muss. Sven, danke dir für die vielen Kaffeespaziergänge und dafür, dass du mich immer zum Lachen bringst. Auch wenn es ungefähr neun Jahre gedauert hat, bis ich dich vernünftig kennenlernen durfte, find ich's jetzt umso schöner und ein Tag ohne Kontakt zu dir fühlt sich einfach nicht mehr richtig an. Danke euch beiden, dass wir oftmals die gleichen Ansichten teilen und sehr offen und ehrlich über alles reden können.
- Meinen Freunden aus fünf Jahren Biochemie-Studium. Nicolai Schaefer, danke, dass wir uns seit Tag 1 unseres Studiums kennen und wir uns trotz deines Studiengangwechsels nicht aus den Augen verloren haben. Danke, für deine lebensbejahende Art und dass du immer du selbst bist. Hannah Buntz, danke für die vielen (ungewollten) Wodka-Ahoi-Shots, deine quirlige Art und dafür, dass du immer Fotos gemacht hast, wodurch wir sehr viele schöne Erinnerungen haben! Juliana Pfeifer und Felix Ott, danke, dass ihr den weiten Weg auf euch genommen und mich in Australien besucht habt. Ich würde mich sehr freuen, nochmal zusammen zurückzukehren! Juli, danke dir für deine aufgeweckte Art, sobald du dich wohlfühlst und für den dringend notwendigen Tequila-Nachschub an Maikes Hochzeit. Felix, danke für deinen ruhigen, neutralen, aber bestimmten Charakter und deine natürliche Einstellung was das Leben anbetrifft. Danke, dass du immer dich und deine Meinung vertrittst und dabei sachlich und konstruktiv bleibst. Aaron Seider, danke, dass du jederzeit bereit bist, mit mir die neuesten Kinostreifen anzuschauen und mir dabei mit vielen FunFacts und EasterEggs geduldig die Hintergründe erklärst. Danke für deine aufgeschlossene, unvoreingenommene und unfassbar witzige Art und dafür, dass ich dir vor allem seit den letzten vier Jahren ausnahmslos alles anvertrauen kann.
- Patricia Merschel und Moritz Dreßler, danke, dass ich mich oftmals Samstagabend selbst zu euch einladen durfte und ihr mich immer aus meinem Chemie-Alltag rausgeholt habt. Danke,

dass die Freundschaft mit euch so einfach und unkompliziert funktioniert, sogar wenn wir ein Jahr fast nichts voneinander hören.

- Meinen Freundinnen aus der Heimat, insbesondere Nina Hensel. Danke, für deine Freundschaft seit der Grundschule und dafür, dass ich bei dir stets die Sorgen der Promotion vergessen konnte. Danke, dass du immer du selbst bleibst und mir ehrlich deine Meinung sagst.
- Meiner Familie, besonders meinen Eltern Alice und Gebhard, meinem Bruder Raphael und meiner Schwägerin Katrin. Danke für euer Vertrauen, eure Liebe und die bedingungslose Unterstützung in allen Lebenslagen. Mama und Papa, danke, dass ihr mir die richtigen Werte vermittelt und Grenzen aufgezeigt, aber dabei genügend Freiraum gelassen habt, meine Persönlichkeit zu entwickeln. Raphael und Katrin, danke, dass wir immer zusammenhalten, ihr immer Zeit für mich findet und immer an mich glaubt.
- Max, danke, dass du mich von Anfang an bei meinem Australien-Aufenthalt unterstützt hast und für die Sicherheit und das Vertrauen, das du mir entgegenbringst. Danke für all den Spaß, den wir bei unseren Dates zusammen haben und dafür, dass du mich jeden Tag aufs Neue zum Lachen bringst. Danke für die vielen Kleinigkeiten wie z.B., dass du das Endstück vom Brot isst, die Schleifchen-Nudeln für deinen Geschmack zu lange kochst, nur weil ich’s so lieber mag oder die „previously on“-Zusammenfassung bei Serien mit mir schaust, obwohl wir beide eigentlich wissen, was in der Folge zuvor passiert ist. Danke, dass ich auch nach drei Jahren noch neue Eigenschaften an dir kennenlerne. Ich kann es nicht abwarten, endlich das nächste Kapitel mit dir aufzuschlagen.

9 Curriculum Vitae

Name	Rita Tabea Michenfelder
Languages	German (native), English (proficient)

Education

02/2021-04/2024	**Joint PhD** Candidate Group of Prof. Dr. Hans-Achim Wagenknecht Karlsruhe Institute of Technology, Germany and Group of Prof. Dr. Christopher Barner-Kowollik Queensland University of Technology, Australia
08/2019-02/2020	**Internship** *Agilent Technologies* UV-Curing Concepts for ScreenTape Technology Waldbronn, Germany
04/2018-01/2021	**Master** of Science, Chemical Biology Karlsruhe Institute of Technology Final Grade: 1.2
10/2014-03/2018	**Bachelor** of Science, Chemical Biology Karlsruhe Institute of Technology Final Grade: 2.0
09/2005-07/2013	General higher education entrance qualification (**Abitur**) Windeck-Gymnasium Bühl Grade: 1.8

9.1 Publications

1) *DNA Labelling in Live Cells via Visible Light-Induced [2+2] Photocycloaddition*

   R. T. Michenfelder, L. Delafresnaye, V. X. Truong, C. Barner-Kowollik, H.-A. Wagenknecht, *Chem. Commun.* **2023**, *59,* 4012-4015.

   DOI: 10.1039/D3CC00817G

   Parts of this publication have been represented in the current thesis (please refer to chapter 3, p. 31 ff.)

2) *Photochemical Action Plots Map Orthogonal Reactivity in Photochemical Release Systems*

   R. T. Michenfelder, F. Pashley-Johnson, V. Guschin, L. Delafresnaye, V. X. Truong, H.-A. Wagenknecht, C. Barner-Kowollik, *Adv. Sci.* **2024**, *11*, 2402011.

   DOI: 10.1002/advs.202402011

   Parts of this publication have been represented in the current thesis (please refer to chapter 4, p. 57 ff.)

3) *Cyclopropenes as Chemical Reporters for Dual Bioorthogonal and Orthogonal Metabolic Labelling of DNA*

   N. Seul, D. Lamade, P. Stoychev, M. Mijic, **R. T. Michenfelder**, L. Rieger, P. Geng, H.-A. Wagenknecht, *Angew. Chem. Int. Ed.* **2024**, *63*, e202403044.

   DOI: 10.1002/anie.202403044

9.2 Conferences and Oral Presentations

14/09/2023-15/09/2023	**Poster Award** and Oral Presentation XI. Nukleinsäurechemie-Treffen 2023, DNG Würzburg, Germany
21/04/2023	Oral Presentation Royal Australian Chemical Institute (RACI) Symposium at Queensland University of Technology Brisbane, Australia
03/11/2022	Oral Presentation Queensland Annual Chemistry Symposium (QACS) at University of Queensland Brisbane, Australia
29/06/2022-01/07/2022	Poster Presentation Biochemistry, GDCh Münster, Germany
15/09/2021-17/09/2021	Poster Presentation X. Nukleinsäurechemie-Treffen 2021, DNG Bad Herrenalb, Germany

9.3 Student Supervision

November 2023	Supervision of „organisch-chemisches Grundpraktikum für Studierende der Chemie“
October 2023	Supervision of Vertieferarbeit Viktor Guschin
September 2023	Supervision of „organisch-chemisches Fortgeschrittenen-Praktikum für Studierende der Chemie“
January 2022	Supervision of Vertieferarbeit Jan Kunzmann
November 2021	Supervision of „organisch-chemisches Fortgeschrittenen-Praktikum für Studierende der Chemie“
September 2021	Supervision of „organisch-chemisches Grundpraktikum für Studierende der Chemie“
June 2021	Supervision of „organisch-chemisches Fortgeschrittenen-Praktikum für Studierende der Chemie“
March 2021	Supervision of „organisch-chemisches Grundpraktikum für Studierende der Chemie“